Interphase Growth Kinetics and the Partial Electronic Conductivity of Constituents in Sulfide Solid-State Batteries

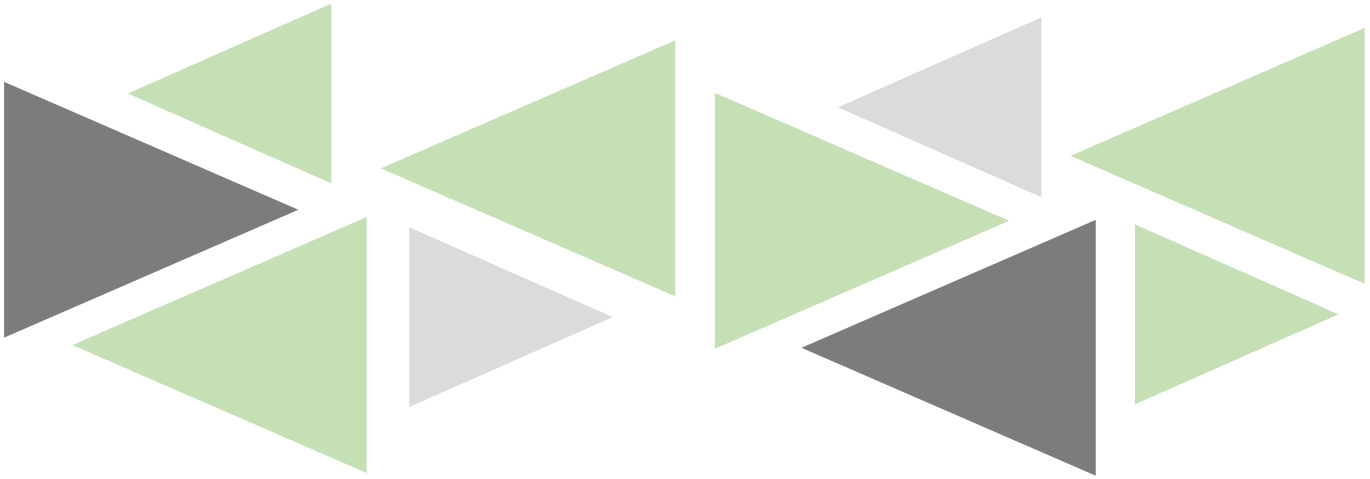

Dissertation

zur Erlangung des akademischen Grades

Doktor der Naturwissenschaft

– Dr. rer. nat. –

vorgelegt dem

Fachbereich 08 – Biologie und Chemie

der Justus-Liebig-Universität Gießen

von

Christoph Daniel Alt

———— Juni 2025 ————

Dekan/Dean	Prof. Dr. Holger Zorn
1. Gutachter / 1st Reviewer	Prof. Dr. Dr. h. c. Jürgen Janek
2. Gutachter / 2nd Reviewer	Prof. Dr. Matthias T. Elm

Eingereicht / Submitted	11.06.2025 / 06/11/2025

Erklärung

Die vorliegende Arbeit wurde im Zeitraum vom 01.08.2021 bis 04.03.2025 am Physikalisch-Chemischen Institut der Justus-Liebig-Universität Gießen unter Betreuung von Prof. Dr. Dr. h.c. Jürgen Janek angefertigt.

Ich erkläre: Ich habe die vorgelegte Dissertation selbstständig und ohne unerlaubte fremde Hilfe und nur mit den Hilfen angefertigt, die ich in der Dissertation angegeben habe. Alle Textstellen, die wörtlich oder sinngemäß aus veröffentlichten Schriften entnommen sind, und alle Angaben, die auf mündlichen Auskünften beruhen, sind als solche kenntlich gemacht. Ich stimme einer evtl. Überprüfung meiner Dissertation durch eine Antiplagiat-Software zu. Bei den von mir durchgeführten und in der Dissertation erwähnten Untersuchungen habe ich die Grundsätze guter wissenschaftlicher Praxis, wie sie in der „Satzung der Justus-Liebig-Universität Gießen zur Sicherung guter wissenschaftlicher Praxis“ niedergelegt sind, eingehalten.

Gießen, den 11.06.2025

_____

Christoph D. Alt

Declaration

This dissertation was prepared and written between 08/01/2021 and 03/04/2025 at the Institute of Physical Chemistry at Justus Liebig University Giessen under the supervision of Prof. Dr. Dr. h.c. Jürgen Janek.

I declare that I have completed this dissertation single-handedly without the unauthorized help of a second party and only with the assistance acknowledged therein. I have appropriately acknowledged and cited all text passages that are derived verbatim from or are based on the content of published work of others, and all information relating to verbal communications. I consent to the use of an anti-plagiarism software to check my thesis. I have abided by the principles of good scientific conduct laid down in the charter of the Justus Liebig University Giessen „Satzung der Justus-Liebig-Universität Gießen zur Sicherung guter wissenschaftlicher Praxis“ in carrying out the investigations described in the dissertation.

Giessen, 06/11/2025

_____

Christoph D. Alt

Abstract

Large-scale electrification of transportation and advancements in energy storage are key to achieving net-zero emissions. Solid-state batteries present a promising energy storage solution, expected to enable the use of high-capacity electrode materials such as lithium metal and lithium alloys, while also improving safety. However, effectively integrating high-capacity electrode materials remains a key challenge in unlocking the potential of solid-state batteries.

The high reactivity of lithium metal poses both safety and operational challenges, leading to dendrite formation and loss of active redox species (*i.e.*, long-term capacity fading). Since most inorganic solid electrolytes undergo reduction upon contact with alkali metal, the corresponding interphase formation and the resulting long-term increase in cell resistance are often underestimated. However, interphase kinetics and the consequent impact on cell performance strongly depend on the composition and properties of the reaction products. Revealing the interphase composition, growth kinetics, and the influence and role of its individual constituents is crucial for developing protective strategies and enhancing material compatibility.

Within this doctoral thesis, the intrinsic transport properties and growth kinetics of the interphase and its constituents for lithiated Li_6PS_5Cl are investigated, emphasizing their impact on long-term cell operation. Following the quantification of the interphase's partial conductivities through bulk-material synthesis, which revealed a significant resistance contribution over the battery's lifespan, conventional physiochemical concepts were revisited. The Wagner diffusion model, predicting diffusion-controlled interphase growth based on experimental data, was analyzed for solid|solid interfaces alongside the Hebb-Wagner method for accurately quantifying low electronic conductivities in lithium-ion conductors. The former addressed the influence of different interface morphologies on evaluating interphase rate constants by impedance measurements, while the latter revealed the partial electronic conductivity of lithium halides (*i.e.*, LiCl, LiBr, and LiI) present in various interphases.

Alloy electrodes, owing to their higher electrode potentials relative to lithium metal, are expected to cause reduced degradation of sulfide solid electrolytes. In this context, $In/(InLi)_x$ electrodes – prominent for exhibiting a stable potential of 0.62 V *vs.* Li^+/Li – were first investigated to assess how preparation influences electrode microstructure and performance. Controlling microstructure is critical to avoid current constriction and ensure consistent operation. Studies on thin indium films deposited on current collectors offered insights into interphase growth kinetics at alloying interlayers – an essential challenge for reservoir-free cells – and highlighted the gradual degradation of Li_6PS_5Cl at the electrode potential of $In/(InLi)_x$.

Overall, this doctoral thesis advances the fundamental understanding of intrinsic degradation processes at the electrode|electrolyte interface. In particular, this work provides a new perspective on how multiphase interphases form and evolve over time, depending on their partial ionic and electronic transport properties. It delivers essential insights on previously inaccessible kinetic parameters that now enable more accurate computational simulations, improve the prediction by analytical models, and guide the rational design of more stable materials and interfaces to minimize capacity losses in (reservoir-free) solid-state batteries.

Zusammenfassung

Die Elektrifizierung des Verkehrs und Fortschritte bei der Energiespeicherung sind ein wichtiges Ziel in der Verringerung von Emissionen. Festkörperbatterien haben sich als vielversprechende Energiespeicherlösung etabliert, um Elektrodenmaterialien mit hohen Kapazitäten einzusetzen, während gleichzeitig eine höhere Sicherheit erreicht werden könnte. Die Integration von Elektrodenmaterialien bleibt jedoch eine zentrale Herausforderung, um das Potenzial von Festkörperbatterien voll auszuschöpfen.

Die Reaktivität von Lithiummetall führt zur Bildung von Dendriten, welche den sicheren Betrieb und die langfristige Speicherkapazität einschränken. Da sich viele anorganische Festelektrolyte bei Kontakt mit Alkalimetallen zersetzen, werden die Auswirkungen von entstehenden Zwischenphasen häufig unterschätzt. Die daraus resultierenden Auswirkungen auf die Zellleistung hängen jedoch stark von der Zusammensetzung und den Eigenschaften der Reaktionsprodukte ab. Untersuchungen der Zusammensetzung, der Wachstumskinetik und der Rolle einzelner Bestandteile sind für die Entwicklung von Stabilisierungsstrategien und der Verbesserung der Materialkompatibilitäten unerlässlich.

In dieser Dissertation werden Transporteigenschaften, die Wachstumskinetik und Bestandteile von Zwischenphasen an der Li|Li_6PS_5Cl-Grenzfläche untersucht. Die Bestimmung der Teilleitfähigkeiten durch Bulk-Material-Synthese verdeutlicht einen signifikanten Widerstandsbeitrag durch entstehende Zwischenphasen über die Lebensdauer einer Batterie. Ein Modell zur Vorhersage des diffusionskontrollierten Zwischenphasenwachstums auf der Grundlage experimenteller Daten wurde ebenso analysiert wie die Hebb-Wagner-Technik zur genauen Bestimmung der elektronischen Teilleitfähigkeit in Lithiumionenleitern. Ersteres befasste sich mit potenziellen Fehlerquellen der Interpretation von Impedanzmessungen zur Vorhersage des Zwischenphasenwachstums, während letzteres die partielle elektronische Leitfähigkeit von Lithiumhalogeniden (LiCl, LiBr und LiI) untersuchte, die in vielen Zwischenphasen vorkommen.

Aufgrund ihres höheren Elektrodenpotenzials wird Legierungsanoden ein geringer Zerfall von sulfidischen Festelektrolyten zugesprochen als bei metallischem Lithium. In/$(InLi)_x$-Elektroden – die ein stabiles Potenzial von 0,62 V *vs*. Li^+/Li auszeichnet – wurden präpariert, um den Einfluss der Mikrostruktur auf die Leistungsfähigkeit der Elektrode zu untersuchen. Untersuchungen an dünnen Indiumschichten boten dagegen Einblicke in die Zwischenphasenentwicklung an Legierungen – eine wesentliche Herausforderung zur Umsetzung von Reservoir-freie Zellen – und verdeutlichten den allmählichen Zerfall von Li_6PS_5Cl in Kontakt mit In/$(InLi)_x$.

Diese Dissertation leistet einen wesentlichen Beitrag zum Verständnis von Degradationsprozessen an der Elektrode|Elektrolyt-Grenzfläche in Festkörperbatterien. Sie liefert neue Erkenntnisse darüber, wie sich Zwischenschichten in Abhängigkeit ihrer partiellen Leitfähigkeiten zeitlich entwickeln. Dabei werden bislang unzugängliche kinetische Parameter quantifiziert, die genauere Simulationen ermöglichen, die Vorhersagekraft analytischer Modelle verbessern und die gezielte Entwicklung stabilerer Materialien und Grenzflächen anleiten – insbesondere zur Minimierung von Kapazitätsverlusten in (reservoir-freien) Festkörperbatterien.

Preliminary Remarks

The terms 'negative' and 'positive' electrode should be used to address both electrodes correctly. During discharge, oxidation and reduction reactions occur at the 'negative' and 'positive' electrodes, respectively. However, this is reversed during charging. Therefore, the terms 'anode' and 'cathode' are imprecise. However, in order to avoid confusion, this thesis will conform to commonly used terminology. The terms 'anode' and 'cathode' (as defined by the reactions during discharge) are used for the 'negative' and 'positive' electrodes, respectively.

This thesis thoroughly discusses the instability of the anode interface and the decomposition reactions of solid electrolytes in contact with lithium metal. It is important to note that the (electro-)chemical instability of electrolytes in contact with cathode materials and resulting interphase formation (commonly referred to as cathode electrolyte interphase, CEI) should not be overlooked. However, this topic lies outside the scope of this work and will not be discussed in detail.

Generative AI and AI-assisted technology was utilized in the preparation of this thesis to improve readability and language. Specifically, *ChatGPT 3.5* (by OpenAI) was employed with the command prompt: "Rephrase the following text without changing or adding content." Following the use of this tool, the author thoroughly reviewed and edited content and language, if necessary, and takes full responsibility for the final content of the present thesis.

Contents

1. Introduction

As of March 2025, the recent withdrawal of the United States from the Paris Climate Agreement places global efforts under significant strain. The impact of this decision on the agreed goal of limiting global temperature rise to 1.5 °C above pre-industrial levels remains uncertain. Without reductions in greenhouse gas emissions, the increasing risk of severe environmental catastrophes poses an escalating threat to plants, animals, and human life.[1–3]

The global transition to renewable energies has gained significant momentum in recent years, with solar and wind energy at the forefront.[4] To address periods of low energy generation due to the intermittent nature of renewable energy, surplus energy (*e.g.*, at night) must be stored efficiently. The transition from combustion-based transportation also requires the use of rechargeable batteries to reduce emissions and improve efficiency for mobile applications.[5]

In the 1980s, lithium-ion batteries (LIBs) with liquid electrolytes (LEs) were developed and have since become the leading battery technology for both mobile and stationary applications.[6,7] Their widespread use is attributed to their high energy and power density, along with excellent cyclability and reliability.[8,9] However, commercial LIBs are approaching their physicochemical limits in terms of energy density, necessitating the development of advanced cell chemistries to meet the growing demands for higher energy and power density, fast-charging, and improved safety.[10] Replacing graphite-based electrodes with lithium metal electrodes (LMEs) or lithium alloys offers possibilities to enhance energy and power densities. Lithium metal provides the highest theoretical storage capacity of 3,861 mAh g^{-1} and the lowest standard redox potential (E_H) of −3.04 V *vs*. SHE.[11] LMEs are expected to enhance storage capacity and enable fast charging, which are key requirements for the automotive sector.[12]

However, the formation of lithium dendrites during cycling of LMEs and the degradation of organic LEs prevent the safe operation of LMEs in LIBs.[13] Initially, it was believed that dense inorganic solid electrolytes (SEs) could inhibit dendrite growth through their mechanical properties, thereby enabling safer operation of LMEs.[14,15] Thus, by replacing flammable organic LEs, SEs with high ionic conductivity at room temperature might enable fast charging for solid-state batteries (SSBs).[16] Sulfide SEs like Li_6PS_5X (X = Cl, Br, I) exhibit high ionic conductivity and facilitate low-temperature processing.[17] Consequently, SSBs incorporating LMEs could surpass conventional LIBs in both performance and safety.[18–20]

Nevertheless, significant challenges remain in developing competitive SSBs.[21] The brittle nature of SEs prevents sufficient accommodation of electrode volume changes.[22,23] This results in contact loss during discharge, as contraction and cracking of cathode active material (CAM) particles occur, leading to poor active material utilization and capacity fading.[22] Similar issues occur for LMEs, where lithium vacancy accumulation during lithium dissolution creates macroscopic pores at the metal|SE interface.[24] These pores cause contact loss during discharge and inhomogeneous lithium deposition during charge, ultimately causing cell failure.[25,26] Early assumptions about the enhanced safety of SEs are increasingly being challenged.[27–29]

Moreover, to avoid the challenging handling of highly reactive lithium metal foils during cell manufacturing,[30,31] so-called 'anode-free' cells or reservoir-free cells (RFCs) can be assembled.[32,33] Here, the LME is formed during the first charging step by electrodeposition of lithium, initially stored in the lithiated CAMs. This eliminates the need for a dedicated lithium reservoir, reducing the cost, weight, and volume of SSBs. However, ensuring the reliable long-term operation of RFCs depends on efficient utilization of active lithium from CAMs and high capacity retention.[34] Thus, contact loss of active material must be prevented,[22] highly uniform morphologies at the metal|SE interface must be achieved, and – often underestimated – parasitic side reactions must be reduced to mitigate severe capacity fading.[34]

Regarding side reactions, many SEs are prone to reduction in contact with electrode materials, leading to gradual degradation over time.[21] In contact with high-voltage materials (*i.e.*, CAMs), many SEs undergo oxidation, whereas contact with lithium metal leads to their reduction (affecting both conventional SSBs with excess lithium and RFCs).[35–37] As a result, interphases comprising various degradation products form at the electrode|SE interface, featuring oxygenated species on the cathode side and fully reduced species on the anode side. Ion-conducting interphases are referred to as solid-electrolyte interphases (SEIs), in line with the analogous interphase in LEs,[38] and exhibit diffusion-controlled (*i.e.*, 'metastable') growth. In contrast, some SEs form mixed conducting interphases (MCIs) upon reduction with electrode materials, which continue to grow until one component is entirely consumed.[39]

While certain SEIs, such as those of $Li_7La_3Zr_2O_{12}$ (LLZO) or lithium phosphorus oxynitride (LiPON), form interphase layers of only a few nanometer in contact with lithium, sulfide SEs are reported to form SEIs with thicknesses extending to hundreds of nanometers.[40–42] Furthermore, interphase formation consumes active lithium, introduces chemomechanical changes, and increases the risk of dendrite growth.[43,44] Despite these challenges, the impact of interphases on the performance of both conventional SSBs and RFCs is often underestimated.

The increased cell resistance caused by SEI formation further limits the competitiveness of practical SSBs compared to conventional LIBs. This is largely influenced by the reaction products and interphase composition, which dictate the interphase kinetics and rate constants. Therefore, a fundamental understanding of the SEI's properties, its growth rate, and the role of individual constituents is essential for effectively stabilizing interphase formation at the electrode|SE interface and predicting its impact on cell performance.

Alloying materials and interlayers are considered promising for mitigating SE degradation and stabilizing interface morphologies in SSBs, while achieving suitable storage capacities. However, SE degradation at the elevated E_H of lithium alloy electrodes (relative to lithium metal) has neither been systematically investigated nor quantified. Consequently, it is often regarded as insignificant, and with only a few reports addressing this issue. But, considering the electrochemical stability window (ESW) of common SEs, their degradation is expected and should not be neglected.[45–47]

In this doctoral thesis, interphase formation between Li_6PS_5Cl (LPSCl) and both LMEs and alloy electrodes was investigated, along with its impact on cell performance. The intrinsic transport properties and growth kinetics of SEIs and their constituents were examined, while the applicability of impedance measurements for assessing interphase growth in solid-state systems was examined. Complemented by studies on In–Li alloy electrodes, this work offers key insights for accurately predicting interphase growth rates, improving lifetime forecasting, and guiding effective stabilization strategies against degradation and capacity loss in SSBs.

In the first publication of this doctoral thesis, titled "*Quantifying Multiphase SEI Growth in Sulfide Solid Electrolytes*", the transport properties and growth kinetics of reduced sulfide SE were investigated by directly reacting LPSCl with lithium metal powder. This approach effectively models multiphase SEIs, as confirmed by X-ray diffraction (XRD) and X-ray photoelectron spectroscopy (XPS), enabling the determination of both the interphase's partial ionic and electronic conductivity. Using the Wagner diffusion model to estimate SEI growth based on both partial conductivities, the findings highlight the significant long-term impact of inherent interphase layers on cell resistance. The insights gained into interphase kinetics, both ionically and electronically, contribute to optimizing the Li|SE interface through SE modifications or the design of protective interlayers to enable the use of LMEs with sulfide SEs.

In the second publication (submitted), titled "*Interphase Formation in Solid-State Batteries: Influence of Contact Conditions on Impedance-Derived SEI Growth Kinetics*", the reliability of monitoring interphase growth by impedance measurements was investigated for assessing interphase kinetics at rigid solid|solid interfaces. Using kinetic parameters from the first publication, 3D transport simulations was employed to simulate impedance signals during diffusion-controlled interphase growth – according to the using the Wagner diffusion model – for different electrode|SE contact conditions. The study revealed how rigid contacts, current constriction, and partially passivated interfaces influence the cell's impedance signals, affecting the interpretation of derived rate constants in time-resolved experiments. These findings highlight the importance of considering experimental conditions – prior to applying analytical models – to ensure accurate estimations of rate constants and interphase growth in SSBs.

While the first publication revealed the effective partial conductivities of the multiphase SEI in lithiated LPSCl, the Wagner diffusion model describes the crucial role of partial electronic conductivity in governing the interphase growth rate. However, experimental data on the electronic properties of relevant interphase constituents remain scarce in battery-relevant contexts.

The third publication, titled "*The Electronic Partial Electronic Conductivity of Lithium Halides and their Role in SEI Formation in Solid-State Batteries – Hebb-Wagner-type Measurements*", highlights the critical importance of minimizing partial electronic conductivity (σ_{el}) to reduce self-discharge and degradation processes in SSBs. Impedance and Hebb-Wagner-type measurements were applied to examine both the partial ionic and electronic conductivity of relevant lithium halides Li*X* (*X* = Cl, Br, and I) across various lithium activities, being SEI constituents of Li_6PS_5X. Formal defect-physical analysis enabled the decoupling of charge

carrier contributions (*i.e.*, electron and electron hole conductivity) to the overall electronic transport. Ultimately, this work emphasizes the necessity of assessing σ_{el} of lithium-ion conductors (*i.e.*, relevant SEs and interphases), while outlining experimental guidelines for testing SEs prone to degradation.

The final section of this thesis is focused on mitigating SE degradation by employing alloy electrodes with E_H closer to the ESW of sulfide SEs. To this end, the preparation, microstructure, and performance of In–Li electrodes were examined, followed by a quantitative analysis on the degradation of LPSCl in contact with In/(InLi)$_x$ electrodes (E_H = 0.62 V *vs*. Li^+/Li).

In the fourth publication, titled "*In–Li Counter Electrodes in Solid-State Batteries – A Comparative Approach on Kinetics, Microstructure, and Chemomechanics*", the electrode performance of different In–Li electrodes was examined from a fabrication perspective, considering them a more reliable alternative to error-prone LMEs for scientific studies. By analyzing planar and particle-based electrodes, it was demonstrated that preparation parameters impact microstructure and kinetics, ultimately affecting the interlaboratory comparability of results. The findings emphasize the inherent limitations of In–Li counter electrodes, which are highly dependent on their microstructure and fabrication protocol. Overall, the findings contribute to advancing alloy electrode development and high-rate solid-state cathode benchmarking.

In the fifth manuscript (in preparation), titled "*Sulfide Solid Electrolyte Degradation with Alloy Electrodes and the Possible Influence of Metal Oxide Layers*", the degradation of LPSCl in contact with In/(InLi)$_x$ electrodes was explored. Evaporated indium thin films were electrochemically titrated in order to quantify SEI growth by the consumption of active species. Factors affecting electrochemical results and interphase formation, such as metal oxide surface layers (*e.g.*, In_2O_3), were identified. In this context, the Wagner diffusion model was also refined for lithium alloy electrodes and their higher E_H to accurately assess the respective SEI rate constant. Although the rate constant was found to be reduced at E_H = 0.62 V *vs*. Li^+/Li of In/(InLi)$_x$ compared to lithium metal, the findings underscore that interphase formation at metal and alloy surfaces remains a significant challenge, limiting the viability of SSBs.

This doctoral thesis makes a significant contribution to both the fundamental understanding and practical development of SSBs by addressing material compatibility and intrinsic degradation processes. Through a combination of established physicochemical concepts and novel experimental methods – developed in this work – transport kinetics of interphases and their constituents were systematically analyzed. The research provides essential insights and quantifies previously inaccessible kinetic parameters, enabling more accurate computational modeling and analytical prediction of capacity losses due to interphase growth, which are critical for reliable lifetime forecasting of SSBs. It also highlights critical limitations in experimentally probing interphase formation by impedance measurements and extends the investigation to lithium alloy electrodes, evaluating and quantifying interphase formation at their respective electrode potentials. Ultimately, the findings emphasize the long-term risks of uncontrolled interphase formation and guide the rational design of mitigation strategies to ensure reliable performance toward tailored materials and interfaces in both conventional SSBs and RFCs.

2. Fundamentals

This chapter provides a comprehensive review of the relevant scientific knowledge found in literature, placing the findings of this doctoral thesis within a broader, scientific context. The primary focus is on the degradation of sulfide SEs at low potentials and the associated growth kinetics, as interphase formation presents a major challenge in integrating alkali metals into SSBs and developing RFCs. Given that the transport properties of the SEI define its growth kinetics, special attention is also devoted to the minor partial electronic conductivity in lithium-ion conductors and its assessment through direct current (dc) Hebb-Wagner measurements.

2.1. Incorporation of Alkali Metal Electrodes in SSBs

Unfortunately, much like in LIBs, the practical use of LMEs in SSBs remains unfeasible at this time, despite being essential to surpass graphite-based LIBs.[10] The solid|solid interfaces in SSBs have limited ability to adapt to morphological changes, which adversely affects their cell lifetime and safety.[10,21,23] Therefore, effectively managing lithium metal deposition (*i.e.*, charging) and dissolution (*i.e.*, discharging) is essential for reliable cell operation. However, controlling interfacial kinetics remains a critical challenge, while the inherent instability of specific inorganic SEs introduces further complications (discussed in Chapter 2.2.). This chapter explores the underlying causes of morphological changes and the associated interfacial kinetics at planar alkali metal|SE interfaces during operation. It illustrates these phenomena exemplarily for LME-based SSBs.

i. Morphological Changes at the Lithium Metal Electrode Interface

Morphological changes during charge and discharge present inherent challenges in developing both lithium-reservoir (*i.e.*, 'conventional') SSBs and RFCs. Thus, understanding interface properties, solid|solid interfaces, and redox processes is of utmost importance to enable stable and reliable operation of SSBs. Figure 1 summarizes the morphological changes occurring at planar Li|SE interfaces during lithium metal dissolution and deposition at the anode side.

During lithium dissolution (*i.e.*, discharging), the segregation of lithium vacancies at the Li|SE interface and their hampered diffusion within the lithium metal serve as the rate-limiting parameter, acting as the kinetic bottleneck that determines the applicable current density.[48] The anodic dissolution of metals at the interface with inorganic SEs, initially described by Schmalzried and Janek for the Ag|SE interface,[49] has recently been extended to the Li|SE interface.[24] Accordingly, lithium atoms are oxidized at the interface, creating vacancies $V_{Li}^{x}(Li)$ and electrons $e'(Li)$ within the lithium metal. Depending on the ion-conduction

process, the resulting lithium ions occupy either a vacancy V'_{Li^+} or an interstitial site in the SE. This charge transfer process can be expressed using the Kroeger-Vink notation:[50]

$$Li_{Li}(Li) \rightleftarrows \left[Li^{x}_{Li^+}(SE) - V'_{Li^+}(SE)\right] + e'(Li) + V^{x}_{Li}(Li) \qquad \text{(eq. 1)}$$

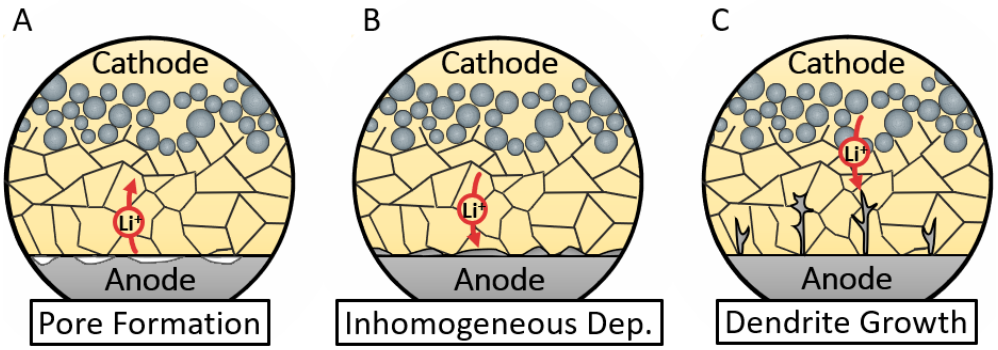

Figure 1: Non-planar morphologies arising during lithium dissolution and deposition in an SSB cell consisting of a composite cathode, solid separator, and planar LME. Failure to adequately compensate for vacancies generated during lithium metal dissolution (*i.e.*, oxidation of lithium atoms) can result in pore formation (A). Similarly, too slow redistribution of adatoms during lithium deposition (*i.e.*, reduction of lithium ions) may lead to inhomogeneous deposition (B) and dendrite growth (C).

With a diffusion flux (j_V), governed by the vacancy diffusion coefficient, vacancies migrate into the bulk of the lithium material to potentially annihilate at a grain boundary or dislocation. This process competes with the applied current density (i_{appl}), which creates a flux $j_{appl} = i_{appl}/(z_{Li^+} \cdot F)$ (with F and $z_{Li^+} = 1$ being the Faraday constant and charge number of lithium ions), resulting in two possible scenarios: (1) if $j_{appl} < j_V$, the injected vacancies are transported into the bulk at a sufficient fast rate, establishing morphologically stable conditions at the interface, and (2) if $j_{appl} > j_V$, vacancies accumulate at the interface, leading to morphological instabilities and the formation of pores at the Li|SE interface (Figure 1A).[51–53]

At room temperature, a critical current density of 0.1 mA cm^{-2} has been estimated for the electro-dissolution of lithium metal.[53] As a result, the limited vacancy diffusion in lithium metal and irregular volume changes present a major challenge for the practical application of SSBs. Particularly, the contact loss at the interface during lithium dissolution contributes significantly to cell polarization (so-called 'current constriction') and current focusing at local contact spots.[52–54] The most common approach to address this limitation is the application of stack pressure, which enhances the effective lithium metal supply through creep and plastic deformation.[54–56] Other strategies to improve the effective j_V include alloying (Chapter 2.1.ii), the development of micro-structured electrodes and interlayers, and microstructural modifications.[57–60] Recent advancements have significantly improved the understanding of the lithium metal's microstructure.[61–64] Using density functional theory, Jäckle *et al.*[65,66] predicted that the lithium self-diffusion is strongly influenced by grain orientations, specifically the

surface terminations where nucleation and diffusion occur. Low energy barriers of 0.14 eV and 0.02 eV have been calculated for lithium self-diffusion along Li(100) and Li(110), respectively.[65] Consequently, research efforts have increasingly focused on tailoring the LME microstructure to optimize transport properties and improve cycling behavior.[67–70]

The cathodic deposition of lithium (*i.e.*, charging) serves as the counterpart to anodic dissolution. In this reverse process (as described in eq. 1), lithium ions $Li_{Li^+}^{x}$(SE) are reduced by electrons e'(Li) at the Li|SE interface, forming lithium atoms Li_{Li}(Li) on the electrode surface. During lithium deposition, the rate-limiting parameter is the diffusion of lithium vacancies toward the interface.[24,71] Specifically, this corresponds to the movement of adsorbed metal atoms, which determines the applicable current density for conventional SSBs and RFCs alike. Vacancies migrate with a diffusion flux j_V, creating vacant sites V_{Li}^{x}(Li) at the interface. This diffusion process once again competes with i_{appl} and the corresponding flux j_{appl}, leading to two potential scenarios: (1) if $j_{appl} < j_V$, the deposited lithium adatoms are transported into the bulk at a sufficient rate, maintaining morphologically stable conditions and ensuring a steady supply of vacant sites at the interface, and (2) if $j_{appl} > j_V$, lithium adatoms accumulate at the interface due to an low supply of vacant sites, resulting in morphological instabilities and an inhomogeneous lithium distribution at the Li|SE interface (Figure 1B).[72–74]

When lithium adatoms accumulate, their redistribution within the electrode – driven by the self-diffusion of lithium – is essential for preserving planar geometries. However, this redistribution process becomes too slow under high current densities (*i.e.*, $j_{appl} \gg j_V$) or in the presence of inhomogeneous current distributions with locally increased currents (*i.e.*, current focusing).[24] Consequently, these conditions promote the growth of lithium filaments and dendrites originating from the anode (Figure 1C), ultimately leading to cell failure.[74] Raj *et al.*[26] and Kasemchainan *et al.*[25] identified incomplete pore refilling, microcontacts, and the consequent loss of contact as the primary driver of current focusing during cell operation. However, contamination layers and interfacial defects may also contribute to this effect of current focusing.[75–78] The influence of the minor partial electronic conductivity of SEs on lithium deposition and dendrite formation is discussed in Chapter 2.3.ii..

Contrary to the early predictions of Monroe and Newman,[14,15] the use of inorganic SEs does not effectively suppress lithium dendrite growth during charging. As a result, current focusing and dendrite formation significantly undermine the safety and impede the practical implementation of LMEs in SSBs.[27,28] Although numerical simulations support experimental efforts in understanding lithium dendrite growth,[79] a comprehensive strategy to address the various factors contributing to dendrite formation has not yet been established. Potential strategies include increasing the contact area using porous microstructures, mechanically reinforcing SEs, facilitating consumptive side reactions to dissolve lithium dendrites, or implementing operational protocols to counteract inhomogeneous lithium deposition.[59,74,77,80–82]

ii. Lithium Alloy Electrode Materials

Despite significant development efforts, LMEs and their interfaces with SEs have proven to be considerably more challenging, as highlighted in the previous chapter. In recent decades, metals capable of alloying with lithium have been extensively studied as potential replacements for graphite electrodes in LIBs. As a result, lithium alloys are regarded as alternative anode materials that could support various electrode concepts in SSBs and RFCs.[33,83,84] However, while these alloys offer advantages over LMEs and may help mitigate morphological changes in SSBs (Chapter 2.1.i.), their integration introduces new challenges.

High-capacity alloy anode materials (AAMs), which enable lithium storage through alloying, are considered promising for enhancing transport kinetics and stabilizing interface morphologies in SSBs. These "host" AAMs provide suitable sites for the repetitive removal ('dealloying') and insertion ('alloying') of lithium metal. Few metals or metalloids achieve the high specific lithium storage capacity of lithium metal (3,861 mAh g^{-1}), such as Si (3,579 mAh g^{-1}) and Mg (3,350 mAh g^{-1}).[84–86] However, some AAMs stand out due to their superior transport properties and electrochemical performance, such as In, Ge, and Mg.[87–89] Notably, good lithium wettability, low interface overpotentials, and high lithium-ion surface diffusivity promote uniform lithium metal deposition, reducing dendrite growth and the risk of cell shorting (Chapter 2.1.i.).[89–91]

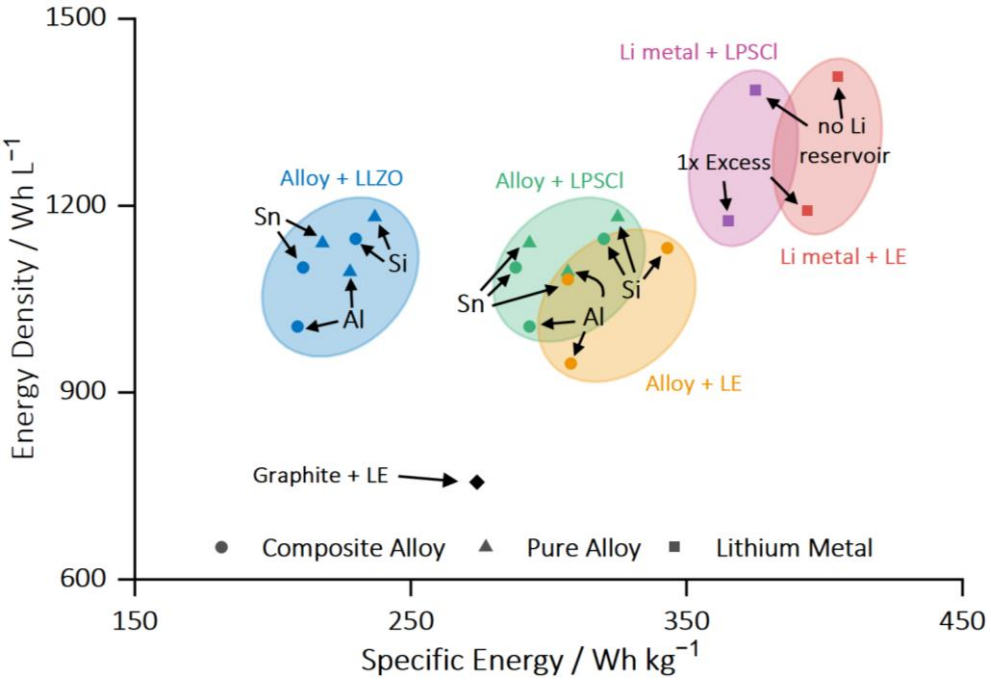

Figure 2: Predicted energy density and specific energy of various SSBs and LIBs with different anode materials, as calculated by Lewis *et al*.[84] Graphite, lithium, and alloy materials (Si, Sn, and Al) were evaluated in combination with a $LiNi_{0.8}Mn_{0.1}Co_{0.1}O_2$ composite cathode (containing 40 vol% of SE). A SE separator thickness of 20 µm was assumed. LLZO refers to $Li_7La_3Zr_2O_{12}$ and LPSCl denotes Li_6PS_5Cl. Reproduced with permission from reference 84. Copyright © Elsevier Inc.

Thus, alloy foils have been extensively studied in academia for both LIBs and SSBs. Specifically, AAMs such as Al, Si, Sn, and others, when paired with high-capacity cathodes, demonstrate the ability to store more lithium per unit mass and volume, compared to conventional LIBs.[92–94] Furthermore, alloy-based SSBs can achieve energy densities comparable to those utilizing LMEs, although with lower specific energies. Figure 2 provides a comparative analysis of the energy metrics of alloy-based SSBs in relation to other battery chemistries.[84]

Thus, alloy-based SSBs are competitive with other battery chemistries in terms of energy metrics. However, their development introduces new research questions and practical challenges, particularly requiring thermodynamic consideration of miscibility of phases as well as their fabrication. Each electrode undergoes structural and volumetric changes during cycling, and AAMs, in particular, experience significant volume expansion (*e.g.*, up to 320 vol% in the case of Li–Si) and changes in mechanical properties.[85] Thus, careful attention to chemomechanical properties is necessary when designing alloy-based SSBs. Moreover, AAMs must be engineered to ensure adequate kinetics and transport properties at the SE interface and within the material itself to achieve high cycling performance.[95] In this context, the In–Li system is examined in the following chapter, with its fabrication, microstructure, and resulting performance further investigated in the fourth publication. Additionally, while the elevated potential of AAMs is expected to mitigate SE degradation processes (Chapter 2.2.),[34,84] further research is needed to understand the influence of alloying materials on interphase growth and composition as well as overall cell performance. This is addressed in the fifth publication, focusing on the In–Li system.

To mitigate the challenges posed by AAMs at the cell-level, while leveraging their advantages, alternative electrode structures with AAMs have been explored in recent studies. For instance, AAM particles, such as silicon, are incorporated into composite structures to improve ionic percolation and enhance cycling performance.[96–98] Additionally, to minimize the use of excess material, metals capable of alloying with lithium, such as Ag, are employed as interlayers in RFCs.[99–101] Thus, these thin interlayers harness the advantageous properties and interface kinetics of AAMs, potentially facilitating the advancement of RFCs. Another strategy involves functional doping by alloy materials, such as Au, in LMEs, which aims to tailor their microstructure, enhance kinetics, and improve lithium deposition.[58,102–104]

The In/$(InLi)_x$ Electrode

One such alloying system, which can be applied in either foil or composite architecture, is the In–Li system. Despite its high raw material costs, weight, and limited practicality for large-scale applications,[105] it has been widely utilized as a counter electrode (CE) in scientific studies.[106] Moreover, material consumption is minimized when used as an interlayer on current collectors (CC), highlighting the potential application in RFCs.

Reliable quantification of high-capacity cathode performance typically requires the use of electrochemically stable reference electrodes in complex cell configurations.[107,108] However, this challenge can be overcome by using electrochemically stable CEs that are characterized by well-defined, stable half-cell potentials, low overpotentials, and high-rate reversibility. Consequently, binary alloy systems with broad two-phase regions, which maintain a constant potential across their compositional range, are ideal candidates. In laboratory cells, the $In/(InLi)_x$ eutectic commonly serves as a reliable substitute for LMEs as it provides both stable operation and enhanced rate capability under diverse operational conditions.[88,109–111] This is further investigated in the fourth publication.

In particular, the In-Li alloy offers a range of advantageous properties and can be easily applied as a CE in SSBs – even at low pressures.[112] Using coulometric titration, Santhosha *et al.*[113] demonstrated that the electrochemical behavior of the In–Li system during lithiation closely aligns with the binary phase diagram of In–Li (Figure 3). Open-circuit voltage (OCV) profiles were recorded after the system reached equilibrium for every titration step, revealing distinct characteristics. The system alternates between one-phase and two-phase regions with increasing lithium content. This is illustrated with different colors in Figure 3, which include the intermetallic phases InLi, In_4Li_5, and In_2Li_3. In two-phase regions, the lithium activity remains constant between the phases, leading to a stable chemical potential of lithium and, consequently, a plateau in the potential profile, as observed for the $In/(InLi)_x$ equilibrium (purple). Conversely, within single-phase regions, the lithium activity and chemical potential change as lithiation progresses, resulting in a sloping potential profile, as shown for the homogeneity range of the InLi phase (yellow).

From a practical point of view, the eutectic two-phase region $In/(InLi)_x$ is particularly relevant for offering a stable E_H = 0.62 V *vs.* Li^+/Li over a broad stoichiometry range (~ 1-47 at% of lithium).[114–116] Recent studies have demonstrated the benefits of a composition located centrally within the two-phase eutectic $In/(InLi)_x$ system, irrespective of the electrode's microstructure.[57,117–119] The intermetallic InLi phase exhibits rapid solid-state diffusion kinetics (D_{Li} = 10^{-8} – 10^{-7} cm^2 s^{-1}), which, compared to lithium's self-diffusion,[51] facilitates good electrochemical performance as well as uniform morphologies and stable cycling.[118–120] Moreover, the higher E_H of $In/(InLi)_x$ is anticipated to mitigate dendrite formation (Chapter 2.1.i.) and to reduce the degradation of inorganic SEs (Chapter 2.2.i.), which is investigated in the fifth publication.

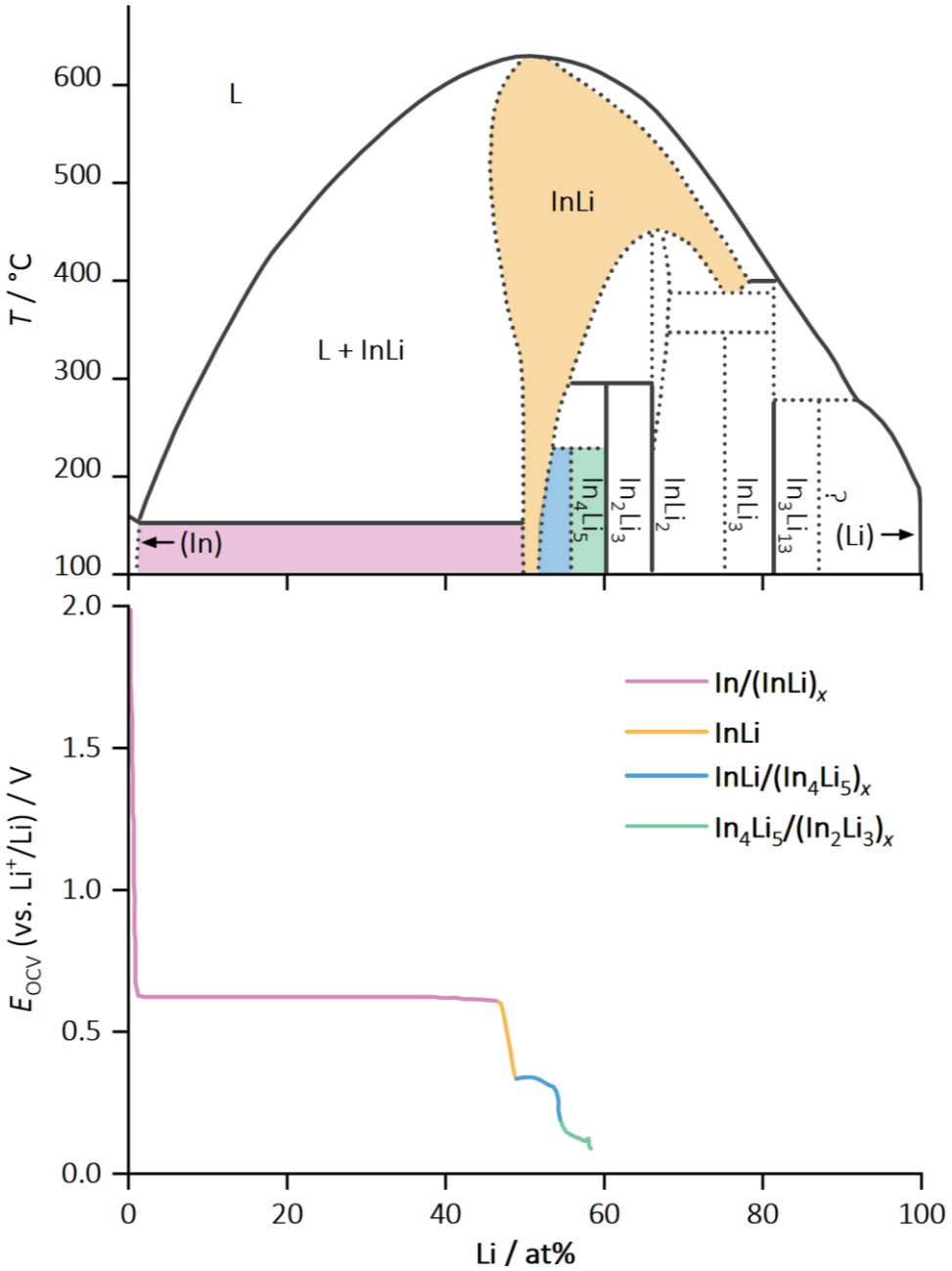

Figure 3: The binary In–Li phase diagram (top) and room-temperature coulometric titration data using a LE (bottom) are presented. The OCV profile (*vs*. Li^+/Li) between titration steps is plotted as a function of lithium content under equilibrium conditions. The *x*-axis (lithium content in at%) is scaled identically for both graphs, allowing for a direct comparison of potentials and phase transitions. Corresponding phase and two-phase regions are highlighted in the phase diagram. Reproduced with permission from reference 113. Copyright © Wiley.

However, numerous studies highlight that In–Li electrodes suffer from mechanical stiffness and sluggish electrode kinetics during cycling.[111,121–123] Nam *et al.*[121] addressed these issues by enhancing electrode kinetics through the incorporation of SE particles into the electrode. Therefore, the performance of In–Li electrodes seems to strongly depend on the specific preparation method of the In/$(InLi)_x$ eutectic.

Recently, variations in the cycling behavior of SSB cells prepared by different research groups were attributed to inconsistencies in the preparation of In–Li electrodes.[124] To address these challenges, the fourth publication of this thesis presents a comparative study investigating seven different preparation methods for In–Li electrodes. Both planar configurations (*e.g.*, foils) and particle-based configurations (*e.g.*, composites) were evaluated for their suitability in cathode testing. The study examined the microstructure of selected electrodes, while also analyzing their rate-dependent electrode kinetics, electrochemical performance, and chemo-mechanical reversibility in full-cell configurations. Limitations for high-capacity testing at elevated rates were identified, highlighting the critical influence of preparation methods and electrode microstructure on the respective electrode kinetics. The combined results underscore the challenges of utilizing In–Li CEs for benchmarking cathode performance, their limitation to laboratory-scale testing, and the lack of comparability of results across different laboratories due to inconsistent preparation protocols.

2.2. Instability of Solid Electrolytes toward Alkali Metal

The adequate incorporation of alkali metal electodes in SSBs relies not only on the morphological stability of the interface during long-term cycling (Chapter 2.1.), but also on the material compatibility between individual components.[11,21,36] This is particularly important for RFCs, which depend on the efficient utilization of active redox species from the cathode material, requiring strict control of capacity losses caused by parasitic side reactions.[34] The consequences of the thermodynamic instability of many inorganic SEs in contact with alkali metals (and other electrode materials) are often underestimated on the cell-level. Therefore, the following chapter addresses the stability of inorganic SE towards lithium metal, focusing on interphase formation and exploring their properties as well as growth kinetics.

i. Types of Interfaces and Multiphase Formation

Ideally, a thermodynamically stable interface forms between two phases without any reactions occurring at the contact spot. However, in practice, most inorganic SEs exhibit a relatively narrow ESW within which they remain thermodynamically stable. Computational techniques, such as density functional theory, enable the prediction of onset reduction and oxidation potentials.[45–47,125] However, it is important to note that kinetic limitations may suppress interface reactions.[126,127] Therefore, thermodynamic calculations often represent the lower bound of the actual ESW.

On the anode side, the higher oxidation states of the SE's cation framework, where for instance P(+5) in LPSCl is reduced to low-valent phosphorous species, determines the onset reduction potential.[128] Outside of this range, particularly at lower potentials, inorganic SEs become (electro-)chemically unstable. This is particularly true when in contact with pure lithium metal, which possesses the lowest possible redox potential (E_H = −3.04 V *vs.* SHE). This instability leads to parasitic side reactions and the reduction of SEs to various stable compounds, forming an additional interphase layer between the electrolyte and electrode.[129] Consequently, this leads to the degradation of the SE structure, resulting in increased impedance and chemo-mechanical alterations due to differing transport properties and molar volumes of such interphases, respectively.[43,44] Furthermore, by compromising the SE microstructure, material incompatibilities also promote dendrite formation in SSBs (Chapter 2.1.i.).

The species of decomposition products varies among the different inorganic SEs (or electrode materials) and thus, the effective properties of the resulting multiphase define their impact on the cell performance. For example, garnet-type SE (like LLZO) are considered macroscopically stable in contact with lithium metal, only forming a marginal interphase (~6 nm thick).[130–132] In contrary, common sulfide SEs (such as LPSCl) in contact with lithium metal continuously form interphases, causing ongoing consumption of both components.[133,134]

Based on their thermodynamic stability and interphase kinetics, electrode|SE interfaces have been classified by Wenzel *et al.*[135] into three cases (Figure 4).

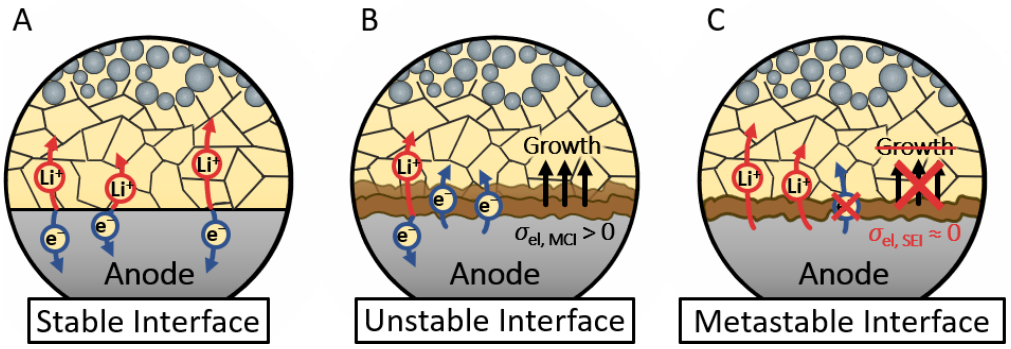

Figure 4: The three interface types between lithium metal and inorganic SEs. The thermodynamically stable interface with no interphase formation (A), the thermodynamically unstable interface with ongoing interphase growth (*i.e.*, MCI) (B), and the 'metastable' interface, where interphase growth is limited by low partial electronic conductivity σ_{el} (*i.e.*, SEI) (C).

Ideally, though rarely achieved with relevant SEs, the interface is thermodynamically stable (depicted in Figure 4A) with no reduction occurring upon contact with lithium. Only fully reduced materials, primarily binary lithium compounds like LiF, LiCl, Li_3N, or Li_3P, are stable against lithium metal.[45–47] However, due to their low lithium-ion conductivity, these compounds are unsuitable for use as SE.[136–144] Recently, Landgraf *et al.*[145,146] reported the successful synthesis of fully reduced, highly disordered SEs: $Li_{2+x}S_{1-x}N_x$ and Li_5NCl_2. Thus, these materials are considered possible alternatives for use in SSBs due to their ionic conductivities reaching up to 1 mS cm^{-1} and stability against lithium metal.

If the electrode|SE interface is thermodynamically unstable, two types of interphases have been reported and are distinguished by their transport properties. MCIs consist of decomposition products, which offer both sufficient partial ionic, but also, electronic conductivity (Figure 4B). Accordingly, lithium ions and electrons can diffuse through the degradation layer, leading to continuous decomposition of SE.[39,147] As a result, MCI growth continues until one of the materials is fully depleted. Conclusively, such interphase growth is not kinetically hindered and MCI-forming SEs are impractical for long-term application. SEs containing metals or metalloids are particularly prone to forming MCIs when in contact with lithium metal, as electronically conductive compounds are likely to emerge during SE degradation. Notable examples include $Li_{1+x}Al_xTi_{2-x}(PO_4)_3$ (forming Ti^0), Li_3InCl_6 (forming In^0), and $Li_{10}GeP_2S_{12}$ (forming Ge^0 and Li_3P) for garnet, halide, and sulfide SEs, respectively.[39,40,148,149]

The second possible type is the SEI formation (Figure 4C), denoted in line with its analog in LIBs.[38] During SE reduction, ionically conducting products form, which exhibit a reduced, though not zero, partial electronic conductivity. As a result, the interphase growth is kinetically hindered and gradually slows down over time (*i.e.*, 'metastable'), due to sluggish electron transport across the interphase layer.[134,150] Thereby, the chemical potential gradient between both materials is reduced and the local equilibrium established, which progressively

stabilizes the interface. However, it has to be emphasized that this self-limiting, diffusion-controlled SEI growth does not stop completely and non-stabilized interfaces can have severe long-term impacts on SSBs.[151] As most decomposition products have lower partial ionic conductivity than the inorganic SE, ongoing interphase growth results in substantial increases in cell resistance over time.[136–144]

It has been demonstrated that stable operation of SSBs can still be achieved in the case of SEI formation for LiPON electrolytes, even with degradation occurring at the Li|LiPON interface.[42] In contrast to MCIs, the diffusion-controlled growth mode of SEIs offers the potential to be optimized and stabilized with minimal impact, or even beneficial (transport) properties, ultimately leading to stabilized cell performance.[152,153] The growth kinetics and 'metastable' interphase thickness, however, depend on the material system and its degradation products. For instance, ternary and higher sulfide SEs are thermodynamically unstable, decomposing into sulfur and phosphorous species. Among these, lithium argyrodites, like Li_6PS_5X, are the most studied sulfide SEs, which decompose into (fully reduced) Li_2S, Li_3P, and LiX (with X = Cl, Br, and I):[154–156]

$$Li_6PS_5X + 8\,Li^0 \rightarrow 5\,Li_2S + Li_3P + LiX \qquad \text{with } X = Cl, Br, I \qquad \text{(eq. 2)}$$

Here, the reaction is driven by the reduction of phosphorous (occurring below 1.75 V *vs.* Li^+/Li)[45–47,155] from P(+5) to P(−3) and low-valent phosphorous species. This process results in the formation of Li_xP and Li_3P, accompanied by the highly stable Li_2S, lithium halides, and possibly amorphous reaction intermediates.[157] These compounds exhibit low partial ionic conductivity (compared to the SE), while their even lower partial electronic conductivity primarily governs the interphase growth kinetics (discussed further in Chapter 2.2.ii.). Burton *et al.*[158] studied the distribution of Li_xP and Li_3P within the interphase. They predicted that preferential paths within the SEI could negatively impact the diffusion-controlled growth mode, even in the absence of lithium metal. Thus, the significant partial electronic conductivity of Li_xP is also suspected to accelerate SEI growth, and to eventually cause MCI growth.[157–159]

Initially, a 'mosaic-like' domain structure, similar to the SEI in LIBs, was proposed.[38,160] However, recent studies by Otto *et al.*[40] and Aktekin *et al.*[155] indicate that the lithiation of sulfide SEs results in interphase thicknesses of several hundred nanometers. Additionally, they observed the formation of layered structures, with a phosphorus-rich region close to the SE. For LiPON, Turrell *et al.*[161] observed a layered structure with fully reduced species at the interface to lithium metal. This microstructure is believed to stabilize the interface by disrupting percolation networks across the interphase. As a result, the SEI thickness is assumed to be effectively constrained, with reported values ranging from 16 and 80 nm.[161–163]

In recent years, computational efforts and theoretical calculations have been helpful in calculating thermodynamic quantities, identifying degradation driving forces, and predicting reaction mechanisms.[164–167] Moreover, they provide valuable insights for evaluating stabilization strategies and guiding the corresponding material selection (*e.g.*, for interlayers).[168–171] From

an experimental point of view, interphases are inherently concealed within the material. Thus, they are challenging to study using conventional surface-sensitive techniques, necessitating complex and innovative strategies to investigate interphase layers.[40,135,154,155] One suitable method is introduced in the first publication of this thesis in order to understand the growth kinetics of multiphase SEI layers and the role of their individual constituents.

The first publication of this thesis is focused on quantifying the kinetics of multiphase SEIs by synthesizing SEI-type bulk-material. It was proven, that this unique method accurately modeled the effective transport properties of LPSCl degradation layers. Accordingly, the partial conductivities of this 'bulk-SEI' were determined and each contribution to the SEI characteristics was assessed. The analysis of individual SEI constituents shows that, although Li_2S accounts for the largest mass and volume fraction, it is not the primary determinant of the interphase's partial conductivities. Using the Wagner diffusion model (Chapter 2.2.ii.), a significant SEI rate constant was estimated, underscoring the severe long-term effects on cell performance. Combined results highlight the urgent need to optimize the Li|LPSCl interface by tuning the SEI's transport properties or introducing artificial interlayers, while improving the predictive accuracy of models for diffusion-controlled growth in SSBs.

ii. Interphase Growth and its Theoretical Description

A recent study by Aktekin *et al.*[41] introduced the coulometric titration time analysis (CTTA) method. This titration technique enables the direct quantification of consumed material by tracking the accumulated charge (q_Σ) consumed during interphase formation (or side reactions) in sulfide SEs (Figure 5A). Therefore, it has been shown that the solid-state reaction (*i.e.*, SEI formation) observed for LPSCl and β-Li_3PS_4 (LPS) can be approximated by a parabolic behavior. This is evidenced by the linear relationship between q_Σ and $t^{0.5}$, as depicted for LPSCl in Figure 5B.

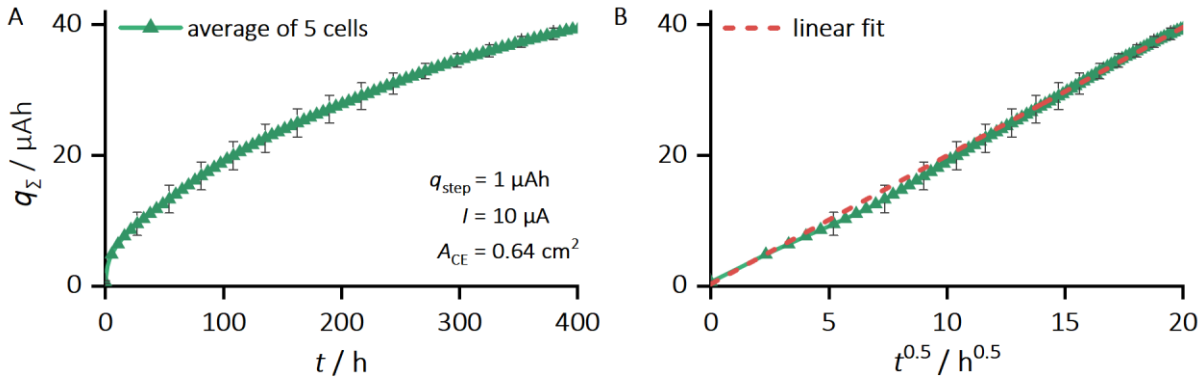

Figure 5: The accumulated charge (q_Σ) consumed over time in a Li|LPSCl|stainless-steel cell during CTTA experiments as a function of t (A) and of $t^{0.5}$ (B). Titration parameters are noted in A. Experiments were conducted at 25 °C and approximately 13 MPa. The error bars correspond to the standard deviation of five duplicate cells. Reproduced with permission from reference 41. Copyright © Springer Nature.

In a typical solid-state reaction, the initial reaction rate is controlled by interfacial processes, such as nucleation and charge transfer, which act as rate-limiting factors.[172] However, the growth mode shifts to being diffusion-controlled once a sufficient product layer is established, determining the growth characteristics and progression over time. Therefore, the underlying parabolic behavior can be described using the Wagner diffusion model.

In 1920, Tammann reported a parabolic growth behavior (*i.e.*, a parabolic rate law) for the tarnishing of metals at elevated temperatures.[173] In 1931, Wagner developed a model for solid-state reactions to describe this phenomenon.[174–176] The kinetic insights and empirical learnings from tarnishing experiments are often transferable to other solid-state reactions and systems. As a result, the Wagner diffusion model is frequently applied to describe degradation reactions (*i.e.*, SEI and CEI growth) and estimate growth kinetics in LIBs and SSBs.[133,177–186]

In order to apply this model to diffusion-controlled solid-state reactions, several assumptions must be made:[172,187]

i. The product layer grows on planar, stable metal surfaces under one-dimensional flux.
ii. The flux through the layer is driven solely by chemical potential gradients between boundaries of constant chemical potential (*i.e.*, local thermodynamic equilibrium).
iii. The product layer is considered to be dense, adherent, fully covering, and consisting of a homogeneous, crystalline phase.
iv. The electroneutrality within solid crystals leads to flux coupling of charge carriers.
v. The layer achieved a sufficient thickness to neglect space and surface charge effects.

In the following, a 'modified' Wagner diffusion model is derived to describe the diffusion-controlled growth of the interphases in SSBs.[185,188]

Considering Fick's first law, along with charge neutrality and flux coupling, the coupled transport of ions ($j_{\mathrm{Li^+}}$) and electrons (j_{el}) corresponds to the transport of neutral lithium species (j_{Li}) across the interphase layer. This transport is driven by the chemical potential gradient of lithium ($\nabla\mu_{\mathrm{Li}}$):

$$j_{\mathrm{Li}} = j_{\mathrm{el}} = j_{\mathrm{Li^+}} = -\frac{L_{\mathrm{el}} \cdot L_{\mathrm{Li^+}}}{L_{\mathrm{el}} + z_{\mathrm{Li^+}}^2 \cdot L_{\mathrm{Li^+}}} \cdot \nabla\mu_{\mathrm{Li}} \qquad \text{(eq. 3)}$$

with $z_{\mathrm{Li^+}} = 1$ being the charge number of lithium ions and L_i being the respective phenomenological transport coefficients of charge carriers. The partial ionic (i = ion) and electronic conductivity (i = el) is related to its transport coefficient by $\sigma_i = (z_i \cdot F)^2 \cdot L_i$, and $\nabla\mu_{\mathrm{Li}}$ can be estimated by the difference in chemical potential of lithium ($\Delta\mu_{\mathrm{Li}}$) between the reaction front and the electrode (*i.e.*, across the interphase thickness):

$$j_{\mathrm{Li}} = -\frac{1}{F^2} \cdot \frac{\sigma_{\mathrm{el}} \cdot \sigma_{\mathrm{ion}}}{\sigma_{\mathrm{el}} + \sigma_{\mathrm{ion}}} \cdot \frac{\Delta\mu_{\mathrm{Li}}}{\xi} = -\frac{1}{F^2} \cdot \frac{\sigma_{\mathrm{el}} \cdot \sigma_{\mathrm{ion}}}{\sigma_{\mathrm{el}} + \sigma_{\mathrm{ion}}} \cdot \frac{\mu_{\mathrm{Li}}(\text{reaction front}) - \mu_{\mathrm{Li}}(\text{electrode})}{\xi} \qquad \text{(eq. 4)}$$

with F, σ_{ion}, σ_{el}, ξ, and μ_{Li} being the Faraday constant, the ionic and electronic conductivity of the interphase, the interphase thickness, and the chemical potential of lithium at the reaction front as well as at the electrode, respectively. Accordingly, the interphase growth rate is determined by the transport properties of the less mobile charged species, which is a result of charge neutrality.

Previous literature has commonly approximated $\Delta\mu_{\mathrm{Li}}$ by the standard chemical potential of lithium metal (μ^0_{Li} = 8.35 kJ mol^{-1}).[133,134] However, this assumption warrants revision. When using an LME, the electrode's chemical potential of lithium μ_{Li}(electrode) is at equilibrium equal to μ^0_{Li}. Consequently, $\Delta\mu_{\mathrm{Li}}$ has to be defined as μ_{Li}(reaction front) $-\,\mu^0_{\mathrm{Li}}$.

Assuming local equilibrium at the reaction front, where the Gibbs free energy change of the reaction ($\Delta_{\mathrm{r}}G$) is zero, and considering the formation of solid compounds (eq. 2), yields:

$$\Delta_{\mathrm{r}}G = 5 \cdot \mu^0_{\mathrm{Li_2S}} + \mu^0_{\mathrm{Li_3P}} + \mu^0_{\mathrm{LiCl}} - \mu^0_{\mathrm{Li_6PS_5Cl}} - 8 \cdot \mu_{\mathrm{Li}}(\text{reaction front}) = 0 \qquad \text{(eq. 5)}$$

Rearranging, subtracting $8{\cdot}\mu^0_{\mathrm{Li}}$ from both sides, and considering the change of standard Gibbs free energy ($\Delta_{\mathrm{r}}G^0$) for the decomposition of LPSCl, yields the final expression for $\Delta\mu_{\mathrm{Li}}$:

$$\Delta_{\mathrm{r}}G^0(\mathrm{Li_6PS_5Cl}) - 8 \cdot \mu_{\mathrm{Li}}(\text{reaction front}) = -8 \cdot \mu^0_{\mathrm{Li}}$$
$$\Delta\mu_{\mathrm{Li}} = \mu_{\mathrm{Li}}(\text{reaction front}) - \mu^0_{\mathrm{Li}} = \frac{1}{8} \cdot \Delta_{\mathrm{r}}G^0(\mathrm{Li_6PS_5Cl}) \qquad \text{(eq. 6)}$$

Therefore, $\Delta\mu_{\mathrm{Li}}$ can be approximated by dividing $\Delta_{\mathrm{r}}G^0(\mathrm{Li_6PS_5Cl})$ by the stoichiometric factor of lithium (x_{Li} = 8 in eq. 2), representing the moles of lithium involved in the decomposition reaction. Using thermodynamic data,[189] $\Delta_{\mathrm{r}}G^0(\mathrm{Li_6PS_5Cl})$ is calculated to be approximately 1269.75 kJ mol^{-1}, leading to an estimated $\Delta\mu_{\mathrm{Li}}$ of approximately 158.7 kJ mol^{-1}. For clarity and consistency, the subsequent equations will continue to use this refined definition of $\Delta\mu_{\mathrm{Li}}$.

The degradation reaction (*i.e.*, its growth rate) can be described using:[172,187]

$$\frac{d\xi}{dt} = \frac{j_{\mathrm{Li}} \cdot M_{\mathrm{int}}}{\rho_{\mathrm{int}} \cdot x_{\mathrm{Li}}} \qquad \text{(eq. 7)}$$

with ρ_{int}, M_{int}, x_{Li}, and t being the mean density of the interphase, the mean molar mass of the interphase, the stoichiometric factor, and the reaction time, respectively.

Inserting eq. 7 into eq. 4 leads to eq. 8:

$$\frac{\rho_{\mathrm{int}} \cdot x_{\mathrm{Li}}}{M_{\mathrm{int}}} \cdot \frac{d\xi}{dt} = -\frac{1}{F^2} \cdot \frac{\sigma_{\mathrm{el}} \cdot \sigma_{\mathrm{ion}}}{\sigma_{\mathrm{el}} + \sigma_{\mathrm{ion}}} \cdot \frac{\Delta\mu_{\mathrm{Li}}}{\xi} \qquad \text{(eq. 8)}$$

By separating the variables and performing definite integration, eqs. 9 and 10 are obtained to describe the parabolic interphase growth (*i.e.*, its absolute thickness *d*). Since the model assumes one-dimensional transport, the absolute value from eq. 4 (right side of eq. 8) is applied.

$$\int_0^d \xi \, d\xi = \frac{1}{F^2 \cdot \rho_{\mathrm{int}} \cdot x_{\mathrm{Li}}} \cdot \frac{M_{\mathrm{int}} \cdot \sigma_{\mathrm{el}} \cdot \sigma_{\mathrm{ion}}}{\sigma_{\mathrm{el}} + \sigma_{\mathrm{ion}}} \cdot \Delta\mu_{\mathrm{Li}} \cdot \int_0^t dt \qquad \text{(eq. 9)}$$

$$d = \sqrt{\frac{2}{F^2 \cdot \rho_{\mathrm{int}} \cdot x_{\mathrm{Li}}} \cdot \frac{M_{\mathrm{int}} \cdot \sigma_{\mathrm{el}} \cdot \sigma_{\mathrm{ion}}}{\sigma_{\mathrm{el}} + \sigma_{\mathrm{ion}}} \cdot \Delta\mu_{\mathrm{Li}} \cdot \sqrt{t}} \qquad \text{(eq. 10)}$$

If the partial conductivities of the interphase are accurately known, the interphase resistance can be determined from *d*, and vice-versa. Using $\sigma_{\mathrm{ion}} = d \cdot A / R_{\mathrm{int}}$, the ionic interphase resistance (R_{int}) can be described by eq. 11:

$$R_{\mathrm{int}} = \frac{1}{\sigma_{\mathrm{ion}} \cdot A} \cdot \sqrt{\frac{2}{F^2 \cdot \rho_{\mathrm{int}} \cdot x_{\mathrm{Li}}} \cdot \frac{M_{\mathrm{int}} \cdot \sigma_{\mathrm{el}} \cdot \sigma_{\mathrm{ion}}}{\sigma_{\mathrm{el}} + \sigma_{\mathrm{ion}}} \cdot \Delta\mu_{\mathrm{Li}} \cdot \sqrt{t}} \qquad \text{(eq. 11)}$$

with *A* being the electrode|SE interface area.

In the specific case of SEIs and CEIs, where the interphase's ionic conductivity is much greater than the electronic conductivity ($\sigma_{\mathrm{ion}} \gg \sigma_{\mathrm{el}}$), eqs. 10 and 11 can be simplified as follows:

$$d \cong \sqrt{\frac{2}{F^2 \cdot \rho_{\mathrm{int}} \cdot x_{\mathrm{Li}}} \cdot M_{\mathrm{int}} \cdot \sigma_{\mathrm{el}} \cdot \Delta\mu_{\mathrm{Li}} \cdot \sqrt{t}} = k \cdot \sqrt{t} \qquad \text{(eq. 12)}$$

$$R_{\mathrm{int}} \cong \frac{1}{\sigma_{\mathrm{ion}} \cdot A} \cdot \sqrt{\frac{2}{F^2 \cdot \rho_{\mathrm{int}} \cdot x_{\mathrm{Li}}} \cdot M_{\mathrm{int}} \cdot \sigma_{\mathrm{el}} \cdot \Delta\mu_{\mathrm{Li}} \cdot \sqrt{t}} = k' \cdot \sqrt{t} \qquad \text{(eq. 13)}$$

Thus, a square-root of time behavior with the parabolic rate constants *k* and *k*' is obtained, which is in good agreement with experimental results (Figure 5). Hereafter, it will be referred to as the Wagner diffusion model, specifically adapted for the diffusion-controlled growth of interphases in SSBs.

As mentioned before, the Wagner diffusion model was initially introduced to analyze reactions at gas|solid interfaces. In the second publication of this thesis, the accuracy of rate constants derived from impedance data was investigated for predicting interphase growth at solid|solid interfaces in SSBs, utilizing the Wagner diffusion model. By incorporating kinetic parameters from the first publication into 3D transport simulations, microscopic diffusion-controlled SEI growth and its corresponding cell-level impedance response were analyzed for various electrode|SE contact conditions. The study revealed that factors such as current

constriction, complex transport properties in SEs, or partially passivated interfaces alter the macroscopic cell impedance. If the actual contact area is unknown, these phenomena can compromise the accurate determination of rate constants. Consequently, this work highlights potential pitfalls in data interpretation for time-resolved experiments and emphasizes the need to carefully consider experimental conditions for a reliable prediction of diffusion-controlled interphase growth using the Wagner diffusion model for solid-state systems.

It is important to note that a purely diffusion-controlled SEI formation will theoretically never come to a complete stop but will progressively slow down over time. The process can only be stopped, if sufficiently strong opposing forces counteract the chemical driving force. Alternatively, an accumulation of reaction products can be achieved such that its kinetics are slowed down to virtually zero rate (as is assumed for LiPON). Therefore, achieving control over the interface and interphase properties is essential for positioning LME-based SSBs as a competitive alternative to LIBs. Potential strategies to stabilize the metal|SE interface include the use of fully reduced thermodynamically stable SEs, inorganic modifications of SEs and their SEI, or the incorporation of artificial interlayers with low electronic conductivity.[145,146,153] However, SE modifications fall beyond the scope of this thesis, with only guidelines and estimations being discussed in the first publication.

In the context of artificial alloying interlayers for RFCs, their higher E_H is anticipated to mitigate and reduce SE degradation processes (Chapter 2.2.i.).[34,84] For In–Li electrodes (Chapter 2.1.ii.), recent studies have identified the formation of In_xS_y compounds at the interface with the In/$(InLi)_x$ eutectic, as evidenced by electron microscopy and XPS.[190–192] However, the combined findings remain inconclusive.

Therefore, interphase formation at the In/$(InLi)_x$|LPSCl interface was investigated in the fifth publication of this doctoral thesis. The electrochemical results are intended to guide a complementing *operando* XPS study aimed at revealing the interphase composition. The findings revealed a reduced degradation of LPSCl at lithiated indium CCs compared to lithium metal, which was quantified using CTTA. Potential factors affecting the interpretation of CTTA results, including interface morphologies and metal oxide surface layers, were also identified and discussed. In this context, the Wagner diffusion model was also refined for lithium alloy electrodes and their higher E_H to assess the SEI rate constant. Conclusively, these findings deepen the understanding of interphase formation at alloy electrodes and interlayers, while supporting *operando* XPS experiments to track SEI formation and its composition at In/$(InLi)_x$|LPSCl interfaces.

2.3. Partial Electronic Conductivity of Lithium Solid Electrolytes

The partial electronic conductivity (σ_{el}) of interphase layers plays a pivotal role in governing both growth kinetics and resistance contributions at the cell-level (Chapter 2.2.ii.). Beyond these aspects, σ_{el} also impacts other critical properties of SSBs, particularly with regard to long-term performance and safety. Consequently, the following chapter explores the role of σ_{el} within the context of defect chemistry and its extended effects on the long-term cell performance. Furthermore, this chapter also addresses the challenges associated with measuring the partial conductivity of minority charge carriers and explores the application of the Hebb-Wagner method for accurately determining the minor partial conductivity in lithium SEs.

i. Defect Chemistry in Lithium Solid Electrolytes

Defect chemistry combines thermodynamic and kinetic principles to understand and predict the behavior of point defects in ionic solid solutions, linking thermodynamic variables to the concentrations of lattice defects.[193,194] In ionic materials, deviations from perfect stoichiometry are unavoidable, leading to the formation of (point) defects. Nonstoichiometry changes, often induced by elemental doping, can additionally introduce electronic defects, such as electrons or electron holes. Consequently, defects have a profound impact on the physical and electrochemical properties of materials. A core objective of defect chemistry is to relate defect behavior to material design, enabling performance optimization in applications like batteries, fuel cells, and sensors. Theoretical descriptions such as Kroeger-Vink notation[50] and Brouwer diagrams have been developed to describe defects in relation to the crystal lattice or to illustrate their concentrations as functions of the activity of specific components, such as oxygen, lithium, or sodium.

In the field of solid-state ionics, oxygen-ion conductors gained considerable attention in the late 20th century for advancing solid oxide fuel cells (SOFCs).[195,196] Oxygen SEs have been systematically optimized through defect chemical modifications to enhance ionic conductivity (σ_{ion}) and ensure compatibility with cathode materials.[197,198] In contrast, lithium-ion conducting SEs initially received less attention but have recently regained interest due to their potential to enable SSBs to surpass conventional LIBs in performance.[10,199] Despite this renewed interest, σ_{el} of lithium-ion conducting SEs has received limited attention – apart from a few cases[200,201] – and is usually considered sufficiently low. Therefore, research has primarily focused on optimizing these SEs to compete with LEs for advanced SSB applications, emphasizing improvements in σ_{ion} by introducing structural lattice disorder.[202–205]

Thus, lithium-ion conductors – like oxygen-ion conductors – have to be regarded as mixed ionic-electronic conductors (MIECs), as their behavior is fundamentally governed by their point defect chemistry (*i.e.*, concentrations of point defects).[206] Moreover, an often-overlooked aspect within the SSB community is that σ_{el} of an inorganic SE is neither a fixed nor constant value at a given temperature.[127,207,208] Instead, σ_{el} is intrinsically tied to the actual thermodynamic state of the SE. Specifically, σ_{el} depends on the concentration of electronic

defects, which varies with the lithium activity (or chemical potential), a parameter directly influenced by the cell potential (U_{cell}):

$$U_{\text{cell}} = \varphi(\text{cathode}) - \varphi(\text{anode}) = -\frac{1}{F}\Delta\mu_{\text{Li}} = -\frac{R \cdot T}{z_{\text{Li}^+} \cdot F} \cdot \ln\frac{a_{\text{Li}}(\text{cathode})}{a_{\text{Li}}(\text{anode})} \qquad \text{(eq. 14)}$$

Here, φ, $\Delta\mu_{\text{Li}}$, R, T, $z_{\text{Li}^+} = 1$, and a_{Li} represent the electric potential, lithium chemical potential difference between electrodes, ideal gas constant, temperature, charge number of lithium ions (or number of transferred electrons), and the lithium activity of the cathode and anode material, respectively. Conclusively, the effective σ_{el} of an inorganic SE employed as a separator varies with the state-of-charge of the SSB cell, as will be demonstrated below.

The incorporation and extraction of lithium into and from the bulk SE can be expressed using eq. 15, represented in Kroeger-Vink notation.[50]

$$\text{Li}^0 + \text{V}'_{\text{Li}} \rightleftharpoons \text{Li}^{\text{x}}_{\text{Li}} + \text{e}' \qquad \text{(eq. 15)}$$

V'_{Li}, $\text{Li}^{\text{x}}_{\text{Li}}$, and e' denote lithium ion vacancies, lithium atoms occupying regular lattice sites within the SE, and electrons, respectively. Based on the mass action law with the equilibrium constant K_{Li}, the lithium activity a_{Li} within the material is given:

$$a_{\text{Li}} = \frac{1}{K_{\text{Li}}} \cdot \frac{[\text{Li}^{\text{x}}_{\text{Li}}]}{[\text{V}'_{\text{Li}}]} \cdot [\text{e}'] \qquad \text{(eq. 16)}$$

In this context, square brackets denote the concentration of electrons, lithium atoms, and lithium vacancies. When the lithium SE primarily displays typical point defects, the charge from the missing lithium ions (*i.e.*, V'_{Li}) are balanced by electron holes in the extrinsic regime (*i.e.*, $[\text{V}'_{\text{Li}}] = [\text{h}^{\bullet}]$). Assuming that the concentration of lithium atoms $[\text{Li}_{\text{Li}}]$ as well as the equilibrium between electrons and holes remain constant (*i.e.*, $[\text{e}'][\text{h}^{\bullet}] = K_{\text{el}}$), eq. 16 simplifies to proportional relationships for $[\text{e}']$ and $[\text{h}^{\bullet}]$:[127]

$$a_{\text{Li}} \propto [\text{e}']^2 \text{ and } a_{\text{Li}} \propto [\text{h}^{\bullet}]^{-2} \qquad \text{(eq. 17)}$$

Thus, for a Li||$\text{LiNi}_{\text{x}}\text{Mn}_{\text{y}}\text{Co}_{1\text{-x-y}}\text{O}_2$ cell ($a_{\text{Li}} = 1$ at the LME), the lithium activity within the SE varies by 28 orders of magnitude between the charged (≈ 4.2 V) and discharged (≈ 2.6 V) states, calculated using eq. 14. Consequently, as given by eq. 17, the concentration of electronic defects (in the extrinsic region of the SE) changes by 14 orders of magnitude and directly impacts the effective σ_{el} of SEs.

In this context, defect chemical considerations are a key factor in controlling the material properties and σ_{el} in SSBs. Eventually, design rules (*e.g.*, elemental doping or substitution) need to be found for future improved SEs, as is the case for oxygen-ion conductors.[209] Moreover, controlling the electron mobility may be crucial to minimize the effects of impurities (*i.e.*, variations in electronic defect concentrations) and ensure sufficiently low σ_{el}.

ii. Consequences of Partial Electronic Conductivity in SSBs

Typically, σ_{el} of inorganic SEs is several orders of magnitude smaller than its ionic counterpart and is thereby clearly underestimated as a factor in cell performance. In fact, a detailed understanding of the defect chemistry of inorganic SEs is essential to explain transport and storage phenomena in SSBs, as electronic minority defects are expected to play a crucial role at the cell-level, particularly in high-voltage systems.[200] Thus, even small σ_{el} values can have a substantial impact on the stability of SEs and electrode interfaces in battery cells, and affect their long-time storage capability.[201]

Figure 6 highlights the potential consequences of minor but ineffectively suppressed σ_{el}. Typical values range from 10^{-10} to 10^{-7} S cm^{-1}, if accurate. σ_{el} is directly linked to self-discharge rates in battery cells, causing the detrimental electronic leakage across the SE (Figure 6A).[127,208] Similar to parasitic redox shuttle reactions in LIBs, this leakage currents determine the long-term performance, shelf life, and storage characteristics of SSBs. During aging, a value of 10^{-8} S cm^{-1} for σ_{el} results in a 20% capacity loss after just 10 days for a 4 V-cell with a capacity of 5 mAh cm^{-2}, a separator thickness of 100 µm, and an area of 1 cm^2. As this behavior has not yet been observed experimentally, it suggests that the reported σ_{el} of inorganic SEs in the literature are likely overestimated.[200] This discrepancy highlights significant challenges in accurately quantifying σ_{el} for many relevant electrolytes. Here, the remarkable shelf life of LiPON-based batteries (exceeding ten years) is believed to stem from its very low σ_{el} (10^{-12} – 10^{-15} S cm^{-1}), which effectively minimizes electronic leakage.[210,211]

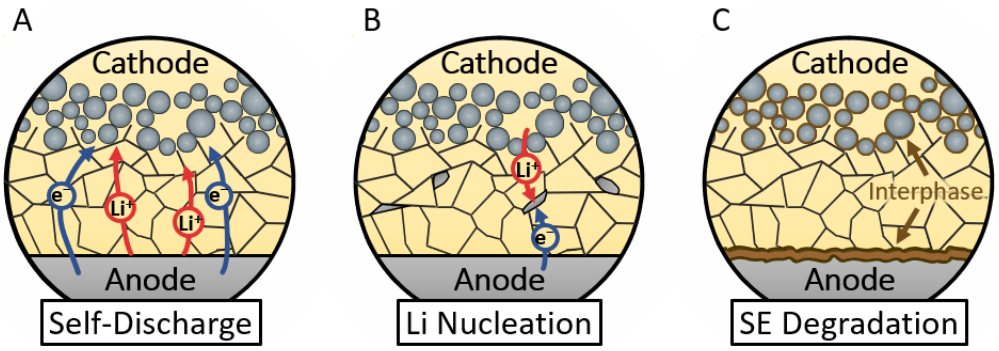

Figure 6: The manifold impact of minor but ineffectively suppressed electronic conductivity in inorganic SEs within SSBs. These effects include an increased battery self-discharge rate (A), reduced cell lifetime due to internal lithium metal nucleation (B), and accelerated interphase formation at both electrodes (C).

Furthermore, recent studies suggest that σ_{el} increases the risk of internal lithium metal nucleation (*i.e.*, the recombination of e^- and Li^+) through electronic pathways (Figure 6B).[212–217] Within the microstructure of SEs, grain boundaries may act as ionic bottlenecks or contain trapped surface charges, promoting internal lithium deposition.[218–220] At these bottlenecks, a locally-increased chemical potential of lithium may trigger nucleation, potentially resulting in dendrite formation and eventual cell failure (Chapter 2.1.i.). Both theoretical and experimental studies suggest that minor σ_{el} values (< 10^{-8} S cm^{-1}) can compromise the electrochemical

stability of SEs (Figure 6C).[211,221–223] Thus, degradation processes (Chapter 2.2.) are accelerated by considerable σ_{el}, impairing the material's long-term performance and stability, especially for SSBs with high energy densities.

Providing a brief perspective on alternative cell chemistries: Enhancing σ_{el} in SEs has recently gained significant attention for advancing sulfur-based solid-state cathodes.[224] In conventional architectures, sulfur conversion reactions are kinetically limited at the three-phase boundaries involving sulfur, carbon, and SE.[209] However, Wang *et al.*[225] showed that increasing σ_{el} by incorporating MIECs, based on TiS_2–$Li_7P_3S_{11}$, facilitates the conversion of active sulfur into Li_2S and improves the active material utilization in sulfur cathodes.

Unfortunately, the reliable characterization of electronic properties is currently limited to garnet or LiPON SEs.[226–232] For other lithium-ion conducting SEs, such as halides or sulfides, their inherent (electro-)chemical instabilities and side reactions at low potentials make precise determination of σ_{el} challenging.[134,233,234] These degradation reactions can alter the material under investigation, potentially inducing parasitic ionic currents that interfere with conductivity measurements. Consequently, careful selection of measurement parameters and electrode materials is essential to ensure accurate results. However, no standardized testing protocol or universally suitable electrode material has been reported to mitigate parasitic reactions effectively and allow precise σ_{el} measurements for sensitive SEs. Shao *et al.*[200] proposed a two-step method to evaluate such SEs by significantly decomposing them at their interface to lithium metal. However, this approach yields a measured σ_{el} that represents a combination of the SE and interphase contributions. Thus, accurate analysis of σ_{el} is currently feasible only for stable materials or fully reduced compounds.

iii. Hebb-Wagner Measurements

Determining and separating the partial conductivity (and also the chemical diffusivity) of minority charge carriers in MIECs is inherently challenging.[235] In the early 20th century, only the total electrical conductivity could be measured, as the available techniques and instruments were unable to distinguish the contributions from individual charge carriers. This limitation was overcome in the 1950s with the development of the Hebb-Wagner method by Hebb,[236] and Wagner,[237–239] providing an alternative technique to electronic leakage testing. This method represented a groundbreaking advancement, allowing for the precise separation and independent analysis of minority partial conductivities in MIECs, such as σ_{el} in ion conductors. From a modern perspective, the Hebb-Wagner method laid the foundation for subsequent research into defect chemistry, transport mechanisms, and the electronic properties of solid-state ionics. Thus, it became a widely adopted method for studying ionic salts and ion conductors, particularly silver and cuprous halides, as well as oxygen-ion conducting oxides.[240–249]

The following section outlines the physical principles and experimental requirements for Hebb-Wagner measurements applied to lithium-based SSB materials, followed by a discussion of the formal treatment of the polarization process.

In Hebb-Wagner measurements, the minority charge carrier conductivity (here, σ_{el} of a lithium-ion conducting SE) can be quantified in an asymmetrical cell setup (Figure 7). By utilizing two distinct types of electrodes, ionic and electronic contributions can be effectively distinguished. A selectively blocking electrode (BE) restricts electron transport, while a reversible electrode (RE) allows for the exchange of both ionic and electronic charge carriers. The RE maintains a constant a_{Li} and, correspondingly, a fixed μ_{Li}. A direct current (dc) voltage is applied to the material under investigation. During polarization, the lithium content in the material and a_{Li} of the BE adjust according to the voltage. Depending on the direction of polarization, a steady state is established,[250] where the net flux of lithium ions becomes zero. At this point, the steady state current density (i_{ss}) between both electrodes is entirely carried by electronic charge carriers, enabling the determination of the material's σ_{el}.

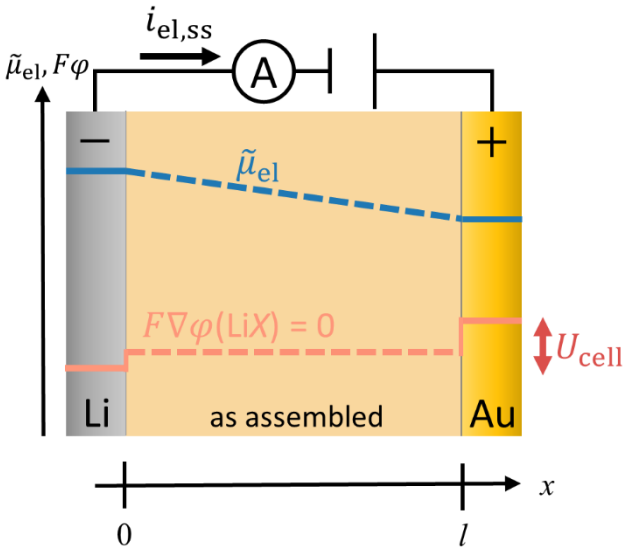

Figure 7: Hebb-Wagner cell configuration for measuring σ_{el} of lithium-ion solid conductors, using one ion-blocking gold (BE) and one reversible lithium metal electrode (RE) – shown in the initial (as assembled) state. The electrochemical potential of electrons ($\tilde{\mu}_{el}$) and the electric potential (φ) are depicted. In both cases, electronic current is conducted, while the ionic current is suppressed by the BE. x is the spatial coordinate within the material of thickness l. For the sake of simplicity, the trend of $\tilde{\mu}_{el}$ within LiX is linearized. The real profile of $\tilde{\mu}_{el}$ depends on the specific defect structure and will not be linear. Reproduced with permission from reference 251. Copyright © Elsevier Inc.

Accurate measurements, however, depend on controlling the experimental parameters (*e.g.*, the temperature) and ensuring the compatibility of materials to avoid internal side reactions.[252–254] It is critical that the electrode potentials, particularly at the RE, remain within the stability range of the material to prevent degradation-induced ionic currents.[254] Additionally, the cell voltage must not exceed the material's decomposition voltage (U_{decomp}), which can be calculated using thermodynamic data as:

$$U_{\text{decomp}} = -\Delta_{\text{r}}G^0/(z_{Li^+} \cdot F) \quad \text{(eq. 18)}$$

where, for simplicity, $\Delta_{\text{r}}G^0$ is the change of standard Gibbs free energy for the decomposition of the respective material. In the context of lithium-ion conducting SEs, being often prone to reduction at low voltages, many inorganic SEs have been inaccurately studied in the past with setups employing two BEs or lithium metal as the RE. Only fully reduced materials can be studied with lithium metal without risking the validity of experimental results. Thus, the careful selection of electrodes in Hebb-Wagner measurements is of utmost importance, particularly for materials susceptible to degradation, where significant challenges persist.

The formal description of the Hebb-Wagner method for steady state polarization under ion-blocking conditions can well be established, including the relationship between σ_{el} and a_{Li}.[237,238] This formalism can be easily extended from lithium-ion conductors to other solid conductors, such as sodium or potassium SEs. Analysis begins by considering the flux of lithium ions (j_{Li^+}) within the SEs (eq. 19).[237–239] This flux arises due to the local gradient of the electrochemical potential of lithium ions ($\nabla\tilde{\mu}_{\text{Li}^+}$). $\nabla\tilde{\mu}_{\text{Li}^+}$ can be expressed as presented in eq. 20, corresponding to the equilibrium condition $\text{Li}^0 \rightleftharpoons \text{Li}^+ + \text{e}^-$ for the occurring redox reaction.

$$j_{\text{Li}^+} = -\frac{\sigma_{\text{ion}}}{(z_{\text{Li}^+} \cdot F)^2} \cdot \nabla\tilde{\mu}_{\text{Li}^+} \quad \text{(eq. 19)}$$

$$\nabla\mu_{\text{Li}} = \nabla\tilde{\mu}_{\text{Li}^+} + z_{\text{Li}^+} \cdot \nabla\tilde{\mu}_{\text{el}} = \nabla\tilde{\mu}_{\text{Li}^+} + \nabla\tilde{\mu}_{\text{el}} \quad \text{(eq. 20)}$$

Here, $z_{\text{Li}^+} = 1$and $\tilde{\mu}_{\text{el}}$ are the charge number of lithium ions and the electrochemical potential of electrons, respectively. By precisely controlling the polarization direction, lithium ions migrate (j_{mig}) toward the RE with depletion occurring near the BE, leading to a lithium concentration gradient within the material. To counterbalance this gradient, a diffusion flux (j_{diff}) emerges. Over time, the resulting net flux of lithium ions stabilizes, reaching a fully compensated steady state (ss) where $j_{\text{Li}^+,\text{ss}} = j_{\text{mig}} + j_{\text{diff}} = 0$. As a result, the gradient of the electrochemical potential of lithium ions is zero (eq. 21) and eq. 20 simplifies to eq. 22, where x is the spatial coordinate within the material for one-dimensional transport between both electrodes. The relaxation time required for equilibrium depends on multiple factors, necessitating careful selection of waiting periods.[250]

$$\nabla\tilde{\mu}_{\text{Li}^+,\text{ss}} \cong 0 \quad \text{(eq. 21)}$$

$$\nabla\tilde{\mu}_{\text{el,ss}} = \nabla\mu_{\text{Li,ss}} \Leftrightarrow \frac{d\tilde{\mu}_{\text{el,ss}}}{dx} = \frac{d\mu_{\text{Li,ss}}}{dx} \quad \text{(eq. 22)}$$

At steady state, the current density (i_{ss}) through the sample is entirely carried by electronic species, such that ($i_{\text{ss}} = i_{\text{el,ss}}$). $\nabla\tilde{\mu}_{\text{el,ss}} = \nabla\mu_{\text{Li,ss}}$ follows from the assumption that the

concentration of lithium ions does not change (eq. 21), which also implies that the polarized SE is electrically field-free ($\nabla\varphi \cong 0$). Any electron transport occurring in the polarized state is exclusively driven by their concentration gradient.

The corresponding partial electronic current density (i_{el}) is described by eq. 23, where the charge number of electrons $z_{el} = -1$. σ_{el} accounts for the combined contributions from both hole (p) and electron (n) transport. By integrating eq. 23 over the sample thickness (l) and incorporating eq. 22, eq. 24 is derived for steady state conditions. This demonstrates that σ_{el} is dependent on μ_{Li} under steady state conditions.

$$i_{el} = j_{el} \cdot z_{el} \cdot F = -\frac{\sigma_{el}(x)}{z_{el} \cdot F} \cdot \nabla\tilde{\mu}_{el} = +\frac{\sigma_{el}(x)}{F} \cdot \frac{d\tilde{\mu}_{el,ss}}{dx} \qquad \text{(eq. 23)}$$

$$\int_0^l i_{el,ss}(x)\, dx = \frac{1}{F} \cdot \int_{\tilde{\mu}_{Li}(RE)}^{\tilde{\mu}_{Li}(BE)} \sigma_{el}\left(\tilde{\mu}_{el,ss}\right) \cdot d\tilde{\mu}_{el,ss}$$
$$\Leftrightarrow \quad i_{el,ss}(x) = \frac{1}{l \cdot F} \cdot \int_{\mu_{Li}(RE)}^{\mu_{Li}(BE)} \sigma_{el}(\mu_{Li}) \cdot d\mu_{Li} \qquad \text{(eq. 24)}$$

By integrating eq. 22 across the sample from RE to BE, eq. 25 is derived:

$$\int_{\tilde{\mu}_{el}(RE)}^{\tilde{\mu}_{el}(BE)} d\tilde{\mu}_{el} = \tilde{\mu}_{el}(BE) - \tilde{\mu}_{el}(RE) = \Delta\tilde{\mu}_{el}$$
$$\int_{\mu_{Li}(RE)}^{\mu_{Li}(BE)} d\mu_{Li} = \mu_{Li}(BE) - \mu_{Li}(RE) = \Delta\mu_{Li} \qquad \text{(eq. 25)}$$

Considering eq. 14, eq. 26 is obtained:

$$\Delta\mu_{Li} = \Delta\tilde{\mu}_{el} = -F \cdot \Delta\varphi = -F \cdot U_{cell} \qquad \text{(eq. 26)}$$

Overvoltages at the BE are neglected in this analysis.[242,253] It is evident, that μ_{Li}(BE) is adjusted with the applied voltage, while μ_{Li} is fixed at the RE in Hebb-Wagner configurations.

Differentiating eq. 24 with respect to μ_{Li}(BE) leads to the final expression (eq. 27) for σ_{el} at the BE. This requires substituting eq. 26. Thus, $i_{el,ss}$ can be adjusted by U_{cell}, while enabling σ_{el}(BE) to be determined from the slope $di_{el,ss}/dU_{cell}$. Additionally, it emphasizes that σ_{el} is influenced not only by μ_{Li} or U_{cell}, but also varies within the material.[242]

$$\sigma_{el}[\mu_{Li}(BE)] = F \cdot l \cdot \frac{di_{el,ss}}{d\mu_{Li}(BE)} = -l \cdot \frac{di_{el,ss}}{dU_{cell}} \qquad \text{(eq. 27)}$$

If the mobilities (u_n and u_p) remain unaffected by the cell voltage, the electron and hole conductivities (σ_n and σ_p) are directly proportional to their respective defect concentrations (c_i),

with $\sigma_i = e \cdot u_i \cdot n_i = F \cdot u_i \cdot c_i$, where e the elementary charge and n_i the respective charge carrier density. Consequently, σ_n and σ_p follow the power law dependence on $a_{Li}^{\pm\alpha}$ (eqs. 28 and 29), given c_i, where α is a characteristic exponent related to the redox reaction at the RE.[243] Eqs. 28 and 29 can be rearranged using the general equilibrium expression for the chemical potential of lithium: $\mu_{Li} = \mu_{Li}^0 + R \cdot T \cdot \ln a_{Li}$, where T is the temperature. In this context, σ_n^0 and σ_p^0 represent the respective standard partial conductivities for $a_{Li} = 1$.

$$\sigma_n = \sigma_n^0 \cdot a_{Li}^{\alpha} = \sigma_n^0 \cdot \exp\left[+\frac{\alpha \cdot (\mu_{Li} - \mu_{Li}^0)}{R \cdot T}\right] \quad \text{(eq. 28)}$$

$$\sigma_p = \sigma_p^0 \cdot a_{Li}^{-\alpha} = \sigma_p^0 \cdot \exp\left[-\frac{\alpha \cdot (\mu_{Li} - \mu_{Li}^0)}{R \cdot T}\right] \quad \text{(eq. 29)}$$

Combining eqs. 24, 26, 28, and 29, along with $\sigma_{el} = \sigma_n + \sigma_p$, the final form of the Hebb-Wagner relation (eq. 30) is obtained. This equation establishes the formal connection between $i_{el,ss}$ and U_{cell}, facilitating the separation and analysis of electron and electron hole contributions.

$$i_{el,ss} = \frac{RT}{\alpha l F}\left(\sigma_n^0\left[\exp\left(-\frac{\alpha F U_{cell}}{RT}\right) - 1\right] + \sigma_p^0\left[1 - \exp\left(+\frac{\alpha F U_{cell}}{RT}\right)\right]\right) \quad \text{(eq. 30)}$$

At low voltages, the current is predominantly carried by electrons, approaching a threshold value, corresponding to σ_n^0. As the voltage increases, the current shifts to being primarily transported by electron holes, exponentially increasing. Thus, a plateau in the $i_{el,ss}$–U_{cell} curve reflects the n–p transition between both regimes – from negative to positive U_{cell}. For a comprehensive analysis, it has been demonstrated that a_{Li} and, consequently, μ_{Li}, are both controlled by the voltage applied across the electrolyte. Accordingly, these parameters alter c_n and c_p, which influence σ_{el} within the SE.

The findings from the first publication on the transport properties of interphases in SSBs and their individual components revealed a significant knowledge gap: the electronic properties of lithium halide compounds (Li*X*, where *X* = Cl, Br, or I) remain largely unexplored.[255] Since the σ_{el} of SEIs is governed by the properties of their individual constituents, these individual characteristics strongly influence the overall behavior of interphases in SSBs. Consequently, the third publication in this thesis is focused on examining the transport properties of LiCl, LiBr, and LiI, which are known degradation products of lithium argyrodite SEs (Li_6PS_5X). Furthermore, the critical importance of minimizing σ_{el} to reduce self-discharge and degradation processes in SSBs is emphasized. Li*X* compounds, being binary ionic salts with fully reduced anions, serve as ideal model systems with lithium metal acting as a suitable electrode material.[45–47] Using the dc Hebb-Wagner method, these compounds were analyzed to determine their ionic conductivity as well as the contributions of both electron holes and electrons to the overall electronic transport. Therefore, $i_{el,ss}$ was analyzed as a function of U_{cell} using eq. 30, and evaluated in a battery-relevant context.

3. Results and Discussion (Publications)

Knowledge of the degradation kinetics of sulfide SEs in contact with lithium metal was scarce at the beginning of this thesis. Due to its nanoscale nature and the concealed interface, investigations were limited to few analytical techniques. Therefore, scientific studies only slowly unveil the growth mode, composition, and microstructure of a few model-type SEIs, impeding the accurate prediction of interphase formation and growth rates in SSBs.

Simple approximations based on the characteristics of the constituent phases appeared to inaccurately describe the properties of SEIs. Accordingly, the first publication provided insight into the transport properties and growth kinetics of typical multiphase SEIs at the Li|LPSCl interface. Therefore, both the partial ionic and electronic conductivity of synthesized SEI-type bulk-material was determined. Using these parameters, the long-term impact of continuous SEI growth on cell performance is assessed, underscoring its compromising influence on sustained cell operation.

The Wagner diffusion model was originally developed to analyze reactions occurring at gas|solid interfaces and recent time-resolved experiments on interphase growth in SSBs revealed discrepancies from expectations of the Wagner diffusion model. Consequently, the reliability of impedance measurements to extract interphase kinetics at solid|solid interfaces was evaluated in the second publication (submitted). Using 3D transport simulations, it is shown that rigid contacts, current constriction, and partially passivated interfaces influence cell impedance responses and can lead to misinterpretations or inaccuracies in estimating interphase rate constants and growth over time. This underscores the need for careful application and a more profound understanding of contact conditions and area to accurately estimate interphase growth in SSBs. Furthermore, these results highlight the practical value of the bulk-synthesis approach introduced in the first publication for accurately determining reaction and growth rates.

During the preparation of the first publication, it was also observed that there was only little experimental research reported on the electronic properties of lithium-ion conductors in battery-relevant contexts. The third publication is aimed to address this gap by examining the partial electronic transport properties of relevant lithium-ion conductors (*i.e.*, LiCl, LiBr, and LiI) from a defect-chemical perspective. The contributions of electrons and holes to the partial electronic conductivity were effectively decoupled by comprehensively applying the dc Hebb-Wagner method. Thus, an effective testing protocol was established to evaluate the electronic conductivity of practical lithium-ion SEs, highlighting the importance of accounting for electronic properties in SSBs to mitigate self-discharge and degradation processes.

In–Li electrodes are frequently used in scientific studies to replace LMEs for inducing less degradation of sulfide SEs, due to their electrode potentials being closer to the ESW of sulfide SEs, and inhibiting pore and dendrite formation. Consequently, the final section of this doctoral thesis is focused on the preparation of In/$(InLi)_x$ electrodes, their performance, and the degradation of LPSCl at E_H = 0.62 V (*vs.* Li^+/Li) of In/$(InLi)_x$.

Recently, it was reported that significant variations in cycling behavior and specific capacities of SSB cells prepared by different research groups are partly due to inconsistencies in the preparation of In–Li electrodes.[124] Therefore, the suitability of In–Li electrodes (as CEs) for solid-state cathode benchmarking was examined in the fourth publication from a fabrication perspective. In this comparative study, it is explored how preparation affects electrode microstructure, electrode kinetics, and the interlaboratory comparability of results. Findings reveal the constraints of In–Li CEs, which are impacted by their individual microstructure, in facilitating high-rate testing of high-capacity solid-state cathodes.

Interphase studies in literature are typically focused on the Li|SE interface, whereas SE degradation at higher electrode potentials is generally anticipated less detrimental to SSB performance. In the fifth publication (in preparation), interphase formation at lithiated indium CCs was investigated through electrochemical titration, revealing a reduced degradation of LPSCl at lithiated indium CCs (compared to lithium metal). Supported by SEM and XPS analysis, possible factors affecting the interpretation of CTTA results, including interface morphologies and metal oxide surface layers, were identified. Moreover, the Wagner diffusion model was refined to account for lithium alloy electrodes and their elevated E_H, enabling the assessment of respective interphase rate constants. Conclusively, findings enhance the understanding of interphase formation at alloy electrodes, providing a foundation for *operando* XPS experiments aimed at revealing the interphase composition.

3.1. Quantifying Multiphase SEI Growth in Sulfide Solid Electrolytes (1st Publication)

In this publication, the transport properties and growth kinetics of reduced sulfide SEs were investigated. Through a novel synthesis approach, the limitations of conventional methods were overcome, surpassing inadequate approximations, and establishing a basis for modeling and quantifying interphase growth.

An effective modeling of the multiphase SEI in SSB cells with LMEs was introduced by directly reacting the LPSCl with lithium metal powder. Using XRD and XPS, the obtained composite of binary lithium phases (referred to as 'bulk-SEI') was confirmed to closely resemble the 'actual' SEI. Thus, both partial conductivities (σ_{ion} and σ_{el}) were determined using dc polarization (*i.e.*, Hebb-Wagner-type measurements) in order to estimate the diffusion-controlled interphase growth, using the Wagner diffusion model. The derived kinetic predictions closely align with reports on cell-level multiphase SEIs, and emphasize the negative impact of SE degradation on the long-term performance of SSBs.

This publication presents, for the first time, experimental data on the transport properties of typical multiphase SEIs, with the resulting kinetic predictions contributing to a deeper understanding of SEI growth. Thus, findings enhance the ability to model SEI transport parameters and design guidelines were established to stabilize the Li|SE interface through proper control of the partial conductivities.

The experiments presented in this publication were designed and executed by the first author under the supervision of K. Peppler and J. Janek. The synthesis and investigation of bulk-SEI were also performed by N.U.C.B. Müller under supervision of the first author and P. Minnmann. L. M. Riegger performed the XPS measurements of the bulk-SEI and analyzed the corresponding data. B. Aktekin supported the analysis of XPS data and assisted with scientific discussion during the review process. The first author performed scanning electron microscopy (SEM), energy dispersive X-ray spectroscopy (EDX), XRD, electrochemical measurements, and the corresponding data analysis. The manuscript was written by the first author and edited by all co-authors.

Reprinted with permission from Christoph D. Alt, Nadia U.C.B. Müller, Luise M. Riegger, Burak Aktekin, Philip Minnmann, Klaus Peppler, and Jürgen Janek. Quantifying multiphase SEI growth in sulfide solid electrolytes, *Joule*, 2024, 8, 1–22. DOI: 10.1016/j.joule.2024.07.006. Copyright © 2024 The Author(s). Published by Elsevier Inc.

Joule

CellPress
OPEN ACCESS

Article

Quantifying multiphase SEI growth in sulfide solid electrolytes

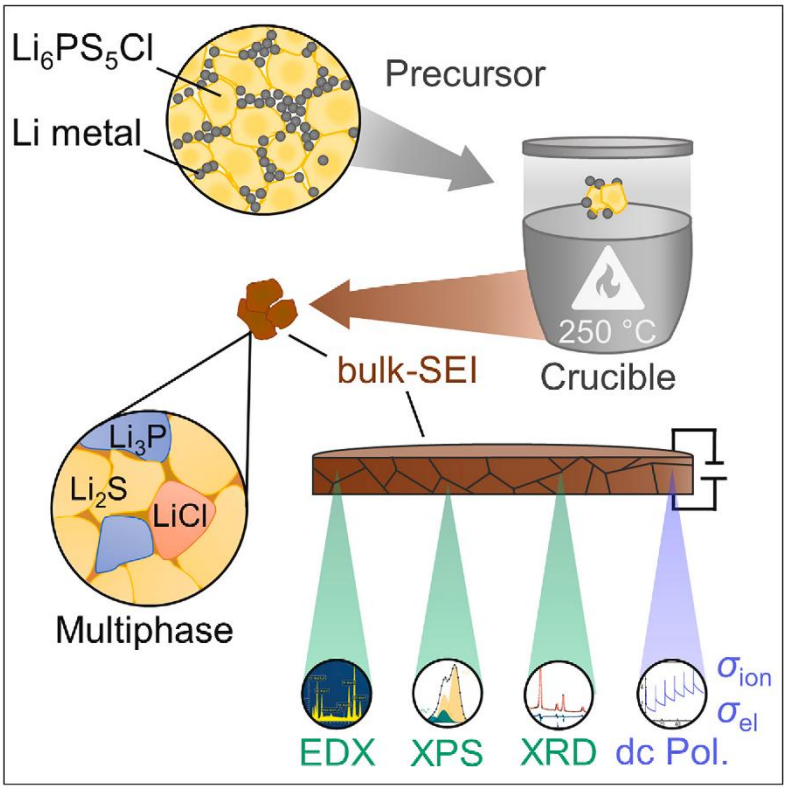

The incorporation of lithium metal anodes could increase the energy density of solid-state batteries, potentially surpassing that of lithium-ion batteries. However, this is hindered by the chemical reduction of solid sulfide electrolytes in contact with lithium metal. The objective of this study is to better understand the transport properties of typical multiphase SEIs, providing quantitative design guidelines for stabilizing the Li|solid electrolyte interface and its kinetics.

Christoph D. Alt, Nadia U.C.B. Müller, Luise M. Riegger, Burak Aktekin, Philip Minnmann, Klaus Peppler, Jürgen Janek

juergen.janek@pc.jlug.de

Highlights

A transferable approach simulated the degradation of sulfide solid electrolytes

dc polarization reveals the ionic and electronic conductivity of bulk-SEI material

Using the Wagner-type diffusion model, SEI growth kinetics is evaluated

Quantitative design guidelines are given to attain sufficient long-term stability

Alt et al., Joule 8, 1–22
October 16, 2024 © 2024 The Author(s).
Published by Elsevier Inc.
https://doi.org/10.1016/j.joule.2024.07.006

Joule

CellPress
OPEN ACCESS

Article

Quantifying multiphase SEI growth in sulfide solid electrolytes

Christoph D. Alt,[1,2] Nadia U.C.B. Müller,[1,2] Luise M. Riegger,[1,2] Burak Aktekin,[1,2] Philip Minnmann,[1,2] Klaus Peppler,[1,2] and Jürgen Janek[1,2,3,*]

SUMMARY

The incorporation of lithium metal anodes in solid-state batteries (SSBs) is impeded due to the chemical reduction of sulfide solid electrolytes (SEs) in contact with lithium metal. Growth mode, composition, and microstructure of a few model-type SE interphases (SEIs) are slowly unveiled. The objective of this study is to better understand the transport properties of typical multiphase SEIs by direct reaction of the SE with lithium metal powder. Hence, the composition and conduction properties (σ_{ion} and σ_{el}) of synthesized bulk-scale SEI-type material (of Li_6PS_5Cl) are analyzed. The kinetic predictions using a Wagner-type diffusion model align well with recent results of electrochemical studies on cell-level multiphase SEIs. Accordingly, these findings enhance the ability to model transport parameters with greater accuracy and contribute to a deeper understanding of SEI growth and kinetics in SSBs. The need to stabilize the Li|SE interface by controlling the partial conductivities of the resulting SEI is emphasized.

INTRODUCTION

In the ongoing transition toward sustainable electric transportation, solid-state batteries (SSBs) are being recognized as a promising advancement of conventional lithium-ion batteries (LIBs).[1–3] SSBs often utilize solid electrolytes (SEs) that replace flammable liquid organic electrolytes of LIBs, potentially ensuring the safe operation of the system.[4–6] Among the multitude of lithium-ion-conducting materials, lithium thiophosphate-based SEs, such as lithium argyrodites Li_6PS_5X (X = Cl, Br, I), have garnered significant attention from both academia and industry. They are considered suitable to be employed in SSBs for being highly conductive (up to 20 mS cm^{-1}),[7,8] and reasonably malleable to form sufficient interfacial contacts. Integrating lithium metal anodes (LMAs) in SSBs, which is not feasible in LIBs due to the significant dendrite risk, is expected to boost their energy and power densities.[9–12]

As for all electrochemical cells, the performance of SSBs relies on the interplay of the negative electrode (often addressed as anode), separator electrolyte, and positive electrode (often addressed as cathode).[13,14] The SE separates the electrodes and allows ion transport while preventing electronic conduction. Due to their very low (anode) and very high (cathode) potentials, the electrodes can either reduce or oxidize the SE at the corresponding interface, which poses stability issues. Based on thermodynamic data, Zhu et al.[15] and Richards et al.[16] computed the (onset) potentials for reduction and oxidation, along with the resulting equilibrium phases. In particular, the stabilization of Li|SE interfaces is a major challenge in the development of lithium thiophosphate-based SSBs if no other stable separator SE is being

CONTEXT & SCALE

Lithium-ion batteries (LIBs) are approaching physicochemical limits in terms of energy density and fast-charging capability. To meet the demands of future (mobile) applications, the integration of lithium metal anodes in solid-state batteries holds the potential to enable high-performance storage beyond LIBs. However, morphological changes during operation and degradation of (sulfide) solid electrolytes in contact with lithium metal are unsolved issues, both of which are closely interconnected.

To enable lithium metal solid-state batteries, it is crucial to control and optimize the lithium|solid electrolyte interface. This study provides new insight into the characteristics and growth kinetics of the resulting interlayer through a direct reaction of sulfide solid electrolyte with lithium metal powder. Our findings highlight the importance of controlling the partial conductivities of the resultant multiphase layer to stabilize the metal anode. Quantitative design guidelines are derived.

used (like garnet-type SE).[17,18] When in contact with lithium metal, which exhibits the lowest possible redox potential (i.e., $E_H[Li^+/Li] = -3.04$ V vs. SHE), ternary and higher thiophosphate SEs are thermodynamically unstable. In the case of lithium argyrodites, they are reduced and decomposed to binary lithium compounds, as described in Equation 1.[15,19] These binary decomposition products are thermodynamically stable against lithium metal, and thus, local equilibrium (with lithium metal) will be established. Essentially, P(+5) is reduced to P(−3) and other low-valent phosphorous species,[15] which drive the reaction along with the formation of highly stable Li_2S and LiCl (for the sake of simplicity, the formation of stoichiometric Li_3P is assumed in the following):

$$Li_6PS_5X + 8\,Li^0 \rightarrow 5\,Li_2S + Li_3P + LiX \text{ with } X = Cl, Br, I \qquad \text{(Equation 1)}$$

During this (chemical) degradation, a multiphase reaction layer is formed. The morphological stability and growth of this interphase are determined by its transport properties.[20,21] Assuming a classical diffusion-controlled solid-state reaction, the persistent degradation of sulfide SEs can only be stopped once sufficiently strong counter-acting forces compensate the chemical driving force or if a product is somehow accumulated such that the kinetics is slowed down to a virtually zero rate. As some of the interphase components like lithium halides and lithium phosphide show lithium-ion conductivity—even if it is low—it is expected that the electronic conductivity within the degradation layer will define the interphase growth rate. Two types of interphases have been defined and reported[21]: (1) mixed ion/electron-conducting interphases (MCIs), which grow more or less continuously due to both high ionic and electronic partial conductivity[22] and eventually cause short circuiting of SSBs, and (2) predominantly ion-conducting interphases with negligible partial electronic conductivity. Consequently, the latter are denoted SE interphases (SEIs) in line with the analog interphase in liquid electrolytes.[23–25] They are assumed to show a square-root of time growth behavior in the ideal case, which can be described by a Wagner-type model.[19,26] We like to highlight already at this early stage that a purely diffusion-controlled SEI formation will theoretically not come to a rest but will get slowed down with time.

Hence, for Li_6PS_5Cl (and other thiophosphate SEs), Wenzel et al.[19] and Riegger et al.[27] observed that the SEI growth (in contact with lithium foil) persisted for several hours to days with a significant slowdown in growth. In experiments based on a novel electrochemical titration technique, Aktekin et al.[28] further described a square-root of time relationship for the SEI growth in anode-free cells (i.e., for freshly deposited lithium). These findings imply that the electronic conductivity of the formed SEI is too high to effectively suppress continuous growth. On the contrary, Otto et al.[29] reported that the degradation reaction of Li_6PS_5Cl with vapor-deposited lithium exhibited self-limiting kinetics, ultimately resulting in a layered SEI microstructure. This disagreement on the long-term SEI growth highlights the importance of gaining a better understanding of SEI conduction characteristics with respect to SEI growth. In view of the great relevance of this SEI for the future of sulfide-based SSBs, the unclear understanding is not satisfying.

SEIs show completely differing chemical, structural, and mechanical properties compared with pristine sulfide SEs, mainly due to the multiphase composite character and the negative volume change during growth relative to the SE itself.[30] Hence, various effects occur such as interface cracking and pore formation, loss of accessible lithium, and hampered lithium-ion transfer.[13,20] As a result of the additional SEI layer, the charge transfer resistance at the interface between lithium metal and the SE is typically increased. By destroying the SE structure, the SEI formation

[1]Institute of Physical Chemistry, Justus Liebig University, Heinrich Buff Ring 17, 35392 Giessen, Germany

[2]Center for Materials Research, Justus Liebig University, Heinrich Buff Ring 16, 35392 Giessen, Germany

[3]Lead contact

*Correspondence: juergen.janek@pc.jlug.de

https://doi.org/10.1016/j.joule.2024.07.006

has a detrimental impact on full cell level, supporting dendrite formation and a corresponding decrease in cycle life.[30,31] Hence, the presence of a SEI has a significant impact on the fundamental characteristics and long-term performance of SSBs, which several approaches aim to inhibit.[32–34] Eventually, controlled degradation,[35–37] and stabilized Li|SE interfaces,[38] while supporting sufficient ionic conductivity and reduced SEI impedance, may enable the commercialization of SSBs.

Despite their critical role, studies on the electrical and microstructural properties of SEIs are scarce due to the lack of suitable methods (i.e., due to limited spatial resolution and difficulties in sample preparation). Examining the SEI presents challenges because of its nanoscale nature and the concealed (buried) interface. Hence, investigations are mostly limited to surface sensitive characterization techniques,[21,29,39] electron microscopy,[40,41] or electrochemical impedance spectroscopy.[27,42] Other properties of SEIs are typically approximated to mirror the characteristics of their constituent (bulk) phases, despite limited understanding of their individual distribution and nature in complex SEI layers. On one side, there is a lack of experimental evidence regarding the composite structure of multiphase SEI layers and the widely acknowledged presumption of electronically insulating characteristics. On the other side, there is little experimental research on these individual phases in battery-relevant contexts, specifically concerning partial ionic and electronic transport properties. Hence, establishing correlations between assumptions about the SEI layer, validating experimental results, and interpreting electrochemical data is a complex task.

In this study, we introduce a novel approach to gain deeper comprehension of the multiphase SEI layer at a new scale. Li_6PS_5Cl (LPSCl) as model SE is utilized to investigate the SEI properties of sulfide SEs in contact with lithium metal. We synthesize bulk-phase SEI-type material ("bulk-SEI") through direct synthesis from LPSCl and micron-size lithium metal powder. This enables the assessment of various SEI properties without the need for approximation based on individual constituent phases. X-ray powder diffraction (XRD) and X-ray photoelectron spectroscopy (XPS) measurements are conducted to confirm the successful synthesis of the bulk-SEI and validate the chemical composition. The morphology of the synthesized bulk-SEI particles is examined using scanning electron microscopy (SEM). The presence of domains enriched in S, P, or Cl is confirmed by complementary energy dispersive X-ray spectroscopy (EDX). dc polarization under selectively blocking conditions, i.e., the Wagner-Hebb configuration,[43,44] is utilized for electrochemical characterization. Thereby, we quantify the partial ionic and electronic conductivities of the synthesized multiphase bulk-SEI. Based on these data, we assess SEI growth as well as its thickness using a Wagner-type diffusion model, which is in very good agreement with electrochemical studies on cell-level multiphase SEIs, and discuss its effect on SSBs. The findings from these studies provide a comprehensive and holistic understanding of the nanoscale SEI characteristics. Ultimately, we establish a guideline by estimating suitable partial conductivities for the SEI to optimize the Li|LPSCl interface and achieve sufficient long-term stability.

RESULTS AND DISCUSSION

To be a suitable separator material to incorporate LMAs and commercialize SSBs, a (sulfide) SE must fulfill various criteria, including high ionic conductivity. In the case of lithium thiophosphate-based SSBs, the challenges posed by the evolution and growth of multiphase SEIs result in increased ionic resistance and require further investigation.

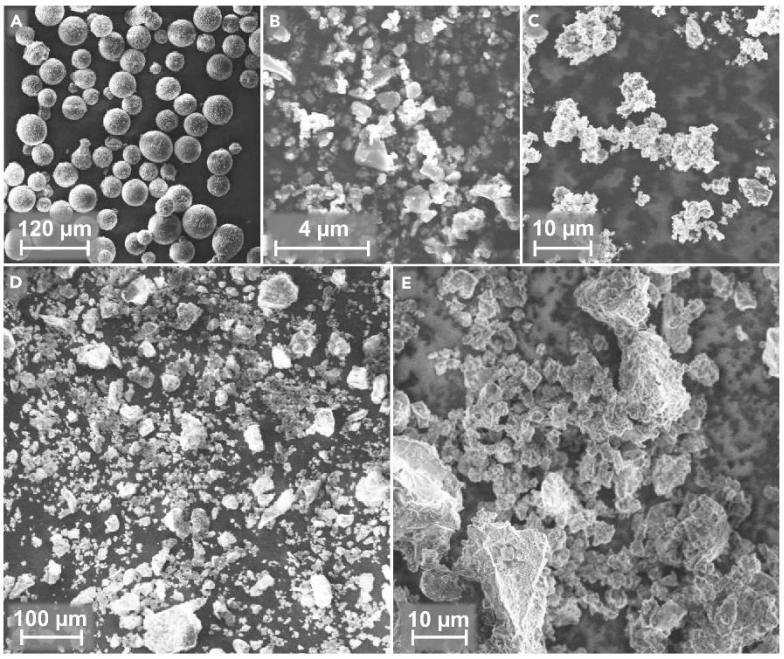

Figure 1. Scanning electron microscope images of the starting materials and the synthesized bulk-SEI

(A–C) Lithium metal powder (A), LPSCl powder (B), and the homogeneous mixture of both materials (hand-ground, serving as precursor) (C).

(D and E) Image of the synthesized bulk-SEI particles after annealing at 250°C and subsequent hand grinding in the mortar are shown in (D) and (E). No remains of spherical lithium metal powder have been identified. The particle size appears to be significantly increased, while differences in shape to the initial LPSCl and untreated mixture are found.

Material synthesis and chemical analysis of multiphase bulk-SEI

Detailed information on the prepared lithium metal powder is given in the supplemental information. This includes SEM images of single particles and the particle size distribution (Figures S1 and S2; Section A) and XRD results (Figure S4; Section C). Moreover, Figure S9 (Section D) presents the XPS depth-profiling results of lithium metal particles, which reveal the passivation layer comprising lithium hydroxide, Li_2O, lithium carbonate, and carbon species.

In Figure 1, SEM images of the starting materials are compared: freshly prepared lithium metal powder (A), LPSCl powder (B), and their hand-ground mixture before annealing (C). XRD analysis of the mixture (Figure S6; Section C, supplemental information) did solely disclose minor signs of reaction (as evidenced by clear LPSCl and lithium metal reflections), and electrochemical testing revealed high electronic conductivity—even after few weeks of storage. Hence, it was employed as precursor in the subsequent heat treatment process at 250°C. Please note that this is an extra (synthesis) step, which may lead to unavoidable deviations from the characteristics (i.e., morphology and properties) of the actual SEI in SSBs. Images of the resulting bulk-SEI particles (Figures 1D and 1E, at different magnifications) provide first insights into their morphology. It comprises micron-sized, agglomerated secondary particles with various shapes and sizes. The absence of spherical particles (i.e., lithium metal powder) in the precursor (C) and the final product (D and E) provides an initial indication of the successful mixing and subsequent reaction, respectively.

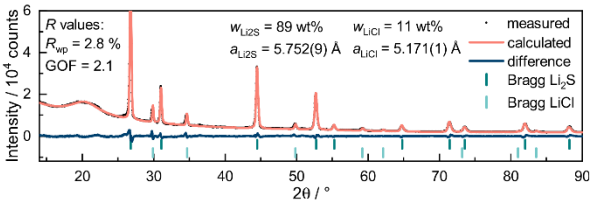

Figure 2. Representative X-ray diffraction pattern of the synthesized bulk-SEI and the corresponding Rietveld refinements

Single phases of Li_2S (ICSD: 196932) and LiCl (ICSD: 52235) are identified. *w*, *a*, R_{wp}, and GOF are the mass fraction, lattice constant, weighted profile R-factor, and goodness of fit, respectively.

The particle size of the product appears even after consecutive grinding to be increased compared to the initial particle size of the sulfide SE and the precursor mixture. As mentioned above, the increased particle size could be related to the annealing step. Additional SEM images with further details on the bulk-SEI's morphology are shown in Figure S3; Section B, supplemental information.

The properties of the synthesized bulk-SEI are notably responsive to the carefully measured stoichiometric ratio of reactants. Specifically, residuals of LPSCl may impact the partial ionic conductivity, while lithium metal residuals may affect the electronic conductivity. If residuals persist, we anticipate the latter to have a more significant impact. To avoid this, we adjusted the amounts of lithium metal powder and LPSCl to their corresponding molar ratio without risking an over-stoichiometric amount of lithium metal. Thus, to confirm the successful synthesis, ensure the absence of any remaining reactants, and acquire further information about the crystalline nature of the obtained bulk-SEI, phase analysis by means of powder XRD was performed (see Figure 2). While the interfering background in the 2θ range of 17°–23° is caused by the polyimide cover, the XRD pattern reveals distinct reflections corresponding to single phases of Li_2S and LiCl. Identifying both compounds indicates the (partially) successful synthesis according to the chemical reaction (Equation 1).

However, no traces of the expected Li_3P or any related phosphorous compounds, including intermediates, are detected via XRD. The most prominent reflections of phase-pure Li_3P occur at 23.4°, 24.0°, 26.8°, 42.3°, and 43.4° (ICSD: 26880). However, the detection of Li_3P is hindered by the polyimide cover, particularly up to 24°, and the Li_3P reflection at 26.8° superimposes with the most prominent peak of Li_2S. Additionally, no clear reflections are observed at 42.3° and 43.4°. Figure S7 (Section C, supplemental information) provides the magnified XRD pattern in the range of 40° to 62°.

The potential presence of multiple lithiated phosphorus compounds (e.g., Li_xP intermediates) significantly reduces the probability of their detection in the bulk-SEI due to the low fractions of each phosphorus compound. Moreover, another possible reason is the increased reactivity of Li_3P to moisture, with the polyimide covers used here only minimizing exposure to air. To the best of our knowledge, the observation of Li_3P in SEI studies has only been reported but remains challenging under ultra-high vacuum (UHV) conditions (e.g., by XPS).[45,46] Lastly, Li_3P may be in an amorphous (non-crystalline) state in the bulk-SEI, which is also often assumed in studies of phosphorus as an electrode material in batteries.[47–49]

The Rietveld refinement of the XRD pattern provides lattice constant values of *a* = 5.753 Å for the Li_2S phase and *a* = 5.171 Å for the LiCl phase, which are in good

agreement with previously reported values.[50,51] Furthermore, the refinement process reveals the mass fractions of the synthesized bulk-SEI for each identified compound. Li_2S represents the predominant fraction at 89 wt %, while LiCl accounts for only 11 wt % of the overall composition. It should be noted that the starting LPSCl material used in the synthesis already contained 3 wt % of LiCl as an impurity (identified by XRD refinement; see Figure S5; Section C, supplemental information). However, a direct comparison of these mass fractions obtained through XRD measurements to the expected values (of chemical reaction [Equation 1]) is not feasible due to the potential presence of unidentified or non-crystalline phases.

Notably, reflections of the initial constituents (lithium metal and LPSCl) are neither detected nor identified, especially in comparison with reference diffractograms of both materials and the precursor (see Figures S4–S6; Section C, supplemental information). Therefore, Figure S8 (Section C, supplemental information) provides a comparison of XRD patterns (raw data) between LPSCl, precursor mixture, and synthesized bulk-SEI. As mentioned above, we intentionally avoided using over-stoichiometric amounts of lithium metal during preparation. Hence, we did not aim to compensate for lithium loss originating from passivation films present on lithium metal powders. In addition, we believe that lithium metal powder would further be subjected to passivation during grinding and synthesis due to its high reactivity and increased surface area (even under inert conditions in gloveboxes). Therefore, some lithium metal is inevitably consumed due to passivation reactions (e.g., Li_2O, lithium hydroxide, and lithium carbonate formation), making it more likely for residual LPSCl to be present in the bulk-SEI. Additional lithium compounds, such as lithium hydroxide and Li_2O, are also not identified. With respect to residual LPSCl, there is a slight increase in intensity at ~36.5°. However, despite this observation, the primary (most prominent) reflections of LPSCl at 25.6°, 30.0°, and 31.5° are not detected for the bulk-SEI. We believe that these features are not conclusive for the presence of lithium metal or LPSCl residuals. Thus, we assume that residual amounts of either lithium metal or LPSCl are sufficiently small, distributed within the multiphase SEI, and passivated or isolated so that they do not affect the properties of the bulk-SEI, as will be discussed in the next section.

In order to gain additional chemical information, resolve the unidentified, missing, or amorphous phases, and provide a thorough understanding of the chemical composition of the bulk-SEI, a chemical analysis using XPS was carried out next. Furthermore, we conduct additional analysis to verify the absence of lithium metal traces within the bulk-SEI and to quantify any residual amounts of LPSCl that may not have been fully consumed. This is crucial to ensure that the properties of the bulk-SEI remain uncompromised.

Figure 3 shows the Li 1s, S 2p, and P 2p XP spectra of the synthesized bulk-SEI. No lithium metal signals at binding energies (BEs) below 53 eV and plasmon-loss features at ~60 eV are detected in the Li 1s spectrum. We also performed depth profiling, which did not provide additional information on the bulk-SEI structure or identify residual amounts of lithium metal (Figure S10; Section E, supplemental information). This is in contrast to the XP spectra of lithium metal powder (compare Figure S9; Section D, supplemental information). Hence, these results verify the prior findings and consequently validate the complete consumption of lithium metal. Please note that minor impurities of lithium hydroxide and carbonates (both at 55.4 eV) as well as Li_2O (54.5 eV) cannot be prevented—even at dynamic vacuum conditions during synthesis. This can be attributed to the highly reactive nature of lithium metal and its increased surface area in powder form. However, as crystalline

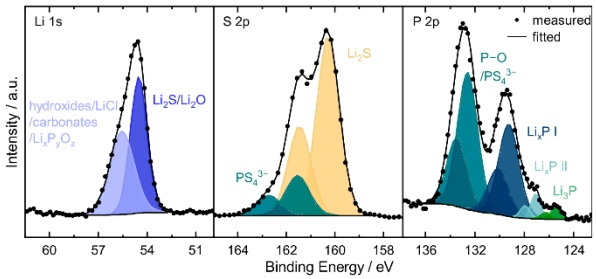

Figure 3. X-ray photoelectron Li 1s, P 2p, and S 2p spectra of the synthesized bulk-SEI
The analysis of these spectra revealed the successful synthesis of bulk-SEI. In the S 2p and P 2p spectra, the evolution of Li_2S and Li_3P (and related polyphosphides) is clearly evidenced, respectively. In the Li 1s spectra, it is evident that lithium metal is absent and has been entirely consumed. However, only minor residual amounts of LPSCl (P–O/PS_4^{3-} doublets in the S 2p and P 2p spectra) may remain present, as confirmed by quantitative analysis (Figure S11).

impurities could not be identified by XRD measurements, we consider the impurity fractions to be negligible. XPS quantification (Figure S11; Section E, supplemental information) showed that the major impurities are lithium hydroxides resulting from reactions with trace amounts of moisture and oxygen and that the peak at 55.4 eV (in Li 1s) is mainly dominated by the Li_2S with smaller contributions of Li_2O. Both aspects are identified by comparing the quantification of the Li 1s with the O 1s and S 2p spectra, respectively. Unfortunately, signals of LiCl and (oxygenated) phosphorous species superimpose with those of lithium hydroxides.

The complete reduction of LPSCl to various decomposition products is evident in the S 2p and P 2p spectra. In the S 2p spectrum, the distinct signal at 160.3 eV can be assigned to Li_2S. This finding matches the thermodynamic predictions. Thus, Li_2S is formed during the reduction of LPSCl by lithium metal (as also confirmed by XRD). The prevalence of Li_2S is consistent with the chemical reaction (Equation 1), comprising the main volume fraction of the SEI (theoretically 71 vol % Li_2S).

In contrast to our XRD results, the P 2p spectrum shows indeed reduced phosphorus species in different lithiated (non-stoichiometric) states. While the signal of Li_3P at a BE of 125.4 eV can be clearly identified, two other well-separated doublets (127.1 and 129.3 eV, respectively) are detected, indicating lithium polyphosphides with slightly decreased lithium content (such as LiP_5, LiP_7, or Li_xP with $x < 3$). As these compounds are not detected in the XRD pattern, they are possibly in an amorphous state. Quantification results in Figure S11 (Section E, supplemental information) show that the total amount of phosphorous in the bulk-SEI is as expected. However, the identification of multiple species explains the lower-than-expected atomic fraction of Li_3P and the difficulties encountered in XRD analysis.

Depending on the XPS measurement conditions, it is common in SEI studies to detect low intensities of Li_3P as well as contributions (at higher intensities) of various phosphorous species (Li_xP).[19,45] Wenzel et al.[46] reported the high reactivity of Li_3P with trace amounts of oxygen and moisture inside the XPS chamber (i.e., UHV conditions), resulting in the consumption of freshly reduced Li_3P. This demonstrates that observation of Li_3P in SEI studies is still difficult, even under UHV conditions, and especially for XRD and other post mortem techniques.[28] To verify these challenges in the analysis of Li_3P, we synthesized samples of Li_3P (see supplemental experimental procedures, supplemental information). Our XPS study (Figure S14; Section F, supplemental information) shows large contributions from Li_xP and only minor

signals from Li_3P for the bulk-phase Li_3P reference sample, emphasizing the instability of Li_3P. Further, it has been reported that the availability and amount of lithium present during the SE degradation reaction are understood to affect the fraction of Li_3P.[45] Hence, the identification of three reduced phosphorous species may be attributed to regions with different lithium metal accessibilities in our synthesis reaction. Nonetheless, we believe that during the cycling of SSBs, there may also be variations in lithium availability influencing the growth of the SEI.

Similar to the S 2p spectrum (at 161.6 eV), the P 2p spectrum also shows signals of residual PS_4^{3-} species at 132.6 eV, also overlapping with those of oxygenated phosphorous species (P–O). The latter species are also identified in measurements of bulk-phase Li_3P (Figure S14; Section F, supplemental information), which are used as reference to identify the BE of P–O (between 132 and 134 eV). PS_4^{3-} signals potentially indicate that LPSCl is not entirely consumed and minor residuals may remain present in the obtained bulk-SEI material. Quantification results in Figure S11 (Section E, supplemental information), however, show that P–O contributes more significantly to the shared peak with PS_4^{3-}, highlighting the relatively low amount of residual LPSCl. This becomes evident by comparing the quantification of the S 2p spectra, which demonstrates the low contribution of PS_4^{3-} in P 2p as the atomic percentage for PS_4^{3-} in S 2p should be four times higher compared with P 2p. Since we could also not identify any remaining LPSCl by XRD measurements, we consider its residual quantity to be insignificant. Therefore, we assume that the properties of the bulk-SEI remain unaffected, and any potential residual amount of precursor is likely to be small and distributed within the bulk-SEI.

In the Cl 2p spectrum, the signal caused by LPSCl and LiCl exhibit similar BEs and cannot be distinguished. Therefore, it is not possible to analyze the reduction of LPSCl in the Cl 2p spectrum. However, the evolution of LiCl in the bulk-SEI by decomposition of LPSCl is clearly observed by XRD analysis. Furthermore, the O 1s spectrum, although not presented here, substantiates the development of lithium hydroxides and carbonates, Li_2O, and oxygenated phosphorous species (P–O). We emphasize that impurities such as Li_2O do not compromise the validity of our synthetic approach as Li_2O can form due to trace amounts of oxygen and moisture during storage, synthesis, or measurement.[52] The O 1s, C 1s, and Cl 2p spectra are presented in Figure S12 (Section E, supplemental information). XP spectra (for reference purposes) of pristine LPSCl are provided in Figure S15 (Section F, supplemental information).

Observing the evolution of Li_2S, Li_3P (and lithium polyphosphides), and LiCl by XPS and XRD, the successful synthesis of bulk-SEI is demonstrated. Combined XRD, XPS, and quantitative analysis provide assurance that the insignificant amounts of residual precursor material should not interfere with the accurate description and modeling of multiphase SEI properties in the synthesized bulk-SEI material. We note that, alongside the heat treatment, mechanochemical reactions taking place in SSBs (under stack pressure) may potentially lead to changes in the SEI composition. Since our results show the presence of several phases, the local distribution of elements is analyzed using EDX mapping.

The expanded SEM image of a single large bulk-SEI particle, along with EDX mapping for sulfur, phosphorous, and chlorine, is shown in Figure 4. It reveals a predominant sulfur signal, which may indicate the distribution of Li_2S. Considering the non-uniformity in the predominant sulfur signal and by reviewing the combined mapping, domains with distinct phases are found. This becomes obvious in regions

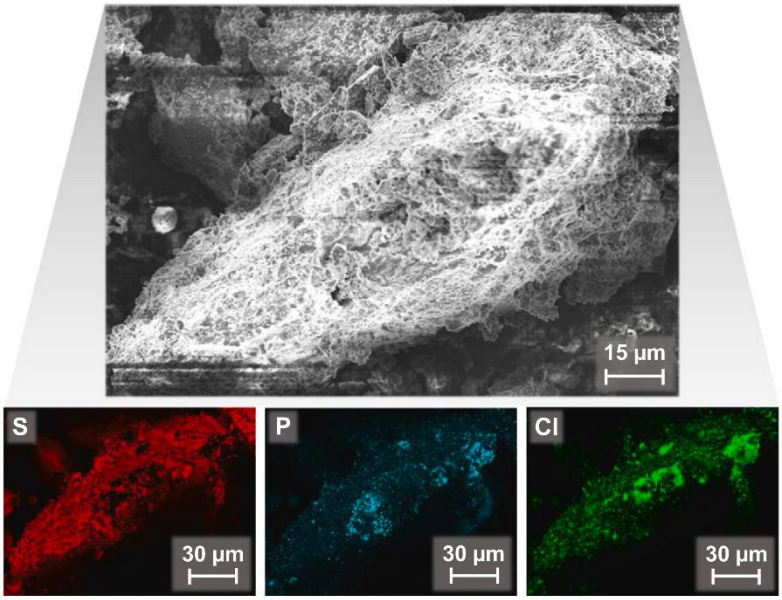

Figure 4. SEM image and corresponding EDX element mappings of one bulk-SEI particle
SEM image (top) and EDX element mappings (bottom) were recorded at 8 kV for the elements sulfur, phosphorous, and chloride. Areas with elevated concentrations of sulfur, phosphorous, and chlorine are found, represented by the corresponding $K_{\alpha 1}$ lines, which likely indicate the distribution of Li_2S, Li_3P, and LiCl, respectively.

where the sulfur signal is weak, and elevated concentrations of phosphorus and chlorine are detected. The latter signals may indicate the presence and distribution of Li_3P (or other phosphorous species) and LiCl, respectively. Below, we will discuss the potential domain structure and the effect of non-uniform distribution of individual phases in multiphase SEIs.

Upon reviewing the elemental quantification for these three elements, we note mass ratios of 66 wt % for sulfur, 15 wt % for phosphorous, and 19 wt % for chlorine. The deviations, especially in the chlorine signal, can be attributed to the LiCl impurity phase in the starting LPSCl material, as identified by XRD refinement (refer to Figure S5). Reference measurements of pristine LPSCl determined a mass ratio of 68 wt % for sulfur, 14 wt % for phosphorous, and 18 wt % for chlorine (Figure S16; Section G, supplemental information). Hence, the obtained quantification of the bulk-SEI shows only minor shifts in the elemental ratio after synthesis. While the mass ratio of sulfur decreased, the elemental concentrations of phosphorus and chlorine increased slightly as well. However, this variation falls within the accuracy of EDX measurements. At this point, we want to emphasize that these EDX results solely reveal the elemental fractions, regardless of their binding state and chemical environment.

Assuming for simplicity that sulfur, phosphorous, and chlorine are mainly bound in SEI species, the mass ratios match well with the theoretical values of 71 wt % Li_2S, 16 wt % Li_3P, and 13 wt % LiCl for the SEI. For the sake of completeness, the elemental distribution of oxygen (in total, 5 wt %) is shown in Figure S17 (Section G, supplemental information). Signals of oxygen are evenly distributed across the particle surface at comparable low concentration. We assume that

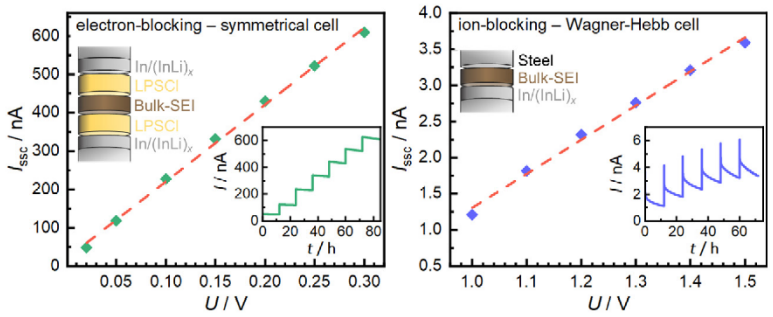

Figure 5. Determination of partial conductivities by dc polarization using selectively blocking cell configurations

(A and B) The electron-blocking setup and respective I_{ssc}-V correlation (A) and the ion-blocking Wagner-Hebb setup and respective I_{ssc}-V correlation (B) are used to evaluate σ_{ion} and σ_{el}, respectively. This is done by linearly fitting the data (red dashed lines) and using Equation 2. Each steady-state current I_{ssc} is obtained by analyzing the initial I-V curves (inlays) at different applied voltages for 12 h (at each voltage).

(surface) contaminations, e.g., lithium hydroxide as identified by XPS, are the reason for the observed oxygen signals due to reactions with trace amounts of oxygen and moisture. However, this is not necessarily indicating or evidencing the presence (or position) of residual lithium metal precursors since naturally formed SEI can also consist of species containing oxygen.

Conduction properties

The conduction characteristics ultimately determine the nature and growth of SEIs. Therefore, a comprehensive investigation and quantification of both the partial ionic (σ_{ion}) and electronic conductivity (σ_{el}) of SEIs play pivotal roles in assessing SEI growth and its long-term impact on battery performance.

We expect the SEI to be a mixed ion-electron conductor with low partial conductivities. Hence, conductivity measurements on pure bulk-SEI powder were performed to investigate its partial ionic and electronic transport properties. Moreover, the observed conductivity may also indicate the presence of residual precursor material, as remains of lithium metal and LPSCl should increase σ_{el} and σ_{ion}, respectively. Since impedance measurements were found to be ineffective in deconvoluting the partial conductivities, we used dc polarization. Specifically, dc Wagner-Hebb measurements with one selectively blocking electrode are reported to effectively separate (low) ionic and electronic conductivities at fixed redox potentials (i.e., controlled lithium-ion activities).[43,44]

Unfortunately, for assessing σ_{ion}, the corresponding Wagner-Hebb configuration (with one electron-blocking and one reversible electrode) was unsuitable due to the lack of stable conditions. Thus, two electron-blocking electrodes were utilized (depicted in Figure 5A). σ_{ion} is calculated by taking the slope from linear regression for the steady-state current I_{ssc} of successive dc measurements under electron-blocking conditions (see Figure 5A) according to Equation 2:

$$\sigma_i = \frac{dI_{res}}{dV} \cdot \frac{l}{A} \qquad \text{(Equation 2)}$$

with V being the applied voltage, l the pellet thickness, A the cell area, and i indicating the respective charge carrier—for either ionic (ion) or electronic (el) conduction.

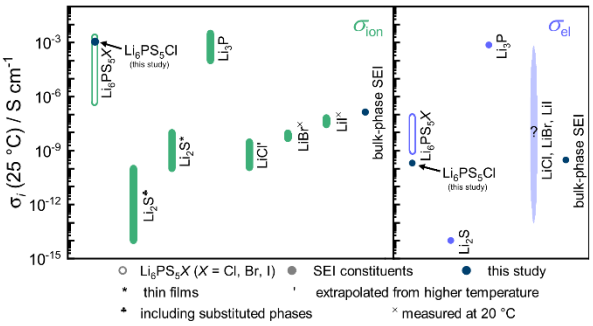

Figure 6. The partial ionic and electronic conductivities σ_i (i = ion and el, respectively) at 25°C of Li_6PS_5X (X = Cl, Br, and I; excluding substituted phases) and their typical SEI constituents

σ_i of the bulk-SEI and the initially used sulfide SE (Li_6PS_5Cl) in this work are depicted in dark blue. For some materials, a range of values is reported by different authors. The values of Li_6PS_5X (X = Cl, Br, and I),[53–58] Li_2S,[59–61] Li_3P,[62–64] LiCl,[65,66] LiBr,[66,67] and LiI[66–69] were taken from the reported data. An asterisk, an apostrophe, a spade, and a cross indicate the values for thin film materials, data estimated by extrapolation from higher temperatures, data including substituted phases, and data recorded at 20°C, respectively.

We determined the room temperature (25°C) partial ionic conductivity to be σ_{ion} = 134 nS cm^{-1} for the bulk-SEI of LPSCl. To put this value within a wider context, we further compare reported conductivity values for various single-phase SEI constituents of lithium argyrodites Li_6PS_5X (X = Cl, Br, I) (Figure 6, left). It is noteworthy that neither the individual values for these SEI constituents (i.e., Li_2S, Li_3P, and LiCl) nor the value of the LPSCl used align with σ_{ion} estimated in this study (represented in dark blue, σ_{ion} = 134 nS/cm). This proves a substantial underestimation of the SEI's partial ionic conductivity compared with several previous studies (related to various sulfide SEs) by at least one order of magnitude when simply assuming the ionic conductivity of bulk-type, microcrystalline Li_2S.[46] As will be shown below, this underestimation results in inaccurate approximations of the SEI layer thickness (and potentially other properties). Nevertheless, this discrepancy is particularly relevant given that Li_2S constitutes the dominant volume fraction within the SEI, accounting for 71 vol %. Consequently, other SEI constituents (i.e., Li_3P) must enable a higher overall ionic conductivity, or the Li_2S formed in the (bulk-)SEI has a higher conductivity than bulk-Li_2S, e.g., due to amorphous phase fractions, nanocrystalline regions, or interface contributions. A more thorough examination of this observation, however, falls outside the scope of this study and requires further investigation. Please note once more that the heat treatment during synthesis may lead to deviations from the actual SEI at the Li|LPSCl interface, potentially affecting both the formation of phases and the overall conductivity. It is our working hypothesis that we come close to the true SEI with our approach, as confirmed below by the quantitative SEI growth considerations.

σ_{el} was determined by dc Wagner-Hebb measurements with one ion-blocking and one reversible electrode (depicted in Figure 5B) and calculated (using Equation 2) to be σ_{el} = 0.3 nS cm^{-1} at room temperature for the bulk-SEI of LPSCl. In Figure 6 (right), this value is compared with reported conductivity values for some single-phase SEI constituents of lithium argyrodites Li_6PS_5X (X = Cl, Br, I). While it agrees well with the value of the LPSCl used, it may not indicate an increased dendrite risk with respect to its comparable σ_{el}. Further, it clearly deviates from the reported electronic conductivity of bulk-Li_2S (~0.1 pS cm^{-1}) by a factor of three orders of magnitude.[61] This latter value is commonly used for the approximation of the conduction

properties of SEIs. The origin of this value for Li_2S remains unspecified by the authors. Comparing the value for (crystalline) Li_3P, it appears again that each SEI constituent may contribute to the overall σ_{el} of the bulk-SEI. Please note that the values for σ_{ion} and σ_{el} of crystalline Li_3P serve as a preliminary approximation, although they may differ from those in the amorphous state or in other Li_xP compounds. Unfortunately, to the best of our knowledge, reliable values for σ_{el}, especially for LiCl but also for LiBr and LiI, have not been reported in literature. Thus, we like to emphasize that the lack of reliable information on σ_{el} of corresponding binary lithium compounds hinders further analysis and calls for additional experimental studies.

These measurements and results represent the first experimental data being reported for the σ_{ion} and σ_{el} of SEI-type materials. The values obtained in this study can serve as valuable parameters for assessing further SEI properties by simulation and modeling.

SEI growth kinetics and implications for SSBs

Consequently, we intend to assess the partial conductivities of ionic and electronic charge carriers in the SEI with regard to their implication on SSB performance and lifetime. When comparing the ionic conductivity of lithium argyrodites Li_6PS_5X (X = Cl, Br, I) (shown left in Figure 6), it becomes evident that the SEI conductivity exhibits a significantly lower conductivity than the lithium argyrodites. Notably, the difference becomes especially pronounced (several orders of magnitude) when compared with lithium argyrodites with high ionic conductivity (as utilized in this study, represented in dark blue).

In order to compute various properties and assess potential implications, we consider published data for SEI resistances extracted from impedance measurements. Riegger et al.[27] documented area-specific ionic resistances of up to 80 Ω cm^2 for multiphase SEI layers of degraded LPSCl (in contact to passivated lithium foil). Using this value, as well as σ_{ion} from our study, and assuming self-limited growth, we estimate a SEI layer thickness of up to d $\sim$ 110 nm. This thickness estimation is plausible, considering that the partial ionic conductivity within nanoscale multiphase layers may locally increase. Consequently, this would mark a further increase in SEI layer thickness.

Wenzel et al.[46] estimated a SEI layer thickness of only a few nm by the analysis of impedance measurements. However, the authors based their assumptions on the SEI's partial ionic conductivity on the properties of bulk-Li_2S, which substantially underestimates the SEI's partial ionic conductivity, as discussed above. Thus, the estimates of SEI layer thickness by Wenzel et al. are too low by at least one order of magnitude.

However, for a comprehensive analysis of SEI growth, it is essential to take kinetic considerations into account. The diffusion-controlled growth of the SEI can be approximated and described by a Wagner-type diffusion model if the growing layer is approximated as a dense and fully covering interphase. Adapting this model leads to Equation 3, with a square-root of time behavior for the consumption of SE material:[19]

$$d = \sqrt{\frac{2}{F^2 \cdot \rho_{SEI} \cdot x} \frac{M_{SEI} \cdot \sigma_{el} \cdot \sigma_{ion}}{\sigma_{el}+\sigma_{ion}} \cdot \mu_{Li}^0 \cdot \sqrt{t}} \cong \sqrt{\frac{2}{F^2 \cdot \rho_{SEI} \cdot x} M_{SEI} \cdot \sigma_{el} \cdot \mu_{Li}^0 \cdot \sqrt{t}} = k \cdot \sqrt{t} \quad \text{(Equation 3)}$$

with d, F, ρ_{SEI}, x, M_{SEI}, σ_{ion}, σ_{el}, μ^0_{Li}, t, and k being the SEI layer thickness, the Faraday constant, the mean density of the SEI, the stoichiometric factor (moles of the lithium metal required for the stoichiometric decomposition reaction—in our case 8), the mean molar mass of the SEI, the mean ionic and electronic conductivity of the SEI, the chemical potential of pure lithium metal (μ^0_{Li} = 8.35 kJ mol^{-1}), the reaction time, and the parabolic rate constant, respectively. This equation was derived by approximating the gradient of the chemical potential by μ^0_{Li}/d, as described elsewhere.[26] Additionally, it is important to highlight that Equation 3 is applicable under conditions of one-dimensional transport, purely chemical potential gradient-driven flux, and boundaries with constant chemical potentials.[70]

Further, Equation 3 can be transferred to Equation 4 by substituting d with $\sigma_{SEI} = d/R_{SEI}$ and assuming $\sigma_{SEI} \cong \sigma_{ion} \gg \sigma_{el}$, with σ_{SEI} being the mean SEI conductivity and R_{SEI} being the area-specific ionic resistance of the SEI:

$$R_{SEI} = \frac{1}{\sigma_{SEI}} \cdot \sqrt{\frac{2}{F^2 \cdot \rho_{SEI} \cdot x} \frac{M_{SEI} \cdot \sigma_{el} \cdot \sigma_{ion}}{\sigma_{el}+\sigma_{ion}} \cdot \mu^0_{Li} \cdot \sqrt{t}} \cong \frac{1}{\sigma_{ion}} \cdot \sqrt{\frac{2}{F^2 \cdot \rho_{SEI} \cdot x} M_{SEI} \cdot \sigma_{el} \cdot \mu^0_{Li} \cdot \sqrt{t}} = k' \cdot \sqrt{t} \quad \text{(Equation 4)}$$

Hence, a new parabolic rate constant k' is derived, describing the temporal evolution of resistance due to SEI growth. Consequently, the SEI growth can be anticipated to extrapolate the SEI layer thickness and the corresponding SEI resistance over extended periods (i.e., up to the typical battery lifetime of 10 years). Taking Equations 3 and 4 as well as the findings from our study on σ_{ion} and σ_{el} of the bulk-SEI, the parabolic rate constants were calculated to be k = 0.43 nm s$^{-0.5}$ and k' = 320 mΩ cm^2 s$^{-0.5}$ for LPSCl. After 1 day, the SEI layer thickness is approximated to be d = 126 nm with a resistance of R_{SEI} = 95 Ω cm^2. These values increase from 334 nm and 250 Ω cm^2 to 7.6 μm and 5.7 kΩ cm^2 over a period of 1 week and 10 years, respectively. This agrees well with recent findings on SEI layer thickness by Aktekin et al.[28] and Otto et al.[29] of ~315 and ~305 nm for 1 week (from electrochemical titration and ToF-SIMS studies), respectively. Therefore, the values obtained for σ_{ion} and σ_{el} in this study validate previous findings on the SEI dimensions.

The very good agreement between our current results and the SEI growth kinetics determined using a completely different electrochemical approach (i.e., coulometric titration time analysis, CTTA, in anode-free cells) demonstrates the viability of our bulk-SEI synthesis approach. Figure S18 (Section H, supplemental information) compares the temporal evolution of SEI growth predicted from bulk-SEI properties using the Wagner-type diffusion model (d_{SEI} vs. t or $t^{0.5}$) with the SEI growth quantitatively observed in CTTA experiments.[28] In this comparison, Equation 3 and the parabolic rate constant (k = 0.43 nm s$^{-0.5}$) obtained in our study were used. Conversely, CTTA results can also be used to calculate k and σ_{el} from the slope of the linear fit in d_{SEI} vs. $t^{0.5}$ and Equation 3, yielding values of 0.46 nm s$^{-0.5}$ and 0.34 nS cm^{-1}, respectively. These numbers closely match the values determined for the bulk-SEI in this study (k = 0.43 nm s$^{-0.5}$ and σ_{el} = 0.3 nS cm^{-1}). This agreement with the naturally formed SEI in a real cell, along with the characterization results of the synthesized bulk-SEI, provides strong evidence for: (1) a minimal to negligible impact of the elevated reaction temperature used; (2) unaltered bulk-SEI properties by potentially present precursor material traces (in respect to various properties)—or that the cell-level SEI also contains the same unreacted or unknown minor phases; (3) an effective simulation of multiphase SEI properties via bulk-SEI synthesis; and (4) an accurate modeling of transport parameters derived from those properties to predict SEI

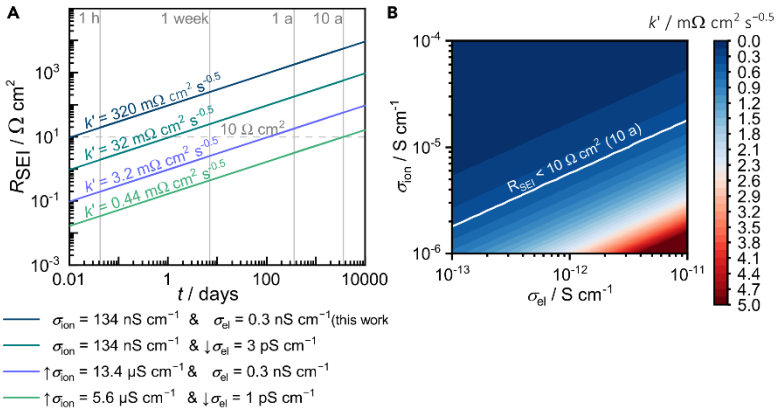

Figure 7. Modeling of the SEI (ionic) resistance as a function of time and the parabolic rate constant k' as a function of σ_{ion} and σ_{el}

(A) The SEI (ionic) resistance is calculated as a function of time for different combinations of σ_{ion} and σ_{el}, including the results of this work. The corresponding k' values are denoted on each profile. As a demonstration, we varied both partial conductivities by 2 orders of magnitude. A potential threshold for an optimized SEI resistance at 10 Ω cm^2 is marked (in gray), requiring k' to be less than 0.44 mΩ cm^2 s$^{-0.5}$ for a lifetime of 10 years (indicated in green).

(B)The contour map of the parabolic rate constant k' is calculated for values up to 5 mΩ cm^2 s$^{-0.5}$. The threshold value of 0.44 mΩ cm^2 s$^{-0.5}$ indicates a SEI (ionic) resistance of ~10 Ω cm^2 and lower over a period of 10 years.

growth and kinetics in SSB cells. Additionally, the combination of both approaches validates the application of the Wagner-type diffusion model for the detailed analysis and description of SEI growth.

Hence, the good agreement between two entirely different approaches is a significant validation for the effectiveness of our synthetic SEI approach. Our experimental results on the partial conductivities enable kinetic considerations and calculations in estimating SEI growth using Wagner-type diffusion models. Consequently, we anticipate that our data will establish crucial parameters and encourage further endeavors in future simulations and modulations of SEI growth. In particular, we want to emphasize that our findings can serve as the basis for designing SEs that combine both high ionic conductivity and stable yet minimized SEI formation. This is discussed in the next section.

Randau et al.[1] emphasized that the cell impedance of operational SSBs should not exceed a value of 40 Ω cm^2 but rather should be even lower to meet the typical resistances of LIBs. As a potential threshold for SEI resistance, we consider 10 Ω cm^2 to be a reasonable value to ensure the sufficient kinetic performance of SSBs. Therefore, we calculated the resistance increase of the SEI for up to 10 years (according to Equation 4) for different partial conductivities (σ_{ion} and σ_{el}) and resulting k' values (see Figure 7A).

Starting from the partial conductivities obtained in this study, it is demonstrated that reducing σ_{el} and increasing σ_{ion} leads to a decrease in the parabolic rate constant and, consequently, a decrease in resistance (and thickness) over time. Combining both reduces k' further (as seen in the green line). While a value of 32 mΩ cm^2 s$^{-0.5}$ for k' is insufficient to significantly reduce the SEI resistance, a reduction to less than 5 mΩ cm^2 s$^{-0.5}$ seems suitable for several weeks to months. However, to meet the long-term criteria of 10 Ω cm^2 over 10 years, further reduction

of k' to ~0.44 mΩ cm^2 s$^{-0.5}$ is crucial—or finding a mechanism to stop the diffusion-controlled SEI formation at all. To complete the picture: with an upper limit of 0.44 mΩ cm^2 s$^{-0.5}$ for k', this corresponds to a growth rate of $k \leq 0.25$ pm s$^{-0.5}$ and a SEI layer thickness of $d \leq 4.4$ nm after 10 years.

Hence, our experimental findings and computations underscore the need for SEI optimization to decrease its impedance and growth rate to stabilize the Li|SE interface (i.e., by reducing the mean σ_{el} or improving the mean σ_{ion} of SEIs). However, suitable values for k' can be achieved through various combinations of σ_{ion} and σ_{el}. Therefore, we plotted the relationship between k' and σ_{ion} as well as σ_{el}, considering values up to 5 mΩ cm^2 s$^{-0.5}$ in Figure 7B. The findings from Figure 7A served as a threshold value ($k' < 0.44$ mΩ cm^2 s$^{-0.5}$, white profile).

In line with Equation 4, k' exhibits a reciprocal relationship with σ_{ion}, whereas it follows a square-root relationship with σ_{el}: $R_{SEI} \sim \sigma_{ion}^{-1} \cdot \sigma_{el}^{0.5}$. Therefore, enhancing σ_{ion} is a more effective strategy for optimizing the Li|SE interface. However, considering feasibility, we assume that improving σ_{ion} of the SEI up to 10^{-4} S cm^{-1} is unlikely, given the typical values for σ_{ion} in common SEs (~10^{-3} S cm^{-1}). As a result, it becomes crucial to optimize both σ_{ion} and σ_{el} of the SEI to facilitate the long-term viability of SSBs for practical applications. We like to highlight the critical role of Li_3P for the SEI growth and resistance, as it appears to be a true mixed conductor. Its volume fraction is below the typical limit for 3D percolation, but it will increase the mean ionic conductivity of the SEI and thus reduce R_{SEI}. Unfortunately, it will also increase the mean electronic conductivity of the SEI and thus increase the growth rate of the SEI. It is worth noting that Na_3P is the critical SEI component in the analog case of SEI formation in sodium thiophosphates like Na_3PS_4. As demonstrated by Wenzel et al.,[71] Na_3PS_4 degrades rapidly by reaction with sodium metal, as the volume fraction of Na_3P in the SEI is even higher than in the case of Li_6PS_5Cl, and as Na_3P has a higher electronic conductivity than Li_3P.

The question whether SEI layers in SSBs exhibit self-limiting growth remains controversial, given that the growth rate (i.e., k) of the SEI is determined by σ_{el} (with respect to Equation 3: $R_{SEI} \sim \sigma_{el}^{0.5}$). The value of σ_{el} determined in this study cannot be disregarded and raises doubts about the self-limited growth mode during SEI evolution. In a recent theoretical study on $Li_xPO_yN_z$, Li et al.[72] emphasized the critical importance of low electronic conductivity in preventing SEI formation, achieving interface stabilization.[38] This would consequently lead to a thin SEI layer and minimal interphase resistance. Please note that $Li_xPO_yN_z$ shows the lowest reported values for σ_{el} in literature for a SE (10^{-14}–10^{-12} S cm^{-1}).[73–75] Our findings strongly suggest that σ_{el} of the multiphase SEI investigated in our study will be too high to effectively impede ongoing SEI growth in lithium thiophosphate-based SSBs, as long as no reasonable countermeasure is being taken. However, it is important to note that the electronic insulating properties of multiphase SEIs are not thoroughly explored or comprehensively understood yet, making additional assessments speculative. We also need to stress that our knowledge on the role of the SEI in thiophosphate electrolytes is limited. Cells in academic labs will usually not be studied longer than a few weeks. The resistance growth due to SEI formation may not be critical within the period of time, and thus, is probably underrated.

Upon assessing the potential consequences for SSBs by the multiphase SEI's conduction properties evaluated here, further aspects require consideration. The separation of individual phases within the multiphase bulk-SEI observed in EDX measurements may suggest the presence of advantageous conduction pathways on the

nanoscale, potentially leading to percolation phenomena along interfaces. Independent on the actual microstructure (i.e., domains or layers), advantageous conduction pathways within SEI layers may have detrimental effects on the long-term performance of SSBs. On the one hand, beneficial ionic pathways (i.e., by Li_3P) may support the conduction of lithium ions, effectively bypassing regions with lower ionic conductivity (i.e., Li_2S and LiCl). Resulting in inhomogeneous Li|SEI|SE interface conditions, this would hinder a homogeneously distributed lithium-ion flux during battery cycling due to increased constriction phenomena,[76] and disturb the formation of uniform metal stripping and plating morphologies. On the other hand, the existence of favorable electronic pathways by individual phases will strongly influence the SEI growth, leading to inhomogeneous and ongoing SEI formation, eventually causing cell failure. Hence, our EDX studies underscore the essential need for comprehensive investigations into the microstructure of composite (multiphase) SEI layers in future research.

We like to emphasize the importance of implementing effective measures—during the design of SEs—to stabilize and suppress interphase evolution for the above consequences. The inherent characteristics of multiphase SEI layers require optimization, especially with regard to σ_{ion} and σ_{el}, to effectively minimize implications for SSBs. The ionic impedance and layer thickness of SEIs currently prevent the development of long-term operational SSBs with lithium metal, once unmodified sulfide SEs are used. Hence, controlling the interface and interphase properties can ultimately lead to the realization of SSBs through the integration of LMAs, positioning SSBs as viable competitors to LIBs. One possible approach involves examining and enhancing fully reduced SEs that are thermodynamically stable at low operating potentials, aiming to eliminate degradation.[77,78] If (inorganic) modifications of sulfide SEs are found to be inadequate, introducing artificial interlayers (e.g., polymer-based ones) with moderate to high ionic conductivity and electronic insulating characteristics could potentially facilitate the stabilization of the Li|SE interface. We would like to note that Guo et al.[30] provide a more in-depth discussion of challenges of various engineering approaches at the Li|SE interface.

Conclusions

In this study, we present a novel and well transferable approach to simulate the degradation of various sulfide SEs, aiming to gain a deeper understanding of the properties of multiphase SEIs. Through a bulk-type solid-state reaction between the SE and micron-sized lithium particles, we obtain a composite of binary lithium phases that we suggest as a reasonable model for the SEI in SSB cells with LMAs. The formation of a bulk-SEI comprising Li_2S, Li_3P, and LiCl from the model electrolyte Li_6PS_5Cl and lithium metal powder has been proven. Subsequent conductivity measurements resulted in both partial ionic and electronic conductivity directly from the bulk-SEI material. The results reveal a significant underestimation in prior reports, particularly in case of the ionic conductivity by at least one order of magnitude. On the one hand, the electronic conductivity of the SEI controls its temporal evolution and its thickness as function of time. On the other hand, the ionic conductivity governs the resistance of the SEI, influencing both the performance and lifetime of SSBs. We hope that our experimental data (i.e., σ_{ion} and σ_{el}) will establish crucial benchmark parameters for upcoming simulations and further experimental evaluations. Our findings and computational results underscore the need to optimize the Li|SE interface and both partial conductivities, while motivating for further exploration and innovation to achieve lithium thiophosphate-based SSBs with high energy and power density.

EXPERIMENTAL PROCEDURES

Resource availability

Lead contact

Further information and requests for resources and reagents should be directed to and will be fulfilled by the lead contact, Jürgen Janek (juergen.janek@pc.jlug.de).

Materials availability

This study did not generate new, unique reagents.

Data and code availability

All data associated with the study are included as supplemental data with this article.

Synthesis and cell assembly were carried out in an argon-filled glovebox (*LabMaster-PRO*, MBraun, Garching, Germany), with $p(O_2)/p$ and $p(H_2O)/p < 1$ ppm. Electrochemical measurements were carried out in sealed cell casings at 25°C using a *VMP 300* potentiostat (BioLogic, Seyssinet-Pariset, France).

Preparation of materials

The lithium metal powder utilized in this study was synthesized by (droplet) emulsion, similar to the method described in elsewhere.[79] To this end, tetradecane (anhydrous, 99+ %, Sigma-Aldrich, Germany) as inert medium was gradually heated to 270°C in a custom-built stainless-steel reactor using a hotplate. The temperature was then maintained for 5 min to ensure thermal equilibration. Subsequently, 0.7–1 g of small lithium chunks, obtained by cutting lithium metal rods (99.8%, abcr, Germany), were added to the reactor. To achieve complete melting of lithium metal, the reactor was heated for additional 10 min. To create a lithium metal droplet emulsion, the tetradecane and lithium melt were stirred at 26,000 rpm for 5 min using an *X10* stirrer equipped with a *10G* tool (ystral, Germany). Once the stirring stopped, the mixture was slowly cooled down to ambient temperature, causing the lithium droplets to solidify into lithium metal particles. Subsequently, the inert liquid was removed via filtration, and the lithium metal powder was rinsed three times with hexane (anhydrous, 95%, Sigma-Aldrich, Germany). Lastly, the powder was dried at room temperature under argon to eliminate any remaining traces of tetradecane and hexane.

To synthesize bulk material (bulk-SEI) corresponding to the composition of the SEI, lithium argyrodite Li_6PS_5Cl (LPSCl) as SE (POSCO JK Solid Solution, Yangsan, South Korea) was mixed with a stochiometric amount of freshly prepared lithium metal powder based on the chemical reaction (Equation 1). Through grinding by hand in an agate mortar, a homogeneous mixture was achieved after 10 min, accompanied by a noticeable darkening of color. The mixture was then subjected to heating at 250°C for several hours under dynamic vacuum in an *MB-VOH-600* oven (MBraun, Garching, Germany). This additional heat treatment is used to complete the reaction between reactants. The resulting powder exhibited a reddish-brown color and was once more hand-ground to achieve a finer texture.

The morphology of the synthesized bulk-SEI was investigated by means of SEM using a field emission *GeminiSEM 560* (Carl Zeiss Microscopy, Oberkochen, Germany). For sample transfer, a transfer module system *EM VCT500* (Leica, Wetzlar, Germany) was used to prevent the exposure of samples to moisture and atmosphere. SEM images were taken using a secondary electron detector. Complementary EDX was performed using a *ULTIM MAX* EDX detector with 170 mm^2 SSD sensor (Oxford Instruments NanoAnalysis, High Wycombe, UK). The electron acceleration voltage during

spectra acquisition was set to 8 kV, images are acquired with a resolution of 512 pixels (100 µs pixel dwell time). Measurements of several different particles were conducted. The software *AZtec 4.3* (Oxford Instruments NanoAnalysis, High Wycombe, UK) was used for automatic identification and quantification of the elements sulfur, phosphorous, chlorine, and oxygen.

Characterization

XRD and XPS were employed for structural and detailed chemical analysis, respectively. The powder XRD pattern was obtained using an *Empyrean 2* diffractometer (Malvern Panalytical Ltd, Malvern, UK) configured in θ-θ geometry and equipped with a sample spinner. A monochromatic Cu-K_α X-ray beam with a wavelength of 154 pm was used. The measurements were conducted at an operating voltage of 40 kV and 40 mA, with a step size of 0.026° and a duration of 200 s per step. To prevent contamination during measurement, a polyimide foil was used to seal the sample under argon atmosphere. Rietveld refinements were carried out utilizing *TOPAS Academic v6.0* software[80] in combination with coding program jEdit.[81]

XPS measurements were conducted with a *Versaprobe 4* (ULVAC-PHI, Inc., Chanhassen, USA). A monochromatized Al K_α X-ray source was employed (beam diameter of 200 µm, X-ray power of 50 W), while the pressure in the XPS chamber was in the range of 10^{-7} to 10^{-6} Pa and the sample surface was charge neutralized by slow electrons and argon ions during measurements. XPS depth profiling was performed by Ar^+ sputtering with a grid size of 2 × 2 mm^2 with an initial sputtering step of 0.5 kV for 1 min, followed by a step of 1 kV for 1 min, and five sputtering steps of 2 kV for 1 min each. Using a transfer shuttle, cross contaminations with atmosphere were avoided. Data analysis was carried out with the *CasaXPS* software (Casa Software, Devon, UK).

Cell assembly and electrochemical testing

For measurements of the partial ionic conductivity, an electron-blocking symmetric cell configuration was used. 80 mg of bulk-SEI were compacted by hand in a polyether-ether-ketone casing using stainless-steel pistons. 80 mg of sulfide SE (LPSCl) were homogeneously distributed on each side of the bulk-SEI. By applying a uniaxial pressure of 380 MPa for 3 min at room temperature, the layered materials were densified, resulting in a pellet thickness of ~520 µm for the bulk-SEI. Finally, indium foil (100 µm thickness, 9 mm diameter, 99.999%, ChemPUR, Germany) and lithium foil (100 µm thickness, 6 mm diameter, 99.9%, China Energy Lithium, China) were placed on both sides of the stack to serve as lithium reservoir. Lithium diffuses into the indium metal and forms an $In/(InLi)_x$ phase field with a stable potential of 0.62 V vs. Li^+/Li.[82]

For the measurement of the partial electronic conductivity using Wagner-Hebb dc polarization,[43,44] a one-sided ion-blocking cell configuration was utilized. 80 mg of bulk-SEI were directly compressed at 380 MPa for 3 min at room temperature. While one side of the pellet was equipped with a reversible $In/(InLi)_x$ electrode, the employed stainless-steel piston served as an ion-blocking electrode on the other side. The ion-blocking electrode (steel) and the reversible electrode ($In/(InLi)_x$) served as working electrode and counter electrode, respectively.

Consecutively, while applying a pressure of 40 MPa to the cell stack, the different partial charge carrier conductivities were evaluated through dc polarization at different applied potentials. The potential range was 20–300 mV and 1.0–1.5 V for the electron- and ion-blocking cell, respectively. The current response was continuously monitored for 12 h at each potential step to determine the respective conductivity from the steady-state current I_{ssc}. After a waiting period of at least 6 h, we

consider the system to be in a steady state if the current response has remained stable within 3% over 1 h (or longer).

SUPPLEMENTAL INFORMATION

Supplemental information can be found online at https://doi.org/10.1016/j.joule.2024.07.006.

ACKNOWLEDGMENTS

The authors thank Dr. Felix Hartmann for his help with the Rietveld refinement of X-ray diffractograms. We thank Dr. Christian Schneider and Dr. Max Plass for their help in synthesizing Li_3P reference material. C.D.A. and J.J. acknowledge the financial support by the Bundesministerium für Bildung und Forschung (BMBF) within the ALANO project (grant no. 03XP0396J). P.M., L.M.R., B.A., and J.J. acknowledge funding by the BMBF within the FestBatt—Cluster of Competence for Solid-State Batteries (grant nos. 03XP0433D and 03XP0430A).

AUTHOR CONTRIBUTIONS

C.D.A.: conceptualization, methodology, validation, formal analysis, investigation, writing—original draft, writing—review & editing, visualization; N.U.C.B.M.: investigation; L.M.R.: investigation; B.A.: investigation, formal analysis, writing—review & editing; P.M.: conceptualization, methodology, investigation; K.P.: investigation, project administration, funding acquisition; J.J.: conceptualization, methodology, resources, supervision, writing—original draft, writing—review & editing, and funding acquisition.

DECLARATION OF INTERESTS

The authors declare no competing interests.

DECLARATION OF GENERATIVE AI AND AI-ASSISTED TECHNOLOGIES IN THE WRITING PROCESS

During the preparation of this work, the authors used *ChatGPT 3.5* (by OpenAI) to improve readability and language. After using this tool, the authors reviewed and edited the content as needed and take full responsibility for the content of the publication.

Received: March 1, 2024
Revised: April 22, 2024
Accepted: July 12, 2024
Published: August 12, 2024

REFERENCES

1. Randau, S., Weber, D.A., Kötz, O., Koerver, R., Braun, P., Weber, A., Ivers-Tiffée, E., Adermann, T., Kulisch, J., Zeier, W.G., et al. (2020). Benchmarking the Performance of All-Solid-State Li Batteries. Nat. Energy *5*, 259–270. https://doi.org/10.1038/s41560-020-0565-1.

2. Liu, J., Bao, Z., Cui, Y., Dufek, E.J., Goodenough, J.B., Khalifah, P., Li, Q., Liaw, B.Y., Liu, P., Manthiram, A., et al. (2019). Pathways for Practical High-Energy Long-Cycling Li-Metal Batteries. Nat. Energy *4*, 180–186. https://doi.org/10.1038/s41560-019-0338-x.

3. Bachman, J.C., Muy, S., Grimaud, A., Chang, H.-H., Pour, N., Lux, S.F., Paschos, O., Maglia, F., Lupart, S., Lamp, P., et al. (2016). Inorganic Solid-State Electrolytes for Lithium Batteries: Mechanisms and Properties Governing Ion Conduction. Chem. Rev. *116*, 140–162. https://doi.org/10.1021/acs.chemrev.5b00563.

4. Wang, M.J., Kazyak, E., Dasgupta, N.P., and Sakamoto, J. (2021). Transitioning Solid-State Batteries from Lab to Market: Linking Electro-Chemo-Mechanics with Practical Considerations. Joule *5*, 1371–1390. https://doi.org/10.1016/j.joule.2021.04.001.

5. Famprikis, T., Canepa, P., Dawson, J.A., Islam, M.S., and Masquelier, C. (2019). Fundamentals of Inorganic Solid-State Electrolytes for Batteries. Nat. Mater. *18*, 1278–1291. https://doi.org/10.1038/s41563-019-0431-3.

6. Bates, A.M., Preger, Y., Torres-Castro, L., Harrison, K.L., Harris, S.J., and Hewson, J. (2022). Are Solid-State Batteries Safer than Lithium-Ion Batteries? Joule *6*, 742–755. https://doi.org/10.1016/j.joule.2022.02.007.

7. Kato, Y., Hori, S., Saito, T., Suzuki, K., Hirayama, M., Mitsui, A., Yonemura, M., Iba, H., and Kanno, R. (2016). High-Power All-Solid-State

Batteries using Sulfide Superionic Conductors. Nat. Energy *1*, 16030. https://doi.org/10.1038/nenergy.2016.30.

8. Patel, S.V., Banerjee, S., Liu, H., Wang, P., Chien, P.-H., Feng, X., Liu, J., Ong, S.P., and Hu, Y.-Y. (2021). Tunable Lithium-Ion Transport in Mixed-Halide Argyrodites $Li_{6-x}PS_{5-x}ClBr_x$: An Unusual Compositional Space. Chem. Mater. *33*, 1435–1443. https://doi.org/10.1021/acs.chemmater.0c04650.

9. Janek, J., and Zeier, W.G. (2016). A Solid Future for Battery Development. Nat. Energy *1*, 16141. https://doi.org/10.1038/nenergy.2016.141.

10. Krauskopf, T., Richter, F.H., Zeier, W.G., and Janek, J. (2020). Physicochemical Concepts of the Lithium Metal Anode in Solid-State Batteries. Chem. Rev. *120*, 7745–7794. https://doi.org/10.1021/acs.chemrev.0c00431.

11. Lee, Y.-G., Fujiki, S., Jung, C., Suzuki, N., Yashiro, N., Omoda, R., Ko, D.-S., Shiratsuchi, T., Sugimoto, T., Ryu, S., et al. (2020). High-Energy Long-Cycling All-Solid-State Lithium Metal Batteries Enabled By Silver–Carbon Composite Anodes. Nat. Energy *5*, 299–308. https://doi.org/10.1038/s41560-020-0575-z.

12. Shen, Y., Zhang, Y., Han, S., Wang, J., Peng, Z., and Chen, L. (2018). Unlocking the Energy Capabilities of Lithium Metal Electrode with Solid-State Electrolytes. Joule *2*, 1674–1689. https://doi.org/10.1016/j.joule.2018.06.021.

13. Janek, J., and Zeier, W.G. (2023). Challenges in Speeding up Solid-State Battery Development. Nat. Energy *8*, 230–240. https://doi.org/10.1038/s41560-023-01208-9.

14. Culver, S.P., Koerver, R., Krauskopf, T., and Zeier, W.G. (2018). Designing Ionic Conductors: The Interplay between Structural Phenomena and Interfaces in Thiophosphate-Based Solid-State Batteries. Chem. Mater. *30*, 4179–4192. https://doi.org/10.1021/acs.chemmater.8b01293.

15. Zhu, Y., He, X., and Mo, Y. (2015). Origin of Outstanding Stability in the Lithium Solid Electrolyte Materials: Insights from Thermodynamic Analyses Based on First-Principles Calculations. ACS Appl. Mater. Interfaces *7*, 23685–23693. https://doi.org/10.1021/acsami.5b07517.

16. Richards, W.D., Miara, L.J., Wang, Y., Kim, J.C., and Ceder, G. (2016). Interface Stability in Solid-State Batteries. Chem. Mater. *28*, 266–273. https://doi.org/10.1021/acs.chemmater.5b04082.

17. Hatzell, K.B., Chen, X.C., Cobb, C.L., Dasgupta, N.P., Dixit, M.B., Marbella, L.E., McDowell, M.T., Mukherjee, P.P., Verma, A., Viswanathan, V., et al. (2020). Challenges in Lithium Metal Anodes for Solid-State Batteries. ACS Energy Lett. *5*, 922–934. https://doi.org/10.1021/acsenergylett.9b02668.

18. Albertus, P., Anandan, V., Ban, C., Balsara, N., Belharouak, I., Buettner-Garrett, J., Chen, Z., Daniel, C., Doeff, M., Dudney, N.J., et al. (2021). Challenges for and Pathways toward Li-Metal-Based All-Solid-State Batteries. ACS Energy Lett. *6*, 1399–1404. https://doi.org/10.1021/acsenergylett.1c00445.

19. Wenzel, S., Sedlmaier, S.J., Dietrich, C., Zeier, W.G., and Janek, J. (2018). Interfacial Reactivity and Interphase Growth of Argyrodite Solid Electrolytes at Lithium Metal Electrodes. Solid State Ionics *318*, 102–112. https://doi.org/10.1016/j.ssi.2017.07.005.

20. Lee, C., Han, S.Y., Lewis, J.A., Shetty, P.P., Yeh, D., Liu, Y., Klein, E., Lee, H.-W., and McDowell, M.T. (2021). Stack Pressure Measurements to Probe the Evolution of the Lithium–Solid-State Electrolyte Interface. ACS Energy Lett. *6*, 3261–3269. https://doi.org/10.1021/acsenergylett.1c01395.

21. Wenzel, S., Leichtweiss, T., Krüger, D., Sann, J., and Janek, J. (2015). Interphase Formation on Lithium Solid Electrolytes—An in situ Approach to Study Interfacial Reactions by Photoelectron Spectroscopy. Solid State Ionics *278*, 98–105. https://doi.org/10.1016/j.ssi.2015.06.001.

22. Wenzel, S., Randau, S., Leichtweiß, T., Weber, D.A., Sann, J., Zeier, W.G., and Janek, J. (2016). Direct Observation of the Interfacial Instability of the Fast Ionic Conductor $Li_{10}GeP_2S_{12}$ at the Lithium Metal Anode. Chem. Mater. *28*, 2400–2407. https://doi.org/10.1021/acs.chemmater.6b00610.

23. Peled, E. (1979). The Electrochemical Behavior of Alkali and Alkaline Earth Metals in Nonaqueous Battery Systems—The Solid Electrolyte Interphase Model. J. Electrochem. Soc. *126*, 2047–2051. https://doi.org/10.1149/1.2128859.

24. Jagger, B., and Pasta, M. (2023). Solid Electrolyte Interphases in Lithium Metal Batteries. Joule *7*, 2228–2244. https://doi.org/10.1016/j.joule.2023.08.007.

25. Zhao, Q., Stalin, S., and Archer, L.A. (2021). Stabilizing Metal Battery Anodes through the Design of Solid Electrolyte Interphases. Joule *5*, 1119–1142. https://doi.org/10.1016/j.joule.2021.03.024.

26. Wenzel, S., and Justus Liebig University, Giessen. (2016). Thermodynamic and Kinetic Instability of Inorganic Solid Electrolytes at Lithium and Sodium Metal Electrodes (Universitätsbibliothek Gießen. JLUpub). https://doi.org/10.22029/jlupub-10375.

27. Riegger, L.M., Mittelsdorf, S., Fuchs, T., Rueß, R., Richter, F.H., and Janek, J. (2023). Evolution of the Interphase between Argyrodite-Based Solid Electrolytes and the Lithium Metal Anode—The Kinetics of Solid Electrolyte Interphase Growth. Chem. Mater. *35*, 5091–5099. https://doi.org/10.1021/acs.chemmater.3c00676.

28. Aktekin, B., Riegger, L.M., Otto, S.-K., Fuchs, T., Henss, A., and Janek, J. (2023). SEI Growth on Lithium Metal Anodes in Solid-State Batteries Quantified with Coulometric Titration Time Analysis. Nat. Commun. *14*, 6946. https://doi.org/10.1038/s41467-023-42512-y.

29. Otto, S.-K., Riegger, L.M., Fuchs, T., Kayser, S., Schweitzer, P., Burkhardt, S., Henss, A., and Janek, J. (2022). In Situ Investigation of Lithium Metal–Solid Electrolyte Anode Interfaces with ToF-SIMS. Adv. Materials. Inter. *9*, 2102387. https://doi.org/10.1002/admi.202102387.

30. Guo, R., Hobold, G.M., and Gallant, B.M. (2022). The Ionic Interphases of the Lithium Anode in Solid State Batteries. Curr. Opin. Solid State Mater. Sci. *26*, 100973. https://doi.org/10.1016/j.cossms.2021.100973.

31. Krauskopf, T., Dippel, R., Hartmann, H., Peppler, K., Mogwitz, B., Richter, F.H., Zeier, W.G., and Janek, J. (2019). Lithium-Metal Growth Kinetics on LLZO Garnet-Type Solid Electrolytes. Joule *3*, 2030–2049. https://doi.org/10.1016/j.joule.2019.06.013.

32. Wu, B., Wang, S., Lochala, J., Desrochers, D., Liu, B., Zhang, W., Yang, J., and Xiao, J. (2018). The Role of the Solid Electrolyte Interphase Layer in Preventing Li Dendrite Growth in Solid-State Batteries. Energy Environ. Sci. *11*, 1803–1810. https://doi.org/10.1039/C8EE00540K.

33. Xu, R., Cheng, X.-B., Yan, C., Zhang, X.-Q., Xiao, Y., Zhao, C.-Z., Huang, J.-Q., and Zhang, Q. (2019). Artificial Interphases for Highly Stable Lithium Metal Anode. Matter *1*, 317–344. https://doi.org/10.1016/j.matt.2019.05.016.

34. Hao, H., Liu, Y., Greene, S.M., Yang, G., Naik, K.G., Vishnugopi, B.S., Wang, Y., Celio, H., Dolocan, A., Tsai, W.-Y., et al. (2023). Tuned Reactivity at the Lithium Metal–Argyrodite Solid State Electrolyte Interphase. Adv. Energy Mater. *13*, 2301338. https://doi.org/10.1002/aenm.202301338.

35. Ye, L., Lu, Y., Wang, Y., Li, J., and Li, X. (2024). Fast Cycling of Lithium Metal in Solid-State Batteries by Constriction-Susceptible Anode materials. Nat. Mater. *23*, 244–251. https://doi.org/10.1038/s41563-023-01722-x.

36. Ye, L., and Li, X. (2021). A Dynamic Stability Design Strategy for Lithium Metal Solid State Batteries. Nature *593*, 218–222. https://doi.org/10.1038/s41586-021-03486-3.

37. Tan, D.H.S., Chen, Y.-T., Yang, H., Bao, W., Sreenarayanan, B., Doux, J.-M., Li, W., Lu, B., Ham, S.-Y., Sayahpour, B., et al. (2021). Carbon-free high-loading silicon anodes enabled by sulfide solid electrolytes. Science *373*, 1494–1499. https://doi.org/10.1126/science.abg7217.

38. Cheng, D., Wynn, T.A., Wang, X., Wang, S., Zhang, M., Shimizu, R., Bai, S., Nguyen, H., Fang, C., Kim, M., et al. (2020). Unveiling the Stable Nature of the Solid Electrolyte Interphase between Lithium Metal and LiPON via Cryogenic Electron Microscopy. Joule *4*, 2484–2500. https://doi.org/10.1016/j.joule.2020.08.013.

39. Gibson, J.S., Narayanan, S., Swallow, J.E.N., Kumar-Thakur, P., Pasta, M., Lee, T.-L., and Weatherup, R.S. (2022). Gently Does It!: in situ Preparation of Alkali Metal-Solid Electrolyte Interfaces for Photoelectron Spectroscopy. Faraday Discuss. *236*, 267–287. https://doi.org/10.1039/d1fd00118c.

40. Xu, Y., Jia, H., Gao, P., Galvez-Aranda, D.E., Beltran, S.P., Cao, X., Le, P.M.L., Liu, J., Engelhard, M.H., Li, S., et al. (2023). Direct in situ Measurements of Electrical Properties of Solid-Electrolyte Interphase on Lithium Metal Anodes. Nat. Energy *8*, 1345–1354. https://doi.org/10.1038/s41560-023-01361-1.

41. Luo, S., Liu, X., Zhang, X., Wang, X., Wang, Z., Zhang, Y., Wang, H., Ma, W., Zhu, L., and Zhang, X. (2022). Nanostructure of the Interphase Layer between a Single Li Dendrite and Sulfide Electrolyte in All-Solid-State Li

Batteries. ACS Energy Lett. *7*, 3064–3071. https://doi.org/10.1021/acsenergylett.2c01543.

42. Bron, P., Roling, B., and Dehnen, S. (2017). Impedance Characterization Reveals Mixed Conducting Interphases between Sulfidic Superionic Conductors and Lithium Metal Electrodes. J. Power Sources *352*, 127–134. https://doi.org/10.1016/j.jpowsour.2017.03.103.

43. Wagner, C. (1955). Thermodyn. Kinetics. In Proceedings 7th Meeting International Communications on Electrochemistry (Butterworth), p. 361.

44. Hebb, M.H. (1952). Electrical Conductivity of Silver Sulfide. J. Chem. Phys. *20*, 185–190. https://doi.org/10.1063/1.1700165.

45. Narayanan, S., Ulissi, U., Gibson, J.S., Chart, Y.A., Weatherup, R.S., and Pasta, M. (2022). Effect of Current Density on the Solid Electrolyte Interphase Formation at the Lithium|Li_6PS_5Cl Interface. Nat. Commun. *13*, 7237. https://doi.org/10.1038/s41467-022-34855-9.

46. Wenzel, S., Weber, D.A., Leichtweiss, T., Busche, M.R., Sann, J., and Janek, J. (2016). Interphase Formation and Degradation of Charge Transfer Kinetics between a Lithium Metal Anode and Highly Crystalline $Li_7P_3S_{11}$ Solid Electrolyte. Solid State Ionics *286*, 24–33. https://doi.org/10.1016/j.ssi.2015.11.034.

47. Marino, C., Boulet, L., Gaveau, P., Fraisse, B., and Monconduit, L. (2012). Nanoconfined Phosphorus in Mesoporous Carbon as an Electrode for Li-ion Batteries: Performance and Mechanism. J. Mater. Chem. *22*, 22713. https://doi.org/10.1039/c2jm34562e.

48. Park, C.-M., and Sohn, H.-J. (2007). Black Phosphorus and its Composite for Lithium Rechargeable Batteries. Adv. Mater. *19*, 2465–2468. https://doi.org/10.1002/adma.200602592.

49. Peng, C., Chen, H., Zhong, G., Tang, W., Xiang, Y., Liu, X., Yang, J., Lu, C., and Yang, Y. (2019). Capacity Fading induced by Phase Conversion Hysteresis within Alloying Phosphorus Anode. Nano Energy *58*, 560–567. https://doi.org/10.1016/j.nanoen.2019.01.035.

50. Finch, G.I., and Fordham, S. (1936). The Effect of Crystal-Size on Lattice-Dimensions. Proc. Phys. Soc. *48*, 85–94. https://doi.org/10.1088/0959-5309/48/1/312.

51. Kubel, F., Bertheville, B., and Bill, H. (1999). Crystal structure of dilithiumsulfide, Li_2S. Z. Kristallogr. New Cryst. Struct. *214*, 302. https://doi.org/10.1515/ncrs-1999-0303.

52. Aktekin, B., Kataev, E., Riegger, L.M., Garcia-Diez, R., Chalkley, Z., Becker, J., Wilks, R.G., Henss, A., Bär, M., and Janek, J. (2024). Operando Photoelectron Spectroscopy Analysis of Li_6PS_5Cl Electrochemical Decomposition Reactions in Solid-State Batteries. ACS Energy Lett. *9*, 3492–3500. https://doi.org/10.1021/acsenergylett.4c01072.

53. Rayavarapu, P.R., Sharma, N., Peterson, V.K., and Adams, S. (2012). Variation in Structure and Li^+-Ion Migration in Argyrodite-type Li_6PS_5X (X = Cl, Br, I) solid electrolytes. J. Solid State Electrochem. *16*, 1807–1813. https://doi.org/10.1007/s10008-011-1572-8.

54. Kraft, M.A., Culver, S.P., Calderon, M., Böcher, F., Krauskopf, T., Senyshyn, A., Dietrich, C., Zevalkink, A., Janek, J., and Zeier, W.G. (2017). Influence of Lattice Polarizability on the Ionic Conductivity in the Lithium Superionic Argyrodites Li_6PS_5X (X = Cl, Br, I). J. Am. Chem. Soc. *139*, 10909–10918. https://doi.org/10.1021/jacs.7b06327.

55. Boulineau, S., Courty, M., Tarascon, J.-M., and Viallet, V. (2012). Mechanochemical Synthesis of Li-Argyrodite Li_6PS_5X (X=Cl, Br, I) as Sulfur-Based Solid Electrolytes for All Solid State Batteries Application. Solid State Ionics *221*, 1–5. https://doi.org/10.1016/j.ssi.2012.06.008.

56. Zhou, L., Park, K.-H., Sun, X., Lalère, F., Adermann, T., Hartmann, P., and Nazar, L.F. (2019). Solvent-Engineered Design of Argyrodite Li_6PS_5X (X = Cl, Br, I) Solid Electrolytes with High Ionic Conductivity. ACS Energy Lett. *4*, 265–270. https://doi.org/10.1021/acsenergylett.8b01997.

57. Heo, Y.J., Seo, S.-D., Hwang, S.-H., Choi, S.H., and Kim, D.-W. (2022). One-Pot Aprotic Solvent-Enabled Synthesis of Superionic Li-Argyrodite Solid Electrolyte. Int. J. Energy Res. *46*, 17644–17653. https://doi.org/10.1002/er.8324.

58. Deiseroth, H.-J., Maier, J., Weichert, K., Nickel, V., Kong, S.-T., and Reiner, C. (2011). Li_7PS_6 and Li_6PS_5X (X: Cl, Br, I): Possible Three-dimensional Diffusion Pathways for Lithium Ions and Temperature Dependence of the Ionic Conductivity by Impedance Measurements. Zeitschrift anorg. allg. Chem. *637*, 1287–1294. https://doi.org/10.1002/zaac.201100158.

59. Lorger, S., Usiskin, R.E., and Maier, J. (2019). Transport and Charge Carrier Chemistry in Lithium Sulfide. Adv. Funct. Materials *29*, 1807688. https://doi.org/10.1002/adfm.201807688.

60. Lorger, S., Narita, K., Usiskin, R., and Maier, J. (2021). Enhanced Ion Transport in Li_2O and Li_2S Films. Chem. Commun. (Camb) *57*, 6503–6506. https://doi.org/10.1039/d1cc00557j.

61. Zhang, K., Wang, L., Hu, Z., Cheng, F., and Chen, J. (2014). Ultrasmall Li_2S Nanoparticles Anchored in Graphene Nanosheets for High-Energy Lithium-Ion Batteries. Sci. Rep. *4*, 6467. https://doi.org/10.1038/srep06467.

62. Nazri, G. (1989). Preparation, Structure and Ionic Conductivity of Lithium Phosphide. Solid State Ionics *34*, 97–102. https://doi.org/10.1016/0167-2738(89)90438-4.

63. Maltsev, A.P., Chepkasov, I.V., Kvashnin, A.G., and Oganov, A.R. (2023). Ionic Conductivity of Lithium Phosphides. Crystals *13*, 756. https://doi.org/10.3390/cryst13050756.

64. Li, J., Liu, D., Sun, H., Qu, D., Xie, Z., Tang, H., and Liu, J. (2023). Mixed Ion-Electron Conducting Li_3P for Efficient Cathode Prelithiation of All-Solid-State Li-Ion Batteries. Smartmat. *4*, e1200. https://doi.org/10.1002/smm2.1200.

65. Sharon, M., and Pradhananga, R.R. (1981). Ionic Conductivity of Pure and Ca_{2+}- and Sr_{2+}-Doped Single Crystals of LiCl. J. Solid State Chem. *40*, 20–27. https://doi.org/10.1016/0022-4596(81)90355-8.

66. Armstrong, R.D., and Landles, K. (1982). Lithium Ion Conducting Solids for Ambient Applications. J. Appl. Electrochem. *12*, 533–535. https://doi.org/10.1007/BF00614979.

67. Mercier, R., Tachez, M., Malugani, J.P., and Robert, G. (1985). Effect of Homovalent (I_- Br_-) Ion Substitution on the Ionic Conductivity of LiI_{1-x} Br_x Systems. Solid State Ionics *15*, 109–112. https://doi.org/10.1016/0167-2738(85)90088-8.

68. Poulsen, F.W. (1981). Ionic Conductivity of Solid Lithium Iodide and its Monohydrate. Solid State Ionics *2*, 53–57. https://doi.org/10.1016/0167-2738(81)90020-5.

69. Jackson, B.J.H., and Young, D.A. (1969). Ionic Conduction in Pure and Doped Single-Crystalline Lithium Iodide. J. Phys. Chem. Solids *30*, 1973–1976. https://doi.org/10.1016/0022-3697(69)90174-7.

70. Schmalzried, H. (1995). Chemical Kinetics of Solids (Wiley-VCH Press).

71. Wenzel, S., Leichtweiss, T., Weber, D.A., Sann, J., Zeier, W.G., and Janek, J. (2016). Interfacial Reactivity Benchmarking of the Sodium Ion Conductors Na_3PS_4 and Sodium β-Alumina for Protected Sodium Metal Anodes and Sodium All-Solid-State Batteries. ACS Appl. Mater. Interfaces *8*, 28216–28224. https://doi.org/10.1021/acsami.6b10119.

72. Li, Y., Canepa, P., and Gorai, P. (2022). Role of Electronic Passivation in Stabilizing the Lithium- $Li_xPO_yN_z$ Solid-Electrolyte Interphase. PRX Energy *1*, 023004. https://doi.org/10.1103/PRXEnergy.1.023004.

73. Le Van-Jodin, L., Ducroquet, F., Sabary, F., and Chevalier, I. (2013). Dielectric Properties, Conductivity and Li+ Ion Motion in LiPON Thin Films. Solid State Ionics *253*, 151–156. https://doi.org/10.1016/j.ssi.2013.09.031.

74. Su, Y., Falgenhauer, J., Polity, A., Leichtweiß, T., Kronenberger, A., Obel, J., Zhou, S., Schlettwein, D., Janek, J., and Meyer, B.K. (2015). LiPON Thin Films with High Nitrogen Content for Application in Lithium Batteries and Electrochromic Devices Prepared by RF Magnetron Sputtering. Solid State Ionics *282*, 63–69. https://doi.org/10.1016/j.ssi.2015.09.022.

75. Li, J., Dudney, N.J., Nanda, J., and Liang, C. (2014). Artificial Solid Electrolyte Interphase To Address the Electrochemical Degradation of Silicon Electrodes. ACS Appl. Mater. Interfaces *6*, 10083–10088. https://doi.org/10.1021/am5009419.

76. Eckhardt, J.K., Fuchs, T., Burkhardt, S., Klar, P.J., Janek, J., and Heiliger, C. (2023). Guidelines for Impedance Analysis of Parent Metal Anodes in Solid-State Batteries and the Role of Current Constriction at Interface Voids, Heterogeneities, and SEI. Adv. Materials Inter. *10*, 2202354. https://doi.org/10.1002/admi.202202354.

77. Landgraf, V., Tu, M., Cheng, Z., de Leeuw, J., Ganapathy, S., Wagemaker, M., and Famprikis, T. (2023). Entropy-Induced High Conductivity in Fully-Reduced Electrolytes for Solid-State Batteries with Lithium Metal Anodes. Preprint at ChemRxiv.

78. Landgraf, V., Famprikis, T., de Leeuw, J., Bannenberg, L.J., Ganapathy, S., and Wagemaker, M. (2023). Li_5NCl_2: A Fully-Reduced, Highly-Disordered Nitride-Halide Electrolyte for Solid-State Batteries with Lithium-Metal Anodes. ACS Appl. Energy Mater. *6*, 1661–1672. https://doi.org/10.1021/acsaem.2c03551.

79. Kolesnikov, A., Wulfers, T., Kolek, M., Bieker, P., Stan, M.C., and Winter, M. (2022). Lithium Powder Synthesis and Preparation of Powder-Based Composite Electrodes for Application in Lithium Metal Batteries. Energy Tech. *10*, 2100871. https://doi.org/10.1002/ente.202100871.

80. Coelho, A.A. (2018). TOPAS and TOPAS-Academic: An Optimization Program Integrating Computer Algebra and Crystallographic Objects Written in C++. J. Appl. Crystallogr. *51*, 210–218. https://doi.org/10.1107/S1600576718000183.

81. jEdit v4.3. http://www.jedit.org/index.php.

82. Santhosha, A.L., Medenbach, L., Buchheim, J.R., and Adelhelm, P. (2019). The Indium–Lithium Electrode in Solid-State Lithium-Ion Batteries: Phase Formation, Redox Potentials, and Interface Stability. Batteries Supercaps *2*, 524–529. https://doi.org/10.1002/batt.201800149.

3.2. Interphase Formation in Solid-State Batteries: Influence of Contact Conditions on Impedance-Derived SEI Growth Kinetics (2nd Publication)

In this submitted publication, the capability of impedance measurements for assessing and predicting interphase growth was investigated. By employing 3D transport simulations – based on transport parameters determined in the first publication – it was analyzed how rigid solid|solid contacts influence the accurate interpretation of cell-level impedance responses.

Based on the Wagner diffusion model, diffusion-controlled interphase growth was simulated to analyze the influence of different electrode|SE contact conditions. Consequently, the reliability of extracted interphase rate constants from the cell's impedance response was critically examined. The findings revealed that factors such as current constriction, complex transport properties in SEs, or partially passivated interfaces alter the cell-level impedance signal and affect the accurate extraction of rate constants, if the actual contact morphology is unknown.

This work highlights potential pitfalls in data interpretation for time-resolved experiments and emphasizes the need to carefully consider experimental conditions for a reliable prediction of diffusion-controlled interphase growth using the Wagner diffusion model in solid-state systems. Furthermore, these results also underscore the practical value of the experimental approach established in the first publication.

C. D. Alt$^{\perp}$ and S. Kremer$^{\perp}$ share the first authorship ($^{\perp}$), having equally contributed to the design and execution of all experiments under the supervision of J. Janek and J. K. Eckhardt. C. D. Alt adapted the Wagner diffusion model with the corresponding model analysis, provided the kinetic parameters for the simulation, and placed the results in the context of existing literature. S. Kremer designed the computational models, carried out simulations, data analysis as well as visualization. L. S. performed the experiments. J. K. Eckhardt implemented the simulation code, supported the analysis of data and the design of experiments. Both first authors jointly analyzed the corresponding data, while C. D. Alt, S. Kremer, and J. K. Eckhardt drafted the manuscript, which was revised by all co-authors.

The manuscript was submitted to *ACS Applied Materials & Interfaces* by the American Chemical Society.

Interphase Formation in Solid-State Batteries: Influence of Contact Conditions on Impedance-Derived SEI Growth Kinetics

Sascha Kremer[1,2⊥], Christoph D. Alt[1,2⊥], Luca Schuster[1,2], Jürgen Janek[1,2], and Janis K. Eckhardt[2*]

[1]Institute of Physical Chemistry, Justus-Liebig-University Giessen, Heinrich-Buff-Ring 17, Giessen D-35392, Germany.
[2]Center for Materials Research (ZfM), Justus-Liebig-University Giessen, Heinrich-Buff-Ring 16, D-35392 Giessen, Germany.

*janis.k.eckhardt@theo.physik.uni-giessen.de

Abstract

The continuous formation of solid electrolyte interphases (SEI) limits the long-term performance of batteries by increasing cell overvoltages and by consuming redox-active species. The temporal evolution of the SEI resistance in sulfide-based solid-state batteries with lithium metal anode has been shown to be well described by diffusion-controlled interphase growth. Yet, recent studies reveal that the extracted SEI rate constants are highly sensitive to experimental conditions like stack pressure. In this study, we evaluate the reliability of SEI growth rates derived from cell-level impedance measurements of solid-state battery systems. Through comprehensive 3D transport simulations, we show that poor contact conditions, as often encountered in solid-state cells, can lead to erroneous SEI rate constant estimates and deviations from the expected time dependence, *e.g.*, square-root-of-time. Notably, poor contact conditions may remain undetected in experimental data, potentially leading to misinterpretation of interphase growth kinetics. Supported by experiments with symmetrical Li|Li_6PS_5Cl|Li cells, our findings highlight the importance of a careful evaluation of experimental conditions, such as stack pressure and surface quality, to ensure a reliable analysis of fundamental interphase growth kinetics in solid-state battery systems.

1. Introduction

In the technological race against climate change, solid-state batteries (SSBs) promise to be a potential advancement of conventional lithium-ion batteries (LIBs).[1,2] However, the thermodynamic compatibility of SSB components remains a major challenge for ensuring their safe and reliable long-term operation.[3,4] Precisely, inorganic solid electrolytes (SEs) in contact with a low-potential lithium metal negative electrode, *i.e.*, $E_H[Li^+/Li] = -3.04\,V$ vs. SHE and high-potential positive electrode active material (CAM) are prone to degradation.[5–7] Such reactions deplete active material, form resistive multiphase degradation layers, and continue to pose obstacles in developing practical SSBs.[8,9]

Depending on the partial ionic and electronic conductivities (σ_{ion}) and (σ_{el}) of degradation layers, they are categorized as either *mixed conducting interphases* (MCIs, where $\sigma_{ion} \approx \sigma_{el}$) or *solid electrolyte interphases* (SEIs, where $\sigma_{ion} \gg \sigma_{el}$). Both, MCIs as well as SEIs, usually possess a much lower σ_{ion} compared to their corresponding SEs.[10] Therefore, their continuous growth significantly increases battery impedance and reduces cycle life, with only very few exceptions like in the case of "LiPON".[11–13] Assuming a solid-state reaction limited by coupled ion and electron transport, MCIs are expected to grow continuously eventually causing short circuiting. In contrast, dense SEIs may exhibit self-limiting growth once a passivating layer fully covers the reactive interface. However, in practice, no SEI is perfectly homogeneous and electronically insulating.[14–17] Therefore, purely diffusion-controlled interphase growth is not expected to cease entirely, but rather to decelerate over time.[18–20]

The time-dependent evolution of the SEI has been studied extensively for liquid electrolyte-based batteries, with many authors reporting a square-root-of-time dependence for the resistance growth – consistent with a diffusion-controlled interface reaction.[21–28] In the field of solid-state batteries, the literature is comparatively scarce, but several authors have reported analogous behavior: For instance, evidence for diffusion-controlled interphase growth has been reported for sulfide and halide SEs in contact with lithium metal and CAM.[29–31] Wenzel *et al.*[18,19] identified this characteristic for the SEI resistance of lithium argyrodites (Li_6PS_5X, X = Cl, Br, I) and $Li_7P_3S_{11}$ in contact with lithium metal. A similar trend was observed by Zuo *et al.*[28] for the interphase formation at the $Li_{10}GeP_2S_{12}$|cathode interface. While these studies mainly rely on electrochemical impedance

spectroscopy (EIS), similar results were obtained using other techniques. For instance, Aktekin *et al.*[20] confirmed the square-root-of-time dependence for SEI growth between Li_6PS_5Cl and lithium metal using coulometric titration time analysis (CTTA).

In a recent work by Riegger *et al.*[32], a more complicated picture of SEI growth kinetics at the Li| Li_6PS_5Cl interface is presented. Through impedance measurements on symmetric Li|Li_6PS_5Cl|Li cells, they observed considerable variance in SEI rate constants, strongly influenced by factors such as applied pressure and initial surface passivation of lithium foils.[33] Kovalenko *et al.*[34] reported similar observations for CTTA experiments, demonstrating a significant influence of the applied stack pressure. These findings highlight the importance of careful consideration of experimental conditions and show that mechanical and morphological interface conditions may skew *apparent* growth kinetics.

Motivated by these findings, we critically assess the reliability of SEI growth rates derived from impedance data of solid-state systems. Using a 3D microstructure-resolved impedance-network model (**Figure 1**), we systematically evaluate how realistic contact conditions – as typically faced in solid-state batteries – effect the *apparent* interphase kinetics inferred from cell-level impedance measurements. In our model, we assume *local* diffusion-controlled interphase growth with a square-root-of-time dependence, consistent with the Wagner diffusion model. However, the insights gained are broadly applicable to other growth kinetics.

We find that poor contact conditions, which often go undetected experimentally, alter impedance signals like changes in the *local* interphase kinetics itself. For instance, interfacial pores may lead to an *apparent* increase in the rate constant of SEI growth, while staying undetected in the impedance data. Native passivation layers – that are typically found on surfaces of reactive alkali metals like lithium metal – may lead to an *apparent* saturation of interphase growth. We demonstrate this strong dependence on contact conditions through pressure-dependent impedance measurements on Li|Li_6PS_5Cl|Li cells. Together, our results underscore the complexity of impedance analysis and the necessity of accounting for realistic contact conditions to obtain reliable parameters for interphase formation in solid-state batteries.

2. Theoretical Background

This chapter outlines the fundamental principles and assumptions underlying our modeling approach. We assume diffusion-controlled interphase growth and accordingly a *local* resistance increase with square-root-of-time. In **Section 2.1**, we first briefly summarize the Wagner diffusion model that predicts this characteristic time-dependence for diffusion-controlled interface reactions at planar interfaces. Rather than presenting a full theoretical derivation – which can be found in monographs *e.g.* by Schmalzried[35,36] – we aim to convey a qualitative understanding of the key assumptions involved. This forms the basis for understanding the simplifications made in the network modeling approach (**Section 2.2**), that is used to account for realistic contact conditions typically found in solid-state systems.

2.1. Diffusion-Controlled Interphase Growth in Solid-State – The Wagner Diffusion Model

The basic model of diffusion-controlled interphase growth was introduced by Wagner in 1931.[37–39] Originally developed to explain the parabolic rate law observed for the tarnishing of metals at elevated temperatures, the model describes interfacial processes driven by fundamental solid-state processes at solid|gas interfaces.[30] Reactants diffuse in opposite directions, localizing redox reactions to a narrow interfacial reaction zone. Once a thin but continuous product layer forms, further growth becomes diffusion-limited. As reactants´ transport across the layer continues, material consumption persists, but at a diminishing rate. This leads to the characteristic time dependence, where growth slows down as the layer thickness increases.

In the model, the growth of reaction layers at planar solid|gas interfaces is derived under one-dimensional flux conditions. A dense, adherent, and homogeneous, product phase is assumed that fully covers the interface. The reaction layer is considered sufficiently thick to neglect space and surface charge effects. Growth is driven solely by chemical potential gradients across the reaction layer, while the chemical potentials in both adjacent phases remain constant (*i.e.*, local thermodynamic equilibrium). Electroneutrality enforces flux coupling among charged species. Thus, interphase formation is limited by the transport of the least mobile species within the reaction layer.

Under these assumptions, the growth rate of the reaction layer can be determined based on its transport properties. Adapting the model for solid|solid interfaces requires accounting for the free reaction enthalpy of the corresponding decomposition reaction. With the chemical potential gradient of the active metal (e.g., lithium or sodium) across the interphase being the reaction's driving force, the Wagner diffusion model enables the evaluation of interphase formation over time (**eq. 1**). The resulting reaction layer thickness (d) as a function of the reaction time (t) is given by:

$$d = \sqrt{\frac{2}{F^2 \cdot \rho_{\text{int}} \cdot x_{\text{Me}}} \frac{M_{\text{int}} \cdot \sigma_{\text{el}} \cdot \sigma_{\text{ion}}}{\sigma_{\text{el}} + \sigma_{\text{ion}}} \cdot \Delta\mu_{\text{Me}} \cdot \sqrt{t}} = k \cdot \sqrt{t} \quad \textbf{(eq. 1)}$$

where F, ρ_{int}, x_{Me}, M_{int}, σ_{ion}, σ_{el}, $\Delta\mu_{\text{Me}}$, and k represent the Faraday constant, the mean mass density of the SEI layer, the stoichiometric factor (*i.e.*, number of moles of active metal required for the stoichiometric decomposition reaction), the mean molar mass of the interphase layer, the ionic and electronic conductivity of the interphase layer, the chemical potential difference of the active metal across the interphase, and the resulting rate constant, respectively.

If the dominant partial conductivity of the interphase is known, the interphase resistance can be determined from the linear relationship between d vs. $t^{0.5}$, and vice versa. For ion-conducting interphases in SSBs, the ionic interphase resistance R_{SEI} can be expressed using $\sigma_{\text{ion}} = d/(A \cdot R_{\text{SEI}})$:

$$R_{\text{SEI}} = \frac{1}{A \cdot \sigma_{\text{ion}}} \cdot \sqrt{\frac{2}{F^2 \cdot \rho_{\text{int}} \cdot x} \frac{M_{\text{int}} \cdot \sigma_{\text{el}} \cdot \sigma_{\text{ion}}}{\sigma_{\text{el}} + \sigma_{\text{ion}}} \cdot \Delta\mu_{\text{Me}}} \cdot \sqrt{t} = k' \cdot \sqrt{t} \quad \textbf{(eq. 2)}$$

Here, A represents the contact area between both phases and the rate constant k′ determines the interphase resistance growth. Revisiting **(eq. 1)** and **(eq. 2)** reveals that k and k′ are connected by A and σ_{ion}:

$$k = k' \cdot A \cdot \sigma_{\text{ion}} \quad \textbf{(eq. 3)}$$

If one partial conductivity dominates, k and k' can be simplified by considering only the lower, rate-limiting partial conductivity in the square-root-term. In the case of an SEI in SSBs, where $\sigma_{\text{ion}} \gg \sigma_{\text{el}}$, electronic transport primarily governs SEI's thickness increase. The ionic conductivity, in contrast, determines the SEI's resistance increase at a given thickness d.

Notably, this study is focused on the Li|Li_6PS_5Cl interface as a model system. In **Section S1** of the Supporting Information, we derive the reaction's driving force (*i.e.*, $\Delta\mu_{\text{Li}}$) for interphase formation using thermodynamic data. If all transport properties are known, **(eq. 1)** and **(eq. 2)** can be applied to predict interphase growth (*i.e.*, d) and the associated resistance contribution (*i.e.*, R_{SEI}) to evaluate its impact on overall cell resistance and long-term performance of SSBs.[27,40] This approach, including the derivation of the reaction's driving force, is readily adaptable to other model systems and cell chemistries beyond lithium metal and Li_6PS_5Cl.

2.2. Accounting for Poor Contact Conditions – 3D Transport Simulations

In the Wagner diffusion model, a morphologically stable, planar (2D) interface is assumed. This results in homogeneous (*i.e.*, dense and coherent) interphase growth and quasi-1D charge transport across the interface. While this assumption is reasonable for reactions at solid|gas or solid|liquid interfaces, it is less applicable to solid-state systems with rigid solid|solid contacts. Actual interfaces in SSBs – or simplified symmetric model cells – often deviate substantially from these idealized conditions, as summarized in **Figure 1**: The ideal case of a flat, continuous contact (1) is never encountered in practice. Instead, pores (2), partially penetrated native passivation layers (3), and interface roughness (4) complicate the contact geometries. Additional factors such as lithium dendrite or whisker formation (5), the complex microstructure of SEs (6), and the morphology, grain structure, and heterogeneous surface chemistry of cathode active materials (7) add to the interfacial complexity.

As a result, interfacial transport properties extracted from macroscopic cell-level impedance measurements cannot be directly assigned to the underlying *microscopic* processes. Instead, they represent *effective* properties of the interface influenced by the complex interface geometry. This becomes particularly relevant given that the *actual* interface morphology – including contact area, local composition, and mechanical integrity – is typically unknown and may evolve dynamically during a measurement.

To systematically investigate how the complexity of solid|solid interfaces influences the impedance and potentially hinders the extraction of meaningful and reproducible interphase rate constants, we use a set of idealized, yet representative, 3D microstructural models. These include: (1) an intimate planar contact, serving as the ideal reference case, (2) a contact with macroscopic interfacial pores, and (3) punctured passivation layers (revisit **Figure 1**). Each computational model comprises a square cross-sectional area ($L_x = L_y = 100$ µm) and consists of a 100 µm thick SE layer in contact with a 20 µm thick lithium metal electrode. The electrode area ($A_{\text{electrode}}$) corresponds to the full sample surface, assuming ideal mechanical stability and contact. For simplicity, the SE is treated as dense and free of microstructural features. The interfacial morphology is varied and systematically explored throughout this study, with details specified in each section.

For the transport simulations, we use an electric network model where each model system with its specific interfacial morphology is discretized and represented as a 3D voxel-based microstructure. Ion-transport between

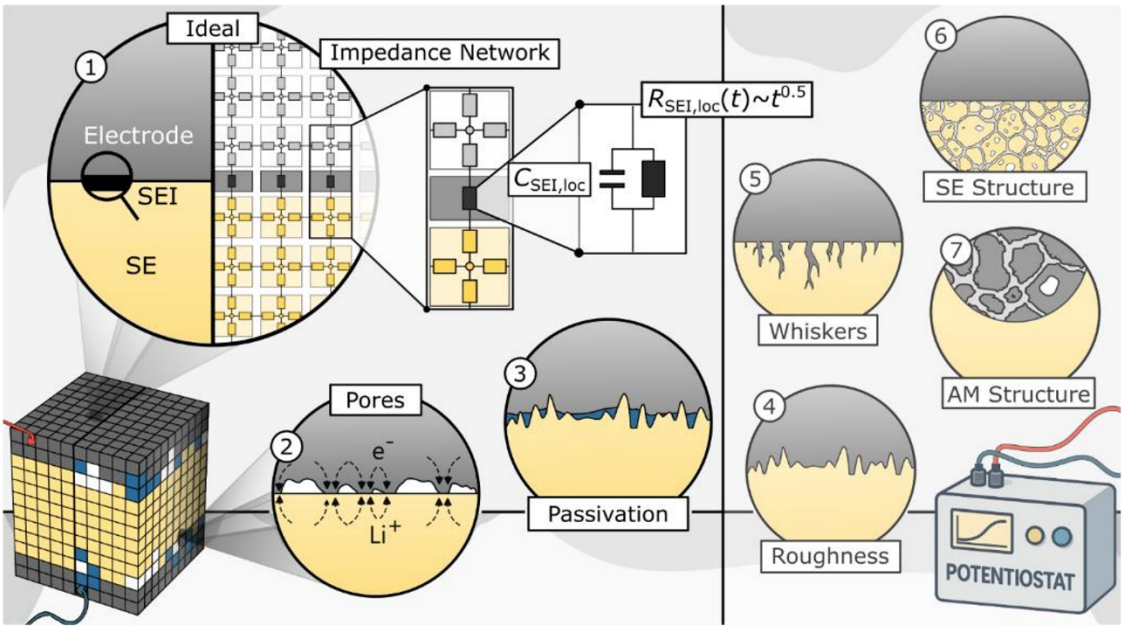

Figure 1. **Computational Model Systems for Investigating the Impact of Contact Conditions on Impedance-Derived SEI Growth Kinetics.** The influence of different interfacial contact and microstructural conditions is investigated using 3D microstructure-resolved transport simulations. Simplified geometrical model systems are translated into electrical impedance networks. The local SEI resistance at the interface is modeled to evolve with a square-root-of-time dependence ($R_{\mathrm{SEI,loc}}\sim t^{0.5}$). The reliability of derived interphase rate constants extracted from cell-level impedance data is evaluated.

voxels is modeled by local equivalent circuit elements, each defined by the phase or interface it belongs to (see **Figure 1**). In the modeling approach, we do not explicitly simulate chemical degradation. Instead, interphase effects are treated implicitly by introducing time-dependent interphase resistors and capacitors ($R_{\mathrm{SEI,loc}}$, $C_{\mathrm{SEI,loc}}$) at the electrode|SE interface into the electric network, as described by **(eq. 2**). The change in local parameters mimics the increase in interphase thickness over time, while the local transport properties (σ_{SEI}, $\varepsilon_{\mathrm{SEI}}$) remain constant. The interphase itself is modeled as a homogeneous layer.

While these simple models cannot fully capture the complexity of real solid-state systems, we believe that they can still offer valuable insight into how local interfacial imperfections on the micro- to mesoscale will manifest in the impedance evolution of the overall system, *i.e.* on the cell level—and consequently affect the interpretation of extracted rate parameters. We see this approach not as a fully predictive tool, but as a way to build intuition and provide guidance for interpreting impedance measurements and extracted rate constants under non-ideal interfacial conditions.

A more detailed model description is provided in the *Computational Details* section. Further information about the electrical network model and impedance spectrum calculations is available in our previous publication.[41]

3. Results and Discussion

In this chapter, we investigate how contact conditions impact the capability of tracking *local, microscopic* interphase growth from *macroscopic* cell-level impedance measurements. In our simulations, we assume (1D) diffusion-controlled interphase growth at each contact point at the electrode|SE interface, according to (**eq. 2**). The resulting time-series of the cell-level impedance is used to extract the underlying *microscopic* interphase rate constants (k'). Throughout this analysis, we denote the (*apparent*) rate constants obtained from macroscopic impedance data as (k'_{exp}). Any discrepancy between actual *microscopic* rates (k') and the extracted *apparent* values (k'_{exp}) arises solely from the influence of the interfacial morphology in the computational model system.

In **Section 3.1.**, we begin by examining an ideal planar interface with intimate contact to establish a baseline for analyzing interphase growth kinetics based on impedance data. **Section 3.2.** extends this analysis to more complex interfacial configurations, including the presence of pores and (native) surface passivation layers. In **Section 3.3.**, we translate the insights gained from simulations to the experimental context, highlighting challenges in reliably interpreting impedance evolution in terms of *microscopic* interphase formation. This discussion is supported by the analysis of experimental impedance data from

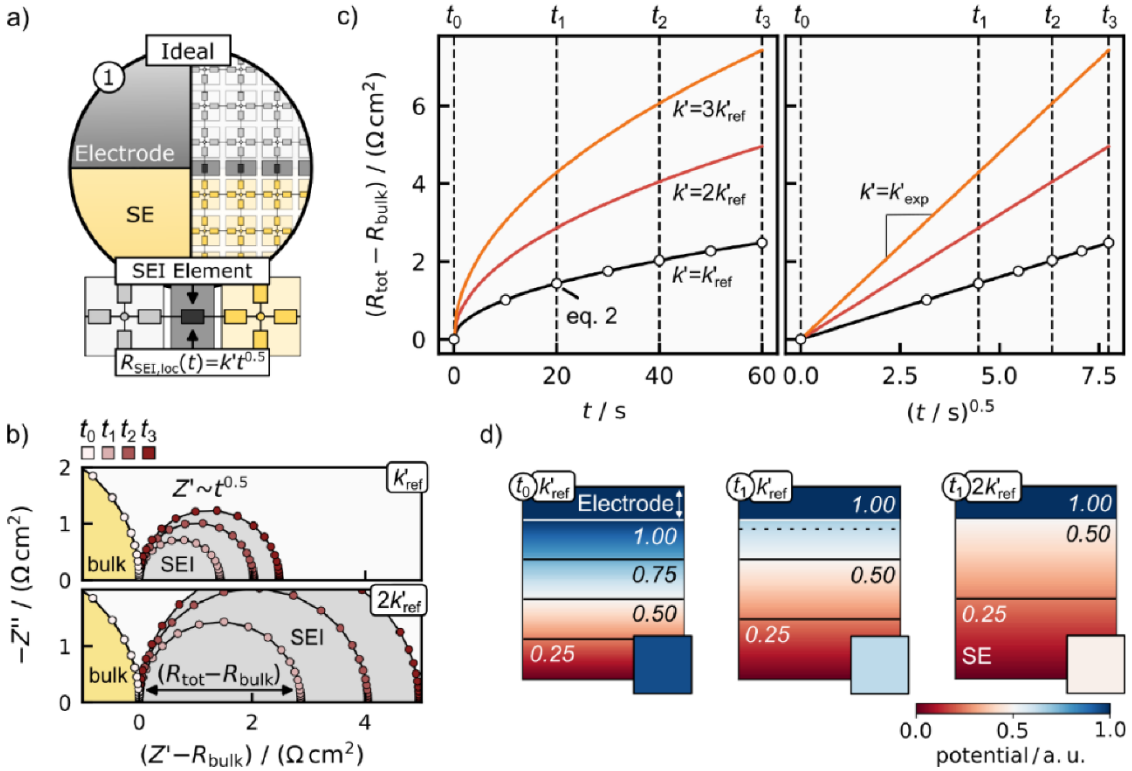

Figure 2. **Analysis of Homogeneous Interphase Growth at a Planar Interface**. (a) It is assumed that the electrode and the SE are homogeneous, and that the increase in interphase thickness and local interphase resistance ($R_{SEI,loc}$) at the interface follow a square-root-of-time dependence. (b) The bulk impedance (yellow) remains constant over time, while the interphase impedance (gray) increases at different rates depending on the assumed microscopic growth rate k' in the simulations. (c) The microscopic rate k' determines the increase in macroscopic resistance ($R_{tot} - R_{bulk}$) over time, or the linear slope when plotted against the square-root-of-time. The resistance difference is anticipated to be indicative for interphase growth. (d) Transport through the system is time-independent. It is quasi-1D as indicated by the uniform potential drop along the transport direction and the constant in-plane potential (see inset) below the interface (dashed line).

symmetric Li|Li_6PS_5Cl|Li cells obtained under different pressure conditions.

3.1. Impedance-Derived Rate Constants for Homogeneous and Planar Interfaces

To outline the analysis methodology, we begin with an idealized scenario consistent with the Wagner diffusion model: a planar, quasi-2D interface without any interfacial defects, as illustrated schematically in **Figure 2a**. In the simulation series, we consider three different *microscopic* interphase rate constants k', ranging from $1k'_{ref}$, to $3k'_{ref}$, with $k'_{ref} = 3.2 \cdot 10^{-1} \Omega\,cm^2\,s^{-0.5}$ adopted from Alt *et al.*[40] We model the impedance at different times, starting from t_0 – when interphase growth is initiated by establishing contact between materials, but no interphase has been formed yet – and progressing to t_3, the final stage of the simulation.

In experimental practice, impedance data is normalized to the geometric electrode area ($A_{electrode}$), assuming a planar interface of perfect, intimate contact between electrode and sample. Obtaining reliable measurements of the *actual* contact area A in experiments is challenging and, in most cases, not feasible. Therefore, we adapt this experimental practice and normalize all simulated impedance values to $A_{electrode}$, despite the potential mismatch with the *actual* contact area A in the computational model systems.

Figure 2b shows the time-dependent impedance evolution in Nyquist representation. At the starting point t_0, the impedance spectrum displays only a bulk semicircle (yellow), indicating the absence of an interphase. To better visualize subsequent impedance changes, the bulk resistance (R_{bulk}) is subtracted from the real part of the impedance (Z'), effectively shifting the spectra along the Z'-axis. With increasing time, a second semicircle emerges and increases in size. It reflects the interphase growth, which is governed by k' as simulation input parameter. Higher values of k' result in a more rapid increase in interphase thickness and corresponding interphase resistance, as illustrated by the comparison between the $1k'_{ref}$ and the $2k'_{ref}$ simulation series. Notably, the bulk semicircle remains constant over time, confirming that the observed impedance changes originate solely from the evolving interphase.

To obtain mechanistic insights into interphase evolution, either the total resistance (R_{tot}) or the SEI resistance (R_{SEI}) is typically plotted as a function of time.[18–20] Isolating R_{SEI} requires a detailed understanding of the underlying impedance features, which is challenging for complex experimental data.[32,33] For symmetric cells with planar electrodes, it is reasonable to assume that all impedance contributions other than the bulk impedance originate from the electrode|SE interface. Consequently, changes in the resistance difference ($R_{tot} - R_{bulk}$) are anticipated to be indicative for SEI growth (*i.e.*, labeled "SEI" in **Figure 2b**). In the case of the Li|Li_6PS_5Cl interface, this assumption is further justified due to the negligible charge transfer resistance (*i.e.*, high exchange current density).[42,43]

Figure 2c shows the macroscopic resistance difference ($R_{tot} - R_{bulk}$) as a function of time (vs. t and $t^{0.5}$) for different k'. Notably, directly calculating the SEI resistance $R_{SEI}(t)$, according to (**eq. 2**) (open circles) using $A = A_{electrode}$, shows perfect agreement with the resistance difference ($R_{tot} - R_{bulk}$) derived from the impedance analysis approach (black solid line, $k' = k'_{ref}$). However, this only holds true for this idealized interface, but not necessarily for more complex interface morphologies, which will be discussed in **Section 3.2**.

The slope of the different resistance curves changes with the simulated *microscopic* interphase rate constants k: Higher values lead to a steeper resistance increase. To extract k'_{exp} from a measurement, the data is typically linearized by plotting the respective resistance – here, ($R_{tot} - R_{bulk}$) – over $t^{0.5}$, as done in the right graph of **Figure 2c**. The slope obtained from linear interpolation of the resistance curves corresponds to the *apparent* rate constant k'_{exp} (see (**eq. 3**) for calculating k_{exp}). For this idealized interface, k'_{exp} values match perfectly with the respective simulation input values k.

Homogeneous SEI (resistance) growth is also reflected in the DC potential distribution. **Figure 2d** shows the evolution of the DC potential within the system for different k' at various time points (t_i). A cross-section along the transport direction reveals a negligibly small potential drop in the metal electrode (upper dark blue region), attributed to its high σ_{el}. Across the SE, the potential drop remains uniform gradually transitioning to the defined potential difference in the simulations. The forming interphase layer causes an increasing fraction of the potential drop to be localized at the electrode|SE interface, which is reflected in the shifting equipotential lines within the SE. The higher the interphase resistance, the more pronounced this potential drop becomes, as seen at t_1 for different k'.

Transport across the system is quasi-1D, as indicated by the uniform in-plane potential distribution perpendicular to the transport direction just below the electrode (dashed line, see insets in **Figure 2d**). However, this idealized behavior and the resulting agreement between *apparent* and *microscopic* rate constants (k'_{exp} and k', respectively) cannot be expected for interface conditions typically found in solid-state systems.

3.2. Impedance-Derived Rate Constants for Interfaces with Poor Contact Conditions

3.2.1. The Influence of Pores, Contact Area, and Current Constriction

One of the main challenges in solid-state is achieving intimate contact between two solid materials, such as the electrode and the SE. In most practical cases, residual pores at the interface lead to contact areas A smaller than the electrode area $A_{electrode}$. This introduces a more complex transport behavior.[44–46]

To explore the impact of interfacial pores (or more generally, insulating interfacial phases), we consider a model system featuring a single cubic contact spot (**Figure 3**). This contact spot is surrounded by an insulating phase along the edges of the simulation domain. In the simulation series, we systematically vary the *relative* contact area (A_r) from 100% (perfect contact) down to 10% (minimal contact) of $A_{electrode}$. All transport properties remain constant across different simulations, with $k' = 1k'_{ref}$. Notably, interphase growth is restricted to the regions where the electrode is in direct contact with the SE. As in experimental studies, where detailed information about the *actual* contact area A is limited, the impedances and extracted resistances are normalized to $A_{electrode}$.

Figure 3b shows that when adding interfacial pores, an additional impedance contribution appears in the spectrum, besides the bulk and "SEI" signal. It originates from current constriction ("cstr") at the electrode|SE interface.[47–49] The constriction signal does not always appear as a distinct contribution in the impedance spectrum. Instead, it may also overlap with the bulk or SEI signal, depending on the characteristic frequency of the processes.[49] In the case of current constriction due to pores, the characteristic frequency is a function of the pore depth and SE conductivity.[49] Only shallow, wide pores are presumed to have capacities large enough to make the constriction signal separable from the bulk signal.

The comparison of the different simulation series shows that the constriction resistance (R_{cstr}) and the SEI resistance (R_{SEI}) extracted from cell-level impedance measurements are sensitive to A_r variations. R_{cstr} increases in size as A_r decreases, while the increase of R_{SEI} over time is enhanced with decreasing A_r. This is also

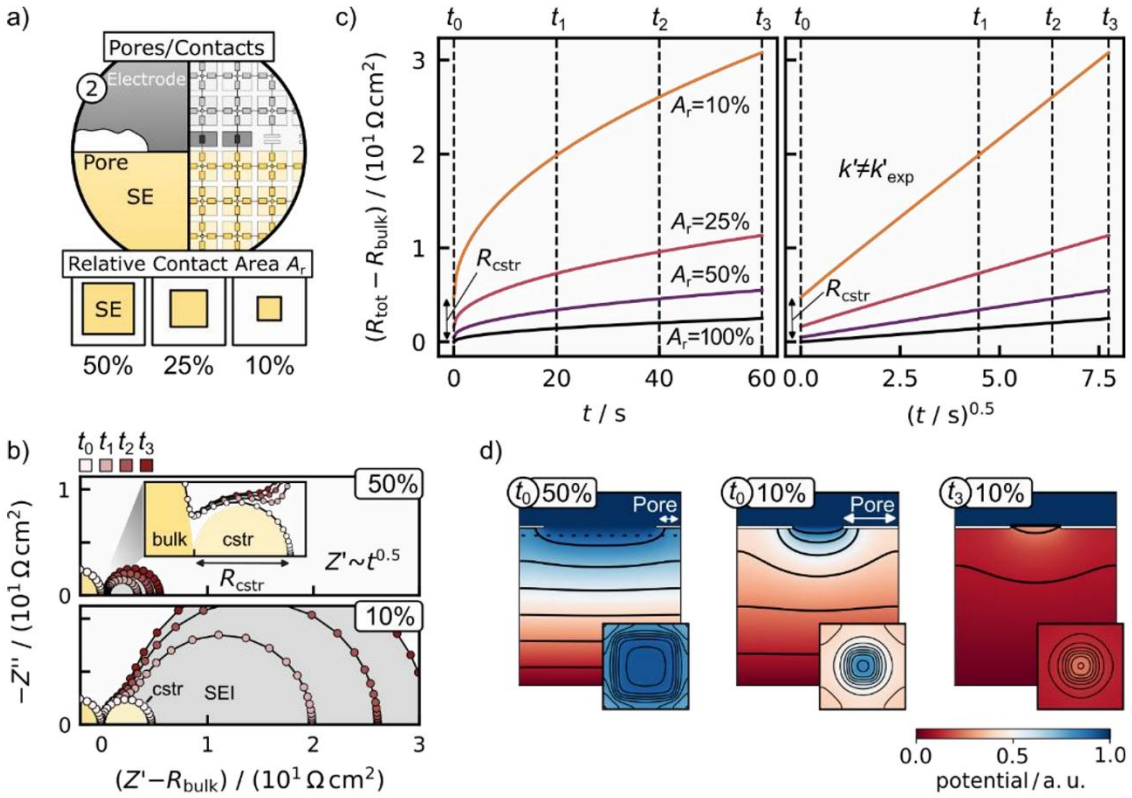

Figure 3. **Influence of Interfacial Pores on the SEI Growth Analysis**. The microscopic interphase rate constant k' was kept constant in the simulations. (a) The relative contact area A_r between the homogeneous metal electrode and the SE is systematically varied by changing the size of a cubic contact spot surrounded by a pore phase. (b) The resulting geometric constriction effect can appear as a distinct signal in the impedance spectrum. The magnitude of the two interface resistances (R_{cstr}, R_{SEI}) depends on A_r. (c) The apparent growth rate k'_{exp} (*i.e.*, slope of the resistance curves) differs from the microscopic rate k' due to incorrect normalization of the resistance with respect to $A_{electrode}$ rather than A_r (see black curve as a reference). (d) Current paths through the system are multidimensional, as indicated by the inhomogeneous potential drop along the transport direction and within a layer near the interface (dashed line).

evident when considering the t-dependence of $(R_{tot} - R_{bulk})$, as shown in **Figure 3c**. Compared to the ideal reference curve for A_r = 100% (discussed in **Section 3.1.**), two key differences emerge: (*i*) the individual resistance curves exhibit an offset along the Z''-axis, and (*ii*) k'_{exp} is significantly larger for smaller A_r, although the underlying k' remains unchanged across simulations.

The vertical offset of the resistance curves along *y*-axis is due to R_{cstr}. It resembles the reduction in *effective* SE conduction volume close to the interface. This is evident in the DC potential distribution, both at t_0, before any SEI formation, and at t_3, when an SEI layer has formed (**Figure 3d**). Along the transport direction, the equipotential lines near the interface exhibit distinct curvature, while the in-plane potential distribution below the interface (dashed line) becomes inhomogeneous. Interfacial pores induce complex transport behavior, giving rise to curved 3D current pathways and a corresponding increased potential drop close to the interface.

However, the main discrepancy between *apparent* k'_{exp} and *microscopic* k' arises from a systematic error in data normalization. As discussed in detail in **Section 3.1.**, experimental impedance data are commonly normalized to $A_{electrode}$, implicitly assuming an intimate contact with the SE (*i.e.*, $A = A_{electrode}$). However, this is rarely guaranteed for solid|solid interfaces (*i.e.*, $A < A_{electrode}$). According to (**eq. 2**), R_{SEI} is inversely proportional to A rather than $A_{electrode}$. The incorrect normalization of the area-specific resistance $(R_{tot} - R_{bulk})$ leads to the different slopes of the resistance curves shown in **Figure 3c**.

As a result, k'_{exp} reflects an *apparent* value rather than the *intrinsic* k'. Its strong dependence on A makes it difficult to distinguish whether changes in the slope of resistance curves arise from variations in A or from genuine changes in the underlying interphase growth kinetics. For instance, if A_r is only 10% of $A_{electrode}$, k'_{exp} will overestimate k' by an order of magnitude, as evident from (**eq. 2**). As we discuss in more detail in the following sections, this is a major challenge since the *actual* contact area A in solid-state systems is rarely known, difficult to quantify, and may even evolve during operation.

3.2.2. Uncertainty in the Contact Area – The Influence of the Contact Distribution

The uncertainty in A is a fundamental challenge in solid-state systems and intensively discussed in contact physics literature.[50–52] While external pressure can influence A to some extent, its exact value often remains unknown and is often only a small fraction of $A_{\mathrm{electrode}}$.[53] One approach to estimate A is to correlate it with R_{cstr}. As shown in the previous section, R_{cstr} may appear as an additional contribution in the impedance data, *i.e.*, as an additional offset in a plot of $(R_{\mathrm{tot}} - R_{\mathrm{bulk}})$ vs. t. Theoretical models from electrical contact literature provide estimates for A based on R_{cstr} for simple model geometries.[54] However, R_{cstr} is highly dependent on the spatial contact distribution, which in practice makes resistance measurement unsuitable to determine A.[47,54,55]

This has direct implications for the interpretation of impedance data and the extraction of k'_{exp}. Even if the initial impedance spectra of two symmetric cells seem similar, the underlying interfacial area may differ substantially. Although these differences in A are not directly observable, they result in significantly different values of k'_{exp}. For instance, A_{r} might vary between 20% and 100% of $A_{\mathrm{electrode}}$ without noticeable evidence in the electric data, other than an *apparent* increase of k'_{exp}.[47,56]

These findings are general and not limited to alkali metal electrodes or symmetric cells. When studying interphase formation at the cathode|SE interfaces in SSBs, the CAM undergoes significant volume changes depending on the state of charge (SOC).[57] As a result, both the local pressure and the contact area A between CAM particles and the SE change dynamically with the SOC. This complicates the comparison of interphase rate constants obtained for different particle sizes or at different SOC – even under idealized, potentiostatic conditions. This uncertainty may motivate additional pressure-dependent measurements and (*post mortem*) investigations in interphase studies, such as cross-section or tomographic analysis to obtain estimates for A.

For the interested reader, we show and discuss the influence of the contact distribution on our specific model case in **Section S2** of the Supporting Information. Here, the contact distribution influences the cell impedance (*i.e.*, R_{cstr}), but does not affect the extracted k'_{exp}.

3.2.3. The Influence of (Native) Surface Passivation

Ensuring detailed knowledge about the contact area A between the electrode and sample is one prerequisite for reliable analysis of interphase growth kinetics. However, even if A is known, the presence of (ionically) insulating passivation layers can produce a similar effect. Unfortunately, reactive alkali metals like lithium or sodium rapidly form native passivation layers upon exposure to trace atmospheric gases such as nitrogen, oxygen, water vapor, and carbon dioxide.[58] Even gas residues in the parts-per-million (ppm) range, commonly present in glovebox atmospheres, are sufficient to form passivation layers tens of nanometers thick.[59] Depending on their thickness and mechanical properties, these passivation layers may be partially penetrated by surface asperities of the SE during cell assembly. The extent of this penetration is affected by factors, such as surface roughness and applied stack pressure, and significantly influence charge transfer at the electrode interface.[33,59]

To systematically investigate to which extent thin, partially covering passivation layers may influence the extraction of meaningful and reproducible interphase growth kinetics, we adapt the model system from **Section 3.2.1.** with A_{r} = 50% (see **Figure 4a**). This time the single contact spot is surrounded by a passivation phase with a non-zero σ_{ion}. Throughout the simulation series, we systematically vary the ionic resistance of the passivation layer (R_{p}) between $R_{\mathrm{ref}}/100$ to $400R_{\mathrm{ref}}$, where $R_{\mathrm{ref}} = 9\ \Omega{\cdot}\mathrm{cm}^2$. We assume that the ionically conducting passivation layer has a negligible σ_{el} compared to the interphase. Thus, SEI is formed only at the contact spot, but not at the passivation|SE interface.

The resulting impedance spectra for a highly conductive interlayer ($R_{\mathrm{p}} = R_{\mathrm{ref}}/100$) and a highly resistive interlayer ($R_{\mathrm{p}} = 400R_{\mathrm{ref}}$), are shown in **Figure 4b**. Both impedance series reveal a bulk signal alongside an interfacial contribution, which varies significantly depending on R_{p} and t. For the simulation with $R_{\mathrm{p}} = R_{\mathrm{ref}}/100$, the assigned bulk signal does not solely include bulk contributions at t_0, but is slightly larger (see inset: Z' is larger than 0, after subtraction of R_{bulk}). This is due to transport across the interlayer, which does not always appear as a separate signal in the impedance spectrum. In the case of $R_{\mathrm{p}} = 400R_{\mathrm{ref}}$, the initial interface signal is significantly larger, and the size matches that of R_{cstr} for A_{r} = 50%, discussed for the pore case in **Section 3.2.1.**. This shows that initially only a negligible amount of current flows through the passivation layer which effectively acts like a pore.[49,60]

With increasing t, an additional semicircle appears in the Nyquist diagram. The assignment of this contribution solely to the interphase, like done before, is not possible anymore, since it also includes impedance contributions from the passivation layer. For $R_p = R_{ref}/100$, the interface signal in the impedance spectra remains minimal over time. As shown in the enlarged inset, the signal exhibits only a slight initial increase before stabilizing. Impedance growth at t_1 has more or less completely saturated. A different trend is observed for $R_p = 400R_{ref}$. In

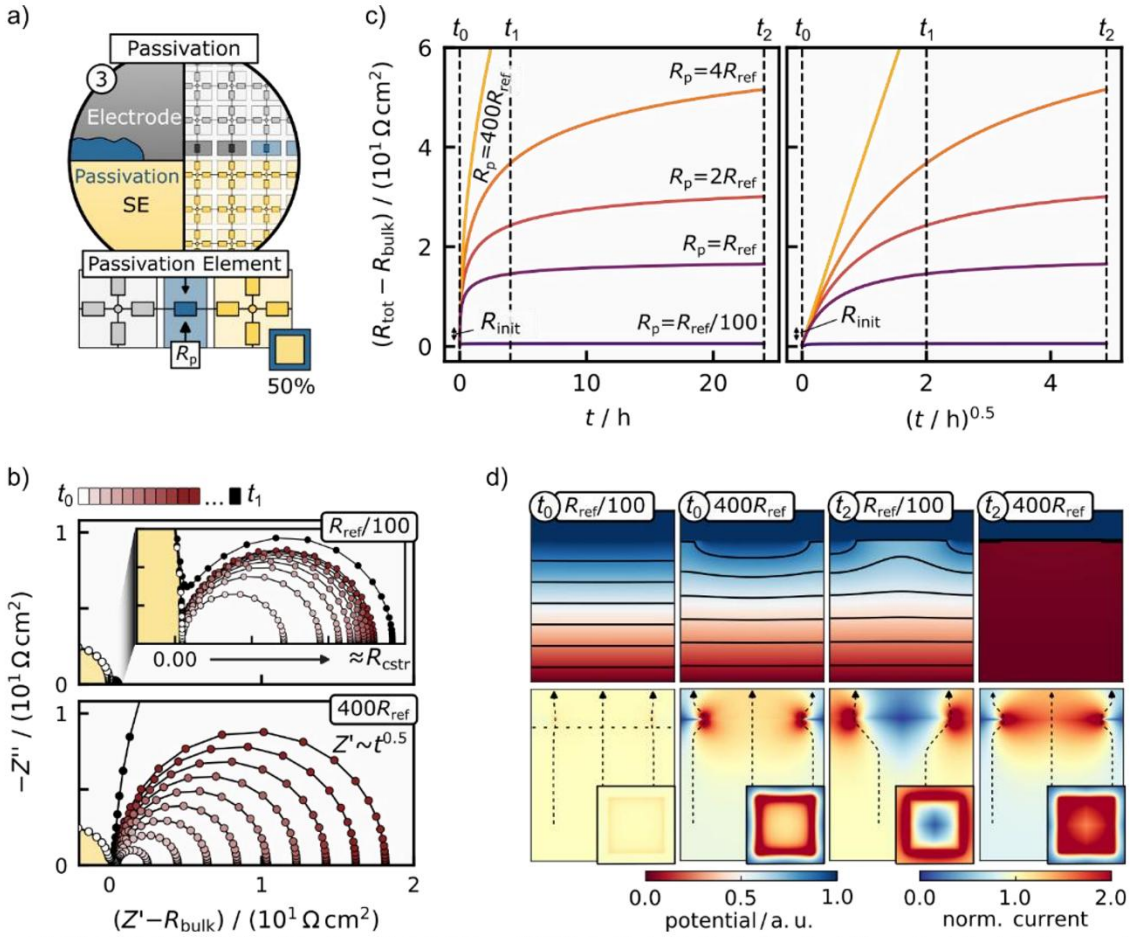

Figure 4. **The Effect of Electric Interlayer Properties on SEI Growth Analysis**. In the simulations, A_r at the interface was kept constant at 50% of $A_{electrode}$. (a) The homogeneous interlayer is penetrated by the SE, forming a cubic contact spot. (b) The impedance growth of the interface signal shows significant differences depending on electric properties R_p of the passivation layer. (c) The evolution of the macroscopic interface resistance differs from the square-root-of-time dependent growth that was assumed as the input for the simulation. (d) The discrepancy between the microscopic and macroscopic levels is due to a temporal change in current paths at the interface (see black arrows). Switching between transport pathways (across the SEI or passivation layer) results in a resistance plateau over time. The time to reach the plateau depends on the electrical properties of the interlayer and the surface coverage (see **Figure S2**).

this case, the impedance increase does not saturate in the simulated timeframe (*i.e.*, 24 h).

Figure 4c shows the resistance growth over time for different R_p. Except for the case with $R_p = R_{ref}/100$, $(R_{tot} - R_{bulk})$ initially follow a square-root-of-time dependence that gradually levels off into a plateau. This is particularly evident in the linearized representation (vs. $t^{0.5}$), where the initial linear increase transitions into saturation. Notably, the transition time t_{trans} depends on the magnitude of R_p and the interface coverage of the passivation layer: The higher R_p, the later the transition occurs. In the simulated timeframe, the resistance in the highly conductive case ($R_p = R_{ref}/100$) immediately enters the plateau region, while no transition is observed in the highly resistive case ($R_p = 400R_{ref}$).

Similar results are observed considering the extend of interface coverage: With increasing interface coverage by passivation, t_{trans} increases to reach saturation. A more detailed discussion on this, including simulation results, is given in **Section S3.1.** of the Supporting Information.

The discrepancy between resistance trends results from the competitive transport pathways at the interface and a resulting switch between preferred transport pathways over time, *i.e.*, transport across the interlayer or across the forming SEI at the electrode|SE contact. This is reflected in the DC potential and current distribution, as shown in **Figure 4d**. In the highly conductive case ($R_p = \frac{R_{ref}}{100}$) at t_0, the potential and current are distributed almost uniformly across the interface, closely resembling the ideal scenario of a planar interface without passivation (see **Figure 2d**). With the increase in SEI thickness, a shift in transport pathways occurs. At some point, all current flows through the passivation layer rather than the SEI layer (see black current lines in **Figure 2d**). Therefore, the extracted resistance difference (R_{tot} −

R_{bulk}) reaches a plateau. The corresponding resistance reflects R_p (normalized by the passivation layer area) plus the corresponding R_{cstr}.

In the highly resistive case ($R_p = 400R_{ref}$), no major changes in the current pathways are observed in the simulated timeframe. All the current flows through the forming SEI layer (see black current lines in **Figure 2d**). As a result, the appearance of diffusion-controlled resistance growth is sustained at the cell level, but with a two times larger *apparent* rate constant k'_{exp} (due to $A_r = 50\%$). The preferred transport pathway at any given t depends on the resistance ratio between $R_{SEI}(t)$ and R_p, as well as the induced R_{cstr}. For large values of R_p or small areal coverage with passivation, the resistance plateau shifts to larger t (*i.e.*, outside the simulation timeframe).

The dependence of resistance evolution on passivation layer properties highlights the critical role of measurement duration. In experiments, it is unfeasible to capture the "complete" resistance curve over an infinite timespan. Instead, only discrete snapshots can be recorded, constrained by experimental timescales and delays between cell assembly and the onset of measurements. As a result, the measured data may either directly display a fully developed plateau—reflecting the effective passivation layer properties—or fail to capture the transition region within the available timeframe. In the latter case, a larger *apparent* rate constant k'_{exp} will be obtained

Reported literature values for passivation layer thicknesses and their transport properties on alkali-metals show large uncertainty and are likely not easily comparable between different research groups, gloveboxes or even samples. Assuming a negligible σ_{el}, the estimated t_{trans} for passivated lithium foils can vary widely from a few minutes up to several years, depending on the specific passivation layer properties (see detailed discussion in **Section S3.2.** of the Supporting Information).

3.2.4. Other Factors Influencing the Apparent Interphase Growth Kinetics

In practice, a variety of additional factors may influence the macroscopic impedance signal and, consequently, the *apparent* interphase growth kinetics. Beyond interfacial pores and (native) surface passivation, these include: (*i*) surface roughness due to imperfect lithium morphology or whisker formation under DC load;[33,61,62] (*ii*) the microstructure of the solid electrolyte, particularly grain boundaries and internal porosity;[63,64] (*iii*) complex electrode architectures, such as those in composite cathodes;[65] and (*iv*) the microstructure of metal electrodes and interphases (*i.e.*, composing various product phases and cavities).[66–69] These factors will introduce additional uncertainty, which we do not explore here. Nonetheless, they represent important directions for future work.

3.3. Consequences for the Analysis of Experimental Impedance Data – SEI Formation at the Li|Li_6PS_5Cl interface

To complement the theoretical insights from our simulation study, we now turn to experimental impedance data, which is inherently more complex. In this section we aim to demonstrate how poor contact manifests in real experimental data and, if not adequately accounted for, misleads the interpretation of *apparent* interphase kinetics.

To this end, symmetric Li|Li_6PS_5Cl|Li cells were assembled and characterized via EIS under different pressure conditions. Fresh lithium discs were cut from a rod to reduce the amount of native surface passivation to a practical minimum. A spring-loaded setup (schematically shown in **Figure 5a**) was used to apply constant uniaxial pressures (p) ranging from 1 to 20 MPa during cell assembly and EIS characterization. In addition, a reference cell was fabricated by isostatic pressing at 75 MPa, followed by impedance characterization at ambient pressure (1 atm). A comparison allows us to decouple the effects of initial contact formation from the impact of ongoing mechanical load during measurement. In all cases, impedance spectra were recorded continuously over a period of ~12 days in a climate chamber at 25 °C. For the uniaxially pressed cells, measurements were taken approximately one minute after applying stack pressure, while for the isostatically pressed cell, the initial spectrum was recorded ~30 minutes after the isostatic pressing procedure. All impedance spectra were normalized to $A_{electrode}$ and multiplied with a factor of 0.5 to account for the two interfaces in each cell.

Figure 5 summarizes the experimental results. The initial impedance spectra (**Figure 5a**) show a clear pressure dependence: The total impedance decreases with increasing stack pressure. The offset along the Z'-axis represents the effective bulk resistance R_{bulk*} of the solid electrolyte pellet, including grain boundary effects. Given the high σ_{ion} of Li_6PS_5Cl (~2 mS·cm^{-1}), the corresponding conductivity relaxation is outside the measured frequency range.

Interestingly, the Z'-axis offset decreases with increasing p, which is unlikely to stem from further densification as all pellets were pre-compacted at 375 MPa. Instead, we attribute this behavior to an increase of the interfacial contact area A at higher p, reducing current constriction and hence the associated R_{cstr}. As previously discussed, the impedance signature of current constriction depends on factors such as pore depth and σ_{ion}. In systems with a broad distribution of pore depths, no distinct constriction

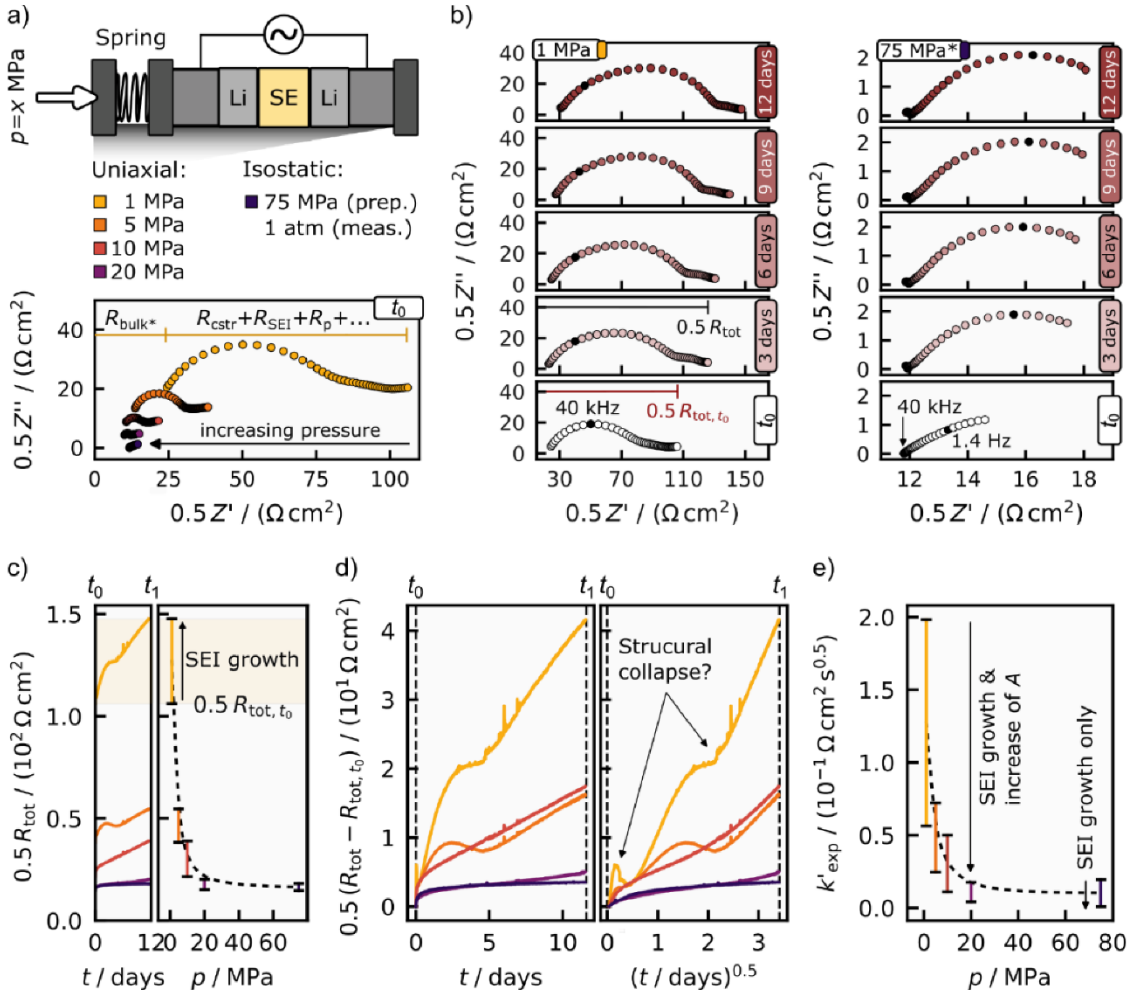

Figure 5. Influence of (Stack-) Pressure on the Impedance Evolution of Symmetric Li|LPSCl|Li Cells and Apparent Interphase Growth Kinetics. (a) Schematic illustration of the uniaxial stack pressure setup used for EIS measurements. Comparison of the initial impedance spectra (*i.e.*, at t_0) at different applied stack pressures or isostatic (formation) pressure. (b) Temporal impedance evolution for the measurement at 1 MPa (left) and for the isostatically pressed sample (75 MPa*, right). The black datapoint in each spectrum of a measurement series (either 40 kHz or 1.4 Hz) corresponds to the same frequency. The impedance value at the lowest frequency is used as a proxy for the total resistance R_{tot} of the respective cell. (c) The change of R_{tot} over time is strongly pressure dependent. The length of the bars along the *y*-axis indicates ΔR_{tot} of the respective cell in the timeframe between the start of the measurement (t_0) and its end (t_1). (d) The change in total resistance $R_{tot} - R_{tot,0}$ over t and $t^{0.5}$ shows distinct differences in curvature with p. (e) Pressure-dependent rate constants extracted from cell-level impedance measurements. The length of the bars along the *y*-axis indicates the variation in k'_{exp} depending on the time range considered for linear interpolation (see **Figure S3**).

semicircles are expected; instead, the effect is smeared over a wide frequency range, possibly including frequencies beyond the measurement range.[47]

The assignment of the remaining impedance features is even more challenging. They may arise from interface layers and corresponding phenomena including SEI, native passivation, or dynamic current constriction. As discussed in **Section 3.2.3.**, for the presence of several (parallel connected) phases at the interface, impedance signals cannot be easily assigned to individual phases. Instead, the measured impedance represents an effective interfacial response: Specific impedance features may originate from localized conductivity relaxations of distinct phases or more complex transitions, that lead to completely different current pathways.[49]

The comparison of the impedance evolution for the cell at 1 MPa (left, **Figure 5b**) and the isostatically pressed sample (right, **Figure 5b**) clearly underscores the critical influence of (stack) pressure in affecting the impedance response. In the isostatic case, where the interfacial contact area A is expected to approach the electrode area ($A \approx A_{electrode}$), the broad impedance contributions identified before seem to play only a minor role: The impedance data show only a low-frequency Warburg-short-like signal. Similar behavior is frequently observed for other SEs, such as $Li_7La_3Zr_2O_{12}$ or $Na_{3.4}Zr_2Si_{2.4}P_{0.6}O_{12}$ in

contact with their parent metal electrode.[70–72] However, its origin remains unclear.

To analyze the impact of SEI formation, we adopt the approach used in the simulation studies and monitor R_{tot} over t. Since we cannot clearly distinguish between bulk and constriction related impedance contributions, we refrain from subtracting $R_{\mathrm{bulk}*}$. As a proxy for R_{tot}, we extract Z' from the lowest frequency point of each spectrum (0.3 Hz), as indicated in **Figure 5b** for various time points (t_0, 3 to 12 days). While this approach simplifies the analysis, it relies on the assumption that the SEI is the only component in the cells that changes with t. Due to the "mixed" origin of the distinct impedance signals, we identify this analysis approach as the most suitable.

Figure 5c shows the extracted R_{tot} over t (left panel) and p (right panel). By applying (stack) pressure, we obtain a similar trend in the R_{tot} vs. t like in the simulation studies, where we changed A_{r}: The offset along the R_{tot}-axis decreases with increasing p consistent with a A_{r} increase due to plastic deformation of lithium. The length of the vertical lines (ΔR_{tot}) in the plot of R_{tot} vs. p, indicates the SEI related change of R_{tot} between the start of the measurement (t_0) and the end (t_1). The black, dashed line (drawn for a guide to the eye) highlights the non-linear pressure dependence of R_{tot}, which is typical of contact resistance.[33] In our simulation study, we observed a similar dependence for the *apparent* SEI resistance ($R_{\mathrm{tot}} - R_{\mathrm{bulk}}$) by linearly changing A_{r}.

To analyze the resistance evolution in more detail, we consider the resistance change ($R_{\mathrm{tot}} - R_{\mathrm{tot},0}$) as a function of time (vs. t or $t^{0.5}$). **Figure 5d** shows the evolution of ($R_{\mathrm{tot}} - R_{\mathrm{tot},0}$) over 12 days. The comparison of the resistance curves shows distinct differences: (*i*) the trend deviates from a square-root-of-time relationship; (*ii*) the cells investigated under low p (e.g., 1 MPa, yellow) exhibit a significantly steeper resistance increase than the cells at high-pressure (e.g., 75 MPa isostatic, dark purple), and (*iii*), all cells investigated under stack pressure show distinct regions of saturation or even a decrease in ($R_{\mathrm{tot}} - R_{\mathrm{tot},0}$).

The cause of these features, that are particularly pronounced under low stack and formation pressure, is unclear. One hypothesis is mechanical or morphological failure of the SEI (e.g., collapse of fragile contact points) potentially linked to slight temperature fluctuations of the climate chamber. This is supported by the observation, that each drop in ($R_{\mathrm{tot}} - R_{\mathrm{tot},0}$) is followed by a renewed, but more gradual increase. This is potentially due to the formation of fresh lithium contacts. Here, lithium creep may play an important role.[44,45,53]

To quantify our observations, we perform linear regression within regions in the R_{tot} vs. $t^{0.5}$-plot which seem to show a linear trend (see **Figure S3**). The extracted k'_{exp} shown in **Figure 5e** resemble the trends already observed for R_{tot} vs. p, *i.e.*, k'_{exp} decreases in a non-linear way with increasing p. This trend is consistent with our simulation results (see **Figure 3**). Increasing the (stack) pressure will lead to a larger A, which, in turn, reduces the resistance increase according to (**eq. 2**). Error bars reflect the variation due to different linear regression windows. A broad range for k'_{exp} is observed at low p, while the spread decreases at high p, which is consistent with a change in contact area A during a measurement.

It is important to stress that the choice of fitting windows and the analysis itself is arbitrary and not grounded on a rigorous mechanistic model. Rather, this approach is used to qualitatively illustrate general trends and to highlight the impact of pressure conditions on the *apparent* interphase evolution and corresponding rate parameters. The analysis shows that macroscopic impedance trends may be mainly determined by geometric or contact-related effects, rather than intrinsic interphase kinetics, if contact conditions are not properly considered.

Conclusions

Our findings demonstrate that reliable analysis of interphase formation, based on impedance data, critically depends on detailed knowledge of interfacial morphology. Macroscopic impedance trends may be mainly determined by geometric or contact-related effects rather than intrinsic interphase kinetics. Competing transport pathways (*e.g.*, through both SEI and a native passivation layer on reactive alkali metal electrodes) can lead to an *apparent* saturation in cell resistance that does not reflect a saturation of the *local* interphase growth. Another major source of uncertainty arises from the often-implicit assumption of intimate interfacial contact, typically introduced by normalizing resistances to the geometric electrode area. Poor contact conditions manifest in different ways in the impedance data (*e.g.*, by distinct signals, or an overall scaling) and may often remain completely undetected.

The choice of measurement conditions must be guided by the intended purpose of the investigation. If the goal is to study the fundamental kinetics of interphase growth, conditions should be selected to ensure intimate and stable interface contact to minimize morphological artifacts. In contrast, if the objective is to understand how the *effective* SEI resistance under application-relevant pressure conditions impacts the overall cell resistance, then lower or varying pressures may be appropriate. Anyhow, in this case, extracted resistance growth behavior should not be

assigned to fundamental properties and kinetics of interphase formation.

To ensure meaningful interpretation and cross-study comparability, detailed reporting of sample preparation (including pressure conditions) and measurement protocols are essential. Moreover, applying additional techniques like CTTA may help to cross-check impedance-derived parameters. Ultimately, advancing the mechanistic understanding of solid|solid interphase evolution will require integrating impedance analysis with complementary techniques capable of resolving both chemical and morphological interphase evolution in operando.

Computational Details

Generation of Three-Dimensional Microstructures

The microstructural model systems with all their geometrical parameters used in the computations are presented at the beginning of each simulation series in the **Results and Discussion** section. The icons in **Figure 2-4** show the considered experimental system in comparison to the corresponding computational model system. All microstructures were built using Numpy.[73]

Transport Description and Choice of Materials Parameters

All transport computations are based on a microstructure-resolved 3D network model that describes ionic transport. The modeling approach is illustrated in **Figure 1** for an ideal interface contact. To this end, the model system is discretized, and transport is described between the individual voxels. The local transport properties depend on the phase assignment of each voxel. Bulk and grain boundary transport in different materials (*i.e.*, SE, interlayer, electrode) are represented by *RC*-elements, while pores are modeled as capacitors. Transport across an interphase is considered as an additional *RC*-element between two voxels of different materials. The local transport parameters of these processes are considered constant (*i.e.*, time-independent) within a simulation series. Low-frequency diffusion processes are not considered in the simulations, and the electronic conductivity of the solid electrolyte and the interphase is assumed to be negligible.

For the time-dependence of the local SEI parameters ($R_{\mathrm{SEI,loc}}$, $C_{\mathrm{SEI,loc}}$), we assume a diffusion-controlled interphase growth following (**eq. 2**). This implies that the interphase growth mode at each interface element remains quasi-1D and is not affected by its constituent phases. Since the interphase is significantly thinner than the voxel resolution of our simulation, it is not explicitly resolved as a structural domain. This means that charge transport through the interphase is only considered in the direction perpendicular to the electrode interface, with no lateral transport within the interphase plane. This is similar to the assumption of the Wagner diffusion model presented in **Section 2.2.**, and an acceptable simplification given the thin nature of the interphase and the significantly lower ionic conductivity compared to the bulk solid electrolyte.

The local circuit parameters ($R_{i,\mathrm{loc}}$, $C_{i,\mathrm{loc}}$) in the electric network are determined using the standard formulas for resistors and plate capacitors. The material-specific transport parameters for the metal and SE are based on literature data.[74,75] Unless stated otherwise, the following parameters are used: (*i*) The permittivity of the pores is set to vacuum permittivity, *i.e.*, $\varepsilon_{\mathrm{pore}} = \varepsilon_0$. (*i*) The parameters for Li_6PS_5Cl are set to σ_{SE} = 2.0 mS cm^{-1}, and $\varepsilon_{\mathrm{SE}} = 20 \cdot \varepsilon_0$. The partial conductivity of the forming SEI at the Li|Li_6PS_5Cl interface is set to $\sigma_{\mathrm{ion}} = 134\ \mathrm{nS} \cdot \mathrm{cm}^{-1}$ and $\sigma_{\mathrm{el}} = 0.3\ \mathrm{nS} \cdot \mathrm{cm}^{-1}$, based on recent literature values.[40]

Experimental Details

Preparation of materials and cell assembly were carried out in an argon-filled glovebox (*LabMasterPRO*, MBraun, Garching, Germany), with $p(O_2)/p$ and $p(H_2O)/p < 1$ ppm.

Preparation of Materials

Commercial Li_6PS_5Cl powder (POSCO Chemical Co, Korea) with a particle size of 5 µm was used as separator. Lithium metal electrodes were prepared by cutting lithium metal (99.8% purity, MaTecK Material-Technologie & Kristalle GmbH, Jülich, Germany) from a rod. The passivation layer was mechanically removed, and the lithium was subsequently pressed manually between two pouch foils to achieve a thickness of ~100 µm. Circular electrodes (d = 9 mm) were punched out from these foils. A steel foil (AISI 304 steel, d = 10 mm) with a thickness of 20 µm was used as a current collector.

Cell Assembly

Cells were assembled using press-cell casings with a 10 mm polyetheretherketone (PEEK) mantle and tested under stack pressures ranging from 1 to 20 MPa. To prepare the SE separator, 90 mg of Li_6PS_5Cl powder were uniaxially pressed between stainless-steel stamps at 380 MPa for three minutes. Afterwards, a hand-pressed lithium metal foil and a stainless-steel foil were placed on each side of the compacted pellet. The cell was then mounted in a pressure frame equipped with a metal spring and force sensor. Stack pressures of 1, 5, 10, and 20 MPa were applied.

Reference pouch cells were prepared using a similar setup. First, Li_6PS_5Cl pellets (90 mg) were pre-compacted at 400 MPa to enhance density. Then, assembled cells consisting of lithium metal and stainless-steel foils on both sides were isostatically pressed at 75 MPa to ensure intimate interfacial contact. Finally, the assembled cell was sealed in a pouch with nickel current collectors.

Electrochemical Measurements

Electrochemical characterization was performed in a climate chamber (25 °C, Binder GmbH, Germany) using VMP3 or VMP300 potentiostats (BioLogic, France). Press cells were measured while applying the respective pressure. Electrochemical measurements of pouch cells were performed at atmospheric pressure. All cells were measured within one hour after assembly.

Potentiostatic electrochemical impedance spectroscopy (PEIS) was performed in a frequency range between 3 MHz and 100 mHz with a voltage amplitude of 10 mV. After each PEIS measurement, the open cell voltage (OCV) was measured for 2 minutes. The procedure was then repeated for several days until the experiment was completed. For impedance analysis, only data in the frequency range between 3 MHz and 100 mHz was considered, due to artifacts in the higher and lower-frequency range.

Data Availability Statement

The data that support the findings of the study are available from the corresponding author upon reasonable request.

Author Contributions

$^{\perp}$S.K. and C.D.A. contributed equally to this work.

S.K. designed the experiments and models, carried our specific literature search, carried out simulations, data analysis as well as visualization, designed experiments and wrote the first draft of the manuscript. C.D.A. carried out a specific literature search and model analysis, designed the experiments, and wrote the first draft of the manuscript. L.S. performed the experiments. J.J. raised funding and contributed to the scientific discussions. J.K.E. designed the experiments, implemented the simulation code, performed initial simulations, interpreted the data, and wrote the first draft of the manuscript. All authors discussed the results and contributed to the preparation of the manuscript.

Acknowledgements

S.K. and J.J. acknowledge financial support by the German Federal Ministry of Education and Research (BMBF) within the cluster of competence FESTBATT (project 03XP0428E). C.D.A. and J.J. acknowledge financial support by the BMBF within the ALANO project (grant no. 03XP0396J). J.K.E. acknowledges financial support by the Hessian State Ministry of Higher Education, Research, and the Arts (HMWK). S.K. and J.K.E. acknowledge computational resources provided by the HPC Core Facility and the HRZ of the Justus-Liebig-University Giessen. J.K.E. would like to thank MSc. Philipp Risius and Dr. Marcel Giar of HPC-Hessen, funded by the HMWK, for programming advice.

Competing Interests

The authors declare no competing financial interests.

Declaration of Generative AI and AI-assisted Technologies

During the preparation of this work the authors used *ChatGPT 3.5* (by OpenAI) in order to improve readability and language and visualizations. After using this tool, the authors reviewed and edited the content as needed and take full responsibility for the content of the publication.

References

1. Chu, S. & Majumdar, A. Opportunities and Challenges for a Sustainable Energy Future. *Nature* **488,** 294–303; 10.1038/nature11475 (2012).
2. Larcher, D. & Tarascon, J.-M. Towards Greener and More Sustainable Batteries for Electrical Energy Storage. *Nature Chemistry* **7,** 19–29; 10.1038/nchem.2085 (2015).
3. Wang, M. J. *et al.* Transitioning Solid-State Batteries from Lab to Market: Linking Electro-Chemo-Mechanics with Practical Considerations. *Joule* **5,** 1371–1390; 10.1016/j.joule.2021.04.001 (2021).
4. Bates, A. M. *et al.* Are Solid-State Batteries Safer than Lithium-Ion Batteries? *Joule* **6,** 742–755; 10.1016/j.joule.2022.02.007 (2022).
5. Kochetkov, I. *et al.* Different Interfacial Reactivity of Lithium Metal Chloride Electrolytes with High Voltage Cathodes Determines Solid-State Battery Performance. *Energy Environ. Sci.* **15,** 3933–3944; 10.1039/D2EE00803C (2022).
6. Guo, R., Hobold, G. M. & Gallant, B. M. The Ionic Interphases of the Lithium Anode in Solid State Batteries. *Current Opinion in Solid State and Materials Science* **26**; 10.1016/j.cossms.2021.100973 (2022).
7. Zhu, Y., He, X. & Mo, Y. Origin of Outstanding Stability in the Lithium Solid Electrolyte Materials: Insights from Thermodynamic Analyses Based on First-Principles Calculations. *ACS Applied*

Materials & Interfaces **7,** 23685–23693; 10.1021/acsami.5b07517 (2015).

8. Otto, S.-K., Riegger, L. M., Fuchs, T., Kayser, S., Schweitzer, P., Burkhardt, S., Henss, A., Janek, J. In Situ Investigation of Lithium Metal–Solid Electrolyte Anode Interfaces with ToF-SIMS. *Adv. Mater. Interfaces* **13**; 10.1002/admi.202102387 (2022).

9. Walther, F. *et al.* Visualization of the Interfacial Decomposition of Composite Cathodes in Argyrodite-Based All-Solid-State Batteries Using Time-of-Flight Secondary-Ion Mass Spectrometry. *Chem. Mater.* **31,** 3745–3755; 10.1021/acs.chemmater.9b00770 (2019).

10. Han, S. Y. *et al.* Stress Evolution During Cycling of Alloy-Anode Solid-State Batteries. *Joule* **5,** 2450–2465; 10.1016/j.joule.2021.07.002 (2021).

11. Turrell, S. J. *et al.* Origin of Stability in the Solid Electrolyte Interphase formed between Lithium and Lithium Phosphorus Oxynitride. *Chem. Mater.*; 10.1021/acs.chemmater.5c00483 (2025).

12. Cheng, D. *et al.* Unveiling the Stable Nature of the Solid Electrolyte Interphase between Lithium Metal and LiPON via Cryogenic Electron Microscopy. *Joule* **4,** 2484–2500; 10.1016/j.joule.2020.08.013 (2020).

13. Hood, Z. D. *et al.* Elucidating Interfacial Stability between Lithium Metal Anode and Li Phosphorus Oxynitride via In Situ Electron Microscopy. *Nano Letters* **21,** 151–157; 10.1021/acs.nanolett.0c03438 (2021).

14. Liang, Y. *et al.* In-situ XPS Investigation of the SEI Formed on LGPS and LAGP with Metallic Lithium. *Chemical communications (Cambridge, England)* **60,** 12597–12600; 10.1039/D4CC04462B (2024).

15. Narayanan, S. *et al.* Effect of Current Density on the Solid Electrolyte Interphase Formation at the Lithium|Li_6PS_5Cl Interface. *Nat Commun* **13,** 7237; 10.1038/s41467-022-34855-9 (2022).

16. Wenzel, S. *et al.* Interfacial Reactivity Benchmarking of the Sodium Ion Conductors Na3PS4 and Sodium β-Alumina for Protected Sodium Metal Anodes and Sodium All-Solid-State Batteries. *ACS Applied Materials & Interfaces* **8,** 28216; 10.1021/acsami.6b10119 (2016).

17. Aktekin, B. *et al.* Operando Photoelectron Spectroscopy Analysis of Li_6PS_5Cl Electrochemical Decomposition Reactions in Solid-State Batteries. *ACS Energy Lett.,* 3492–3500; 10.1021/acsenergylett.4c01072 (2024).

18. Wenzel, S. *et al.* Interphase Formation and Degradation of Charge Transfer Kinetics between a Lithium Metal Anode and Highly Crystalline $Li_7P_3S_{11}$ Solid Electrolyte. *Solid State Ionics* **286,** 24–33; 10.1016/j.ssi.2015.11.034 (2016).

19. Wenzel, S. *et al.* Interfacial Reactivity and Interphase Growth of Argyrodite Solid Electrolytes at Lithium Metal Electrodes. *Solid State Ionics* **318,** 102; 10.1016/j.ssi.2017.07.005 (2018).

20. Aktekin, B. *et al.* SEI Growth on Lithium Metal Anodes in Solid-State Batteries Quantified with Coulometric Titration Time Analysis. *Nat Commun* **14,** 6946; 10.1038/s41467-023-42512-y (2023).

21. Broussely, M. *et al.* Aging Mechanism in Li Ion Cells and Calendar Life Predictions. *Journal of Power Sources* **97-98,** 13–21; 10.1016/S0378-7753(01)00722-4 (2001).

22. Keil, P. *et al.* Calendar Aging of Lithium-Ion Batteries. *J. Electrochem. Soc.* **163,** A1872-A1880; 10.1149/2.0411609jes (2016).

23. Kolzenberg, L. von, Latz, A. & Horstmann, B. Chemo-Mechanical Model of SEI Growth on Silicon Electrode Particles. *Batteries & Supercaps* **5**; 10.1002/batt.202100216 (2022).

24. Liu, Y. *et al.* Alloyable Viscous Fluid for Interface Welding of Garnet Electrolyte to Enable Highly Reversible Fluoride Conversion Solid State Batteries. *Adv Funct Materials* **33**; 10.1002/adfm.202208013 (2023).

25. Ploehn, H. J., Ramadass, P. & White, R. E. Solvent Diffusion Model for Aging of Lithium-Ion Battery Cells. *J. Electrochem. Soc.* **151,** A456; 10.1149/1.1644601 (2004).

26. Xiong, Z. *et al.* 4.2V Polymer All-Solid-State Lithium Batteries Enabled by High-Concentration PEO Solid Electrolytes. *Energy Storage Materials* **57,** 171–179; 10.1016/j.ensm.2023.02.008 (2023).

27. Attia, P. M., Chueh, W. C. & Harris, S. J. Revisiting the $t^{0.5}$ Dependence of SEI Growth. *J. Electrochem. Soc.* **167,** 90535; 10.1149/1945-7111/ab8ce4 (2020).

28. Zuo, T.-T. *et al.* A Mechanistic Investigation of the $Li_{10}GeP_2S_{12}$|$LiNi_{1-x-y}Co_xMn_yO_2$ Interface Stability in All-Solid-State Lithium Batteries. *Nat Mater* **12,** 6669; 10.1038/s41467-021-26895-4 (2021).

29. Kwon, P. J. *et al.* Chemo-electrochemical Evolution of Cathode–Solid Electrolyte Interface in All-Solid-State Batteries. *ACS Energy Lett.* **9,** 4746–4752; 10.1021/acsenergylett.4c02062 (2024).

30. Sakuma, M. *et al.* Reactions at the Electrode/Electrolyte Interface of All-Solid-State Lithium Batteries Incorporating Li–*M* (*M* = Sn, Si) Alloy Electrodes and Sulfide-Based Solid Electrolytes. *Solid State Ionics* **285,** 101–105; 10.1016/j.ssi.2015.07.010 (2016).

31. Chaney, G. *et al.* Two-Step Growth Mechanism of the Solid Electrolyte Interphase in Argyrodyte/Li-Metal Contacts. *ACS Applied Materials & Interfaces* **16,** 24624–24630; 10.1021/acsami.4c02548 (2024).

32. Riegger, L. M. *et al.* Evolution of the Interphase between Argyrodite-Based Solid Electrolytes and the Lithium Metal Anode ─ The Kinetics of Solid Electrolyte Interphase Growth. *Chem. Mater.* **35,** 5091–5099; 10.1021/acs.chemmater.3c00676 (2023).

33. Zhang, X. *et al.* Pressure-Driven Interface Evolution in Solid-State Lithium Metal Batteries. *Cell Reports Physical Science* **1,** 100012; 10.1016/j.xcrp.2019.100012 (2020).

34. Sivavec, J., Kravchyk, K. V. & Kovalenko, M. V. Impact of Stack Pressure on Coulometric Titration Time Analysis. *Comm chemistry* **8,** 96; 10.1038/s42004-025-01496-0 (2025).

35. Schmalzried, H. *Chemical Kinetics of Solids* (Wiley-VCH, Weinheim, 1995).

36. Schmalzried, H. *Solid State Reactions.* 2nd ed. (Verl. Chemie, Weinheim u.a., 1981).

37. Wagner, C. Beitrag zur Theorie des Anlaufvorgangs. *Zeitschrift für Physikalische Chemie* **21B,** 25–41; 10.1515/zpch-1933-2105 (1933).

38. Wagner, C. Beitrag zur Theorie des Anlaufvorganges. II. *Zeitschrift für Physikalische Chemie* **32B,** 447–462; 10.1515/zpch-1936-3239 (1936).

39. Wagner, C. & Hammen, H. Bestimmung des Sauerstoff-Überschußgehaltes der Kupferoxydulphase. *Zeitschrift für Physikalische Chemie* **40B,** 197–206; 10.1515/zpch-1938-4013 (1938).

40. Alt, C. D. *et al.* Quantifying Multiphase SEI Growth in Sulfide Solid Electrolytes. *Joule* **8,** 2755–2776; 10.1016/j.joule.2024.07.006 (2024).

41. Eckhardt, J. K. *et al.* Understanding the Impact of Microstructure on Charge Transport in Polycrystalline Materials Through Impedance Modelling. *J. Electrochem. Soc.* **168,** 90516; 10.1149/1945-7111/ac1cfe (2021).

42. Krauskopf, T. *et al.* Toward a Fundamental Understanding of the Lithium Metal Anode in Solid-State Batteries—An Electrochemo-Mechanical Study on the Garnet-Type Solid Electrolyte $Li_{6.25}Al_{0.25}La_3Zr_2O_{12}$. *ACS Applied Materials & Interfaces* **11,** 14463–14477; 10.1021/acsami.9b02537 (2019).

43. Singh, D. K. *et al.* Non-Linear Kinetics of The Lithium Metal Anode on Li_6PS_5Cl at High Current Density: Dendrite Growth and the Role of Lithium Microstructure on Creep. *Advanced Science* **10,** e2302521; 10.1002/advs.202302521 (2023).

44. Spencer Jolly, D. *et al.* Temperature Dependence of Lithium Anode Voiding in Argyrodite Solid-State Batteries. *ACS Applied Materials & Interfaces* **13,** 22708–22716; 10.1021/acsami.1c06706 (2021).

45. Spencer Jolly, D. *et al.* Sodium/Na β″ Alumina Interface: Effect of Pressure on Voids. *ACS Applied Materials & Interfaces* **12,** 678–685; 10.1021/acsami.9b17786 (2020).

46. Meyer, M., Rickert, H. & Schwaitzer, U. Investigations on the Kinetics of the Anodic Dissolution of Lithium at the Interface Li/Li_3N. *Solid State Ionics* **9-10,** 689–693; 10.1016/0167-2738(83)90315-6 (1983).

47. Eckhardt, J. K. *et al.* Interplay of Dynamic Constriction and Interface Morphology between Reversible Metal Anode and Solid Electrolyte in Solid State Batteries. *ACS Applied Materials & Interfaces* **14,** 35545–35554; 10.1021/acsami.2c07077 (2022).

48. Eckhardt, J. K. *et al.* 3D Impedance Modeling of Metal Anodes in Solid-State Batteries-Incompatibility of Pore Formation and Constriction Effect in Physical-Based 1D Circuit Models. *ACS Applied Materials & Interfaces* **14,** 42757–42769; 10.1021/acsami.2c12991 (2022).

49. Eckhardt, J. K. *et al.* Guidelines for Impedance Analysis of Parent Metal Anodes in Solid-State Batteries and the Role of Current Constriction at Interface Voids, Heterogeneities, and SEI. *Adv Materials Inter* **10**; 10.1002/admi.202202354 (2023).

50. Holm, R. *Electric Contacts* (Springer Berlin Heidelberg, Berlin, Heidelberg, 1967).

51. Boyer, L. Contact Resistance Calculations: Generalizations of Greenwood's Formula Including Interface Films. *IEEE Trans. Comp. Packag. Technol.* **24,** 50–58; 10.1109/6144.910802 (2001).

52. Greenwood, J. A. Constriction Resistance and the Real Area of Contact. *Br. J. Appl. Phys.* **17,** 1621–1632; 10.1088/0508-3443/17/12/310 (1966).

53. Wang, M. J., Choudhury, R. & Sakamoto, J. Characterizing the Li-Solid-Electrolyte Interface Dynamics as a Function of Stack Pressure and Current Density. *Joule* **3,** 2165–2178; 10.1016/j.joule.2019.06.017 (2019).

54. Limon, M. S. R., Duffee, C. & Ahmad, Z. Constriction and Contact Impedance of Ceramic Solid Electrolytes, 2025.

55. Fleig, J. & Maier, J. Finite-Element Calculations on the Impedance of Electroceramics with Highly Resistive Grain Boundaries: I, Laterally Inhomogeneous Grain Boundaries. *J Am Ceram Soc.* **82,** 3485–3493; 10.1111/j.1151-2916.1999.tb02270.x (1999).

56. Zhao, L. *et al.* Imaging the Evolution of Lithium-Solid Electrolyte Interface using operando Scanning Electron Microscopy. *Nature Communications* **16,** 4283; 10.1038/s41467-025-59567-8 (2025).

57. Koerver, R. *et al.* Chemo-Mechanical Expansion of Lithium Electrode Materials - On the Route to Mechanically Optimized All-Solid-State Batteries. *Energy Environ. Sci.* **11,** 2142–2158; 10.1039/C8EE00907D (2018).

58. Otto, S.-K. *et al.* In-Depth Characterization of Lithium-Metal Surfaces with XPS and ToF-SIMS: Toward Better Understanding of the Passivation Layer. *Chem. Mater.* **33,** 859–867; 10.1021/acs.chemmater.0c03518 (2021).

59. Otto, S.-K. *et al.* Storage of Lithium Metal: The Role of the Native Passivation Layer for the Anode Interface Resistance in Solid State Batteries. *ACS Appl. Energy Mater.* **4,** 12798–12807; 10.1021/acsaem.1c02481 (2021).

60. Wang, S. *et al.* Effect of H^+ Exchange and Surface Impurities on Bulk and Interfacial Electrochemistry of Garnet Solid Electrolytes. *Chem. Mater.* **36,** 6849–6864; 10.1021/acs.chemmater.4c00738 (2024).

61. Aguesse, F. *et al.* Investigating the Dendritic Growth during Full Cell Cycling of Garnet Electrolyte in Direct Contact with Li Metal. *ACS Applied Materials & Interfaces* **9,** 3808–3816; 10.1021/acsami.6b13925 (2017).

62. Raj, V. *et al.* Direct Correlation Between Void Formation and Lithium Dendrite Growth in Solid-State electrolytes with Interlayers. *Nature Materials* **21,** 1050–1056; 10.1038/s41563-022-01264-8 (2022).

63. Aota, L. S. *et al.* Grain Boundaries Control Lithiation of Solid Solution Substrates in Lithium Metal Batteries. *Advanced Science,* e2409275; 10.1002/advs.202409275 (2024).

64. Cheng, L. *et al.* Effect of Surface Microstructure on Electrochemical Performance of Garnet Solid Electrolytes. *ACS Applied Materials & Interfaces* **7,** 2073; 10.1021/am508111r (2015).

65. Koerver, R. *et al.* Capacity Fade in Solid-State Batteries: Interphase Formation and Chemomechanical Processes in Nickel-Rich Layered Oxide Cathodes and Lithium Thiophosphate Solid Electrolytes. *Chem. Mater.* **29,** 5574–5582; 10.1021/acs.chemmater.7b00931 (2017).

66. Burton, M. *et al.* The Role of Phosphorous in the Solid Electrolyte Interphase of Argyrodite Solid Electrolytes; 10.26434/chemrxiv-2024-1727n-v2 (2025).

67. Becker, J. *et al.* Microstructure of Lithium Metal Electrodeposited at the Steel|Li_6PS_5Cl Interface in "Anode-Free" Solid-State Batteries. *Adv. Energy Mater.*; 10.1002/aenm.202404975 (2024).

68. Jäckle, M. & Groß, A. Microscopic Properties of Lithium, Sodium, and Magnesium Battery Anode Materials Related to Possible Dendrite Growth. *The Journal of Chemical Physics* **141,** 174710; 10.1063/1.4901055 (2014).

69. Mandal, L. *et al.* Evolution of Interfacial Electro-Chemo-Mechanics between Lithium Metal and Halide Solid Electrolyte. *Chem. Mater.* **36,** 10336–10350; 10.1021/acs.chemmater.4c02307 (2024).

70. Kremer, S. *et al.* A Simple Method for the Study of Heteroionic Interface Impedances in Solid Electrolyte Multilayer Cells Containing LLZO. *ACS Applied Materials & Interfaces* **16,** 44236–44248; 10.1021/acsami.4c07845 (2024).

71. Ortmann, T. *et al.* Kinetics and Pore Formation of the Sodium Metal Anode on NASICON-Type Na 3.4 Zr 2 Si 2.4 P 0.6 O 12 for Sodium Solid-State Batteries. *Adv. Energy Mater.* **13**; 10.1002/aenm.202202712 (2023).

72. Haslam, C. & Sakamoto, J. Stable Lithium Plating in "Lithium Metal-Free" Solid-State Batteries Enabled by Seeded Lithium Nucleation. *J. Electrochem. Soc.* **170,** 40524; 10.1149/1945-7111/accab4 (2023).

73. Harris, C. R. *et al.* Array Programming with NumPy. *Nature* **585,** 357–362; 10.1038/s41586-020-2649-2 (2020).

74. Deiseroth, H.-J. *et al.* Li_7PS_6 and Li_6PS_5X (*X*: Cl, Br, I): Possible Three-Dimensional Diffusion Pathways for Lithium Ions and Temperature Dependence of the Ionic Conductivity by Impedance Measurements. *Zeitschrift anorg allge chemie* **637,** 1287–1294; 10.1002/zaac.201100158 (2011).

75. Chen, S. *et al.* Sulfide Solid Electrolytes for All-Solid-State Lithium Batteries: Structure, Conductivity, Stability and Application. *Energy Storage Materials* **14,** 58–74; 10.1016/j.ensm.2018.02.020 (2018).

3.3. The Electronic Partial Electronic Conductivity of Lithium Halides and their Role in SEI Formation in Solid-State Batteries – Hebb-Wagner-type Measurements (3rd Publication)

In this publication, the importance of controlling and minimizing the partial electronic conductivity to mitigate self-discharge and degradation processes in SSBs is evaluated. The established dc Hebb-Wagner method is used to examine σ_{el} of lithium halides Li*X* (*X* = Cl, Br, and I), being SEI constituents of Li_6PS_5X, from a defect-chemical perspective.

Asymmetric Li|Li*X*|Au configurations were examined at temperatures ranging from 45 to 57.5 °C. EIS was used to assess partial ionic conductivity, while dc Hebb-Wagner experiments provided insights into partial electronic conductivity (σ_{el}). By evaluating Li*X* across a range of lithium activities, their σ_{el} was determined for the first time, highlighting that σ_{el} of SEs varies and cannot be assumed constant for a given temperature. Through the formal derivation of equations (*i.e.*, eq. 28 in Chapter 2.3.iii.) and defect-chemical considerations, the analysis of dc Hebb-Wagner experiments successfully decoupled electronic charge carriers. Additionally, experimental guidelines were outlined for accurately determining σ_{el} in SEs that are susceptible to reduction at low potentials.

This publication provides a comprehensive study that integrates fundamental derivations with precise testing protocols from a defect-chemical perspective. It underscores the critical importance of evaluating the electronic properties of lithium-ion conductors and their influence on the performance and stability of SEs and SEIs. By addressing the existing knowledge gap regarding the partial electronic transport properties of lithium halides, the study significantly advances the understanding of interphase kinetics in relation to their individual constituents.

The experiments presented in this publication were designed and executed by the first author under the supervision of M. T. Elm and J. Janek. M. Stein performed photoluminescence experiments. The first author performed all other experiments and corresponding data analysis with the support of J. Kessler-Kühn. M. Stein and J. K. Eckhardt supported the analysis of photoluminescence spectra and EIS data, respectively, and assisted with scientific discussion. The manuscript was written by the first author and edited by all co-authors.

Reprinted with permission from Christoph D. Alt, Jill Kessler-Kühn, Janis K. Eckhardt, Markus Stein, Sangam Chatterjee, Matthias T. Elm, and Jürgen Janek. The partial electronic conductivity of lithium halides and their role in SEI formation in solid-state batteries – Hebb-Wagner-type measurements, *Solid State Ionics.*, 429, 2025, 116991. DOI: 10.1016/j.ssi.2025.116991. Copyright © 2025 The Authors. Published by Elsevier Inc.

Solid State Ionics 429 (2025) 116991

Contents lists available at ScienceDirect

Solid State Ionics

journal homepage: www.elsevier.com/locate/ssi

The partial electronic conductivity of lithium halides and their role in SEI formation in solid-state batteries – Hebb-Wagner-type measurements☆

Christoph D. Alt [a,b], Jill Kessler-Kühn [a,b], Janis K. Eckhardt [b], Markus Stein [b,c], Sangam Chatterjee [b,c], Matthias T. Elm [b,c,*], Jürgen Janek [a,b,*]

[a] Institute of Physical Chemistry, Justus Liebig University, Heinrich Buff Ring 17, 35392 Giessen, Germany
[b] Center for Materials Research, Justus Liebig University, Heinrich Buff Ring 16, 35392 Giessen, Germany
[c] Institute of Experimental Physics I, Justus Liebig University, Heinrich Buff Ring 16, 35392 Giessen, Germany

ARTICLE INFO

Keywords:
Solid-state batteries
Solid-electrolyte interface
Solid electrolyte
Electronic conductivity
SEI
Hebb-Wagner polarization
Interphase formation

ABSTRACT

In the context of solid-state batteries (SSBs), minimizing the partial electronic conductivity (σ_{el}) of solid electrolytes is essential to minimize self-discharge and degradation processes, ensuring the viability of SSBs. Thus, a precise determination of σ_{el} is of high interest as it varies significantly across the operational range of practical SSBs. Here, ion-blocking Hebb-Wagner polarization measurements are a well-established technique for assessing the partial conductivity of minority charge carriers in solid ion conductors (*i.e.*, σ_{el}). However, measuring σ_{el} of lithium-ion conducting solid electrolytes often yields inaccurate results due to electrochemical reduction reactions at low (reference) potentials. This study provides a comprehensive framework encompassing fundamental derivations, accurate testing protocols, and comprehensive data analysis for determining σ_{el} of lithium-ion conducting solid electrolytes. The partial ionic and electronic conductivities of lithium halides (Li*X*, with *X* = Cl, Br, or I) – components of typical interphases in SSBs – were systematically evaluated over a range of the lithium activity. Pristine Hebb-Wagner cells (*i.e.*, reservoir-free SSBs) exhibit "self-polarization", which we discuss as part of the formal treatment, and cause the material to be probed in the extrinsic region. Our experimental findings offer systematic insight into the electronic properties of lithium halides, extrapolated to room temperature, revealing conductivities in the order of 10^{-9} S cm^{-1} or lower within the tested activity range. These findings deepen the understanding of the role of Li*X* in solid electrolyte interphase formation affecting the performance and stability of SSBs.

1. Introduction

Contrary to popular belief, lithium-ion solid electrolytes (SEs) – similar to oxide-ion conductors – must be regarded as mixed ionic-electronic conductors (MIECs), as their properties are governed by their defect chemistry (*i.e.*, activity-dependent concentrations of point defects) [1]. Oxide-ion conductors have been progressively enhanced through defect chemical modification to boost the partial ionic conductivity (σ_{ion}), control the electronic conductivity (σ_{el}), and ensure compatibility with cathode materials [2,3]. However, lithium-ion conducting SEs have primarily been optimized to compete with liquid electrolytes and to enable advanced solid-state batteries (SSBs), focusing on improving σ_{ion} through structural lattice disorder [4–7]. In contrast, σ_{el} of lithium-ion SEs, however, has been largely ignored, except in a few cases [8,9].

Recently, Shao et al. [9] highlighted that electronic minority defects (which are responsible for σ_{el}) in SEs for SSBs can be decisive at the cell level, while quantifying σ_{el} remains challenging for many relevant electrolytes. Even small electronic conductivities can significantly contribute to self-discharge effects, initiate lithium metal nucleation within the SE microstructure, and accelerate parasitic (*i.e.*, undesired and adverse) side reactions, such as SE degradation and solid-electrolyte interphase (SEI) formation [10–18]. Thus, the remarkable calendar life (exceeding ten years) of lithium phosphorus oxynitride (LiPON) batteries is probably due to their very low σ_{el} (10^{-12} to 10^{-15} S cm^{-1}), which effectively suppresses electronic leakage and interphase formation [19–21]. Only a few lithium-ion SEs, such as garnet-type materials and LiPON, have been reliably characterized for their electronic properties

☆ This article is part of a Special issue entitled: 'Solid State Ionics 100' published in Solid State Ionics.

* Corresponding authors at: Center for Materials Research, Justus Liebig University, Heinrich Buff Ring 16, 35392 Giessen, Germany.
E-mail addresses: matthias.elm@physik.uni-giessen.de (M.T. Elm), juergen.janek@pc.jlug.de (J. Janek).

https://doi.org/10.1016/j.ssi.2025.116991
Received 23 May 2025; Received in revised form 5 July 2025; Accepted 31 July 2025
Available online 8 August 2025
0167-2738/© 2025 Published by Elsevier B.V.

3. Results and Discussion

[22–28].

We like to emphasize – which is often overlooked within SSB research – that σ_{el} of a lithium-ion SE is not constant at a given temperature [29–31]. Rather, σ_{el} is directly linked to the actual thermodynamic state of the SE. Specifically, σ_{el} is controlled by the concentration of electronic defects (*i.e.*, electrons and electron holes), which depends on the local lithium activity (*i.e.*, the lithium chemical potential). Furthermore, the lithium activity is inherently linked to the cell voltage (U_{cell}), which is, in turn, determined by the ratio of lithium activity of both electrodes:

$$U_{cell} = -\frac{1}{F}[\mu_{Li}(\text{cathode}) - \mu_{Li}(\text{anode})] = -\frac{1}{F}\Delta\mu_{Li} = -\frac{R\cdot T}{F}\cdot\ln\frac{a_{Li}(\text{cathode, positive electrode})}{a_{Li}(\text{anode, negative electrode})} \quad (1)$$

where R, T, F, μ_{Li}, and a_{Li} are the ideal gas constant, temperature, Faraday constant, the chemical potential of lithium, and the lithium activity of cathode or anode, respectively. This points out that the applied or measured U_{cell} is intrinsically related to $\Delta\mu_{Li}$ by a factor of $-1/F$.

Conclusively, the mean σ_{el} of a SE employed as a separator changes with the state-of-charge of the SSB cell (Eq. 1). For example, for a Li||$LiNi_xMn_yCo_{1-x-y}O_2$ cell (with a_{Li}(anode, negative electrode) = 1), the activity of lithium within the SE at the cathode side changes by 28 orders of magnitude between the charged ($U_{cell} \approx 4.2$ V) and discharged ($U_{cell} \approx 2.6$ V) state, and the concentration of the electronic defects undergoes a change of about 14 orders of magnitude (see discussion of the defect concentrations below) [29]. Therefore, σ_{el} for SEs in SSBs cannot be considered as constant like its ionic counterpart and changes significantly with a_{Li} and the battery's state-of-charge. To minimize the impact of such large variations in charge carrier concentrations (c_{el}) on the electronic transport properties, effective material design should ensure low electronic mobility (u_{el}) to maintain a sufficiently low σ_{el}, with $\sigma_{el} = F\cdot c_{el}\cdot u_{el}$.

In MIECs, the direct determination of the partial conductivity (and chemical diffusivity) of minority charge carries presents a significant challenge [32]. The Hebb-Wagner method, developed in the 1950s independently by Hebb [33] and Wagner [34–36], marked a pivotal breakthrough in the study of solid-state ionics. It became a widely adopted method for the quantitative analysis of σ_{el} of solid ion conductors, particularly in ion-conducting oxides [37–40]. However, challenges in measuring σ_{el} of various halide or sulfide lithium-ion SEs arise from side reactions and (electro-)chemical instabilities [41–44]. Such degradation reactions alter the material under investigation at the electrodes and induce parasitic ionic currents, impacting conductivity measurements and frequently leading to overestimations of σ_{el}. To the best of our knowledge, no testing protocol has been reported in literature so far to effectively address parasitic side reactions and accurately measure σ_{el} of susceptible SEs.

Therefore, the appropriate selection of measurement parameters and electrode materials is crucial, and these have been carefully chosen in our study. Furthermore, we opted to investigate the binary lithium halides LiX (with X = Cl, Br, or I) for several reasons: (1) LiX are binary ionic salts, making them an ideal model system; (2) LiX are fully reduced compounds and are, therefore, not further reduced in contact with lithium metal, simplifying the selection of electrode materials [45–47]; (3) LiX are known degradation products of reactions involving the extensively studied class of lithium halide and argyrodite SEs (*i.e.*, Li_6PS_5X) [44,48–50]; and (4) our recent results for the transport properties of interphases in SSBs and their constituents highlighted that σ_{el} and the electronic properties of LiX remain largely unexplored [51]. Moreover, LiI is one of the lithium-ion conductors earliest explored in the field of solid-state ionics [52–54], with a few studies reporting σ_{el} of LiI–Al_2O_3 composites [55,56]. Recently, lithium halide compounds have evolved into widely used additives, SE precursors or coating materials to enhance the performance of SSB components [57–69]. Interestingly, as previously noted, their σ_{el} has yet to be investigated.

Therefore, our work emphasizes the critical need to investigate and control the electronic properties of SEs and interphases in SSBs. Accordingly, this paper provides a comprehensive discussion of the experimental method for measuring both ionic and (minority) partial electronic conductivities. We present an effective testing protocol and a detailed analysis of our results to determine σ_{el} of lithium MIECs with moderate to low σ_{ion}, specifically LiCl, LiBr, and LiI. To address this, we discussed and conducted dc Hebb-Wagner measurements under ion-blocking conditions for various temperatures. On the way, we always observed an apparent "self-polarization" of the pristine Hebb-Wagner cells, which is also typical for reservoir-free SSBs and is explained as part of the formal treatment. Our results allow for the identification of electronic charge carriers (*i.e.*, electron or hole conductivity), illustrating the dependence of σ_{el} on a_{Li} (*i.e.*, on U_{cell}). The applicability of this experimental approach to actual SEs and potential (experimental) constraints are thoroughly discussed. Conclusively, the limited knowledge of the electronic properties of lithium-ion conductors is evident, and we hope this study will inspire more focused research in investigating and controlling σ_{el} in SSBs.

1.1. Defect chemistry of lithium halides

For a reliable interpretation of the results obtained from the Hebb-Wagner measurements, it is necessary to consider the defect chemistry of LiX and the dependencies of the ionic and electronic defect concentrations on a_{Li}. The change in defect concentrations as a function of the activity of a specific component of the SE, such as oxygen, lithium, or sodium, is typically depicted in so-called Brouwer diagrams.

Schottky defects are the most probable intrinsic ionic defects in lithium halides (LiX, with X = Cl, Br, or I) [70,71]. Using Kröger-Vink notation [72], the formation of Schottky defects as well as the corresponding equilibrium constant (K_S) (*e.g.*, for LiCl) are given by:

$$\text{nil} \leftrightharpoons V'_{Li} + V^{\bullet}_{Cl} \quad \text{with } K_S = a(V'_{Li})a(V^{\bullet}_{Cl}) \approx [V'_{Li}][V^{\bullet}_{Cl}] \quad (2)$$

whereas the ideal case for the activity $a(i) = \gamma_i \frac{[i]}{c^o}$ is assumed with an activity coefficient $\gamma_i = 1$, c^o is the reference concentration and the square brackets denoting the corresponding defect concentrations. In addition, it is reasonable to assume that the mobility of $V^{\bullet}_{Cl}$ is very low in the temperature range examined in this study (*i.e.*, an anion contribution to σ_{ion} can be neglected). Consequently, σ_{ion} of pure LiX is primarily governed by V'_{Li}.

Furthermore, the presence of electronic defects needs to be considered. The formation and recombination of electrons (e') and electron holes ($h^{\bullet}$) – with the corresponding equilibrium constant (K_{el}) – is described in the ideal case by:

$$\text{nil} \leftrightharpoons h^{\bullet} + e' \quad \text{with } K_{el} = [e'][h^{\bullet}] \quad (3)$$

The lithium exchange at the electrodes follows the equilibrium reaction:

$$Li^{\times}_{Li} \leftrightharpoons Li^0(s) + h^{\bullet} + V'_{Li} \quad (4)$$

with Li^0(s) being lithium metal, and the corresponding equilibrium constant (K_{Li}) given by:

$$K_{Li} = \frac{[V'_{Li}][h^{\bullet}]}{[Li^{\times}_{Li}]}\cdot a_{Li} \Rightarrow K'_{Li} \approx [V'_{Li}][h^{\bullet}]\cdot a_{Li} \quad (5)$$

whereas the expression is simplified by assuming that $[Li^{\times}_{Li}]$ remains quasi-constant.

When exchanging lithium (*i.e.* changing the lithium activity in the

SE), the crystal must remain electrically neutral and charge neutrality is maintained:

$$[e'] + [V'_{Li}] = [V^{\bullet}_{Cl}] + [h^{\bullet}] \quad (6)$$

At the so-called stoichiometric point (SP) with an exact composition of Li*X*, the concentrations of ionic defects as well as of electronic defects equal each other, respectively. Thus, $[V'_{Li}] = [V^{\bullet}_{Cl}]$ and $[e'] = [h^{\bullet}]$. Due to the large bandgap of Li*X* [73], it can be assumed that $K_S \gg K_{el}$. Thus, the number of ionic point defects can be assumed to be independent of a_{Li} and much greater than the number of (intrinsic) electronic defect within the stoichiometric range close to the SP:

$$[V'_{Li}] \approx [V^{\bullet}_{Cl}] \gg [h^{\bullet}], [e'] \quad (7)$$

However, the concentrations of electronic defects strongly depend on a_{Li}, if a_{Li} is changed to either side of the stoichiometric composition. Using Eqs. 3, 5, and 7, these dependencies in the near-stoichiometric region can be expressed as:

$$[h^{\bullet}] = \frac{K'_{Li}}{[V'_{Li}]} \frac{1}{a_{Li}} \propto a_{Li}^{-1} \text{ and } [e'] = \frac{[V'_{Li}] K_{el}}{K'_{Li}} a_{Li} \propto a_{Li}^{+1} \quad (8)$$

At lower (or higher) a_{Li} far from the SP, the concentration of $h^{\bullet}$ (e') approaches the concentration of ionic defects and even exceeds $[V'_{Li}]$ ($[V^{\bullet}_{Cl}]$). Thus, a more appropriate approximation for the electroneutrality equation (Eq. 6) is ignoring the corresponding minority defects (*i.e.*, $V^{\bullet}_{Cl}$ and e', or V'_{Li} and $h^{\bullet}$, respectively):

$$\begin{aligned} [V'_{Li}] &\approx [h^{\bullet}] \text{ for low } a_{Li} \\ [V^{\bullet}_{Cl}] &\approx [e'] \text{ for high } a_{Li} \end{aligned} \quad (9)$$

Combining Eqs. 2, 3, 5, and 9 provides the dependencies of electronic defect concentrations for low (or high) a_{Li} – in the so-called extrinsic (non-stoichiometric) region:

$$\begin{aligned} [h^{\bullet}] &= \sqrt{\frac{K'_{Li}}{a_{Li}}} \propto a_{Li}^{-½} \text{ for low } a_{Li} \\ [e'] &= \sqrt{\frac{K_S \cdot K_{el}}{K'_{Li}} a_{Li}} \propto a_{Li}^{+½} \text{ for high } a_{Li} \end{aligned} \quad (10)$$

The dependencies of the defect concentrations $c_{defects}$ (*i.e.*, of the charge carriers) near the SP and within the extrinsic region are summarized in Fig. 1, with α denoting the characteristic exponent ($\alpha = \pm 1$ or $\pm 1/2$). Fig. 1A shows the computed Brouwer diagram for the pure (*i.e.*, intrinsic) material. Fig. 1B includes the effect of an oxygen impurity level. The corresponding derivation of the Brouwer diagram is provided in Section A of the Supporting Information (SI).

1.2. DC Hebb-Wagner polarization

The following section briefly elaborates the basic principle and experimental requirements for Hebb-Wagner measurements on lithium-ion SEs, before we discuss the formal treatment of the polarization process. In Hebb-Wagner measurements, the conductivity of minority charge carriers (*i.e.*, σ_{el} of ion conductors) of a material can be quantified by applying a dc voltage in asymmetric cells. Therefore, a selectively-blocking (*i.e.*, ion-blocking) electrode (BE) and a reversible (*i.e.*, non-blocking) electrode with a fixed potential (RE) are required to distinguish between ionic and electronic contributions (see Fig. 2). The latter facilitates the reversible exchange of ionic and electronic charge carriers, while maintaining a constant activity and chemical potential. Depending on the direction of polarization, a steady state is achieved [74], where the net flux of lithium-ions is zero. Consequently, the steady state current density $i_{el,ss}$ is carried exclusively by electronic charge carriers and can be analyzed to determine σ_{el} of the material.

For an accurate quantification of σ_{el}, it is crucial to ensure not only control over external parameters (*e.g.*, temperature), but also compatibility of materials to prevent side reactions with the electrodes [75–77]. Therefore, the potential of both electrodes, particularly the RE, must be within the stability range of the material to prevent parasitic currents due to degradation [77]. Furthermore, the applied voltage must remain below the material's decomposition voltage. In the context of lithium-ion SEs, which are often susceptible to reduction at low potentials, many studies have been improperly conducted by using two BEs or lithium metal as the RE [78–82]. Since the materials investigated in our study are fully reduced [45–47], lithium metal can be employed as RE, while a gold electrode serves as BE.

The following section briefly outlines the concise formal description of the Hebb-Wagner method for steady state polarization under ion-blocking conditions of lithium-ion SEs [33–36]. Notably, the dependence of σ_{el} on a_{Li} is also elaborated in this section. Systematic derivations for oxide-ion conductors, extensively discussed in literature [39,40,74], can be readily extended from oxide and lithium to other solid ion conductors, such as sodium or potassium SEs.

Considering the equilibrium condition for the redox reaction ($Li^0 \rightleftharpoons Li^+ + e'$), the local gradient of the chemical potential of lithium ($\nabla \mu_{Li}$) is given by:

$$\nabla \mu_{Li} = \nabla \tilde{\mu}_{Li^+} + z_{Li^+} \cdot \nabla \tilde{\mu}_{el} = \nabla \tilde{\mu}_{Li^-} + \nabla \tilde{\mu}_{el} \quad (11)$$

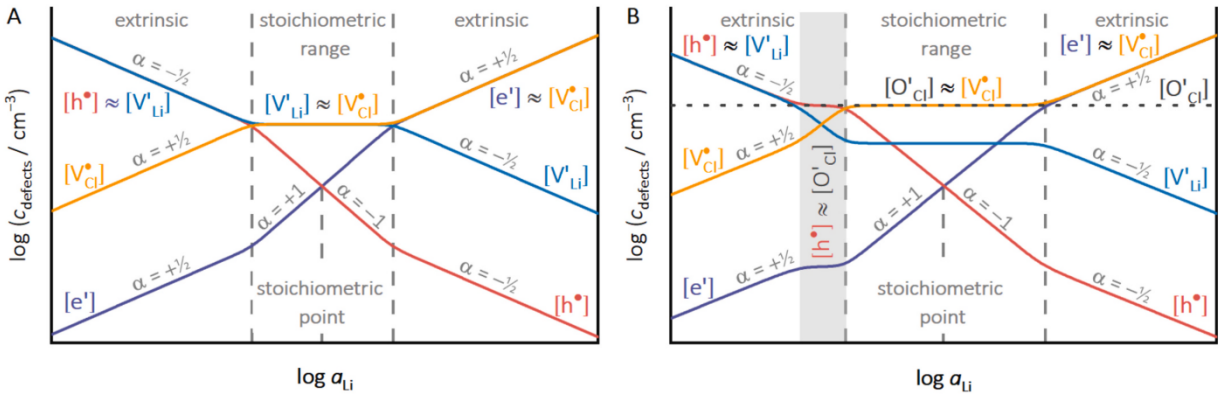

Fig. 1. Dependence of electron, electron hole, lithium and chlorine vacancy concentrations on a_{Li} shown for pure (undoped) Li*X* (A) and in the presence of an oxygen impurity $[O'_{Cl}]$ (B), with the corresponding doping region depicted in gray. The derivation of (B) is provided in Section A of the SI. The characteristic exponent α is given for both the stoichiometric and extrinsic region. At the stoichiometric point, the concentration for electron holes equals the one for electrons. Note that both plots are computed and the units shown are arbitrary.

3. Results and Discussion

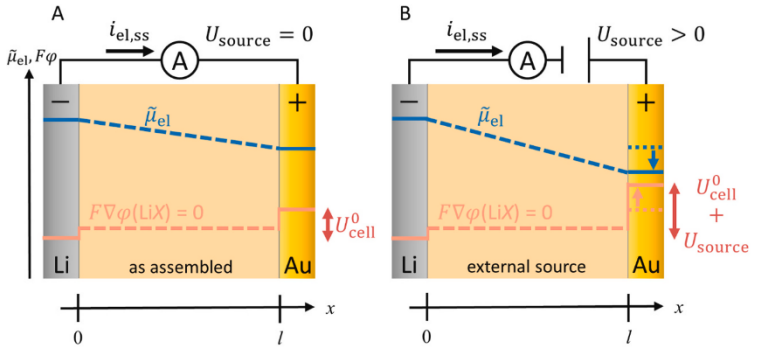

Fig. 2. Hebb-Wagner cell configuration for measuring σ_{el} of lithium-ion solid conductors, using one reversible lithium metal electrode (RE) and one ion-blocking gold electrode (BE) – shown in the initial (as assembled) state (A) and under an applied external potential (*i.e.*, U_{source}) (B). In both cases, the electronic current ($i_{el,ss}$) is conducted, while the ionic current is suppressed by the BE. x is the spatial coordinate within the material of thickness l. In steady state, $\nabla\phi$ within the polarized SE is zero, as any potential difference across the material is compensated by the redistribution of mobile charge carriers. For the sake of simplicity, the trend of $\tilde{\mu}_{el}$ within LiX is linearized. The real profile of $\tilde{\mu}_{el}$ depends on the specific defect structure and will not be linear.

where $\tilde{\mu}_{Li^+}$ and $\tilde{\mu}_{el}$ are the electrochemical potential of lithium ions and electrons, respectively, and $z_{Li^+} = 1$ is the charge number of lithium ions. By carefully controlling the direction of polarization (*i.e.*, applying a positive $U_{cell} > 0$ at the BE relative to the RE) and, thus, the electrochemical potential of the lithium ions ($\nabla\tilde{\mu}_{Li^+}$), lithium ions migrate towards the RE (j_{Li^+}). This creates a gradient of the lithium distribution within the material (*i.e.*, depletion near the BE). In the initial and transient period, the flux of lithium ions within the SE is given by:

$$j_{Li^+} = -\frac{\sigma_{ion}}{(z_{Li^+}F)^2}\nabla\tilde{\mu}_{Li^+} \tag{12}$$

To counterbalance the gradient in lithium distribution, a diffusion flux is established and – over time – the resulting net flux of lithium ions reaches a fully compensated steady state (denoted "ss") and becomes zero. Accordingly, when $j_{Li^+,ss} = 0$, $\nabla\tilde{\mu}_{Li^+}$ becomes zero, which simplifies Eq. 11 to:

$$\nabla\tilde{\mu}_{el,ss} = \nabla\mu_{Li,ss} \Leftrightarrow \frac{d\tilde{\mu}_{el,ss}}{dx} = \frac{d\mu_{Li,ss}}{dx} \tag{13}$$

with x being the spatial coordinate within the material for one-dimensional transport. In our study, a waiting period of 12 h was applied for each polarization step to allow for steady state conditions to be established [74]. We like to add that $\nabla\tilde{\mu}_{el,ss} = \nabla\mu_{Li,ss}$ follows from the assumption, that the concentration of lithium ions does not change as the ionic fluxes compensate each other and, thus, $\nabla\tilde{\mu}_{Li^+,ss} \cong 0$. This also implies that the polarized SE is effectively field-free ($\nabla\phi \cong 0$) at steady state, since any potential difference across the material is already compensated by the redistribution of mobile charge carriers and sufficient high σ_{ion}. Thus, any electron transport occurring in the polarized state is exclusively driven by their concentration gradient.

Notably, the effective voltage U_{cell} between the two electrodes consists of two components: the intrinsic cell voltage in the absence of an externally applied voltage, denoted as U^0_{cell} (Fig. 2A), and the voltage contribution applied by the external source U_{source} (Fig. 2B). The intrinsic cell voltage U^0_{cell}, hereafter also referred to as "self-polarization", arises from the use of two different electrode materials: a fully reversible RE (*i.e.*, lithium metal), and an ion-blocking, electronically reversible BE (*i.e.*, gold). As a result, distinct $\tilde{\mu}_{el}$ are established for each electrode, which define U^0_{cell} (Eq. 14). At the RE, the reversible contact ensures that $\tilde{\mu}_{el}$(RE) is well-defined by μ_{Li} of lithium metal (under steady state conditions with $\nabla\tilde{\mu}_{Li^+} = 0$). Conversely, the Au|Li$X$ interface is solely electronically equilibrated, with the Fermi level in LiX fixed by the Fermi level of the BE material (*i.e.*, its work function). Therefore, both $\tilde{\mu}_{el}$(BE) as well as μ_{Li}(BE) are governed by the electronic properties of the BE material (under the same condition of $\nabla\tilde{\mu}_{Li^-} = 0$). Typically, $\tilde{\mu}_{el}$(BE) is positive relative to $\tilde{\mu}_{el}$(RE) and differs significantly, resulting in a distinct $U^0_{cell} > 0$. For a given BE, U^0_{cell} will be reproducible relative to the lithium metal RE.

An external voltage source U_{source} can be applied to modulate U_{cell} within a specific voltage range, therefore adjusting $\tilde{\mu}_{el}$(BE) and the electric potential at the BE (ϕ(BE)), as well as further lowering μ_{Li}(BE) and a_{Li}(BE) (see Eq. 1).

$$\begin{aligned} U_{cell} = \phi(BE) - \phi(RE) = U^0_{cell} + U_{source} &= -\frac{\tilde{\mu}_{el}(BE) - \tilde{\mu}_{el}(RE)}{F} + U_{source} \\ &= -\frac{\tilde{\mu}'_{el}(BE) - \tilde{\mu}_{el}(RE)}{F} \end{aligned} \tag{14}$$

with the electron electrochemical potential $\tilde{\mu}'_{el}$ as well as lithium activity a'_{Li} at the BE altered by the externally applied voltage U_{source}.

In the steady state ($j_{Li^+,ss} = 0$), the electric current density through the sample is solely carried by the electronic species ($i_{ss} = i_{el,ss}$). Consequently, the molar flux $j_{el,ss}$ of electronic charge carriers (in mol cm^{-2} s^{-1}) between the two electrodes can be expressed by:

$$\begin{aligned} j_{el,ss}(x) &= -\frac{1}{(z_{el}\cdot F)^2}\cdot\sigma_{el}(x)\cdot\frac{d\tilde{\mu}_{el}(x)}{dx} \Leftrightarrow \\ j_{el,ss}\left(\mu_{Li}\right) &= -\frac{1}{l\cdot F^2}\cdot\int_{\mu_{Li}(RE)}^{\mu_{Li}(BE)}\sigma_{el}(\mu_{Li})\cdot d\mu_{Li} \end{aligned} \tag{15}$$

and the current density $i_{el,ss}$ results as

$$i_{el,ss} = z_{el}\cdot F\cdot j_{el,ss} = \frac{1}{l\cdot F}\cdot\int_{\mu_{Li}(RE)}^{\mu_{Li}(BE)}\sigma_{el}(\mu_{Li})\cdot d\mu_{Li} \tag{16}$$

Here, σ_{el} represents the combined contributions of hole (p) and electron (n) transport, while l denotes the sample thickness and z_{el} the charge number of electrons ($z_{el} = -1$). Consequently, σ_{el} is a function of μ_{Li} under steady state conditions, and thus, an averaged electronic conductivity describes the electronic transport through the polarized electrolyte.

Integrating Eq. 13 across the sample (Fig. 1) and using Eq. 14, it follows:

$$\begin{aligned} \int_{\mu_{Li}(RE)}^{\mu_{Li}(BE)} d\mu_{Li} &= \mu_{Li}(BE) - \mu_{Li}(RE) = \Delta\mu_{Li} \\ \int_{\tilde{\mu}_{el}(RE)}^{\tilde{\mu}_{el}(BE)} d\tilde{\mu}_{el} &= \tilde{\mu}_{el}(BE) - \tilde{\mu}_{el}(RE) = \Delta\tilde{\mu}_{el} \end{aligned} \tag{17}$$

$$\Delta\mu_{Li} = \Delta\tilde{\mu}_{el} = -F{\cdot}U_{cell} \tag{18}$$

At this point, any occurring overvoltage at the BE is neglected [38,76]. It is evident, that μ_{Li}(BE) is adjusted when a voltage is applied, as μ_{Li}(RE) remains fixed in Hebb-Wagner configurations.

Differentiation of Eq. 16 with respect to μ_{Li}(BE) and applying Eq. 18, yields the expression for σ_{el} at the BE:

$$\sigma_{el}[\mu_{Li}(BE)] = F{\cdot}l{\cdot}\frac{di_{el,ss}}{d\mu_{Li}(BE)} = -l{\cdot}\frac{di_{el,ss}}{dU_{cell}} \tag{19}$$

As a result, the steady state current density $i_{el,ss}$ is a function of U_{cell} and, consequently, σ_{el}(BE) can be determined from the slope $di_{el,ss}/dU_{cell}$ in a direct manner.

Assuming that the electronic defect mobilities are constant and independent from the electron concentration (*i.e.*, with respect to μ_{Li}) the electron and electron hole conductivities (σ_n and σ_p) follow a power law given by the variation of the electron and electron hole concentrations with respect to a_{Li}: $\sigma_n = \sigma_n^0{\cdot}a_{Li}^{\alpha}$ and $\sigma_p = \sigma_p^0{\cdot}a_{Li}^{-\alpha}$. Here, σ_i^0 denotes the respective partial conductivities for $a_{Li} = 1$ and α is a characteristic exponent associated with the redox reaction at the RE, as derived in the Defect Chemistry Section (Eqs. 8 and 10) [83].

The conductivities can be related to the lithium chemical potential by rearranging the general equilibrium relation between μ_{Li} and a_{Li}: $\mu_{Li} = \mu_{Li}^0 + RT{\cdot}\ln a_{Li}$, where μ_{Li}^0 is the chemical (standard) potential of lithium metal:

$$\sigma_n = \sigma_n^0{\cdot}\exp\left[\frac{\alpha(\mu_{Li}-\mu_{Li}^0)}{RT}\right] \text{ and } \sigma_p = \sigma_p^0{\cdot}\exp\left[-\frac{\alpha(\mu_{Li}-\mu_{Li}^0)}{RT}\right] \tag{20}$$

Combining Eqs. 16, 18 and 20 and considering that $\sigma_{el} = \sigma_n + \sigma_p$, the final Hebb-Wagner relation (Eq. 21) is derived by integration:

$$i_{el,ss} = \frac{RT}{\alpha lF}\left(\sigma_n^0\left[\exp\left(-\frac{\alpha FU_{cell}}{RT}\right)-1\right]+\sigma_p^0\left[1-\exp\left(+\frac{\alpha FU_{cell}}{RT}\right)\right]\right) \tag{21}$$

Eq. 21 describes the relationship between current density $i_{el,ss}$ and U_{cell}, enabling the separation of electron and electron hole contribution, when measuring the steady state current density $i_{el,ss}$. Here, the plateau in the $i_{el,ss}$–U_{cell} curve represents the n–p transition between the two regimes, where the current shifts from being primarily carried by electrons to hole-dominated transport – going from negative to positive U_{cell}. It was thoroughly elaborated that σ_{el} depends on a_{Li} and, consequently, μ_{Li}, both of which are modulated by the cell voltage U_{cell}.

In accordance with Eq. 21, $i_{el,ss} = 0$ at $U_{cell} = 0$ and $i_{el,ss} < 0$ for $U_{cell} > 0$, as depicted in Fig. 2, where $i_{el,ss}$ flows in negative x-direction. When the electrochemical cell is connected to an external voltage source and a positive voltage is applied, the voltage drops across the cell (*i.e.*, ϕ increases from the lithium metal anode to the gold cathode). Thus, the net internal voltage drops in the negative direction, which in turn drives a negative current within the cell. In our experimental setup, the BE and RE were configured as the working and counter electrodes, respectively. Under this configuration, a positive voltage applied by the potentiostat yields a positive measured current. This convention is properly accounted for in our data analysis.

Due to the "self-polarization" of our cells (caused by the two different electrodes), U_{cell} must be corrected by U_{cell}^0, to isolate the change in μ_{Li} by the external voltage U_{source}, leading to:

$$i_{el,ss} = \frac{RT}{\alpha lF}\left(\sigma_n^0\left[\exp\left(-\frac{\alpha F(U_{cell}-U_{cell}^0)}{RT}\right)-1\right] + \sigma_p^0\left[1-\exp\left(+\frac{\alpha F(U_{cell}-U_{cell}^0)}{RT}\right)\right]\right) \tag{22}$$

In our study, Eq. 22 is utilized to analyze $i_{el,ss}$ as a function of the external voltage (*i.e.*, $U_{source} = U_{cell} - U_{cell}^0$) to determine electron and electron hole conductivities, with U_{cell}^0 serving as a fitting parameter. We like to note that the voltage measured initially at the Hebb-Wagner cells, when no external voltage is yet applied, has to the best of our knowledge not been discussed in literature yet. Therefore, it will be part of a follow-up study.

2. Results and discussion

2.1. Partial ionic conductivity – impedance spectroscopy

The lithium-ion conductivity of the halides was determined from electrochemical impedance spectroscopy (EIS) after equilibration at each temperature and prior to initiating polarization steps. An ion-blocking configuration Li|LiX|Au (X = Cl, Br, or I) was used. The impedance spectra recorded of each lithium halide are provided in Fig. S1 (Section B, SI). The spectra show one semicircle in the high frequency region, which is attributed to the ionic transport through the sample. Analysis of the spectra allows the determination of the ionic resistance R of the respective material. Using the geometric parameters (sample thickness l and electrode area A), σ_{ion} can be calculated:

$$\sigma_{ion} = \frac{1}{R}\frac{l}{A} \tag{23}$$

The temperature-dependence of $\sigma_{ion}(T)$ is:

$$\sigma_{ion}(T) = \frac{\sigma_0}{T}\exp\left(-\frac{E_A}{k_B T}\right) \tag{24}$$

The activation energy E_A and the exponential pre-factor σ_0 were determined by linear regression from the slope and intercept of $\ln(\sigma_{ion}{\cdot}T)$ plotted *vs.* $1/T$. The corresponding Arrhenius plot for temperatures T ranging from 45 to 57.5 °C is shown in Fig. 3.

Our data allow for the estimation of room-temperature values of σ_{ion} for LiCl, LiBr, and LiI, which are approximately $\sigma_{ion} = (0.2 \pm 0.1)$, (2.4 ± 1.2), and (24 ± 6) nS cm^{-1} (25 °C), respectively. These values are consistent with literature, aligning with the reported order of magnitude for each lithium halide at room temperature (*i.e.*, 10^{-11} to 10^{-9} S cm^{-1} for LiCl, 10^{-9} S cm^{-1} for LiBr, and 10^{-8} S cm^{-1} for LiI) [54,84–87]. The determined E_A values range from 0.5 to 0.66 eV.

Haven [70] investigated the intrinsic ionic transport-relevant properties (specifically, lithium vacancy concentration and mobility) of single-crystalline lithium halides doped with different concentrations of

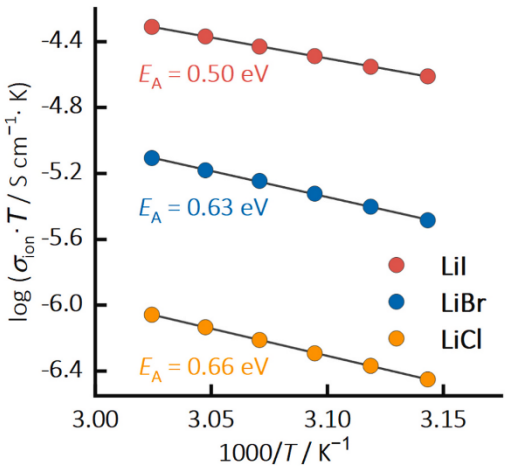

Fig. 3. Arrhenius representation of σ_{ion} for LiCl, LiBr, and LiI, multiplied by the absolute temperature T as a function of $1000/T$ in the temperature range of 45 to 57.5 °C. It was derived from impedance spectra recorded prior to Hebb-Wagner measurements in an ion-blocking configuration Li|LiX|Au, where X represents Cl, Br, or I.

magnesium halides more than 70 years ago. For the pure single crystals, he found significantly higher E_A values (*i.e.*, 1.47, 1.29, and 1.05 eV for LiCl, LiBr, and LiI). The reason is that ion transport in pure solid ion conductors relies on point defect disorder and not on structural disorder of a whole sublattice. E_A comprises then a contribution from the migration enthalpy (ΔH_{mig}) of lithium vacancies and the Schottky defect formation enthalpy (ΔH_F), following the relation: $E_A = \Delta H_{mig} + \Delta H_F/2$. By systematically changing the concentration of magnesium halide, Haven was able to determine the migration enthalpy of the lithium vacancies. As magnesium acts as a (vacancy) donor in lithium halides, the vacancy concentration is fixed by the doping concentration and E_A only comprises ΔH_{mig}. The ΔH_{mig} values (*i.e.*, 0.41, 0.39, and 0.38 eV for LiCl, LiBr, and LiI) obtained for the single crystals are comparable to E_A values obtained in this study, indicating that the vacancy concentration in our samples is also fixed by impurities. The slight increase of E_A of our samples is attributed to their polycrystalline nature (*i.e.*, the presence of grain boundaries). The measured E_A values in our study agree well with findings by Poulsen et al. [54], Mercier et al. [85], Schlaikjer et al. [88] (for polycrystalline LiI), and Jackson et al. [86] (for single-crystalline LiI), as well as Sharon et al. [84] (for polycrystalline LiCl). Solely, our value for polycrystalline LiBr (0.63 eV) is slightly higher than that reported by Mercier et al. [85] (0.48 eV). The assumption of a high lithium vacancy concentration fixed by impurities is also supported when comparing Haven's data to our results, as σ_{ion} of our (commercial) materials is significantly higher, differing by several orders of magnitude. Furthermore, additional evidence for the presence of impurities within Li*X* is provided by photoluminescence (PL) measurements (Fig. S2, Section C, SI) revealing transitions between energy levels of defect states within the band gap of the material. X-ray photoelectron spectroscopy (XPS) revealed Li_2O impurities within LiCl (Fig. S3, Section D, SI). It should be noted, however, that oxygen impurities act as acceptor dopants by generating additional chlorine vacancies, rather than enhancing σ_{ion} through the formation of lithium vacancies.

To explore σ_{ion} in more detail, we further revisited Haven's data for LiCl, LiBr, and LiI in order to estimate the lithium vacancy mobility u_{ion} of our polycrystalline materials. The temperature-dependence of $u_{ion}(T)$ is given by:

$$u_{ion}(T) = \frac{u_0}{T}\exp\left(-\frac{\Delta H_{mig}}{k_B T}\right) \tag{25}$$

As the exponential pre-factor u_0 only depends on properties of the crystal lattice, such as lattice constant and attempt frequency, it can be estimated from the data reported by Haven. The vacancy mobility $u_{ion}(T)$ of our polycrystalline samples can then be calculated using Eq. 25 and ΔH_{mig} given by the E_A values from Fig. 3. Due to the higher ΔH_{mig} of our polycrystalline samples, the calculated u_{ion} values for the tested temperature range are evidently lower (by a few orders of magnitude) than the estimated values from Haven's data for single-crystalline material. Nevertheless, our results enable a comparison of u_{ion} with reported values for LiI. Our estimate of $1 \cdot 10^{-8}$ cm^2 V^{-1} s^{-1} (at 28 °C) is lower than the $3 \cdot 10^{-7}$ cm^2 V^{-1} s^{-1} at 28 °C reported by Schlaikjer et al. [88] for polycrystalline material with $\Delta H_{mig} = 0.43$ eV. This indicates that u_{ion} is likely decreased by the presence of grain boundaries in our polycrystalline pelletized materials with volumetric mass densities of approximately 86 %, 88 %, and 89 % for LiCl, LiBr, and LiI, respectively.

The extrinsic lithium vacancy (number) density n_{ex}, probably arising from impurities, can be estimated using the measured σ_{ion} and estimated u_{ion} through the following relation:

$$\sigma_{ion}(T) = z_{Li^+} \cdot e \cdot u_{ion}(T) \cdot n_{ex} \tag{26}$$

Here, e is the elementary charge and $z_{Li^+} = 1$ is the charge number of lithium ions. In our study, n_{ex} is approximately 10^{19} to 10^{20} cm^{-3} for each lithium halide. This value is several orders of magnitude higher than the intrinsic carrier concentration reported by Haven for undoped LiCl single crystals [70], consistent with the assumption that σ_{ion} is dominated by extrinsic defects caused by impurities. The calculated exponential pre-factors (σ_0, u_0, and n_{ex}) and $\Delta H_{mig} = E_A$ of the LiCl, LiBr, and LiI pellets characterized are summarized in Table S1 (Section E, SI).

2.2. Partial electronic conductivity – Hebb-Wagner measurements

Hebb-Wagner measurements were performed for each lithium halide (*i.e.*, LiCl, LiBr, and LiI) using an ion-blocking configuration Li|Li*X*|Au in order to determine σ_{el}. After equilibration at each temperature and initial EIS steps, a positive voltage (U_{cell}) relative to the RE was applied to the BE, as described in the Experimental Section. U_{cell} was gradually increased to adjust a_{Li} and, thus, μ_{Li} of the BE. It is worth noting that the voltage U_{cell} comprises the applied voltage from the external source U_{source} (*i.e.*, $U_{cell} = U^0_{cell} + U_{source}$), as described in Eq. 14. To allow for steady state conditions [74], a waiting period of 12 h was applied for each polarization step. Due to the polarization, lithium ions migrate towards the RE, balanced by a diffusion flux driven by the resulting lithium concentration gradient. Accordingly, the recorded steady state current density is solely carried by electronic charge carriers ($i_{ss} = i_{el,ss}$). As described in the Experimental Section, U_{cell} was precisely controlled between the OCV and the theoretical decomposition voltage (U_{decomp}) of the respective lithium halide to prevent parasitic currents from degradation reactions.

The determined steady state current densities ($i_{el,ss}$ *vs.* U_{cell}) of LiCl, LiBr, and LiI are presented in Fig. 4 for temperatures ranging from 45 and 57.5 °C. The recorded polarization profiles are provided in Fig. S4 (Section F, SI).

First, $i_{el,ss}$ of LiCl (Fig. 4A) exhibits three distinct regimes with increasing applied voltage: (*i*) a slight linear increase at low voltages, (*ii*) a quasi-plateau near ~3.2 V, and (*iii*) a pronounced exponential rise at higher voltages. The latter marks that hole conduction becomes dominant over electron conduction ($\sigma^0_p \gg \sigma^0_n$). Under these conditions, Eq. 22 can be simplified to:

$$i_{el,ss} = \frac{R \cdot T}{F} \cdot \frac{\sigma^0_p}{\alpha \cdot l}\left[1 - \exp\left(+\frac{\alpha \cdot F \cdot (U_{cell} - U^0_{cell})}{R \cdot T}\right)\right] \tag{27}$$

Due to the observed "self-polarization" in pristine cells, we assume that the applied potential indeed probes the extrinsic region of the material. Consequently, we set the characteristic exponent α to ½ which allows us to accurately fit the experimental data. It should be noted that a satisfying description of the experimental data cannot be achieved using $\alpha = 1$ for the intrinsic region, clearly indicating that the extrinsic regime of the material is probed. Using this approach, $i_{el,ss}$ for LiCl was fitted across all temperatures with Eq. 27 allowing the determination of the temperature-dependent σ^0_p.

As the applied potential probes the extrinsic region of the material, the observed slight increase of $i_{el,ss}$ at low voltages and the quasi-plateau does not correspond to the intrinsic n–p transition described by Eq. 21. Instead the slight increase of $i_{el,ss}$ can be explained by considering the presence of donor impurities. As revealed by XPS (Fig. S3, Section D, SI), Li_2O is present as a minor impurity phase in the tested LiCl with oxygen acting as donor defect in LiCl. Accordingly, as shown in Fig. 1B, an oxygen impurity level pins $[h^\bullet]$ that compensates the defect concentration of oxygen $[O'_{Cl}]$ within a certain voltage range (depicted in gray) between the intrinsic and extrinsic region. Then, the corresponding Brouwer diagram in Fig. 1B (transformed to voltage U on the x-axis in Fig. S5A, Section G, SI) reveals an additional plateau with a constant $[h^\bullet]$ at high voltages (*i.e.*, low a_{Li}). Assuming constant mobilities the steady state current $i_{el,ss}$ as a function of U_{cell} can be calculated by integrating the electronic defect concentrations using Eq. 16. The calculated curves, shown in Fig. S5B, exhibit a distinct change in the slope of $\log(i_{el,ss})$ marking the transition from the intrinsic to the extrinsic conduction regime. The corresponding hole current density $i_{h,ss}$ is depicted in Fig. S5C. A magnified view in Fig. S5D highlights a linear increase in $i_{h,ss}$

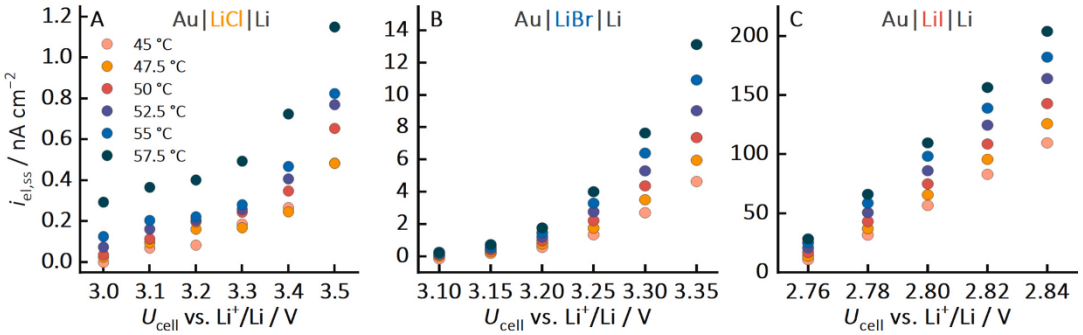

Fig. 4. $i_{el,ss}$ as a function of U_{cell} for LiCl (A), LiBr (B), and LiI (C), derived from Hebb-Wagner measurements in an ion-blocking configuration Li|LiX|Au, where X represents Cl, Br, or I. The temperature T was gradually increased from 45 to 57.5 °C. The recorded polarization profiles are provided in Fig. S4 (Section F, SI).

over the voltage range where a defect level pins [h$^\bullet$]. This linear region is followed by an exponential increase in current as the system enters the extrinsic regime, closely reflecting the experimental behavior observed in Fig. 4A. Accordingly, Eq. 27 provides an appropriate fit at higher voltages, as illustrated by the dotted blue line in Fig. 4D.

For LiBr (Fig. 4B), $i_{el,ss}$ only shows a primarily exponential increase with voltage, again consistent with dominant hole conduction ($\sigma_p^0 \gg \sigma_n^0$). Again, we apply Eq. 27 with $\alpha = ½$, assuming the extrinsic region is probed. In contrast to LiCl, no distinct plateau is observed for LiBr at low voltages.

Fig. 5 shows exemplary fits of $i_{el,ss}$ for LiCl (left) and LiBr (right) at 50 and 52.5 °C, using Eq. 27 and $\alpha = ½$. The complete set of fits for LiCl and LiBr at each temperature is provided in Figs. S6 and S7 (Section H, SI).

The fitting results for σ_p^0 as well as the fitting parameter U_{cell}^0 are summarized in Fig. 6 as a function of inverse temperature. To ensure accurate data fitting, linear trends of the parameters were used as an additional fitting constraint. The data allow for the estimation of $\sigma_p^0 = (4 \pm 2) \cdot 10^{-15}$ S cm^{-1} for LiCl as well as $\sigma_p^0 = (6 \pm 3) \cdot 10^{-15}$ S cm^{-1} for LiBr at room temperature (25 °C). In addition, from these findings the total electronic conductivity $\sigma_{el} = \sigma_h$ for pure LiX at room-temperature can be estimated, spanning from $2 \cdot 10^{-16}$ S cm^{-1} to $8 \cdot 10^{-11}$ S cm^{-1} for LiCl (25 °C) as well as from $1 \cdot 10^{-11}$ S cm^{-1} to $2 \cdot 10^{-9}$ S cm^{-1} for LiBr (25 °C) within the voltage ranges investigated.

On a first view, the σ_{el} values at room temperature may appear quite low. However, given the large electronic band gap of halides – typically exceeding 4 eV [73] – the electronic conductivity measured in this study is significantly higher than anticipated. In a pure halide (*i.e.*, free of impurities), σ_{el} primarily results from electrons thermally excited from the valence band to the conduction band. Assuming parabolic bands, the intrinsic electron density (n_i) in the conduction band, which contributes to σ_{el}, can be estimated:

$$n_i = n_{eff} \exp\left(-\frac{E_g}{2k_B T}\right) = 2\left(\frac{k_B T}{2\pi\hbar^2}\right)^{\frac{3}{2}} \left(m^*_{e,DOS} m^*_{h,DOS}\right)^{\frac{3}{4}} \exp\left(-\frac{E_g}{2k_B T}\right) \quad (28)$$

where $m^*_{e,DOS}$ and $m^*_{h,DOS}$ represent the density of states effective masses of electrons and holes, respectively, k_B is the Boltzmann constant, $\hbar$ is the reduced Planck constant, and E_g is the band gap. Using values derived by density functional theory (DFT) for the effective masses (*i.e.*, $m^*_{e,DOS} = 1.15\, m_e$ and $m^*_{h,DOS} = 4.12\, m_e$) [73] of LiCl along with a band

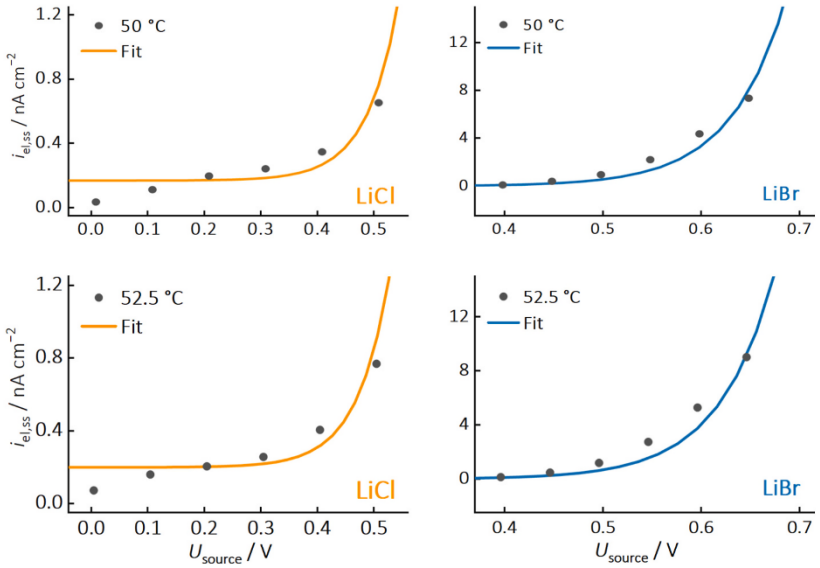

Fig. 5. Exemplary fits of $i_{el,ss}$ as a function of U_{source} for LiCl (left) and LiBr (right) at 50 and 52.5 °C in an ion-blocking configuration Li|LiX|Au (see Fig. 4). Fitting was performed using Eq. 27 with $\alpha = ½$. The voltage U_{cell} was gradually increased by U_{source}, while the temperature T was varied between 45 and 57.5 °C. The complete set of fits for each temperature for LiCl and LiBr is provided in Figs. S6 and S7 (Section H, SI). Fitting parameters and results are given in Fig. 6.

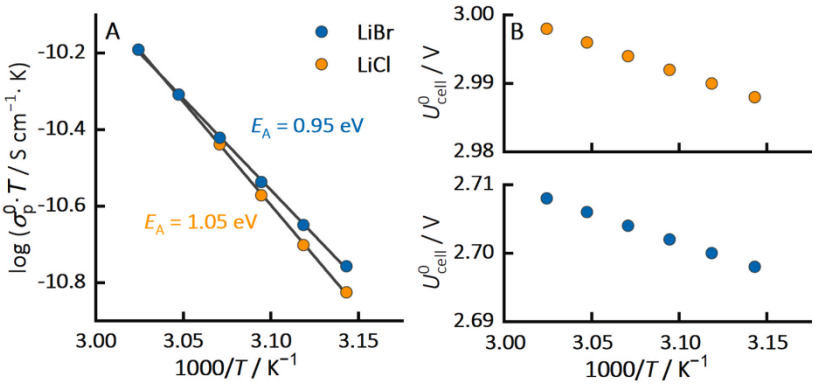

Fig. 6. σ_p^0 (A) and U_{cell}^0 (B) as a function of 1000/T for LiCl and LiBr derived from fitting $i_{el,ss}$ (in Fig. 4A and B). Refer to Figs. S6 and S7 (Section H, SI) for individuals fits of LiCl and LiBr. The corresponding E_A are derived from the respective slope.

gap of $E_g = 9.4$ eV, the estimated intrinsic carrier concentration at 25 °C is extremely low, approximately $n_i \approx 3{\cdot}10^{-60}$ cm^{-3}.

This result shows that virtually no intrinsic charge carriers can populate the conduction or valence bands under these conditions (*i.e.*, the intrinsic σ_{el} should be negligible). Again, σ_{el} appears to arise from impurities, which introduce localized states within the band gap. This is confirmed by the PL measurements, shown in Fig. S2 (Section C, SI), potentially being Li_2O for LiCl (see Fig. S3, Section D, SI). These band gap states act as donors and/or acceptors, where electronic charge carriers are localized. Based on this assumption, E_A for electron-hole conduction, estimated from the temperature-dependence of the conductivity pre-factors in Fig. 6A, are likely associated with the migration enthalpies of electron holes, which hop between impurity sites. Consequently, the impurity concentration in lithium halides not only influences σ_{ion}, but also significantly affects σ_{el}. Unfortunately, reliable reference values for E_A of electronic charge carriers in LiCl and LiBr are scarce in literature, which hinders direct comparison of our results with previously published data.

For LiI (Fig. 4C), $i_{el,ss}$ linearly increases with increasing voltage. In contrast to the findings of Poulsen et al. [56] (who used a graphite-based blocking electrode), no exponential behavior in the steady state current is observed. This may result from incomplete lithium-ion blocking behavior of the graphite in their setup. Nevertheless, the linear trend in our data indicates that hole conduction surpasses electron conduction ($\sigma_p^0 \gg \sigma_n^0$), likely in the extrinsic region of LiI, due to the "self-polarization" of cells. Since the cell's OCV was very close to the decomposition potential of LiI, the investigated potential range was limited to just a few millivolts and quasi-linear trends. As a result, U_{cell}^0 for LiI could not be determined, suggesting that U_{cell}^0 is close to U_{cell}. Consequently, $U_{source} = U_{cell} - U_{cell}^0 \approx 0$ and, thus, the exponential function e^x can be approximated as $(1 + x)$ so that Eq. 22 simplifies to:

$$j_{el,ss} = \left(\sigma_n^0 + \sigma_p^0\right)\frac{U_{cell} - U_{cell}^0}{l} \approx \sigma_p^0 \cdot \frac{U_{cell} - U_{cell}^0}{l} \tag{29}$$

Accordingly, σ_p^0 (equivalent to σ_{el} in this case for $\sigma_p^0 \gg \sigma_n^0$ due to the "self-polarization") in the fully ion-blocking state can be determined for each temperature through linear regression of $i_{el,ss}$ (Fig. 4C). The resulting values are presented in Fig. 7 as a function of inverse temperature ranging from 45 to 57.5 °C.

From the plot, E_A for hole migration in LiI is approximately 0.44 eV, while the estimated room-temperature hole conductivity σ_p^0 is 22 nS cm^{-1} (25 °C). Poulsen et al. [56] reported $E_A = 0.58$ eV and $\sigma_{el} = 22.5$ nS cm^{-1} for undoped polycrystalline LiI at 54 °C and 2.5 V. This agrees with our estimation, which yields $\sigma_p^0 = 90$ nS cm^{-1} at 54 °C.

It should be noted that in literature, Hebb-Wagner measurements for

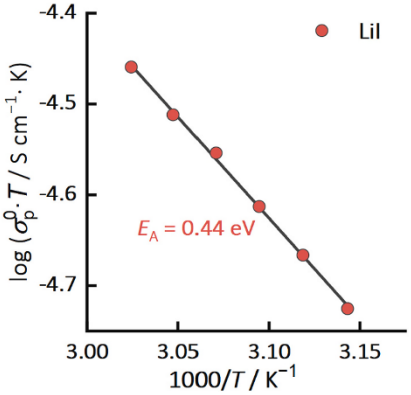

Fig. 7. Arrhenius representation of σ_p^0, multiplied by the absolute temperature T for LiI as a function of 1000/T in the temperature range of 45 to 57.5 °C. It was obtained using Eq. 29 and linear regression of the trends in Fig. 4C.

highly ion-conducting SEs are typically avoided by using two ion-blocking electrodes and often only a small voltage range can be tested before reaching U_{decomp}, as was the case for LiI in our study. Thus, using Eq. 29 is a common approach when determining σ_{el} from polarization measurements [79–82]. However, since a RE is not used, this method does not establish a reference for a_{Li} (and μ_{Li}), providing only an upper estimate for σ_{el} [89]. As a result, the obtained values often deviate from the actual σ_{el} of practical SEs [9].

2.3. *LiX being degradation products of Li_6PS_5X in SSBs*

As highlighted in the introduction, the transport properties of Li*X* are largely unexplored [51]. While several studies have examined σ_{ion} of LiI, research on other lithium halides is scarce, and their σ_{el} has been largely neglected. However, in the broader effort to commercialize SSBs and control interphase formation, Li*X* (with *X* = Cl, Br, or I) plays a crucial role in understanding the kinetics and properties of SEIs, that evolve in typical sulfide SEs, such as Li_6PS_5X (with *X* = Cl, Br, or I), or halide SEs.

In Fig. 8, σ_{ion} and σ_{el} of LiCl, LiBr, and LiI – determined in this work – are compared to values reported in literature, as well as to those of Li_6PS_5X and other relevant SEI constituents [51]. Our findings present the first set of σ_{ion} and σ_{el} for LiCl, LiBr, and LiI at ambient temperature (25 °C), extrapolated from higher temperatures within the tested potential range. While the σ_{ion} values align with previous reports, the values for both σ_{ion} and σ_{el} fall between those of other SEI constituents (*i.*

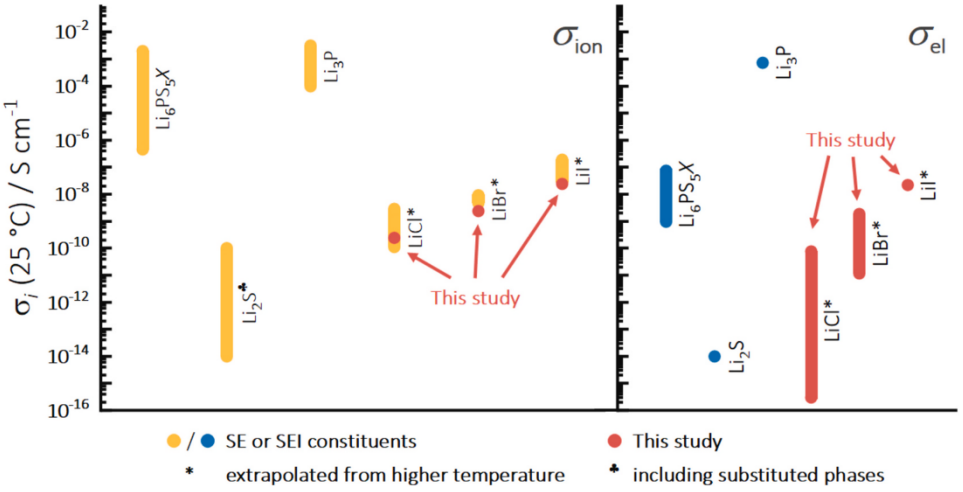

Fig. 8. The determined partial conductivities σ_i (with i = ion or el) at 25 °C for LiCl, LiBr, and LiI from this study (shown in red) are compared to literature values. Additionally, σ_i of Li_6PS_5X (X = Cl, Br, and I) and typical SEI constituents are included. Reported values vary across different studies and compounds. Data for LiCl [84,87], LiBr [85,87], LiI [54,56,85–88], Li_6PS_5X (X = Cl, Br, and I) [79–82,90,91], Li_2S [92–94], and Li_3P [95–97] were taken from literature. An asterisk and a spade indicate values estimated by extrapolation from higher temperatures and data including substituted phases, respectively. (For interpretation of the references to colour in this figure legend, the reader is referred to the web version of this article.)

e., Li_2S and Li_3P) and are lower than those of Li_6PS_5X.

These results provide a comparative analysis of the fundamental transport properties of lithium halides, deepening the understanding of their role in SEIs and, consequently, in SSBs. Building on our previous work [51], which investigated SEI growth kinetics driven by σ_{el}, we conclude that σ_{el} observed for LiX in this study are too high to effectively limit interphase growth. However, other SEI constituents (*i.e.*, Li_3P) appear to predominantly drive continuous growth by increasing the mean σ_{el}. Simultaneously, further material engineering is necessary to maintain low impedance contributions, as LiX together with Li_2S, appears to reduce the mean σ_{ion} of interphases and, thus, affect cell performance.

Nonetheless, our findings must be interpreted within a broader context to accurately assess the determined values and their implications for understanding SEIs in SSBs. Firstly, even high-purity materials (≥99.9 %), as such tested in this study, inevitably contain a significant amount of impurities, which clearly modify the electrical properties by creating additional electronic charge carriers and/or lithium vacancies. Consequently, our results may not fully represent the electrical properties of LiX in multiphase SEIs, as the presence of impurities within individual SEI constituents remains uncertain. Moreover, in practical SSB environments, U_{cell} and a_{Li} are expected to exhibit significantly greater variations, compared to the controlled conditions in our study, particularly in systems employing lithium metal anodes and high-capacity cathodes. LiX may demonstrate faster transport kinetics within SSBs depending on the cell's voltage (and potential "self-polarization" driven by blocking electrode materials used in "anode-free" cell concepts). Consequently, such "self-polarization" effects may induce dominant acceptor conduction and higher σ_{el} in reservoir-free SSBs, similar to observation in our study. Finally, although every effort has been made to prevent material degradation, parasitic currents resulting from degradation reactions could potentially have a minor influence on our results.

Due to the low self-discharge rates of typical SSBs, such as calendar lifetimes exceeding ten years for LiPON-based SSBs, σ_{el} of inorganic SEs reported in the literature may be overestimated [9]. Typical values in the range of 10^{-9} to 10^{-7} S cm^{-1} (Fig. 8) have been reported from dc polarization experiments, which would suggest rapid capacity loss over time – an effect that has not been observed in experimental studies. Such σ_{el} would lead to a 20 % capacity loss within a period ranging from a few hours to several days for a 4 V-cell with a capacity of 5 mAh cm^{-2}, a separator thickness of 100 µm, and an area of 1 cm^2 [9]. This discrepancy highlights significant challenges in accurately quantifying σ_{el} for many relevant SEs. It is essential to identify appropriate RE materials that prevent the degradation of sensitive SEs and eliminate parasitic currents to effectively improve measurement accuracy. Additionally, measurement setups may require high-resolution potentiostats and optimized experimental conditions to precisely detect the extremely low currents involved in Hebb-Wagner measurements.

From a practical perspective, effective material design to limit electronic mobility by controlling impurity levels is crucial for inorganic SEs to maintain a sufficiently low σ_{el}. This objective may help counteract significant variations in electronic charge carrier concentrations, as described in Eq. 26, within the dynamic environment of SSBs. Therefore, Ahmad et al. [98] recently summarized the recent attempts to control σ_{el} by elemental doping or substitution in different sulfide SEs.

3. Conclusions

Our study presents a comprehensive framework in the defect-chemical context that includes formal treatment for the Hebb-Wagner method, a discussion on "self-polarization" of pristine Hebb-Wagner cells (*i.e.*, cells resembling reservoir-free SSBs to some extent), detailed testing protocols, and thorough data analysis for determining σ_{el} in solid lithium-ion conductors. Lithium halides (LiX, with X = Cl, Br, or I) were examined, revealing the contribution of electron holes to electronic transport under the applied testing conditions. Their partial ionic and electronic conductivities were systematically evaluated – within a relevant voltage range similar to actual cell operation – yielding σ_{el} values of approximately $2 \cdot 10^{-16}$ to $8 \cdot 10^{-12}$ S cm^{-1} for LiCl, $1 \cdot 10^{-11}$ to $2 \cdot 10^{-9}$ S cm^{-1} for LiBr, and $22 \cdot 10^{-9}$ S cm^{-1} for LiI (at 25 °C). With regard to interphases formed in typical sulfide and halide SEs, these values complete a comprehensive dataset on the fundamental transport properties of common SEI components. This comparative analysis of partial conductivities enhances our understanding of the role of lithium halides within SEIs and, in turn, their influence on SEI formation and cell performance. The applicability of the Hebb-Wagner technique for accurately measuring σ_{el} in susceptible lithium-ion SEs is evaluated, and

relevant guidelines are provided. Overall, our findings emphasize the necessity of investigating the electronic properties of SSB materials and their interphases to better understand their impact on the long-term viability of SSBs. We hope that this work on σ_{el} of lithium halides, along with its analysis in the context of interphases, will inspire further research aimed at optimizing solid-state interfaces, ultimately contributing to the development of more stable and efficient SSBs.

4. Experimental

Cell assembly were carried out in an argon-filled glovebox (*LabMasterPRO*, MBraun, Garching, Germany), with $p(O_2)/p$ and $p(H_2O)/p < 1$ ppm. For LiI, exposure to light was minimized during handling due to its light-sensitive nature.

4.1. Preparation of materials and cell assembly

Commercial "ultra dry"/anhydrous Li*X* powders ($\geq$ 99.9 % purity, *X* = Cl, Br, I) were received from Fisher Scientific (Schwerte, Germany). Prior to use, the powders were dried overnight at 300 °C under dynamic vacuum in a glass oven (*B-585*, Büchi Labortechnik, Essen, Germany) and subsequently transferred to the glovebox for further handling. Each powder was then thoroughly hand-ground for 10 min using a mortar and pestle. 100, 120, and 150 mg of LiCl, LiBr, and LiI, respectively, were pelletized (10 mm diameter) using a uniaxial force of 40 kN. The pellet thickness was 714, 501, and 476 μm, respectively. A thin ion-blocking gold electrode (120 nm thick, 9 mm diameter) was deposited onto one side of each pellet under dynamic vacuum using a custom thermal evaporation system connected to a glovebox. The deposition rate was set to approximately 0.2 nm s^{-1}, monitored by an oscillating quartz sensor. Subsequently, lithium foil (100 μm thick, 9 mm diameter, 99.9 %, China Energy Lithium, China) was attached to the opposite side of each pellet, serving as the RE. The assembled cell stack was vacuum-sealed in a pouch cell with nickel current collectors. To ensure optimal contact between the pellet and electrodes, the vacuum-sealed cell was densified under isostatic pressure (60 MPa) for 10 min. Lastly, the cells were stored at 60 °C for one week prior to measurement.

4.2. Electrochemical characterization

Electrochemical measurements were performed using a Biologic *VMP 300* potentiostat (BioLogic, Seyssinet-Pariset, France) inside a climate chamber (*LabEvent*, Weiss Technik, Reiskirchen, Germany). According to the manufacturer, the chamber maintains temperature control with an accuracy of 0.1 °C. No external pressure was applied to the pouch cells during measurements. To ensure proper equilibration, the cells were monitored at OCV for 12 h after each temperature change. Before conducting the dc Hebb-Wagner measurements, an initial electrochemical impedance spectroscopy (EIS) step was performed at rest (OCV). The subsequent dc Hebb-Wagner measurements comprised six individual dc polarization steps per temperature, each lasting 12 h. Following each dc polarization step, an EIS measurement was conducted with a dc offset matching the respective dc polarization value. This procedure was repeated for a total of six temperatures, gradually increasing the temperature from 45 °C to 57.5 °C in 2.5 °C increments.

EIS was carried out with an amplitude of 10 mV across a frequency range from 5 MHz to 1 Hz. For dc Hebb-Wagner experiments, a voltage U_{cell} was applied as follows: U_{source} was increased by increments of 0.1 V between $U_{cell} = 3.0$ and 3.5 V for LiCl, increments of 0.05 V between 3.1 and 3.35 V for LiBr, and increments of 0.02 V between 2.74 and 2.84 V for LiI. These parameters were carefully selected based on preliminary studies to avoid measurements below the OCV or above the decomposition voltage of each material. The decomposition voltage U_{decomp} was calculated using thermodynamic data [99] (neglecting entropy contributions) as $U_{decomp} = -\Delta G^0(LiX)/F$, where ΔG^0, *X*, and *F* are the Gibbs energy, the respective halogen (Cl, Br, or I), and the Faraday constant, respectively.

CRediT authorship contribution statement

Christoph D. Alt: Writing – review & editing, Writing – original draft, Visualization, Validation, Methodology, Investigation, Formal analysis, Conceptualization. **Jill Kessler-Kühn:** Investigation. **Janis K. Eckhardt:** Formal analysis. **Markus Stein:** Investigation, Formal analysis. **Sangam Chatterjee:** Resources, Investigation. **Matthias T. Elm:** Writing – review & editing, Formal analysis, Conceptualization. **Jürgen Janek:** Writing – review & editing, Formal analysis, Conceptualization, Resources, Funding.

Declaration of generative AI and AI-assisted technologies in the writing process

During the preparation of this work the authors used *ChatGPT 3.5* (by OpenAI) in order to improve readability and language. After using this tool, the authors reviewed and edited the content as needed and take full responsibility for the content of the publication.

Declaration of competing interest

The authors declare the following financial interests/personal relationships which may be considered as potential competing interests:

Jürgen Janek reports financial support was provided by Federal Ministry of Education and Research. Christoph D. Alt reports financial support was provided by Federal Ministry of Education and Research. Janis K. Eckhardt reports financial support was provided by the Hessian State Ministry of Higher Education, Research, and the Arts. Matthias T. Elm reports financial support was provided by German Research Foundation. If there are other authors, they declare that they have no known competing financial interests or personal relationships that could have appeared to influence the work reported in this paper.

Acknowledgements

The authors thank Maya Ziegler and Sebastian L. Benz for their support with the XPS measurement and subsequent data analysis. C. D. A. and J.J. acknowledge financial support by Bundesministerium für Bildung und Forschung (BMBF) within the ALANO project (Grant No. 03XP0396J). J. K. E. acknowledges financial support from the Hessian State Ministry of Higher Education, Research, and the Arts (HMWK). M. S. and S.C. acknowledges financial support from HMWK through the LOEWE Transfer Professorship High-Performance Materials. M.T.E. acknowledges the financial support provided by the Heisenberg Program (project number 498993886, grant no. EL 863/6-1) and within project EL 863/8-1 (grant no. 512108624) from the German Research Foundation (DFG).

Appendix A. Supplementary data

Supporting Information is available from Solid State Ionics or from the author. Supplementary data to this article can be found online at https://doi.org/10.1016/j.ssi.2025.116991.

Data availability statement

The data that support the findings of this study are available from the corresponding author upon reasonable request.

References

[1] J. Maier, Physical Chemistry of Ionic Materials, Wiley, 2004.

[2] D. Schweke, et al., Defect chemistry of oxides for energy applications, Adv. Mater. 30 (2018) e1706300, https://doi.org/10.1002/adma.201706300.
[3] M. Backhaus-Ricoult, SOFC – a playground for solid state chemistry, Solid State Sci. 10 (2008) 670–688, https://doi.org/10.1016/j.solidstatesciences.2007.11.021.
[4] S.P. Culver, et al., Designing Ionic conductors: the interplay between structural phenomena and interfaces in thiophosphate-based solid-state batteries, Chem. Mater. 30 (2018) 4179, https://doi.org/10.1021/acs.chemmater.8b01293.
[5] A. Gautam, et al., Engineering the site-disorder and lithium distribution in the lithium superionic argyrodite Li_6PS_5Br, Adv. Energy Mater. 11 (2021) 2003369, https://doi.org/10.1002/aenm.202003369.
[6] W.G. Zeier, Structural limitations for optimizing garnet-type solid electrolytes: a perspective, Dalton Trans. 43 (2014) 16133–16138, https://doi.org/10.1039/C4DT02162B.
[7] M. Botros, J. Janek, Embracing disorder in solid-state batteries, Science 378 (2022) 1273–1274, https://doi.org/10.1126/science.adf3383.
[8] F. Han, et al., High electronic conductivity as the origin of Lithium dendrite formation within solid electrolytes, Nat. Energy 4 (2019) 187–196, https://doi.org/10.1038/s41560-018-0312-z.
[9] B. Shao, Y. Huang, F. Han, Electronic conductivity of lithium solid electrolytes, Adv. Energy Mater. 13 (2023), https://doi.org/10.1002/aenm.202204098.
[10] T. Nakamura, et al., Guidelines for all-solid-state battery design and electrode buffer layers based on chemical potential profile calculation, ACS Appl. Mater. Interfaces 11 (2019) 19968–19976, https://doi.org/10.1021/acsami.9b03053.
[11] H.-K. Tian, et al., Interfacial electronic properties dictate Li dendrite growth in solid electrolytes, Chem. Mater. 31 (2019) 7351–7359, https://doi.org/10.1021/acs.chemmater.9b01967.
[12] T. Krauskopf, et al., Physicochemical concepts of the LITHIUM metal anode in solid-state batteries, Chem. Rev. 120 (2020) 7745–7794, https://doi.org/10.1021/acs.chemrev.0c00431.
[13] L. Zhou, et al., High areal capacity, long cycle life 4 V ceramic all-solid-state Li-ion batteries enabled by chloride solid electrolytes, Nat. Energy 7 (2022) 83–93, https://doi.org/10.1038/s41560-021-00952-0.
[14] I. Kochetkov, et al., Different interfacial reactivity of lithium metal chloride electrolytes with high voltage cathodes determines solid-state battery performance, Energ. Environ. Sci. 15 (2022) 3933–3944, https://doi.org/10.1039/D2EE00803C.
[15] P. Gorai, et al., Devil is in the defects: electronic conductivity in solid electrolytes, Chem. Mater. 33 (2021) 7484–7498, https://doi.org/10.1021/acs.chemmater.1c02345.
[16] H.-K. Tian, B. Xu, Y. Qi, Computational study of lithium nucleation tendency in $Li_7La_3Zr_2O_{12}$ (LLZO) and rational design of interlayer materials to prevent lithium dendrites, J. Power Sources 392 (2018) 79–86, https://doi.org/10.1016/j.jpowsour.2018.04.098.
[17] H. Liu, et al., Controlling dendrite growth in solid-state electrolytes, ACS Energy Lett. 5 (2020) 833–843, https://doi.org/10.1021/acsenergylett.9b02660.
[18] X. Liu, et al., Local electronic structure variation resulting in Li 'filament' formation within solid electrolytes, Nat. Mater. 20 (2021) 1485–1490, https://doi.org/10.1038/s41563-021-01019-x.
[19] N.J. Dudney, Solid-state thin-film rechargeable batteries, Mater. Sci. Eng. B 116 (2005) 245–249, https://doi.org/10.1016/j.mseb.2004.05.045.
[20] B. Put, et al., Electrical characterization of ultrathin RF-sputtered LiPON layers for nanoscale batteries, ACS Appl. Mater. Interfaces 8 (2016) 7060–7069, https://doi.org/10.1021/acsami.5b12500.
[21] Y. Li, P. Canepa, P. Gorai, Role of electronic passivation in stabilizing the Lithium-$Li_xPO_yN_z$ solid-electrolyte interphase, PRX Energy 1 (2022), https://doi.org/10.1103/PRXEnergy.1.023004.
[22] H. Buschmann, et al., Structure and dynamics of the fast lithium ion conductor "$Li_7La_3Zr_2O_{12}$", Phys. Chem. Chem. Phys. 13 (2011) 19378–19392, https://doi.org/10.1039/C1CP22108F.
[23] C. Zhu, et al., Understanding the evolution of lithium dendrites at $Li_{6.25}Al_{0.25}La_3Zr_2O_{12}$ grain boundaries via operando microscopy techniques, Nat Commun. 14 (2023) 1300, https://doi.org/10.1038/s41467-023-36792-7.
[24] M. Philipp, et al., The electronic conductivity of single crystalline Ga-stabilized cubic $Li_7La_3Zr_2O_{12}$: a technologically relevant parameter for all-solid-state batteries, Adv. Mater. Inter. 7 (2020), https://doi.org/10.1002/admi.202000450.
[25] A.G. Squires, et al., Low electronic conductivity of $Li_7La_3Zr_2O_{12}$ solid electrolytes from first principles, Phys. Rev. Mater. 6 (2022), https://doi.org/10.1103/PhysRevMaterials.6.085401.
[26] L. Le Van-Jodin, et al., Dielectric properties, conductivity and Li^+ ion motion in LiPON thin films, Solid State Ion. 253 (2013) 151–156, https://doi.org/10.1016/j.ssi.2013.09.031.
[27] J. Li, et al., Artificial solid electrolyte interphase to address the electrochemical degradation of silicon electrodes, ACS Appl. Mater. Interfaces 6 (2014) 10083, https://doi.org/10.1021/am5009419.
[28] Y. Su, et al., LiPON thin films with high nitrogen content for application in lithium batteries and electrochromic devices prepared by RF magnetron sputtering, Solid State Ion. 282 (2015) 63–69, https://doi.org/10.1016/j.ssi.2015.09.022.
[29] W. Weppner, Engineering of solid state ionic devices, Ionics 9 (2003) 444–464, https://doi.org/10.1007/BF02376599.
[30] W. Weppner, Interfaces in Ionic devices, Ionics 7 (2001) 404–424, https://doi.org/10.1007/BF02373577.
[31] B.V. Lotsch, J. Maier, Relevance of solid electrolytes for Lithium-based batteries: a realistic view, J. Electroceram. 38 (2017) 128–141, https://doi.org/10.1007/s10832-017-0091-0.
[32] R.A. Huggins, Simple method to determine electronic and ionic components of the conductivity in mixed conductors: a review, Ionics 8 (2002) 300, https://doi.org/10.1007/BF02376083.
[33] M.H. Hebb, Electrical conductivity of silver sulfide, J. Chem. Phys. 20 (1952) 185–190, https://doi.org/10.1063/1.1700165.
[34] C. Wagner, Galvanische Zellen mit festen Elektrolyten mit gemischter Stromleitung, Zeitschrift für Elektrochemie 60 (1956) 4–7, https://doi.org/10.1002/bbpc.19560600104.
[35] J.B. Wagner, C. Wagner, Electrical conductivity measurements on cuprous halides, J. Chem. Phys. 26 (1957) 1597–1601, https://doi.org/10.1063/1.1743590.
[36] C. Wagner, Galvanic cells with solid electrolytes involving ionic and electronic conduction, in: Proc. C. I. T. C. E., Electrochem. Semicond 7, 1955, pp. 361–377.
[37] W. Weppner, J. Liu, Polarization studies of the electronic minority charge carriers in Ag^+-ß″-alumina, Zeitschrift für Naturforschung A 46 (1991) 409, https://doi.org/10.1515/zna-1991-0506.
[38] C. Rosenkranz, Determination of local potentials in mixed conductors — two examples, Solid State Ion. 82 (1995) 95–106, https://doi.org/10.1016/0167-2738(95)00208-N.
[39] T. Shimonosona, et al., Electronic conductivity measurement of Sm- and La-doped ceria ceramics by Hebb-Wagner method, Solid State Ion. 174 (2004) 27, https://doi.org/10.1016/j.ssi.2004.07.025.
[40] I. Valov, et al., Ionic and electronic conductivity of nitrogen-doped YSZ single crystals, Solid State Ion. 180 (2009) 1463–1470, https://doi.org/10.1016/j.ssi.2009.09.003.
[41] J. Janek, W.G. Zeier, Challenges in speeding up solid-state battery development, Nat. Energy 8 (2023) 230–240, https://doi.org/10.1038/s41560-023-01208-9.
[42] F. Han, et al., Electrochemical stability of $Li_{10}GeP_2S_{12}$ and $Li_7La_3Zr_2O_{12}$ solid electrolytes, Adv. Energy Mater. 6 (2016), https://doi.org/10.1002/aenm.201501590.
[43] L.M. Riegger, et al., Instability of the Li_7SiPS_8 solid electrolyte at the lithium metal anode and interphase formation, Chem. Mater. 34 (2022) 3659, https://doi.org/10.1021/acs.chemmater.1c04302.
[44] L.M. Riegger, et al., Lithium-metal anode instability of the superionic halide solid electrolytes and the implications for solid-state batteries, Angew. Chem. 60 (2021) 6718–6723, https://doi.org/10.1002/anie.202015238.
[45] W.D. Richards, et al., Interface stability in solid-state batteries, Chem. Mater. 28 (2016) 266–273, https://doi.org/10.1021/acs.chemmater.5b04082.
[46] Y. Zhu, X. He, Y. Mo, Origin of outstanding stability in the Lithium solid electrolyte materials: insights from thermodynamic analyses based on first-principles calculations, ACS Appl. Mater. Interfaces 7 (2015) 23685–23693, https://doi.org/10.1021/acsami.5b07517.
[47] Y. Zhu, X. He, Y. Mo, First principles study on electrochemical and chemical stability of solid electrolyte–electrode interfaces in all-solid-state Li-Ion batteries, J Mater Chem A 4 (2016) 3253–3266, https://doi.org/10.1039/C5TA08574H.
[48] S. Wenzel, et al., Interfacial reactivity and interphase growth of Argyrodite solid electrolytes at Lithium metal electrodes, Solid State Ion. 318 (2018) 102, https://doi.org/10.1016/j.ssi.2017.07.005.
[49] Y. Liang, et al., In-situ XPS investigation of the SEI formed on LGPS and LAGP with metallic lithium, Chem. Commun. (Camb.) 60 (2024) 12597–12600, https://doi.org/10.1039/D4CC04462B.
[50] J.S. Gibson, et al., Gently does it!: in-situ preparation of alkali metal-solid electrolyte interfaces for photoelectron spectroscopy, Faraday Discuss. 236 (2022) 267–287, https://doi.org/10.1039/d1fd00118c.
[51] C.D. Alt, et al., Quantifying multiphase SEI growth in sulfide solid electrolytes, Joule 8 (2024) 2755–2776, https://doi.org/10.1016/j.joule.2024.07.006.
[52] C.C. Liang, The self-discharge mechanism of the Li/LiI/AgI solid electrolyte cell, J. Electrochem. Soc. 118 (1971) 894, https://doi.org/10.1149/1.2408213.
[53] C.C. Liang, J. Epstein, G.H. Boyle, A high-voltage, solid-state battery system, J. Electrochem. Soc. 116 (1969) 1452, https://doi.org/10.1149/1.2411560.
[54] F. Poulsen, W. Ionic, Conductivity of solid lithium iodide and its monohydrate, Solid State Ion. 2 (1981) 53–57, https://doi.org/10.1016/0167-2738(81)90020-5.
[55] C.C. Liang, A.V. Joshi, N.E. Hamilton, Solid-state storage batteries, J. Appl. Electrochem. 8 (1978) 445–454, https://doi.org/10.1007/BF00615840.
[56] F. Poulsen, et al., Properties of LiI-alumina composite electrolytes, Solid State Ion. 9-10 (1983) 119–122, https://doi.org/10.1016/0167-2738(83)90219-9.
[57] L.M. Arnbjerg, et al., Structure and dynamics for $LiBH_4$−LiCl solid solutions, Chem. Mater. 21 (2009) 5772–5782, https://doi.org/10.1021/cm902013k.
[58] A. El Kharbachi, et al., Pseudo-ternary $LiBH_4$·LiCl·P_2S_5 system as structurally disordered bulk electrolyte for all-solid-state lithium batteries, Phys. Chem. Chem. Phys. 22 (2020) 13872–13879, https://doi.org/10.1039/D0CP01334J.
[59] V. Gulino, et al., Phase stability and fast ion conductivity in the hexagonal $LiBH_4$-LiBr-LiCl solid solution, Chem. Mater. 31 (2019) 5133–5144, https://doi.org/10.1021/acs.chemmater.9b01035.
[60] X. Ma, Y. Xu, Enhanced critical current density of garnet $Li_7La_3Zr_2O_{12}$ solid electrolyte by incorporation of LiBr, Electrochim. Acta 409 (2022) 139986, https://doi.org/10.1016/j.electacta.2022.139986.
[61] R. Xu, et al., Room temperature halide-eutectic solid electrolytes with viscous feature and ultrahigh ionic conductivity, Adv. Sci. 9 (2022) e2204633, https://doi.org/10.1002/advs.202204633.
[62] H. Wan, et al., Understanding LiI-LiBr catalyst activity for solid state Li_2S/S reactions in an all-solid-state lithium battery, Nano Lett. 21 (2021) 8488–8494, https://doi.org/10.1021/acs.nanolett.1c03415.
[63] S. Yang, et al., Studies on the inhibition of lithium dendrite formation in sulfide solid electrolytes doped with LiX (X = Br, I), Solid State Ion. 377 (2022) 115869, https://doi.org/10.1016/j.ssi.2022.115869.
[64] J. Malugani, G. Robert, Preparation and electrical properties of the 0,37Li_2S-0,18P_2S_5-0,45LiI glass, Solid State Ion. 1 (1980) 519–523, https://doi.org/10.1016/0167-2738(80)90048-X.

3. Results and Discussion

[65] R. Mercier, et al., Superionic conduction in Li_2S-P_2S_5-LiI-glasses, Solid State Ion. 5 (1981) 663–666, https://doi.org/10.1016/0167-2738(81)90341-6.

[66] E. Rangasamy, et al., An iodide-based $Li_7P_2S_8I$ superionic conductor, J. Am. Chem. Soc. 137 (2015) 1384–1387, https://doi.org/10.1021/ja508723m.

[67] S. Ujiie, A. Hayashi, M. Tatsumisago, Structure, ionic conductivity and electrochemical stability of Li_2S-P_2S_5-LiI glass and glass-ceramic electrolytes, Solid State Ion. 211 (2012) 42–45, https://doi.org/10.1016/j.ssi.2012.01.017.

[68] S. Ujiie, A. Hayashi, M. Tatsumisago, Preparation and ionic conductivity of $(100-x)(0.8Li_2S{\cdot}0.2P_2S_5){\cdot}xLiI$ glass–ceramic electrolytes, J. Solid State Electrochem. 17 (2013) 675–680, https://doi.org/10.1007/s10008-012-1900-7.

[69] Z. Zhang, et al., Lithium halide coating as an effective intergrain engineering for garnet-type solid electrolytes avoiding high temperature sintering, Electrochim. Acta 289 (2018) 254–263, https://doi.org/10.1016/j.electacta.2018.08.079.

[70] Y. Haven, The ionic conductivity of Li-halide crystals, Recl. Trav. Chim. Pays-Bas 69 (1950) 1471–1489, https://doi.org/10.1002/recl.19500691203.

[71] N.F. Mott, M.J. Littleton, Conduction in polar crystals. I. Electrolytic conduction in solid salts, Trans. Faraday Soc. 34 (1938) 485, https://doi.org/10.1039/TF9383400485.

[72] F.A. Kroeger, H.J. Vink, Relations between the concentrations of imperfections in crystalline solids, Solid State Phys. 3 (1956) 307–435, https://doi.org/10.1016/S0081-1947(08)60135-6.

[73] C.R. Gopikrishnan, D. Jose, A. Datta, Electronic structure, lattice energies and born exponents for alkali halides from first principles, AIP Adv. 2 (2012), https://doi.org/10.1063/1.3684608.

[74] N. Ahr, M. Martin, Numerical simulations of the Hebb-Wagner polarization kinetics: (I) weakly acceptor-doped perovskite oxides, Solid State Ion. 386 (2022) 116057, https://doi.org/10.1016/j.ssi.2022.116057.

[75] I. Riess, R. Safadi, H.L. Tuller, Problems with Hebb-Wagner polarization measurements due to overpotentials and decomposition of the sample, Solid State Ion. 72 (1994) 3–6, https://doi.org/10.1016/0167-2738(94)90116-3.

[76] I. Riess, Review of the limitation of the Hebb-Wagner polarization method for measuring partial conductivities in mixed ionic electronic conductors, Solid State Ion. 91 (1996) 221–232, https://doi.org/10.1016/S0167-2738(96)83022-0.

[77] R. Huggins, Use of defect equilibrium diagrams to understand minority species transport in solid electrolytes, Solid State Ion. 143 (2001) 3–16, https://doi.org/10.1016/S0167-2738(01)00827-X.

[78] R. Kanno, M. Murayama, Lithium ionic conductor Thio-LISICON: the Li_2S-GeS_2-P_2S_5 system, J. Electrochem. Soc. 148 (2001) A742, https://doi.org/10.1149/1.1379028.

[79] S. Boulineau, et al., Mechanochemical synthesis of Li-argyrodite Li_6PS_5X (X=Cl, Br, I) as sulfur-based solid electrolytes for all solid state batteries application, Solid State Ion. 221 (2012) 1–5, https://doi.org/10.1016/j.ssi.2012.06.008.

[80] H.-J. Deiseroth, et al., Li_7PS_6 and Li_6PS_5X (X: Cl, Br, I): possible three-dimensional diffusion pathways for lithium ions and temperature dependence of the ionic conductivity by impedance measurements, Zeitschrift anorg allge chemie 637 (2011) 1287–1294, https://doi.org/10.1002/zaac.201100158.

[81] L. Zhou, et al., Solvent-engineered design of argyrodite Li_6PS_5X (X = Cl, Br, I) solid electrolytes with high Ionic conductivity, ACS Energy Lett. 4 (2019) 265–270, https://doi.org/10.1021/acsenergylett.8b01997.

[82] Y.J. Heo, et al., One-pot aprotic solvent-enabled synthesis of superionic Li-argyrodite solid electrolyte, Int. J. Energy Res. 46 (2022) 17644–17653, https://doi.org/10.1002/er.8324.

[83] X. Guo, On the Hebb-Wagner polarisation of $SrTiO_3$ doped with redox-active ions, Solid State Ion. 130 (2000) 267–280, https://doi.org/10.1016/s0167-2738(00)00615-9.

[84] M. Sharon, R.R. Pradhananga, Ionic conductivity of pure and Ca^{2-}- and Sr^{2+}-doped single crystals of LiCl, J. Solid State Chem. 40 (1981) 20–27, https://doi.org/10.1016/0022-4596(81)90355-8.

[85] R. Mercier, M. Tachez, J.P. Malugani, G. Robert, Effect of Homovalent (I^-−Br^-) ion substitution on the Ionic conductivity of $LiI_{1-x}Br_x$ systems, Solid State Ion. 15 (1985) 109–112, https://doi.org/10.1016/0167-2738(85)90088-8.

[86] B. Jackson, D.A. Young, Ionic conduction in pure and doped single-crystalline lithium iodide, J. Phys. Chem. Solid 30 (1969) 1973–1976, https://doi.org/10.1016/0022-3697(69)90174-7.

[87] R.D. Armstrong, K. Landles, Lithium ion conducting solids for ambient applications, J. Appl. Electrochem. 12 (1982) 533–535, https://doi.org/10.1007/BF00614979.

[88] C.R. Schlaikjer, C.C. Liang, Ionic conduction in calcium doped polycrystalline lithium iodide, J. Electrochem. Soc. 118 (1971) 1447, https://doi.org/10.1149/1.2408351.

[89] J. Maier, Conductivity in an activity gradient, J. Phys. Chem. Solid 46 (1985) 197–200, https://doi.org/10.1016/0022-3697(85)90034-4.

[90] P.R. Rayavarapu, et al., Variation in structure and Li^+-ion migration in argyrodite-type Li_6PS_5X (X = cl, Br, I) solid electrolytes, J. Solid State Electrochem. 16 (2012) 1807–1813, https://doi.org/10.1007/s10008-011-1572-8.

[91] M.A. Kraft, et al., Influence of lattice polarizability on the ionic conductivity in the lithium superionic argyrodites Li_6PS_5X (X = Cl, Br, I), J. Am. Chem. Soc. 139 (2017) 10909–10918, https://doi.org/10.1021/jacs.7b06327.

[92] S. Lorger, et al., Enhanced ion transport in Li_2O and Li_2S films, Chem. Commun. 57 (2021) 6503–6506, https://doi.org/10.1039/d1cc00557j.

[93] S. Lorger, R.E. Usiskin, J. Maier, Transport and charge carrier chemistry in Lithium sulfide, Adv. Funct. Mater. 29 (2019), https://doi.org/10.1002/adfm.201807688.

[94] K. Zhang, et al., Ultrasmall Li_2S nanoparticles anchored in graphene nanosheets for high-energy lithium-ion batteries, Sci. Rep. 4 (2014) 6467, https://doi.org/10.1038/srep06467.

[95] G. Nazri, Preparation, structure and ionic conductivity of lithium phosphide, Solid State Ionics 34 (1989) 97–102, https://doi.org/10.1016/0167-2738(89)90438-4.

[96] A.P. Maltsev, et al., Ionic conductivity of lithium phosphides, Crystals 13 (2023) 756, https://doi.org/10.3390/cryst13050756.

[97] J. Li, et al., Mixed ion-electron conducting Li_3P for efficient cathode prelithiation of all-solid-state Li-ion batteries, SmartMat 4 (2023) e1200, https://doi.org/10.1002/smm2.1200.

[98] N. Ahmad, et al., Role of electronic conductivities toward practical all-solid-state lithium-metal/sulfur batteries, Adv. Sustain. Syst. (2024), https://doi.org/10.1002/adsu.202400729.

[99] O. Kubaschewski, C.B. Alcock, P.J. Spencer, Materials Thermochemistry, 6th ed., Pergamon Pr, Oxford u.a, 1993.

3.4. In–Li Counter Electrodes in Solid-State Batteries – A Comparative Approach on Kinetics, Microstructure, and Chemomechanics (4th Publication)

In this publication, different In–Li electrode structures were explored to evaluate their use as CEs, aiming to simplify cell design (*i.e.*, eliminate reference electrodes) and examine their reproducibility. A thorough analysis of their performance and functionality is conducted to enhance the precision of solid-state cathode benchmarking, as a recent report has indicated that performance variations between SSB cells may arise from inconsistencies in the preparation of In–Li electrodes.[124]

Several established and practical In–Li eutectic preparation methods were evaluated. By testing five distinct In–Li preparation techniques and two electrode composites, unidirectional galvanostatic experiments assessed the homogeneity and quality of each electrode preparation approach. The kinetic limitations of two promising In–Li structures were further investigated at various rates, complemented with cross-sectional analysis of their respective microstructure by SEM and electron backscatter diffraction (EBSD). Finally, the rate-dependent electrode performance, along with their electrochemical and chemomechanical reversibility, was tested in a full-cell configuration with $LiNi_{0.82}Mn_{0.11}Co_{0.07}O_2$ cathodes. The electrochemical results highlighted the individual performance and bottlenecks of both In–Li CEs at high rates, while microstructural analysis emphasized the significance of conscious preparation protocols.

These findings reveal the kinetic limitations of In–Li electrodes for benchmarking of high-capacity cathodes, restricting their use to lab-scale testing at moderate rates. The study demonstrates that inconsistent preparation not only affects the electrode microstructure but also its kinetic performance, emphasizing critical preparation challenges. As such, the challenges associated with applying In–Li CEs and the consequences of variations in preparation protocols are detailed, which lead to reduced comparability of results across different laboratories.

The experiments presented in this publication were designed and executed by the first author under the supervision of K. Peppler and J. Janek. The sample preparation was performed by S. Keuntje, I. L. Schneider, and J. Westphal under supervision of the first author. The first author performed all measurements and the corresponding data analysis. P. Minnmann and J. K. Eckhardt supported the analysis of data and assisted with scientific discussion. The manuscript was written by the first author and edited by all co-authors.

Reprinted with permission from Christoph D. Alt, Sören Keuntje, Inga L. Schneider, Johannes Westphal, Janis K. Eckhardt, Philip Minnmann, Klaus Peppler, and Jürgen Janek. In–Li Counter Electrodes in Solid-State Batteries – A Comparative Approach on Kinetics, Microstructure, and Chemomechanics, *Adv. Energy Mater.*, 2024, 2404055. DOI: 10.1002/aenm.202404055. Copyright © 2024 The Authors. Published by Wiley-VCH GmbH.

RESEARCH ARTICLE

ADVANCED ENERGY MATERIALS
www.advenergymat.de

In–Li Counter Electrodes in Solid-State Batteries – A Comparative Approach on Kinetics, Microstructure, and Chemomechanics

*Christoph D. Alt, Sören Keuntje, Inga L. Schneider, Johannes Westphal, Philip Minnmann, Janis K. Eckhardt, Klaus Peppler, and Jürgen Janek**

A key challenge for solid-state batteries is the fabrication of high-capacity cathodes with high area loading and good rate performance. To reliably quantify the performance of high-capacity cathodes, electrochemically stable, and high-rate counter electrodes are essential. Otherwise, a three-electrode setup is required. In–Li alloy electrodes are used for years in a kind of standard approach, since these seem to offer stable operation. In this comparative study, seven preparation methods for In–Li electrodes are examined, determining their suitability for cathode testing. The microstructure of a planar (i.e., foil) and a particle-based (i.e., composite) anode configuration is analyzed in more detail. Their rate-dependent electrode performance as well as electrochemical and chemomechanical reversibility in full-cell configuration are analyzed. The combined results demonstrate the limitations of In–Li electrodes for high-capacity testing, especially at high rates, while confirming their suitability for simple lab-scale testing. Preparation significantly influences the electrode microstructure and kinetics, consequently impacting the performance benchmarks of cathodes. These findings underscore both the challenges involved in applying In–Li counter electrodes and the resulting limited comparability of results from different laboratories.

1. Introduction

With the ongoing shift from combustion-based mobility to sustainable electric transportation, high-energy solid-state batteries (SSB) have garnered significant interest in recent years.[1,2] Inorganic solid electrolytes (SE) offer the possibility to employ lithium metal anodes (LMA) and high-capacity cathode composites, allowing SSBs theoretically to exceed the performance of conventional lithium ion batteries (LIB), which are slowly approaching physicochemical limitations.[3–5] Hence, SSBs are anticipated to offer high power and energy densities, while ensuring safe and reliable operation.[6–10]

In order to fully utilize high-capacity cathode active materials (CAM), which can provide area loadings of up to 10 mAh cm^{-2}, an optimized cathode microstructure with high-rate capability is required.[11,12] Additional issues such as chemomechanical volume changes and related CAM particle cracking need to be addressed.[13,14] For optimization efforts, cathode performance must be quantified reliably, and any effects introduced by deficient counter electrodes (CE) in two-electrode cell setups should be avoided.[15–17] The best way to achieve this is the use of reference electrodes (RE) in three-electrode (3E) setups. This has not been widely reported yet – mostly due to the difficulties in incorporating REs in SSB cells. Miniaturization and geometric challenges (i.e., RE positioning) as well as proper material selection to avoid both SE degradation and reference potential fluctuations, hinder its widespread adoption in SSBs.[18,19] However, first successful integrations of REs have recently been reported. Various approaches like lithiated metal meshes or wires (i.e., out of indium, gold, or silver)[20,21] have been utilized, even achieving µ-REs. Morphological and chemical stability issues (i.e., SEI formation) inhibit the use of lithium metal itself with thiophosphate-based SEs.[22,23]

To avoid the difficulties posed by 3E configurations and reduce preparation requirements, it is essential to introduce electrochemically stable CEs with high rate capability and low overpotential (i.e., defined and stable half-cell potential, favorable kinetics, and reversibility).[16] The binary In–Li alloy system offers

C. D. Alt, S. Keuntje, I. L. Schneider, J. Westphal, P. Minnmann, J. K. Eckhardt, K. Peppler, J. Janek
Institute of Physical Chemistry
Justus Liebig University
Heinrich Buff Ring 17, 35392 Giessen, Germany
E-mail: juergen.janek@phys.chemie.uni-giessen.de

C. D. Alt, S. Keuntje, I. L. Schneider, J. Westphal, P. Minnmann, J. K. Eckhardt, K. Peppler, J. Janek
Center for Materials Research
Justus Liebig University
Heinrich Buff Ring 16, 35392 Giessen, Germany

J. K. Eckhardt
Institute for Theoretical Physics
Justus Liebig University
Heinrich Buff Ring 16, 35392 Giessen, Germany

The ORCID identification number(s) for the author(s) of this article can be found under https://doi.org/10.1002/aenm.202404055

© 2024 The Author(s). Advanced Energy Materials published by Wiley-VCH GmbH. This is an open access article under the terms of the Creative Commons Attribution-NonCommercial-NoDerivs License, which permits use and distribution in any medium, provided the original work is properly cited, the use is non-commercial and no modifications or adaptations are made.

DOI: 10.1002/aenm.202404055

ADVANCED SCIENCE NEWS
www.advancedsciencenews.com

ADVANCED ENERGY MATERIALS
www.advenergymat.de

a range of advantageous attributes, is well-known for its potential plateaus, and has been early introduced in the study of SSB test cells.[24–28] Especially, the two-phase eutectic In/$(InLi)_x$ provides a stable potential of E_H(vs Li^+/Li) = 0.62 V over a wide stoichiometry range (≈1–47 at.% of lithium).[19,29] Degradation of thiophosphate-based SEs is anticipated to be minor at this potential. However, recent findings suggest the emergence of In_xS_y compounds at the interface with the In/$(InLi)_x$ eutectic.[30,31] Notably, Qu et al.[32] and Hänsel et al.[33] have examined the lithium transport properties of various In–Li phases, highlighting fast lithium migration attributed to low activation barriers. Accordingly, the fast diffusion kinetics (D_{Li} = 10^{-8}–10^{-7} cm^2 s^{-1} of the intermetallic InLi phase) are promising to ensure good electrochemical performance and stable SSB cycling.[34–36] In comparison to lithium metal, the volume expansion of indium up to the intermetallic InLi phase of 105 % is lower.[37] Intimate interfacial contact due to the ductile character of indium metal[33,34] enables a low interfacial impedance[29] as well as good local current distribution to provide uniform lithium deposition and dissolution.[34,35,38] To the best of our knowledge, fatal morphological changes of In–Li anodes have only been reported once (after 900 cycles at 3.8 mA cm^{-2} and 150 MPa).[30]

The large-scale application of indium-based electrodes is impeded by raw material costs, interest of other technology sectors, and scarce availability.[39] Nevertheless, the In–Li anode is commonly selected by researchers as a stable CE for lab-scale purpose.[40–42] A significant capacity decay is observed due to the lithiation and alloying if pure indium metal is used as an electrode (shown in Figure S1 and Section SA, Supporting Information). Thus, lab-scale In–Li anodes are mostly manufactured either by stacking (and pressing) indium and lithium metal foils or by mixing metal powders of both alloying components. More complex geometries or pre-lithiation approaches are used less frequently.[34,43] Santhosha et al.[19] demonstrated the benefits of a centrally-located composition within the two-phase eutectic In/$(InLi)_x$. While Wang et al.[36] suggest 14.3 at.% lithium as optimum for fast kinetics, Yanev et al.[44] investigated the boundaries of this phase field up to lithium contents of 50 at.%, and compare three different types of electrode preparation. Hänsel et al.[33] reported kinetic limitations for the (higher lithitated) intermetallic In_3Li_{13} phase.

Summarizing various reports in the literature, In–Li anodes suffer from being mechanically stiffer – compared to pure indium – due to the mechanical properties of the InLi phase (Young's modulus of 46.1 GPa and hardness of 1.82 GPa).[34] Moreover, insufficient electrode kinetics during cycling appear to be associated with the specific preparation of the anode eutectic.[16] To the best of our knowledge, Ikezawa et al.[41] and Nam et al.[16] were the first to report sluggish electrode performance and kinetics using foil type In–Li electrodes. In their study, Nam et al. suspect lithium-deficient layers at the interface between the InLi intermetallic and the SE, thus, identify lithium transport in InLi intermetallic as a bottleneck. Wang et al.[36] and Aspinall et al.[34] provided evidence of the evolution of indium-rich layers in In–Li anodes after discharge processes through microstructural analysis, utilizing electron microscopy and X-ray computed tomography, respectively. Further, Sedlmeier et al.[45] demonstrated the negative effects of In/$(InLi)_x$ phase inhomogeneities by testing thick indium foils (facing toward the SE).

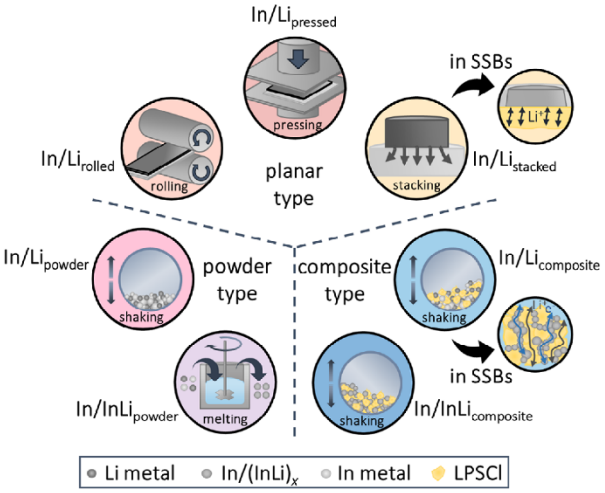

Figure 1. Illustration of the preparation methods tested. For the extensively studied types, namely In/$Li_{stacked}$ and In/$Li_{composite}$, illustrations of their structure and application in SSBs are included. Please note that the dimensions of foils and particles are not necessarily to scale.

However, their approach of contacting first lithium metal with the SE, before the formation of the eutectic will cause severe SE degradation. Nam et al.[16] improved electrode kinetics and rate capabilities by introducing In–Li anode composites including SE particles. This approach aimed to establish ionic percolation paths and reduce the reliance on diffusion within the intermetallic phase. This has recently been confirmed by Yanev et al.[44] through a concise and systematic set of performance studies, clearly recommending the composite approach, once no RE is being used.

While these studies are valuable and individually improve the understanding of single In–Li alloy electrodes, a comparative study is missing. The rate-dependent performance and the underlying microstructure of various In–Li eutectics during repetitive cycling has not been thoroughly investigated or understood yet. This clearly compromises the reliable benchmarking of cathode composites under relevant test conditions and, consequently, the interlaboratory comparability of results.[46]

In this work, we therefore examined several reported and feasible In–Li eutectic preparation methods regarding their suitability for lab-scale utilization as CEs in the investigation of solid-state cathodes. We compared five different In–Li eutectic preparations and two electrode composites, as shown in **Figure 1**. To better understand the inconsistent performances between different electrode types, we complement our detailed electrochemical analysis with results on microstructure and chemomechanics, aiming to establish appropriate selection criteria. Unidirectional galvanostatic experiments reveal the intermixing during preparation and the kinetic limitations (i.e., lithium accessibility) of each type of anode. To fully describe the electrode performance of the most effective preparations methods, namely planar In/$Li_{stacked}$ and particle-based In/$Li_{composite}$, we prepared cross sections to analyze their microstructure using scanning electron microscopy (SEM) and electron backscatter diffraction (EBSD). The analysis of volume changes in planar and particle-based electrodes,

© 2024 The Author(s). Advanced Energy Materials published by Wiley-VCH GmbH

ADVANCED SCIENCE NEWS
www.advancedsciencenews.com

ADVANCED ENERGY MATERIALS
www.advenergymat.de

along with the study of their electrode kinetics (i.e., reversibility and overpotentials) in full-cell configuration, were used to evaluate their integration as stable CEs. It reveals the individual performance, benefits, and bottlenecks of both electrode types concerning high-capacity cathode benchmarking. Conclusively, this work highlights the challenges and consequences of variations in preparation procedures across different laboratories.

2. Results

$In/(InLi)_x$ electrodes were prepared using different methods and can be divided into three groups: 1) planar (i.e., foils), 2) powder, and 3) composite type. Figure 1 illustrates each preparation method. The lithium content was set at 35 at%, which is centrally located in the two-phase region $In/(InLi)_x$. This ensures comparability across all preparation methods. The planar electrodes used are denoted as "In/Li_{rolled}", "$In/Li_{pressed}$", and "$In/Li_{stacked}$". Powder electrode types are referred to as "In/Li_{powder}" and "$In/InLi_{powder}$" for blended or fused (i.e., alloyed) powders, respectively. In–Li alloy composite anodes were prepared from both powder type electrodes and Li_6PS_5Cl (LPSCl), with the resulting materials labeled "$In/Li_{composite}$" and "$In/InLi_{composite}$", respectively.

At this point, we like to acknowledge that the terms "negative" and "positive" electrode should be used to address both electrodes correctly. To align with commonly used terminology, we use the terms "anode" and "cathode".

2.1. Equilibration of In—Li Alloy Electrodes After Preparation

The electrode potential was monitored for 12 h by recording the open-circuit voltage (OCV) of $In/(InLi)_x$ | LPSCl | Li cells (**Figure 2**). During the alloying process, lithium metal is consumed, forming the intermetallic compound InLi, which establishes the characteristic potential of the two-phase eutectic $In/(InLi)_x$ at 0.62 V (vs Li^+/Li). The electrodes are initially not in equilibrium, as indicated by the changing potential. Once a stable potential is reached, equilibrium is achieved. However, even a small amount of residual lithium metal within the WEs would prevent complete equilibration, causing the electrode potential to continue changing over time. Therefore, the successful completion of the alloying process (i.e., complete consumption of lithium metal) is confirmed by achieving a stable potential. In/Li_{rolled} (light red) and $In/InLi_{powder}$ (violet) exhibit a potential of ≈622 mV, while $In/Li_{pressed}$ (dark red), In/Li_{powder} (light violet), $In/Li_{composite}$ (light blue), and $In/InLi_{composite}$ (blue) show potentials of ≈623 mV. Each potential stabilizes within less than 1 h. In the case of $In/Li_{stacked}$ (yellow), relying on long-range lithium diffusion into the indium foil (100 µm thick), a stable potential of ≈618 mV is achieved only after 8 – 10 h. Hence, the utilization of $In/Li_{stacked}$ is inevitably associated with a transient period of several hours prior to electrochemical application.

2.2. Performance in Cell Configurations with Two In—Li Electrodes

The primary cause of dendrite formation and cell failure in SSBs with LMAs is current constriction due to void formation at the stripped lithium electrode.[34,47,48] Accordingly, the as-prepared In–Li electrodes are first evaluated in delithiation experiments. Based on their accessible lithium capacity ($q_{th,delith}$ = 8.4 mAh cm^{-2}), their degree of "bulk" alloying (i.e., intermixing) and suitability for SSB cell testing is approximated.

Figure 3 illustrates the potential profiles (vs $In/(InLi)_x$) for unidirectional galvanostatic stripping at 0.5 mA cm^{-2} in WE | LPSCl | $In/Li_{stacked}$ configuration, referenced to the $In/Li_{stacked}$ CE. With the exception of $In/Li_{pressed}$, each In–Li anode displays initially flat profiles with low potential increases during ongoing lithium stripping, before a steep potential rise indicates lithium depletion.[49] Further discussion on the origin of polarization through analysis of impedance and microstructure is provided below. Clearly, an increasing overpotential caused by polarization affects the overall cell performance and indicates a limitation for the use in high-capacity cell testing.

The accessible capacity (i.e., the amount of extractable lithium) at which polarization initiates varies among the preparation methods. The observed variation is 1) attributed to the degree of intermixing during preparation, which determines the initial spatial distribution of lithium within the electrode, and 2) lithium replenishment properties (governed by diffusion). Consequently, this capacity serves as a key indicator for the suitability of each In–Li electrode type for their use as CE in SSB test cells. We define reliable capacities for each electrode type based on the point where significant polarization (>100 mV) initiates and refer to it as q_{exp}. This value is defined as a threshold, as we consider overpotentials exceeding 100 mV as too high, particularly in full-cells (i.e., during the charging process), as discussed below. Further, we define the lithium accessibility, denoted as $\xi_{exp} = q_{exp}/q_{th} \cdot 100\,\%$, to compare the effective accessible capacities during lithium stripping of a pristine electrode.

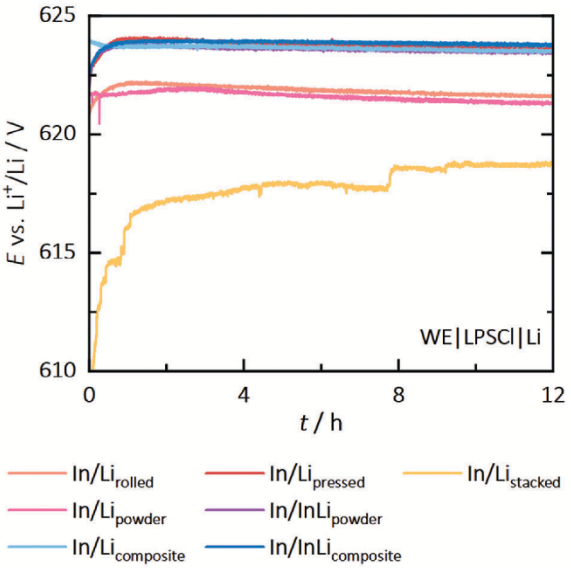

Figure 2. Results of OCV measurements for each In–Li anode (WE | LPSCl | Li). The potential (vs Li^+/Li) is recorded for 12 h after electrode preparation, measured at 25 °C, and and 30 MPa. A single cell was tested for each In–Li anode.

© 2024 The Author(s). Advanced Energy Materials published by Wiley-VCH GmbH

ADVANCED SCIENCE NEWS
www.advancedsciencenews.com

ADVANCED ENERGY MATERIALS
www.advenergymat.de

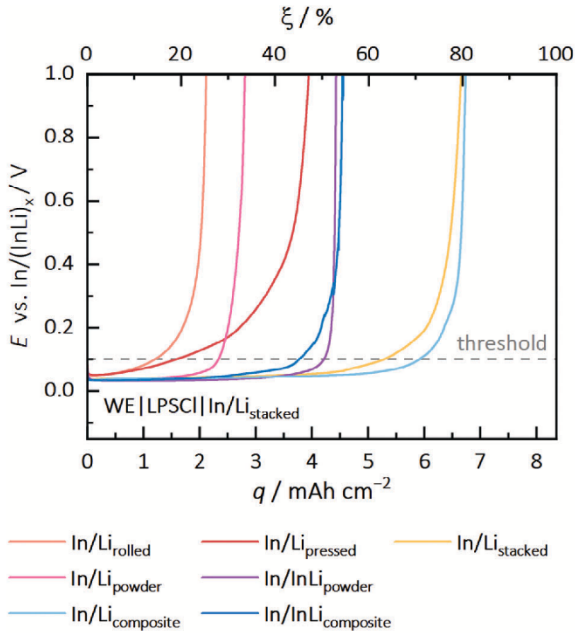

Figure 3. Results of delithiation experiments of each In–Li anode (WE | LPSCl | $In/Li_{stacked}$). Potential profiles (vs $In/(InLi)_x$) for unidirectional galvanostatic stripping at 0.5 mA cm^{-2}, 25 °C, and 30 MPa were recorded until the cut-off potential of 1 V was reached. The threshold of 100 mV is indicated in gray. Stable potentials and low overpotentials up to capacities of 5.9 mAh cm^{-2} indicate the high lithium accessibility within $In/Li_{stacked}$ and $In/Li_{composite}$ (represented in light blue and yellow, respectively). A comparison of the accessible capacities q_{exp} is provided in Figure S3 (Section SB, Supporting Information), including averages and standard deviations for $In/Li_{stacked}$ and $In/Li_{composite}$ for a total number of three cells.

For In/Li_{rolled} and $In/Li_{pressed}$, accessible capacities of approximately $q_{exp} = 1.2$ and 1.6 mAh cm^{-2} were observed before severe polarization began, corresponding to $\xi_{exp} \approx 20\%$. This suggests that mechanical mixing through folding and compressing of foils is difficult to control, resulting in inadequate homogenization and uncontrolled microstructure of the eutectic. Consequently, the properties of these electrode foils are significantly influenced by the specific area (i.e., local composition) designated for use. As reported in the experimental section, the prepared alloy foils became stiff, which is an indication of the intermetallic InLi phase. The stiff nature of these alloyed foils impairs the contact at the interface with the SE.[34] In contrast, the soft indium layer used for the preparation of $In/Li_{stacked}$ provides a better contact at the interface. Accordingly, $In/Li_{stacked}$ exhibited a higher capacity of $q_{exp} = 5.2$ mAh cm^{-2} ($\xi_{exp} = 60\%$), establishing itself as the most effective anode type among the three planar anode types.

q_{exp} of 2.3 and 4.2 mAh cm^{-2} were accessed from In/Li_{powder} and $In/InLi_{powder}$, corresponding to $\xi_{exp} = 27\%$ and 49%, respectively. This suggests insufficient lithium mobility caused by the solid-state transport of lithium within both metallic composites, particle-particle boundaries, and pores. By adding LPSCl to the mixture, ionic percolation paths are introduced, the intermetallic transport pathlength decreased, and kinetic limitations reduced.[16,29] Hence, this enhances the accessible lithium capacity (from deeper regions of the electrode) to $q_{exp} = 3.8$ and 5.9 mAh cm^{-2} for $In/InLi_{composite}$ and $In/Li_{composite}$, corresponding to $\xi_{exp} = 44\%$ and 69%, respectively. Hence, increasing the effective lithium mobility demonstrates the advantage of the composite-type electrode. $In/Li_{composite}$, composed of lithium and indium powder combined with LPSCl, is the most useful concept among the particle-based electrodes.

Figure S3 (Section SB, Supporting Information) presents a comparison of the accessible capacities (q_{exp}), including averages and standard deviations for $In/Li_{stacked}$ and $In/Li_{composite}$ with data derived from three cells each. The statistical analysis yields q_{exp} values of (5.00 ± 0.21) and 5.62 ± 0.29) mAh cm^{-2}, respectively. This highlights satisfactory reproducibility for both of these promising electrodes for further in-depth investigation. Please note that only a single cell was tested for the other, less promising electrode types.

Effective capacities of up to $\xi_{exp} = 69\%$, approaching the theoretical lithiation capacity of the $In/Li_{stacked}$ CE, were achieved. This demonstrates comparable or even higher lithium accessibility to the data reported by Aspinall et al.[34] As a preliminary conclusion, it is apparently not trivial to prepare In–Li anodes with high lithium accessibility. Careful preparation of In–Li eutectic anodes is crucial for mitigating property variations among electrodes prepared in different laboratories, ultimately ensuring consistent performance and facilitating comparable results. Therefore, this emphasizes the necessity for interlaboratory studies, more comprehensive reports of experimental details in literature, and transparent analysis.[46,50]

To evaluate the electrode kinetics for studying high cathode capacities in greater detail, both $In/Li_{stacked}$ and $In/Li_{composite}$ were tested at rates ranging from 0.25 to 5 mA cm^{-2} in symmetric cells with $In/Li_{stacked}$ CEs (see Figure S4, Section SC, Supporting Information). Similar to earlier findings, flat profiles with minimal potential increase during continuous lithium stripping are observed for both anode types at current densities up to 1.5 mA cm^{-2}. These rates are considered sufficient for investigating current lab-scale cathode composites for SSBs with capacities up to 1.5 mAh cm^{-2} at 1C. On the one hand, the trend of increasing overpotential indicates unsuitable performance starting around 1.5 mAh cm^{-2}, which becomes apparent at higher rates, e.g. 5 mA cm^{-2}. This exposes challenges related to sluggish kinetics and inadequate lithium transport from pre-lithiated regions of the stripped WE at high-rate testing. Notably, the potential advantages of the composite type anode (i.e., as a larger contact area and distributed lithium nucleation spots) were not clearly observed in these tests.

Plating experiments of $In/Li_{composite}$ were further conducted to comprehensively analyze its lithiation performance, which is presented in Figure S5 (Section SD, Supporting Information). Both In–Li anode types (with $In/Li_{stacked}$ serving as CE in Figure 3 and Figure S3, Supporting Information) show high effective capacities of lithium and insignificant dendrite susceptibility. Lithiation capacities close to the theoretical capacity ($q_{th,lith} = 7$ mAh cm^{-2}) were achieved. Hence, we assume that the substantial thermodynamic barrier arising from the high alloying potential of $In/(InLi)_x$ (0.62 V vs Li^+/Li) hinders lithium metal plating and, thus, filament growth and cell shorting. These findings suggest favorable lithiation kinetics compared to our delithiation results. Further, this emphasizes the focus on improving the lithium stripping capabilities of In–Li electrodes to

© 2024 The Author(s). Advanced Energy Materials published by Wiley-VCH GmbH

ADVANCED SCIENCE NEWS
www.advancedsciencenews.com

ADVANCED ENERGY MATERIALS
www.advenergymat.de

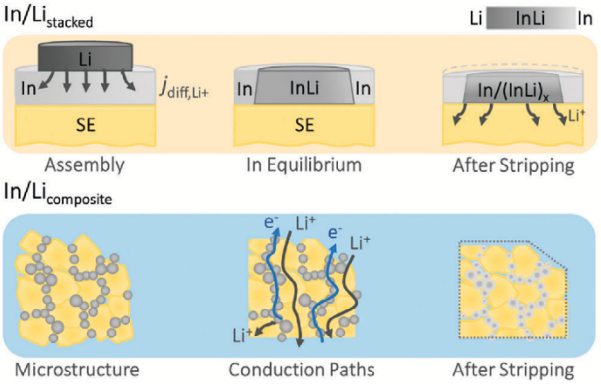

Figure 4. Schematic overview of $In/Li_{stacked}$ (top) and $In/Li_{composite}$ (bottom) electrodes on the cell level. The assembled anode (left) and anticipated equilibrium state (middle) of $In/Li_{stacked}$ are presented, while the microstructure (left) and conduction paths of both charge carriers (middle) in $In/Li_{composite}$ are illustrated. The right side displays the stripped state during lithium depletion conditions for both electrodes. Illustration of foils and particles are not necessarily to scale.

facilitate long-term testing (Figure 3). The enhanced lithium transport properties within the $In/(InLi)_x$ phase field can also be observed when compared to pure indium foil. This is shown in Figure S2 (Section SA, Supporting Information). Consequently, the pre-lithiation of indium, corresponding to the InLi phase formation, proves to be advantageous for enhancing kinetics.

2.3. Microstructural Analysis of Selected In–Li Eutectic Anode Types

We selected $In/Li_{stacked}$ and $In/Li_{composite}$ for further detailed investigation, as these demonstrated the most promising stripping performance and highest reproducibility. This selection is in line with the study of Yanev et al.[44] Consequently, these two electrodes were tested in a greater number of cells, as the other electrode concepts were less suitable for practical applications. The remaining concepts, as prepared for this study, showed insufficient intermixing, inferior stripping performance, or inadequate reproducibility and required optimization. Hence, these anodes may not be adequate CEs to ensure comparable results due to preparation inconsistencies, impeding the independent evaluation of cathode performance in SSBs. To evaluate the mechanism behind the capacity limitations, **Figure 4** first gives a schematic overview of $In/Li_{stacked}$ for planar (top) and $In/Li_{composite}$ for composite type anodes (bottom).

For $In/Li_{stacked}$, lithium atoms diffuse from the smaller lithium foil into the indium foil to form the intermetallic InLi phase (left), i.e., a diffusion-formed "bulk" eutectic. Applied pressure avoids loss of contact during interdiffusion. The two-phase region $In/(InLi)_x$ evolves with an inner core of InLi (≈7.5 mm in diameter) and an outer region of remaining indium, see Figure 4 (top, middle). Incomplete (in-depth) alloying may lead to a deficiency of the InLi phase (i.e., reduced lithium accessibility) at the interface with the SE and cause constriction effects,[44,45] which may become negligible after a first lithiation process. We like to emphasize that it is not only feasible, but important, to position the indium foil between the SE and lithium metal during the alloying process. Otherwise, early SE degradation (i.e., SEI formation) would result from the low potential of lithium metal.

In the case of $In/Li_{composite}$, the 3D phase network comprises intermetallic InLi and indium particles, distributed within the LPSCl microstructure (left). Different paths enable ion and electron transport (bottom, middle), and lithium dissolution/deposition occurs spatially distributed. However, due to the instability of thiophosphate-based SEs, it is important to consider the increased interface area between InLi and LPSCl particles within composites. More lithium will be consumed in side reactions and SEI will form due to the large contact area within the composite, potentially increasing the electrode impedance. We can assume that the volume change of the electrode is stabilized and reduced by the 3D electrolyte "scaffold" (right). This could offer a significant advantage for its use as a CE and for operation under varying stack pressures. After the initial compression during cell fabrication, the immediate contact between the electrode active material and the SE could make it a suitable choice for cell testing (e.g., in pouch cells) at ambient to low external pressures. As indium-based anodes will not be suitable for commercialization, we do not discuss further benefits, such as power density of 3D composite electrodes.[51,52] We rather emphasize the role of high-rate and high-capacity In–Li alloys as CEs in cathode tests.

In the case of $In/Li_{stacked}$, attention to the geometric ratio between the indium and lithium metal foils is crucial. We consider an incorrect choice of parameters, such as variations in composition, areal or thickness ratio, as one of the major factors contributing to decreased interlaboratory comparability. The results of delithiation experiments in Figure S6 (Section SE, Supporting Information) indicate the significant impact of different lithium metal foil thicknesses and diameters on performance. While we varied the thickness ratio between lithium and indium metal foil, we maintained the composition (i.e., volume and capacity). By comparing delithiation capacities in Figure S6 (Supporting Information), we identify an optimum for the lithium metal foil thickness of 100 µm (and 6 mm diameter) combined with 100 µm indium foil (and 9 mm diameter). We anticipate that using thinner or thicker lithium metal foils will create blocking indium layers or reduce the active area, respectively, resulting in lower effective stripping capacities. We suspect that these factors lead to reduced comparability and inaccurate conclusions across various reports in literature, especially when thinner lithium metal foil was used to match the areas of both foils during preparation.

The thickness ratio between the indium and lithium metal foil appears to be a critical factor that may hinder sufficient lithium transport in the two-phase eutectic. Accordingly, the thickness of the lithium foil should be chosen to match the dimension of the indium foil (see calculation in Section SE, Supporting Information). We suggest a thickness ratio of d_{Li}/d_{In} between 0.9 and 1 to avoid blocking indium layers, while ensuring a sufficient alloying reaction up to the interface with the SE. This also compensates for the loss of lithium inventory due to passivation reactions with the SE or trace amounts of moisture inside SSBs and during preparation. However, this suggested ratio results in the lithium foil having a smaller area than the indium foil.

For $In/Li_{composite}$, the incorporation of SE requires precise adjustment of components to increase the effective ionic conductivity, while maintaining appropriate electronic percolation paths

© 2024 The Author(s). Advanced Energy Materials published by Wiley-VCH GmbH

ADVANCED SCIENCE NEWS
www.advancedsciencenews.com

ADVANCED ENERGY MATERIALS
www.advenergymat.de

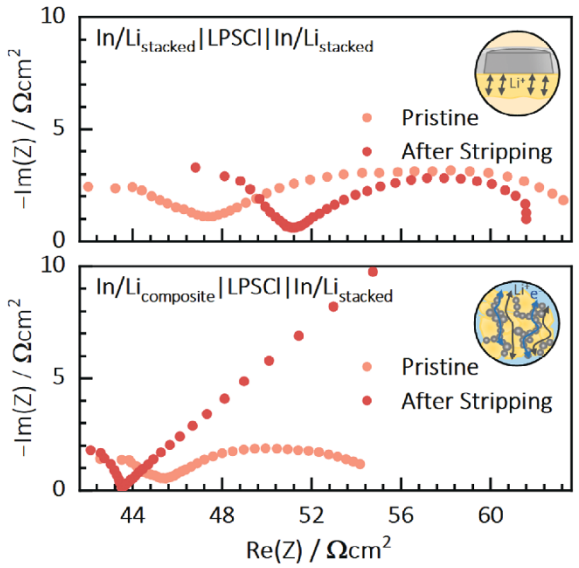

Figure 5. Results of impedance measurements of In/Li$_{stacked}$ (top) and In/Li$_{composite}$ (bottom) cells (WE | LPSCl | In/Li$_{stacked}$) during unidirectional galvanostatic stripping at 0.5 mA cm^{-2}, 25 °C, and 30 MPa with a cut-off potential of 1 V (corresponding to the same cells in Figure 3). Impedance spectra are recorded both before (pristine, light red) and after the delithiation experiment (dark red). The high impedance evolving at 43.6 Ω cm^{-2} indicates a blocking behavior (i.e., full lithium depletion) for In/Li$_{composite}$ after stripping.

within the 3D structure. It is crucial to ensure that excess SE does not obstruct the electronic percolation paths and create isolated metallic domains. At the same time, the indium particles provide sufficient electronic conductivity and contact during ongoing stripping. In our study, we carefully adjusted the volume fraction of SE and In/(InLi)$_x$, assuming complete alloying of lithium with indium and surplus indium, to be ≈64 and 36 vol%, respectively.[16] The particle sizes of the initial lithium and indium metal powder are also expected to influence percolation paths, although investigating this aspect falls outside the scope of this work.[12]

To further investigate the origin of capacity limitation, impedance spectra were recorded for both electrode types. **Figure 5** shows the impedance spectra of In/Li$_{stacked}$ (top) and In/Li$_{composite}$ (bottom) in WE | LPSCl | In/Li$_{stacked}$ configuration. Spectra were recorded both before (depicted in light red) and after (dark red) the delithiation experiments and correspond to the same cells tested at unidirectional galvanostatic stripping currents of 0.5 mA cm^{-2} in Figure 3. The initial impedance of In/Li$_{composite}$ is slightly lower compared to In/Li$_{stacked}$. We believe this is caused by the enhanced contact area between the SE and the composite electrode due to its 3D structure and densification during cell assembly. Hence, we anticipate a lower impedance for this electrode type.

At the end of the delithiation experiments, severe cell polarization is observed for both electrodes (see Figure 3). Usually, the primary reason for polarization effects (i.e., overpotentials) in SSBs with LMAs is current constriction resulting from void formation at the anode at high current densities and too low applied pressure.[47,48] In the case of In–Li anodes, lithium stripping is impeded due to concentration polarization, as discussed in detail for Li–Mg alloy anodes.[53–55] This limitation may be attributed to sluggish lithium transport and constraints (i.e., lithium deficiencies) within the respective electrode material or incomplete lithium intermixing during the preparation process. The latter applies to most of the preparation methods tested (see Figure 3).

During ongoing stripping of In/Li$_{stacked}$, pure indium precipitates (i.e., layers with a deficiency in lithium) form, as observed by Jeong et al.[42]). Later, we suspect that the electrode polarizes due to blocking properties of precipitated indium near the interface. Ultimately, this may lead to a reduction in active area, and current constriction at high depletion levels may dominate the electrode kinetics (similar to void formation in LMAs). Analyzing In/Li$_{stacked}$, the lithium flux gets insufficient after extracting high lithium capacities. Hereby, the cut-off potential of 1 V corresponds to a dc-resistance of ≈2 kΩ cm^{-2}. However, the impedance spectrum following the cut-off ("after stripping") shows an impedance of ≈61 Ω cm^{-2}. This discrepancy in resistance indicates a rapid relaxation of the electrode, suggesting that a complete lithium depletion was not achieved (i.e., small domains of InLi remain). Both OCV and impedance relaxation experiments in Figure S7 (Section SF, Supporting Information) show, that the impedance quickly recovers after the cut-off potential was reached. We like to emphasize that Lee et al.[49] reported similar observations of a rapid recovery of lithium voids within minutes following delithiation experiments. Please note, that the degree of relaxation may only be minor for very deficient systems and that the diffusion inside of In/Li$_{stacked}$ can be further affected by its geometry (see Section SE, Supporting Information).

In contrast, the impedance spectrum ("after stripping") of In/Li$_{composite}$ shows a drastic impedance increase at 43.6 Ω cm^{-2}, indicating a different cause of polarization. The presence of percolation paths for ions and electrons within the composite enhances lithium replenishment during the delithiation experiment. Consequently, we assume that the blocking behavior of the electrode occurs once most or all active lithium is consumed, and large indium-rich (lithium-ion blocking) or inactive domains prevent subsequent relaxation of the electrode due to increasing tortuosity. We believe that this indicates a significant deterioration of the composite structure, which is preventing a recovery of lithium over time (i.e., the replenishment of lithium). This can be observed in Figure S7 (Supporting Information), indicated by the high impedance at low frequencies. It is important to highlight again that inactive or reacted lithium (e.g., during SEI formation) may persist and the lithium transport in composite electrodes may rely on the particle sizes of each component and their respective ratio.[12]

In order to verify the previous conclusion about the electrode microstructure and resulting impedance contributions, cross sections of both In–Li electrode types were prepared by ion-beam polishing and examined by SEM (**Figures 6** and **7**). Using EBSD, phase and inverse pole figure (IPF) maps of In/Li$_{stacked}$ in pristine (top), plated (middle), and stripped (bottom) state were obtained and are shown in **Figure 6**. Both non-pristine electrodes were extracted from a symmetric cell (In/Li$_{stacked}$|LPSCl|In/Li$_{stacked}$; Figure 3).

In the phase maps, the indium and InLi phase regions are colored purple and yellow, respectively. As expected from above

© 2024 The Author(s). Advanced Energy Materials published by Wiley-VCH GmbH

ADVANCED SCIENCE NEWS
www.advancedsciencenews.com

ADVANCED ENERGY MATERIALS
www.advenergymat.de

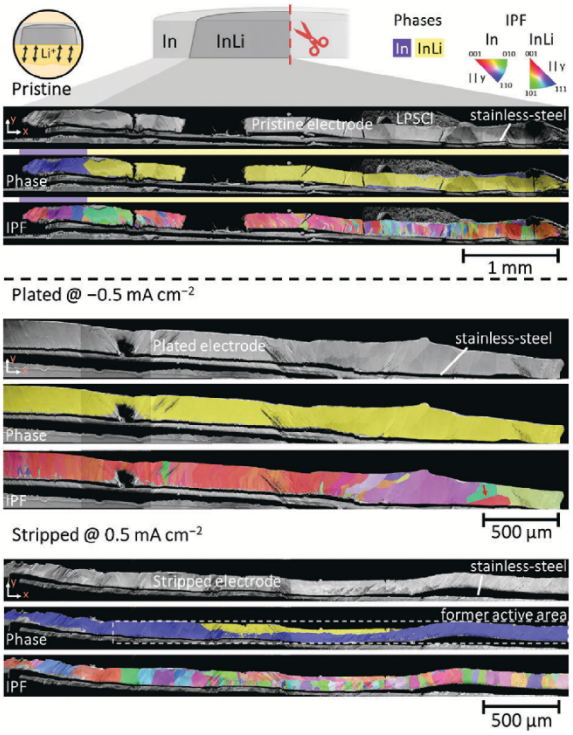

Figure 6. Polished cross sections of In/$Li_{stacked}$ in pristine (top), plated (middle), and stripped state (bottom). SEM images are complemented by phase and IPF maps (given parallel to the y-direction) for indium and intermetallic InLi to reveal their microstructure using EBSD. The WE (stripped) and CE (plated) of unidirectional galvanostatic experiments at 0.5 mA cm^{-2}, 25 °C, and 30 MPa with a cut-off potential of 1 V were studied (Figure 3). For the stripped state, the former active area is approximated and depicted by the dashed rectangular box (white). Parts of the electrodes fell off during sample preparation. One grain exhibiting pseudo-symmetry remains for the plated electrode (marked by a red arrow).[56]

results, and consistent across all samples, no electron backscatter patterns (EBSP) matching the crystal structure of lithium metal were found by the Hough indexing algorithm. IPF maps show the microstructure and grain orientation of both phases parallel to the y-direction. For comparison, a reference measurement of a pristine indium metal foil is provided in Figure S8 (Section SG, Supporting Information).

In the pristine Li/$In_{stacked}$ (top), there is a distinct lateral phase separation between indium metal and InLi. The outer (left) side is composed of indium, while the inner side (right) consists of InLi. This separation is due to the different diameters of the indium and lithium metal foils used during electrode preparation. Consequently, the initial active area is reduced by approximately 1.5 mm in diameter, aligning with our previous assumptions and calculations. Additionally, a thin indium layer (≈20 µm) is visible at the interface to the SE (right side), suggesting an incomplete alloying reaction. A larger magnification of these areas, including selected EBSPs, is added in Figure S9 (Section SH, Supporting Information).

However, since In/$Li_{stacked}$ performed well in the previous tests (Figure 3 and Figure S5, Supporting Information), we consider the effect of such a thin indium layer to be insignificant. Again, we emphasize the importance of matching the thickness of both foils during preparation, as discussed previously. Residuals of lithium metal at the interface to the stainless-steel current collector could not be identified. Examining the IPF map (in y-direction), broad pristine indium grains (up to 100 µm) are observed, while thinner, columnar grains with preferential orientations close to <411> (pink) and <401> (orange) are identified for InLi. The grains of indium at the interface to the SE were smaller (thickness ≈20 µm) and showed a finer microstructure, while the grains of both indium and InLi expanded from the current collector to the SE interface in a columnar shape.[56] In comparison to pristine indium metal foil (Figure S8, Supporting Information), the pre-lithiated InLi grains exhibit a thinner, yet still columnar, shape.

A lithiated In/$Li_{stacked}$ electrode (middle) was analyzed, which served as the CE in Figure 3. The electrode was charged (i.e., lithiated) to nearly ≈99% of its theoretical capacity ($q_{th,lith}$ = 7 mAh cm^{-2}) within the In/$(InLi)_x$ phase field in our study. The phase map indicates a uniform layer growth with the formation of InLi during lithiation, as indium is entirely consumed in the alloying process. This suggests expansion in the active area to access all indium metal (i.e., during the first charging step of full-cells). In fact, we could not localize the former phase boundary of now lithiated indium and pre-lithiated InLi in any map, while we again measured the outer part of the electrode. Higher-lithiated indium alloys, such as In_4Li_5 and In_2Li_3, were not detected. Upon examination of the IPF map, no distinct microstructure was found for the electrochemically-formed InLi phase. Instead, a homogeneously deposited InLi layer and its columnar grain growth in preferential orientations (close to <100>, <030>, and <401>) of the pre-lithiated InLi was observed (pink and orange). The columnar shape of the observed InLi grains appears to be thinner than that of indium, which may be attributed to its moderate homologous temperature at room temperature.

For the stripped electrode (bottom), a bi-layered structure is observed, with InLi at the SE-side and pure indium at the current collector side, consistent with the findings of Jeong et al.[42] Thus, this contrasts with common assumptions that blocking indium layers develop at the SE interface during the early stages of stripping at a moderate rate.[16,34,45] Furthermore, it supports the assumption that the high lithium diffusion within the InLi phase enables gradual delithiation from deeper areas of the electrode, leaving InLi at the interface until high depletion levels are reached.[42] This result also reinforces the conclusion of significant current constriction and reduction in the active area by indium precipitates at the interface at high depletion levels, as observed by the delithiation and impedance measurements (Figures 3 and 5, respectively). The IPF map reveals columnar grains for indium (≈100 µm width), particularly within the delithiated region, restoring a microstructure similar to the pristine indium metal foil (Figure S8, Supporting Information). The remaining InLi grains again show a preferential orientation – similar to the pristine state – close to <411> (pink) and <401> (orange).

In our tests, the intermetallic InLi exhibits a columnar microstructure with grains of thinner sizes compared to indium, while showing preferential orientations across all samples. During plating, the InLi forms in the same preferential orientations

© 2024 The Author(s). Advanced Energy Materials published by Wiley-VCH GmbH

ADVANCED SCIENCE NEWS
www.advancedsciencenews.com

ADVANCED ENERGY MATERIALS
www.advenergymat.de

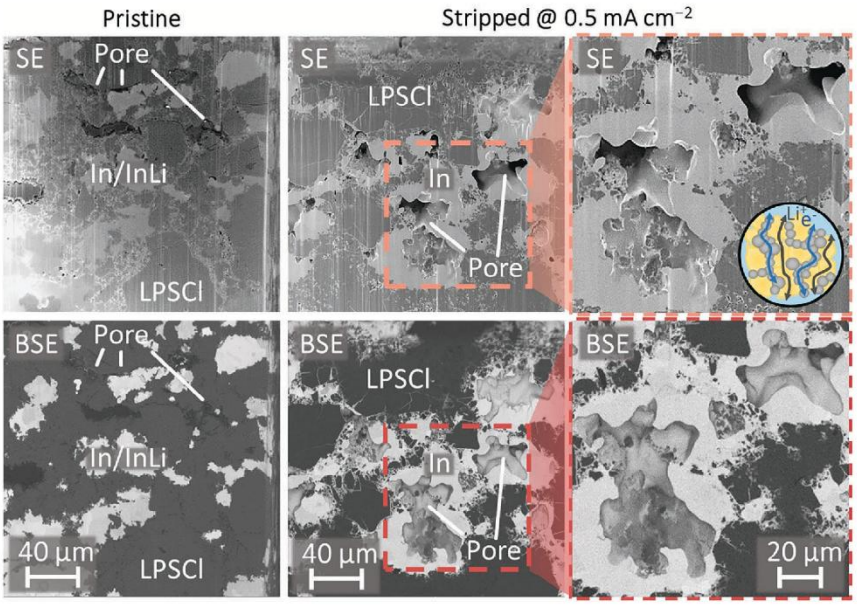

Figure 7. SEM images of a pristine (left) and a fully stripped In/$Li_{composite}$ electrode (middle and right). The cross sections are prepared by focused ion-beam (FIB) milling to reveal the morphology and structure changes after delithiation experiments at 0.5 mA cm^{-2} (cut-off at 1 V), 25 °C, and 30 MPa (Figure 3). The vertical lines observed in the SE imaging are attributed to curtaining effects resulting from the cross section preparation.

as the pre-lithiated InLi. Broad indium grains are obtained during stripping. The incomplete alloying to the interface in the pristine electrode, and the location of residual InLi in the stripped electrode are observed. These observations may be attributed to uneven pressure distribution caused by the stiffness of the InLi phase or other material or preparation inhomogeneities. The electrode thickness changes from its pristine state (≈150 µm) to 170 and 100 µm in the plated and stripped state, respectively. The observed thickness for the plated state is slightly lower than the volumetric predictions based on crystallographic data for the transition from In to InLi.[37]

The combined electrochemical and EBSD results provide strong evidence for: 1) the importance of properly matching both metal foils during cell preparation (see Figure S6, Supporting Information), 2) the minimal impact of inhomogeneous (i.e., incomplete) alloying for the preparation used, 3) the favorable lithium diffusion properties of InLi (i.e., prelithiated electrodes), which improve electrode kinetics and allow access to deeper regions of the electrode, 4) the significant current constriction caused by lithium-deficient indium layers at high depletion levels, and 5) the high accessible capacity during stripping and plating for In/$Li_{stacked}$.

Figure 7 shows the cross sections of In/$Li_{composite}$ in the pristine state (left) and stripped state (middle and right) to reveal the microstructural changes of In/$Li_{composite}$ during stripping. Considering both imaging modes – secondary (SE) and backscattered electrons (BSE) – grain boundaries, morphology details, and material density become evident, respectively. The pristine electrode exhibits a compact structure with only a few irregularly shaped pores (left). The pressure of 380 MPa used for the pristine sample enables high densities. In contrast, the stripped electrode (magnified in the right column) reveals significant pores within the metal fraction of the composite. Hence, this observation indicates a significant deterioration of the composite structure. Moreover, it is worth noting that a smooth morphology of pores is observed. These pores likely indicate the former locations of the InLi phase within the In–Li eutectic or suggest the precipitation of indium on preferred nucleation sites during lithium removal. Apparently, the applied stack pressure of 30 MPa is too low to effectively close the evolving pores during stripping.

Analyzing the material contrasts in the BSE imaging (bottom), three phases are observed in the pristine electrode, while only two phases can be identified for the stripped electrode. In both cases, LPSCl appears significantly darker and it is difficult to distinguish between the brighter particles of In and InLi. This lack of differentiation may be attributed to the effective intermixing or close bulk densities of indium metal and the intermetallic InLi phase (7.31 g cm^{-3} and 5.16 g cm^{-3} (ICSD: 51 960), respectively).

Lastly, it is noteworthy that the non-pristine samples of both electrode types in this microstructural study may not resemble the actual case, if used in full-cell configuration. The nominal CE capacity (here: $q_{th,lith}$ = 7 mAh cm^{-2}) usually exceeds that of the cathode side (i.e., of the CAM), resulting in less phase and volume changes. Moreover, irregularities, inhomogeneities, and incomplete processes during repetitive cycling may further affect the chemomechanical results in full-cell configuration, which we discuss later.

2.4. Reversible Cycling Performance in Full-Cell Configuration

Shifting reference potentials of the CE and significant overpotentials cause early termination of the (dis-)charge process of batteries, and poor capacity utilization. Hence, after

© 2024 The Author(s). Advanced Energy Materials published by Wiley-VCH GmbH

ADVANCED SCIENCE NEWS
www.advancedsciencenews.com

ADVANCED ENERGY MATERIALS
www.advenergymat.de

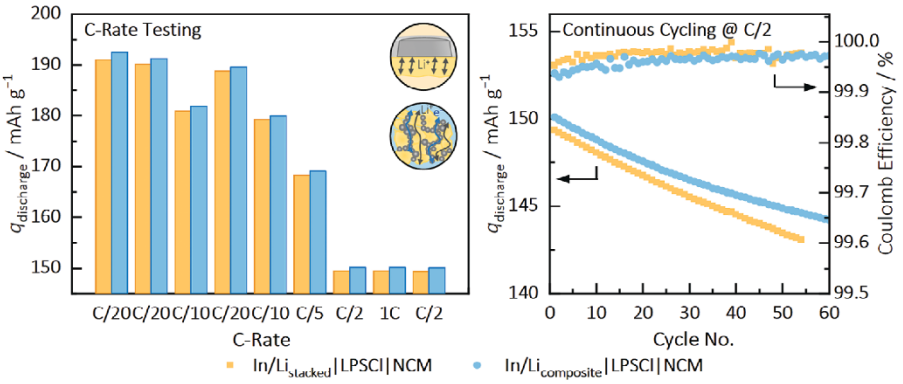

Figure 8. Results of C-rate capability tests, followed by continuous cycling for In/Li$_{stacked}$ (yellow) and In/Li$_{composite}$ (light blue), utilized as CE in fullcell configuration (CE | LPSCl | NCM). Discharge capacities for each cycle at various C-rates (left), as well as the discharge capacities and Coulomb efficiency throughout continuous cycling (right), are presented (one cell for each electrode type, measured at 25 °C and 75 MPa).

assessing the performance under rate-limiting conditions in unidirectional delithiation experiments (Figure 3 and Figure S3, Supporting Information), we advance to evaluate the reversibility and kinetic performance (i.e., overpotentials) of both electrode types in full-cell configuration. Consequently, we employ three different experiments to analyze these important attributes in single cells during galvanostatic cycling. For this, we utilized $LiNi_{0.82}Co_{0.07}Mn_{0.11}O_2$ (NCM) cathode composites (as WEs) with a nominal capacity of 1.85 mAh cm^{-2}, which are referenced to the examined In/(InLi)$_x$ CEs.

First, a C-rate test spanning from C/20 to 1C (corresponding to 0.0925 and 1.85 mA cm^{-2}) was conducted in full-cells (CE | LPSCl | NCM). The results, shown in **Figure 8** (left), indicate high discharge capacities at low C-rates (≈190 mAh g^{-1} at C/20), which decrease with increasing C-rate (≈150 mAh g^{-1} at 1C) for both anode types. Across all rates, slightly higher discharge capacities were achieved with In/Li$_{composite}$.

Second, for a more detailed analysis, the cells were cycled at C/2 (≈0.925 mA cm^{-2}) to assess capacity retention and capacity efficiency during continuous cycling (right). The first ten cycles of the continuous cycling are depicted in Figure S10 (Section SI, Supporting Information). Full-cells with both In–Li anodes exhibited capacity retentions of ≈96 % for the first 55 to 60 cycles. Potential losses may be attributed to volume contraction of NCM, leading to loss of contact and inactive NCM particles, or degradation reactions at the anode and cathode side.[57] Although the results of these tests are mainly focused on the cathode performance, the Coulomb efficiency serves as a first, valuable indicator of the high reversibility and cycling performance of both anodes. For each anode, Coulomb efficiencies exceeding 99.9 % were achieved in each cycle, confirming the suitability of both In–Li anodes at the tested rates for extended cycling durations. Combining all observations, our results are higher or comparable to reports in literature and prove the high capacity utilization and efficiency by both electrode types at various rates and for continuous cycling.

For a more detailed examination of the anode performance, we deconvoluted the contributions of WE and CE using a 3E fullcell configuration (CE | LPSCl | NCM), with a lithiated gold wire serving as the RE.[16,20] Therefore, we monitored the individual potentials of both electrodes in reference to the RE, while performing C-rate tests (as conducted previously). The overpotential of the In–Li CE during cycling for one cycle at each rate (C/20, C/10, and C/5) and five cycles at C/2 is shown in **Figure 9**. The corresponding potentials of the NCM cathode (WE) are presented in Figure S11 (Section SJ, Supporting Information).

For In/Li$_{stacked}$ (left), the overpotential during discharge rose from 8 to 26 mV for C/20 to C/5, respectively. For cycling at C/2 (corresponding to ≈0.925 mA cm^{-2}), the overpotential increased up to 58 mV. During charging, the overpotentials increased from −16 up to −79 mV for C/20 to C/2, respectively. For In/Li$_{composite}$ (right), potential profiles appear smoother and overpotential peaks are reduced, especially during discharge. Nevertheless, the overpotentials during discharge are still very similar to In/Li$_{stacked}$. The charging overpotentials are elevated for low C-rates (−13 to −46 mV for C/20 to C/5, respectively) and slightly reduced (to −76 mV for cycling at C/2). Moreover, these results demonstrate (complementary to the unidirectional galvanostatic measurements), that the anode compositions remain within the In/(InLi)$_x$ two-phase field for the cycled capacity. However, our findings underscore the contrary to common belief, i.e., clear rate limitations by both In–Li anode types at such rates. Thus, this can create an additional performance bottleneck and hinder the accurate benchmarking of cathode performance, particular when it comes to high capacities and rates.

We regard the measured overpotentials of this study as sufficiently low, also compared to the cathode potentials in Figure S11 (Supporting Information), to enable the independent evaluation of solid-state cathodes for the tested current densities. However, we anticipate that increasing rates will lead to substantial overpotentials affecting this task (see Figure S4, Supporting Information). During unidirectional galvanostatic measurements, we consider overpotentials exceeding 100 mV to be concerning. This becomes evident when comparing potential profiles. Significant overpotentials of the CE during the end of charge and discharge processes result in inaccurately referenced WE potentials. This early termination of charging and discharging processes leads to incomplete lithium utilization of the NCM cathode and capacity losses. Considering an overpotential of 100 mV results in capacity losses of 0.4 and 20 mAh g^{-1} for early-terminated

© 2024 The Author(s). Advanced Energy Materials published by Wiley-VCH GmbH

ADVANCED SCIENCE NEWS
www.advancedsciencenews.com

ADVANCED ENERGY MATERIALS
www.advenergymat.de

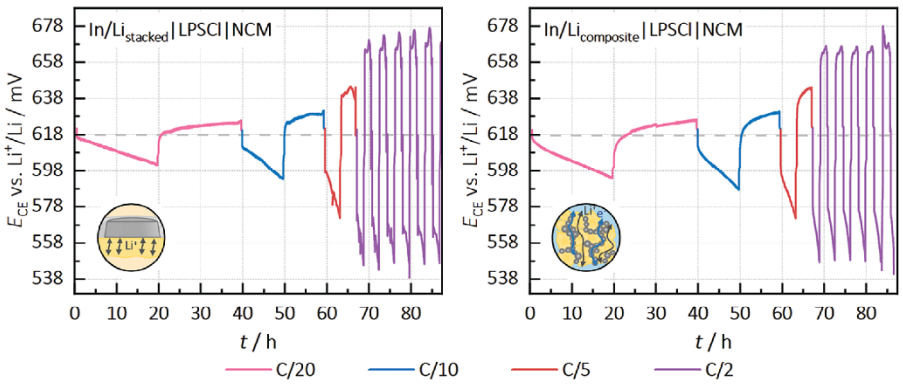

Figure 9. Results of anode kinetic measurements during C-rate capability tests for In/Li$_{stacked}$ (left) and In/Li$_{composite}$ (right), utilized as CE in 3E configuration (CE | LPSCl | NCM with lithiated Au-RE). The CE potential profiles (vs Li$^+$/Li) are presented (one cell for each electrode type, measured at 25 °C and 75 MPa).

discharge and charge processes, respectively. This is also indicated in Figure S10 (Supporting Information). Therefore, appropriate preparation and selection of the CE with suitable kinetics will enhance capacity retention and facilitate the accurate attribution of cathodic effects.

Ikezawa et al.[41] reported similar overpotentials (≈20 mV) for stacked In–Li anodes in full-cell configuration and current densities of ≈0.73 mA cm^{-2} (equivalent 1C in this case). However, they did not provide further information on the Li:In ratio and composition used but observed a significant early termination of (dis-)charging processes, indicating inferior lithium utilization. To the best of our knowledge, Nam et al.[16] first utilized In–Li composites. They reported overpotentials (>100 mV) at low current densities of 0.11 mA cm^{-2}, and even higher overpotentials (>500 mV) at current densities of 1.1 mA cm^{-2}. We attribute these limitations to the low SE content (10–20 wt.%), insufficient ionic percolation paths to deeper regions, and potentially different electrode loadings. Yanev et al.[44] compared In–Li foils and composites and reported overpotentials of up to 250 and 700 mV, respectively, at current densities of 0.28 mA cm^{-2}. However, they noted the early termination of discharge due to increased overpotentials of the foil anode at higher degrees of anode delithiation, whereas it dropped to 20 mV for the composite type. Hence, they consider the composite anode to be more suitable for higher (dis-)charging rates. Concludingly, our results show significantly lower overpotentials for both electrode types at similar or higher (dis-)charging rates compared to reports in literature. However, we could not observe superior kinetics for the composite type used in our tests.

Comparing our results and the available reports in literature, we identify performance variations among electrodes prepared in different laboratories. This is further complicated by inconsistent rate testing, which can lead to misleading conclusions and evaluations across different studies. We emphasize the importance of establishing consistent fabrication and testing protocols, particularly regarding the compositions (In:Li ratio), testing rates, and capacities of In–Li anodes. This is crucial for comparative analysis to better comprehend the mechanisms and kinetics of In–Li electrodes and enhance their suitability as CEs.

Lastly, our objective is to investigate the volume changes of both electrodes during repetitive galvanostatic cycling. Therefore, we analyzed full- cells (CE | LPSCl | NCM) using an uniaxial laboratory press equipped with an active pressure control. This allowed us to maintain constant stack pressure independent of the changes in cell stack thickness during cycling. We opted to utilize NCM as CAM instead of zero-strain materials (such as $Li_4Ti_5O_{12}$) to examine the chemomechanical reversibility of high-voltage full-cells with a high-strain anode. The absolute volume changes of In/(InLi)$_x$ anodes clearly surpass those of NCM.[37,57]

Figure 10 depicts the recorded height changes Δh (top) during galvanostatic cycling (bottom) at C/2 (equivalent to ≈0.925 mA cm^{-2}) for In/Li$_{stacked}$ (left) and In/Li$_{composite}$ (right) for the first five cycles. Unfortunately, continuous high-precision measurements of height changes are hindered by variations in room air-conditioning operation. Considering the height profiles with stable background contributions of a few cycles, the high chemomechanical reversibility observed for ≈40 cycles is remarkable (shown in Figure S12, Section SH, Supporting Information). Jin et al.[35] suggested that porous anode microstructures, evolving during stripping processes, may compensate for volume changes in planar In–Li anodes for LIBs. In our case, the observation of pores and voids inside In/Li$_{composite}$ (as shown in Figure 7) indeed indicates a positive effect on reducing or stabilizing anode height changes. Notably, this result motivates more systematic chemomechanical studies on the characteristics of composite electrodes and the effect of stack pressure (in our case: 75 MPa), potentially closing evolving pores. Consequently, the results of cathode composite studies may support and expedite these efforts for anode composites.[12] For instance, Sakka et al.[58] investigated the influence of pressure on the microstructure (i.e., porosity, contact area, and tortuosity) concerning the electrochemical properties of cathode composites.

Unfortunately, relative height changes (in respect to the initial electrode thickness) are difficult to quantify, especially for the stacked electrode. Despite the background noise, we quantified the absolute height changes by assuming 1D strain, which is constrained by the cell casing. In the cathode composite, the volume fractions of LPSCl and NCM are 61 and 39 vol.% (neglecting carbon additives). Hence, a volume difference of 3%[37,59]

© 2024 The Author(s). Advanced Energy Materials published by Wiley-VCH GmbH

ADVANCED SCIENCE NEWS
www.advancedsciencenews.com

ADVANCED ENERGY MATERIALS
www.advenergymat.de

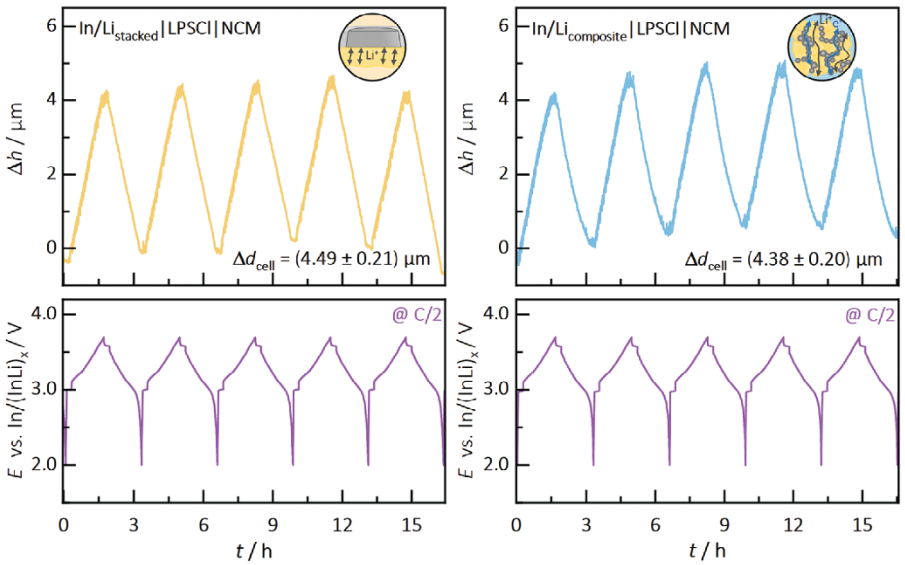

Figure 10. Results of the chemomechanical measurements for continuous cycling at C/2 for In/Li$_{stacked}$ (left) and the In/Li$_{composite}$ (right), utilized as CEs in full-cell configuration (CE | LPSCl | NCM). The height change (Δh, top) and the corresponding full-cell potential profile (vs In/(InLi)$_x$, bottom) are presented for the first five cycles (one cell for each electrode type, measured at 25 °C and 75 MPa).

between charged and discharged states of NCM particles corresponds to a maximal height change of $\Delta d_{NCM} \approx 0.4$ µm. If clearly disturbed cycles (for 40 cycles in Figure S12, Supporting Information) are neglected, the mean height differences ($\Delta d_{In-Li} = \Delta d_{cell} - \Delta d_{NCM}$) of In/Li$_{stacked}$ and In/Li$_{composite}$ result as 3.98 (±0.21) and 4.09 (±0.20) µm, respectively, between charged and discharged states. While these values differ from the theoretical values (≈2.6 µm, calculated from crystallographic data),[37] they are in line with calculations (≈3.9 µm) based on the experimental data of Koerver et al.[57] Apparently, with the setup used and the resolution obtained, we did not observe clear differences between the two electrode types, even though the formation of pores in the particle-based composite electrode could be observed previously. As discussed above, the applied stack pressure may have affected the effective height change of each electrode type. These results highlight the need for high-resolution dilatometry investigations for more precise chemomechanical analysis of electrode materials and composites.

Due to the high chemomechanical reversibility (≈40 cycles, Figure S12, Supporting Information), we anticipate that both In–Li electrodes provide suitable chemomechanics for repetitive cycling in full-cell configuration. The chemomechanical properties of In–Li may even stabilize stack pressure and improve the overall cell performance by counteracting the expansion and shrinkage of NCM particles during cycling.[13,14] We consider the changes in height of ≈4 µm as small to moderate compared to the projected thickness of an optimized SSB cell of ≈150 to 200 µm. However, we suggest that volume changes need to be considered in the evaluation of the cell performance and chemomechanical properties, as it will strongly depend on the type of electrode.

In summary, we observe high reversibility and sufficiently fast electrode kinetics combined with consistent chemomechanical changes during cycling for the two In–Li electrode types tested inside the two-phase eutectic In/(InLi)$_x$. High Coulomb efficiencies, low overpotentials, and predictable volume changes (tested at ≈1 mAh cm^{-2}, C/2) contribute to accurate investigations for ongoing lab-scale studies at moderate capacities, aiding in the advancement of solid-state cathodes. Nevertheless, both In–Li electrode types may require further optimization to align with the (dis-)charge rates of state-of-the-art batteries at 1C (≈3.5 mA cm^{-2}) and with future high-capacity cathodes. Therefore, the transport kinetics (i.e., overpotentials) and rate capabilities need to be adjusted, optimized, and balanced as needed during the anode preparation process.

Both types of electrode rely on the precise adjustment of composition (i.e., the molar ratio of lithium and indium metal),[19] and further optimization may be achieved through systematic variation of geometric parameters. Given its limited potential for adjustment and optimization, we assess the transport kinetics of In/Li$_{stacked}$ as feasible, but only sufficient for modest testing protocols at low to moderate rates and capacities. It is important to highlight the susceptibility to improper kinetics resulting from the selection of different thicknesses for indium and lithium metal. Based on our tests, we recommend using a thickness of 100 µm for both metal foils, with a smaller area allocated for lithium metal. For advanced performance tests, In/Li$_{composite}$ demonstrated its effectiveness in this study, exhibiting slightly lower overpotentials and improved electrochemical as well as chemomechanical reversibility to stabilize testing conditions. This conclusion is further supported by the versatility of the composite type to precisely adjust composition and kinetic performance to individual conditions, starting at a ratio of 60:40 wt.% for In/(InLi)$_x$:SE. These results are in good agreement with the report by Yanev et al.[44] At this point it is important to note, if complete delithiation occurs, a significant deterioration of the composite structure was observed, which has a profound impact on its properties.

© 2024 The Author(s). Advanced Energy Materials published by Wiley-VCH GmbH

Our microstructural analysis of different In–Li anode types, along with reports in the literature, underscores the critical importance of selecting the appropriate types of In–Li anode, understanding the challenges during anode preparation, and recognizing the performance variations among electrodes prepared by different researchers and laboratories. Therefore, this emphasizes the necessity for comprehensive reports in literature, the specified preparation of In–Li anodes, and transparent analysis.[46,50] Notably, solely stating the C-rate without providing the absolute capacity or current density decreases the effective (interlaboratory) comparability of reported values and results. Furthermore, we agree with Aspinall et al.[34] regarding the potential of phase field modeling of the eutectic $In/(InLi)_x$ to provide further insight into the effects of alloy inhomogeneity and spatial lithium deficiencies on electrode kinetics and transport properties. We anticipate that this will contribute to a more refined microstructural understanding of each type of anode, complement our experimental studies, and aid in the establishment of appropriate preparation criteria and guidelines.

3. Conclusion

We compare seven In–Li alloy electrode types within the $In/(InLi)_x$ two-phase field to assess their suitability as electrochemically stable and reliable CEs in the investigation of lab-scale solid-state cathodes. In doing so, we illustrate the specific challenges in preparing both planar and particle-based anodes, highlighting possible errors and the importance of interlaboratory comparison. Through unidirectional galvanostatic experiments we identified the most effective anode types, namely stacking foils of both metals and a mixture of corresponding metallic powders and SE. Both demonstrated effective intermixing, high effective accessibility of lithium, and consistent potential profiles for (dis-)charging rates up to 1.5 mA cm^{-2} (equivalent to capacities of 1.5 mAh cm^{-2} at 1C). Dendrite formation was not observed, even at high current densities of 5 mA cm^{-2}. SEM and EBSD analysis revealed additional insights in the underlying microstructure and the influence of preparation parameters. When used in full-cells, both anodes exhibited good reversibility and sufficiently fast electrode kinetics as CE to facilitate ongoing lab-scale studies at moderate capacities for the advancement of solid-state cathode composites.

High Coulomb efficiencies, low overpotentials (tested at ≈1 mAh cm^{-2}), and predictable volume changes contribute to stable potential referencing and the accurate attribution of cathodic effects in cathode studies. However, the In–Li electrodes evaluated in this study may require further optimization in terms of composition, microstructure and transport properties to match the (dis-)charging rates of state-of-the-art batteries at 1C (≈3.5 mA cm^{-2}) and future high-capacity cathodes. While the stacked foil anode type is simple to prepare, it requires a retention period to ensure proper performance. Composites can be easily tuned and balanced to meet specific requirements (i.e., favorable transport kinetics and high-rate capabilities). Our results highlight the need to optimize the microstructure of eutectic electrodes to keep pace with the continuous improvement of CAMs, SEs and solid-state composites. We emphasize the importance of using the knowledge gained from microstructural studies on cathode composites and studies of the In–Li system to advance anode composites and other intermetallic lithium alloys, respectively.

4. Experimental Section

All experimental procedures were carried out in an argon-filled glovebox (*LabMasterPRO*, MBraun, Garching, Germany), with $p(O_2)/p$ and $p(H_2O)/p < 1$ ppm.

Preparation of In–Li Anodes: Alloys were prepared in the two-phase eutectic phase field $In/(InLi)_x$, which exhibits a constant potential of E_H (vs Li^+/Li) = 0.62 V. In order to achieve comparable performance, every alloying process was tested with 35 at% of lithium (corresponding to $In_{0.65}Li_{0.35}$ or $In_{1-x}/(InLi)_x$ with $x = 0.55$), which was centrally located in the corresponding phase field.[19] In this study, each prepared electrode provides a lithiation capacity $q_{th,lith} = 7$ mAh cm^{-2} and a delithiation capacity $q_{th,delith} = 8.4$ mAh cm^{-2} within the $In/(InLi)_x$ phase field. These capacities correspond to the initial masses of lithium (1.7 mg) and indium metal (51.3 mg), respectively, and were maintained for each electrode type. Figure 1 illustrates each preparation method.

The first type of anode (referred to as "$In/Li_{stacked}$") was prepared by placing lithium foil (100 µm thickness, 6 mm diameter, 99.9 %, China Energy Lithium, China) behind indium foil (100 µm thickness, 9 mm diameter, 99.999 %, ChemPUR, Germany) during cell assembly. This most simple preparation requires the complete dissolution of the lithium into the indium foil, in order to approach the $In/(InLi)_x$ two-phase state.

Direct alloying was tested by two mechanical mixing methods, similar to the works of Dugas et al.[18] and Hennequart et al.[60] Lithium foil was placed between two larger indium sheets and folded repeatedly. After roughly three repetitions it turned dark and stiff, making further processing difficult. Before each folding, the stack was compressed either by a hot press ("$In/Li_{pressed}$") or a calander ("In/Li_{rolled}") at 120 °C. Each resulting foil was then flattened to a thickness of ≈100 µm and anodes with a diameter of 9 mm were punched out.

In–Li anodes made out of powder were prepared by two different preparation methods. Lithium metal powder was synthesized by (droplet) emulsion using an in-house-built setup, as described elsewhere.[61] Indium powder (≈325 mesh, 99.99+ %, abcr, Germany) and lithium metal powder were mixed for 15 min at 15 Hz using a *Pulverisette 23* mini mill (Fritsch, Idar-Oberstein, Germany) and three ZrO_2 balls (5 mm diameter) to obtain a homogeneous In–Li alloy powder ("In/Li_{powder}"). Alloyed In–Li powder ("$In/InLi_{powder}$") was obtained from melt by the same droplet emulsion process. Therefore, the required amount of indium powder was added to the inert medium (prior to lithium metal).

In–Li alloy composite anodes ("$In/Li_{composite}$" and "$In/InLi_{composite}$") were prepared from powders described earlier. Each alloy powder was thoroughly mixed with SE (Li_6PS_5Cl) in a ratio of 60:40 wt.% using a *Pulverisette 23* mini mill (Fritsch, Idar-Oberstein, Germany) in the same way as described earlier. This corresponds to volume fractions of 64.4, 24.2, and 11.4 vol.% for LPSCl, indium, and lithium metal, respectively. Due to the poor control of intermixing and subsequent shifts in local composition, it was opted not to test composite anodes produced by grinding (to powder) of mechanically-mixed anodes.

For current density calculations, an active (anode) area of 0.785 cm^2 was assumed for the sake of simplicity. However, due to the smaller diameter (9 mm) of foil anodes, this may result in slightly higher effective current densities. In unidirectional stripping experiments, the active area might also be further reduced in the case of $In/Li_{stacked}$ anodes, as suggested by the results in Figure 6 and Figure S5 (Supporting Information).

Cell Assembly and Electrochemical Characterization: Lithium argyrodite (Li_6PS_5Cl) SE (POSCO JK Solid Solution Co., Yangsan, South Korea) was used as the separator material and in composites. It exhibited an ionic conductivity of $\sigma_{ion} = 1.1$ mS cm^{-1} at 25 °C. Single-crystalline $LiNi_{0.82}Co_{0.07}Mn_{0.11}O_2$ and carbon nanofibres (CNF) were purchased from MSE Supplies LLC (Tucson, USA), serving as CAM and carbon additive, respectively. A NCM, LPSCl, and CNF mixture (60:37:3 wt.%) was prepared by a *Pulverisette 23* mini mill (as described earlier) and was used as cathode composite for full-cell cycling.

© 2024 The Author(s). Advanced Energy Materials published by Wiley-VCH GmbH

ADVANCED SCIENCE NEWS
www.advancedsciencenews.com

ADVANCED ENERGY MATERIALS
www.advenergymat.de

Each cell was prepared by pelletizing 80 mg of solid electrolyte as separator (≈600 µm thickness) in a polyether-ether-ketone casing (10 mm diameter, equipped with stainless steel rods as contacts). Uniaxial pressure of 380 MPa was applied for 3 min at room temperature. To improve contact and densification, each anode and cathode composite was added in advance to the compression step, while each In–Li foil (9 mm diameter) was added afterward. For anode powders and anode composites 53 and 88.3 mg were used as WE, respectively. To ensure consistency, these masses were adjusted to match the lithium capacity (and composition) of the In–Li foils. For the measurement of the (time-dependent) potentials of the different In–Li anodes, Li foil (100 µm thickness, 9 mm diameter) served as CE. For unidirectional galvanostatic experiments, "$In/Li_{stacked}$" anodes were used as the CE due to their simple preparation. 12 mg of cathode composite was used for galvanostatic cycling experiments in full-cell configuration. For measurements of anode kinetics, the electrode potentials were monitored separately during galvanostatic cycling using an in-house-built 3E configuration.[20] One Au-coated tungsten wire (25 µm diameter) was centered inside a 160 mg separator layer before the densification process and served as basis for a µ-RE, as reported by Hertle et al.[20] For chemomechanical investigations during galvanostatic cycling, *CompreCells* (rhd instruments, Darmstadt, Germany) were used and assembled in the same way as described earlier. Here, 114 mg of LPSCl were used due to the larger diameter (12 mm), while the masses and foil dimensions of electrodes remained unchanged.

If not stated otherwise, electrochemical measurements were carried out at 25 °C using a Biologic *VMP 300* potentiostat (BioLogic, Seyssinet-Pariset, France) with a stack pressure of ≈30 MPa applied by external frames. The OCV was recorded for 12 h to monitor the potential of the alloy anodes after preparation. For unidirectional galvanostatic experiments (stripping), current densities of 0.5 mA cm^{-2} with cut-off potentials of 1 V were used. Before each measurement, the OCV was monitored at rest for 5h. For delithiation experiments at 0.5 mA cm^{-2}, electrochemical impedance spectroscopy (EIS) with an amplitude of 10 mV was carried out before and after applying the current. EIS was measured in a frequency range from 3 MHz to 1 Hz. For galvanostatic cycling in full-cell configuration, a series of C-rate capability tests were performed prior to initiating continuous cycling at C/2. These tests included two cycles at C/20, as well as tests at C/10, C/20, C/5, C/2, and 1C for one cycle. Full-cells were cycled in the potential range of 2.0–3.7 V vs $In/(InLi)_x$ and 2.6–4.3 V vs Li^+/Li in 3E configuration. A stack pressure of 75 MPa was applied and for C-rate calculations a theoretical capacity of 200 mAh g^{-1} was assumed for NCM. When employed, the µ-RE initially underwent lithiation for a duration of 16 h, with a current density of 1.25 µA cm^{-2} (using the excess lithium of the In–Li anode). Thereby, a layer of lithium metal was plated onto the gold following a brief Au alloying step. This provides a stable reference potential within the $AuLi_x/Li$ phase field (i.e., 0 V vs Li^+/Li). The chemomechanics were investigated by recording the height change during galvanostatic cycling at C/2. Therefore, the uniaxial laboratory press *CompreDrive* (rhd instruments, Darmstadt, Germany), equipped with a high-resolution servo drive for active pressure control (set at 75 MPa in this case), was utilized. For the calculation of corresponding volume ratios in the composite cathode, bulk densities of LPSCl and NCM were assumed to be 1.86 and 4.71 g cm^{-3} (ICSD: 131109 and 34304), respectively.

EBSD and FIB-SEM Measurements: Large-area cross section of foil anodes were first cut by hand and then ion-polished at −110 °C under an inert atmosphere using a triple ion beam cutter (*EM TIC 3X*, Leica Microsystems, Wetzlar, Germany) equipped with three argon-ion guns. Operating conditions were set to 7 kV, a current of ≈2.5 mA, and a polishing time of several hours.

Microstructural characterization was carried out using a *Gemini SEM 560* high-resolution field emission SEM (Carl Zeiss Microscopy GmbH, Oberkochem, Germany), equipped with a *Symmetry 3* EBSD detector (Oxford Instruments, Oxford, UK). The system was operated with the *Aztec 6.1* software package (Oxford Instruments, Oxford, UK). EBSPs were recorded at an excitation voltage of 15 kV and a beam current of 3.3 nA. To achieve optimal pattern quality, exposure time, pattern averaging, background correction, and shadow masking were carefully optimized. Patterns were indexed using a Hough algorithm with a resolution of 60 and 11 bands, considering the phases: tetragonal indium (ICSD 53091), cubic InLi (ICSD 51960), and cubic lithium (ICSD 44367). For mathematical data refinement, the *AZtecCrystal* software package (Oxford Instruments, Oxford, UK) was used to perform wild spikes removal followed by replacing zero solution with six neighbors and pseudo-symmetry removal.

The morphology and structure of composite anodes was investigated by means of FIB milling and SEM using a *XEIA3* (Tescan, Brno, Czech Republic). Therefore, pristine anode composites were compressed at 380 MPa beforehand, while stripped samples were investigated as a former cell stack. For imaging the cross sectional area, a U-shaped trench was milled into the surface and subsequently polished using a xenon plasma ion source. Secondary electron and back-scattered electron SEM images were recorded. In both investigations, sample transfer from the glovebox to the vacuum chamber of the SEM was carried by using the transfer module system *EM VCT500* (Leica, Wetzlar, Germany) to prevent the reaction with moisture and atmosphere.

Supporting Information

Supporting Information is available from the Wiley Online Library or from the author.

Acknowledgements

The authors like to thank Dr. Burak Aktekin and Dr. Till Fuchs for their help in preparing the manuscript and fruitful discussion. C.D.A. and J.J. acknowledge financial support by Bundesministerium für Bildung und Forschung (BMBF) within the ALANO project (Grant No. 03XP0396J). P.M., J.K.E., and J.J. acknowledge the funding by the BMBF within the FestBatt – Cluster of Competence for Solid-State Batteries (Grant No. 03XP0430A). The authors acknowledge the German Research Foundation (DFG) POLiS Cluster of Excellence (Project ID 390874152) for financing of the *CompreDrive* (rhd) device.

Open access funding enabled and organized by Projekt DEAL.

Conflict of Interest

The authors declare no conflict of interest.

Data Availability Statement

The data that support the findings of this study are available from the corresponding author upon reasonable request.

Keywords

alloy anode, cathode composite, electrochemistry, electrode kinetics, electron backscatter diffraction, lithium metal anode, solid-state batteries

Received: September 5, 2024
Revised: November 5, 2024
Published online: November 13, 2024

[1] S. Chu, A. Majumdar, *Nature* **2012**, *488*, 294.
[2] D. Larcher, J.-M. Tarascon, *Nat. Chem.* **2015**, *7*, 19.
[3] T. Krauskopf, F. H. Richter, W. G. Zeier, J. Janek, *Chem. Rev.* **2020**, *120*, 7745.

© 2024 The Author(s). Advanced Energy Materials published by Wiley-VCH GmbH

[4] T. Krauskopf, H. Hartmann, W. G. Zeier, J. Janek, *ACS Appl. Mater. Interfaces* **2019**, *11*, 14463.
[5] J. Janek, W. G. Zeier, *Nat. Energy* **2016**, *1*, 16141.
[6] M. J. Wang, E. Kazyak, N. P. Dasgupta, J. Sakamoto, *Joule* **2021**, *5*, 1371.
[7] S. Randau, D. A. Weber, O. Kötz, R. Koerver, P. Braun, A. Weber, E. Ivers-Tiffée, T. Adermann, J. Kulisch, W. G. Zeier, F. H. Richter, J. Janek, *Nat. Energy* **2020**, *5*, 259.
[8] J. Liu, Z. Bao, Y. Cui, E. J. Dufek, J. B. Goodenough, P. Khalifah, Q. Li, B. Y. Liaw, P. Liu, A. Manthiram, Y. S. Meng, V. R. Subramanian, M. F. Toney, V. V. Viswanathan, M. S. Whittingham, J. Xiao, W. Xu, J. Yang, X.-Q. Yang, J.-G. Zhang, *Nat. Energy* **2019**, *4*, 180.
[9] J. C. Bachman, S. Muy, A. Grimaud, H.-H. Chang, N. Pour, S. F. Lux, O. Paschos, F. Maglia, S. Lupart, P. Lamp, L. Giordano, Y. Shao-Horn, *Chem. Rev.* **2016**, *116*, 140.
[10] T. Famprikis, P. Canepa, J. A. Dawson, M. S. Islam, C. Masquelier, *Nat. Mater.* **2019**, *18*, 1278.
[11] J. Janek, W. G. Zeier, *Nat. Energy* **2023**, *8*, 230.
[12] A. Bielefeld, D. A. Weber, J. Janek, *J. Phys. Chem. C* **2019**, *123*, 1626.
[13] P. Minnmann, F. Strauss, A. Bielefeld, R. Ruess, P. Adelhelm, S. Burkhardt, S. L. Dreyer, E. Trevisanello, H. Ehrenberg, T. Brezesinski, F. H. Richter, J. Janek, *Adv. Energy Mater.* **2022**, *12*, 2201425.
[14] R. Ruess, S. Schweidler, H. Hemmelmann, G. Conforto, A. Bielefeld, D. A. Weber, J. Sann, M. T. Elm, J. Janek, *J. Electrochem. Soc.* **2020**, *167*, 100532.
[15] G. Conforto, R. Ruess, D. Schröder, E. Trevisanello, R. Fantin, F. H. Richter, J. Janek, *J. Electrochem. Soc.* **2021**, *168*, 070546.
[16] Y. J. Nam, K. H. Park, D. Y. Oh, W. H. An, Y. S. Jung, *J. Mater. Chem. A* **2018**, *6*, 14867.
[17] C. König, A. Ramanayagam, J. Kraus, B. Roling, *Batteries Supercaps* **2024**, *7*, 202300578.
[18] R. Dugas, Y. Dupraz, E. Quemin, T. Koç, J.-M. Tarascon, *J. Electrochem. Soc.* **2021**, *168*, 090508.
[19] A. L. Santhosha, L. Medenbach, J. R. Buchheim, P. Adelhelm, *Batteries Supercaps* **2019**, *2*, 524.
[20] J. Hertle, F. Walther, B. Mogwitz, S. Schröder, X. Wu, F. H. Richter, J. Janek, *J. Electrochem. Soc.* **2023**, *170*, 040519.
[21] L. M. Riegger, S. Mittelsdorf, T. Fuchs, R. Rueß, F. H. Richter, J. Janek, *Chem. Mater.* **2023**, *35*, 5091.
[22] S. Wenzel, S. J. Sedlmaier, C. Dietrich, W. G. Zeier, J. Janek, *Solid State Ionics* **2018**, *318*, 102.
[23] S. Wenzel, T. Leichtweiss, D. Krüger, J. Sann, J. Janek, *Solid State Ionics* **2015**, *278*, 98.
[24] R. Thümmel, W. Klemm, *Z. Anorg. Allg. Chem.* **1970**, *376*, 44.
[25] W. A. Alexander, L. D. Calvert, R. H. Gamble, K. Schinzel, *Can. J. Chem.* **1976**, *54*, 1052.
[26] K. Takada, N. Aotani, K. Iwamoto, S. Kondo, *Solid State Ionics* **1996**, *86–88*, 877.
[27] M. Tatsumisago, F. Mizuno, A. Hayashi, *J. Power Sources* **2006**, *159*, 193.
[28] C. Wen, R. A. Huggins, *Mater. Res. Bull.* **1980**, *15*, 1225.
[29] Y. Lu, C.-Z. Zhao, R. Zhang, H. Yuan, L.-P. Hou, Z.-H. Fu, X. Chen, J.-Q. Huang, Q. Zhang, *Sci. Adv.* **2021**, *7*, abi5520.
[30] S. Luo, Z. Wang, X. Li, X. Liu, H. Wang, W. Ma, L. Zhang, L. Zhu, X. Zhang, *Nat. Commun.* **2021**, *12*, 6968.
[31] J. Wan, Y.-X. Song, W.-P. Chen, H.-J. Guo, Y. Shi, Y.-J. Guo, J.-L. Shi, Y.-G. Guo, F.-F. Jia, F.-Y. Wang, R. Wen, L.-J. Wan, *J. Am. Chem. Soc.* **2021**, *43*, 839.
[32] J. Qu, J. Xiao, T. Wang, D. Legut, Q. Zhang, *J. Phys. Chem. C* **2020**, *124*, 24644.
[33] C. Hänsel, B. Singh, D. Kiwic, P. Canepa, D. Kundu, *Chem. Mater.* **2021**, *33*, 6029.
[34] J. Aspinall, Y. Chart, H. Guo, P. Shrestha, M. Burton, M. Pasta, *ACS Energy Lett.* **2024**, *9*, 578.
[35] S. Jin, X. Gao, S. Hong, Y. Deng, P. Chen, R. Yang, Y. L. Joo, L. A. Archer, *Joule* **2024**, *8*, 746.
[36] Z. Wang, J. Zhao, X. Zhang, Z. Rong, Y. Tang, X. Liu, L. Zhu, L. Zhang, J. Huang, *eScience* **2023**, *3*, 100087.
[37] W. Zhang, D. Schröder, T. Arlt, I. Manke, R. Koerver, R. Pinedo, D. A. Weber, J. Sann, W. G. Zeier, J. Janek, *J. Mater. Chem. A* **2017**, *5*, 9929.
[38] S. Choudhury, Z. Tu, S. Stalin, D. Vu, K. Fawole, D. Gunceler, R. Sundararaman, L. A. Archer, *Angew. Chem., Int. Ed.* **2017**, *56*, 13070.
[39] European Commission, Directorate-General for Internal Market, Industry, Entrepreneurship, SMEs, M., Grohol, C. Veeh: Publications Office of the European Union, **2023**.
[40] P. Oh, J. Yun, J. H. Choi, K. S. Saqib, T. J. Embleton, S. Park, C. Lee, J. Ali, K. Ko, J. Cho, *Angew. Chem.* **2022**, *134*, 202201249.
[41] A. Ikezawa, G. Fukunishi, T. Okajima, F. Kitamura, K. Suzuki, M. Hirayama, R. Kanno, H. Arai, *Electrochem. Commun.* **2020**, *116*, 106743.
[42] W. J. Jeong, C. Wang, S. G. Yoon, Y. Liu, T. Chen, M. T. McDowell, *ACS Energy Lett.* **2024**, *9*, 2554.
[43] S. Lu, X. Zhang, Z. Yang, Y. Zhang, T. Yang, Z. Zhao, D. Mu, F. Wu, *Nano Lett.* **2023**, *23*, 56.
[44] S. Yanev, C. Heubner, K. Nikolowski, M. Partsch, H. Auer, A. Michaelis, *J. Electrochem. Soc.* **2024**, *171*, 020512.
[45] C. Sedlmeier, R. Schuster, C. Schramm, H. A. Gasteiger, *J. Electrochem. Soc.* **2023**, *170*, 030536.
[46] S. Puls, E. Nazmutdinova, F. Kalyk, H. M. Woolley, J. F. Thomsen, Z. Cheng, A. Fauchier-Magnan, A. Gautam, M. Gockeln, S.-Y. Ham, M. T. Hasan, M.-G. Jeong, D. Hiraoka, J. S. Kim, T. Kutsch, B. Lelotte, P. Minnmann, V. Miß, K. Motohashi, D. L. Nelson, F. Ooms, F. Piccolo, C. Plank, M. Rosner, S. E. Sandoval, E. Schlautmann, R. Schuster, D. Spencer-Jolly, Y. Sun, B. S. Vishnugopi, et al., *Nat Energy* **2024**, *9*, 1310.
[47] J. K. Eckhardt, T. Fuchs, S. Burkhardt, P. J. Klar, J. Janek, C. Heiliger, *ACS Appl. Mater. Interfaces* **2022**, *14*, 42757.
[48] J. K. Eckhardt, T. Fuchs, S. Burkhardt, P. J. Klar, J. Janek, C. Heiliger, *Adv. Mater. Interfaces* **2023**, *10*, 2202354.
[49] K. Lee, E. Kazyak, M. J. Wang, N. P. Dasgupta, J. Sakamoto, *Joule* **2022**, *6*, 2547.
[50] N. M. Vargas-Barbosa, *Nat. Nanotechnol.* **2024**, *19*, 419.
[51] G. V. Alexander, C. Shi, J. O'Neill, E. D. Wachsman, *Nat. Mater.* **2023**, *22*, 1136.
[52] P. W. Jaschin, C. R. Tang, E. D. Wachsman, *Energy Environ. Sci.* **2024**, *17*, 727.
[53] T. Krauskopf, B. Mogwitz, C. Rosenbach, W. G. Zeier, J. Janek, *Adv. Energy Mater.* **2019**, *9*, 1902568.
[54] M. Siniscalchi, J. Liu, J. S. Gibson, S. J. Turrell, J. Aspinall, R. S. Weatherup, M. Pasta, S. C. Speller, C. R. M. Grovenor, *ACS Energy Lett.* **2022**, *7*, 3593.
[55] J. Aspinall, K. Sada, H. Guo, S. Kotakadi, S. Narayanan, Y. Chart, B. Jagger, E. Milan, L. Brassart, D. Armstrong, M. Pasta, *Nat. Commun.* **2024**, *15*, 4511.
[56] T. Fuchs, T. Ortmann, J. Becker, C. Haslam, M. Ziegler, V. Singh, M. Rohnke, B. Mogwitz, K. Peppler, L. Nazar, J. Sakamoto, J. Janek, **2024**.
[57] R. Koerver, W. Zhang, L. de Biasi, S. Schweidler, A. O. Kondrakov, S. Kolling, T. Brezesinski, P. Hartmann, W. G. Zeier, J. Janek, *Energy Environ. Sci.* **2018**, *11*, 2142.
[58] Y. Sakka, H. Yamashige, A. Watanabe, A. Takeuchi, M. Uesugi, K. Uesugi, Y. Orikasa, *J. Mater. Chem. A* **2022**, *10*, 16602.
[59] L. de Biasi, A. O. Kondrakov, H. Geßwein, T. Brezesinski, P. Hartmann, J. Janek, *J. Phys. Chem. C* **2017**, *121*, 26163.
[60] B. Hennequart, M. Platonova, R. Chometon, T. Marchandier, A. Benedetto, E. Quemin, R. Dugas, C. Lethien, J.-M. Tarascon, *ACS Energy Lett.* **2024**, *9*, 454.
[61] C. D. Alt, N. U. Müller, L. M. Riegger, B. Aktekin, P. Minnmann, K. Peppler, J. Janek, *Joule* **2024**, *8*, 2755.

© 2024 The Author(s). Advanced Energy Materials published by Wiley-VCH GmbH

3.5. Sulfide Solid Electrolyte Degradation in Contact with Alloy Electrodes and the Possible Influence of Metal Oxide Layers (5th Manuscript)

This study contributes to a manuscript (currently in preparation) on indium thin films as alloying interlayers in RFCs, with a particular focus on interphase growth. The electrochemical investigations are intended to guide *operando* XPS studies aimed at revealing the interphase composition for In–Li electrodes. While the results are preliminary and require further investigation, findings suggest that film morphologies and metal oxide layers on CC surfaces need to be considered when assessing SE degradation at metal|SE interfaces.

To investigate the degradation of LPSCl in contact with In/$(InLi)_x$ electrodes, indium thin films were prepared by thermal evaporation. XPS analysis confirmed the phase purity and surface passivation, while SEM imaging revealed the film morphology and structure. CTTA experiments successfully quantified SEI growth, revealing a reduced degradation of LPSCl at at E_H = 0.62 V *vs*. Li^+/Li of In/$(InLi)_x$ compared to pure lithium metal. However, metal oxide layers (*i.e.*, In_2O_3) and non-uniform film morphologies are expected to affect the observed results and interpretation toward interphase growth. Moreover, the Wagner diffusion model was refined to consider the higher E_H of lithium alloy electrodes to accurately assess the respective SEI rate constant.

The findings provide initial insights into SEI formation at alloy electrodes with higher E_H, underscoring that interphase formation at metal and alloy surfaces remains a significant challenge, limiting the viability of SSBs. Additionally, results emphasize that previous studies have often overlooked the presence and influence of metal oxide passivation layers and established a basis for *operando* XPS studies to track SEI formation and its composition.

The experimental details can be found in Chapter 7.5.i. The experiments presented in this publication were designed and executed by the first author, supported by B. Aktekin and under the supervision of J. Janek. The sample preparation was performed by J. Westphal under supervision of the first author and B. Aktekin. J. Westphal performed the XPS measurements, while the first author assisted in the corresponding data analysis. S. L. Benz and B. Aktekin supported the analysis of XPS data and assisted with scientific discussion.

Sulfide Solid Electrolyte Degradation in Contact with Alloy Electrodes and the Possible Influence of Metal Oxide Layers

Christoph D. Alt[a,b], Johannes Westphal[a,b], Burak Aktekin[a,b], Sebastian L. Benz[a,b], and Jürgen Janek[a,b,*]

[a]Institute of Physical Chemistry, Justus Liebig University, Heinrich Buff Ring 17, 35392 Giessen, Germany

[b]Center for Materials Research, Justus Liebig University, Heinrich Buff Ring 16, 35392 Gies-sen, Germany

*corresponding author: juergen,janek@pc.jlug.de

Abstract

Interphase studies in the literature predominantly focus on the Li|electrolyte interface, while degradation at higher electrode potentials is often considered less critical to solid-state battery performance. Despite the high cost and weight limiting the broader adoption of In–Li alloy electrodes, the In/$(InLi)_x$ system has proven to be reliably used in battery research. However, interphase formation at this electrode interface remains poorly understood. This study addresses both the practicality and interfacial behavior of indium current collectors by investigating thermally evaporated indium metal for potential use in reservoir-free solid-state batteries. Lithiation of the indium thin films, initiating interphase formation by reducing the electrode potential, was analyzed via coulometric titration time analysis, as interphase growth remains a major challenge in realizing practical reservoir-free configurations. Thus, electrochemical measurements quantified interphase formation on In/$(InLi)_x$ electrodes and the associated charge consumption attributed to interfacial reactions, using a modified Wagner diffusion model. Furthermore, this work highlights the often-overlooked role of native metal oxide layers, particularly In_2O_3, in influencing interphase kinetics and composition. The findings offer new insights into solid electrolyte degradation with alloying materials, operating at higher electrode potentials than lithium metal, and shed light on the crucial goal of interphase stabilization in both conventional as well as reservoir-free solid-state batteries.

Results and Discussion

Thin indium layers (100 and 250 nm) were thermally evaporated onto stainless-steel discs under dynamic vacuum ($p < 10^{-6}$ Pa). Thinner layers (*e.g.*, 10 nm) were also tested, but exhibited poor coverage and film quality, so they were not further investigated. **Figure 1** depicts the surface morphology of 250 nm thick indium films, revealing a rough and non-uniform texture resulting from numerous nucleation sites. Thus, island-like growth with a nanoparticle size ranging from 50 to 100 nm was observed. Such growth could be attributed to the high surface tension of indium metal during deposition.[1–3] However, post-process annealing did not lead to a smoother, more uniform morphology. Therefore, this could have additional implications in coulometric titration time analysis (CTTA) experiments (discussed below) and may even limit the use of thin indium layers in reservoir-free cells (RFCs) due to their deposition characteristics and resulting poor film quality. Electrodeposition of indium, which could not be tested in this study, presents an alternative approach facilitating the deposition of dense, uniform films. and the resulting rate constant, respectively.

Prior to conducting CTTA experiments, the phase purity and surface chemistry of the indium thin films (shown in blue in **Figure 2**) were first analyzed using surface-sensitive X-ray photoelectron spectroscopy (XPS). The results were compared to a 100 µm thick indium foil and bulk indium reference. The latter was also tested in CTTA experiments.

The analysis revealed that the indium films show high phase purity, with no contamination detected. However, the films are partially oxidized, possibly due to a reaction with residual oxygen in the deposition chamber or glovebox environment, leading to the formation of In_2O_3. Plasmon loss features, indicated by black arrows in the In 3d spectra, simultaneously confirm the presence of indium metal at the surface. Interestingly, the observed nanoparticle size in Figure 1 closely matches the finding of Ho *et al.*[4] for In_2O_3 layers on platinum discs. As expected, the commercial indium foil showed clear signals of a native In_2O_3 layer likely due to fabrication and storage in air.

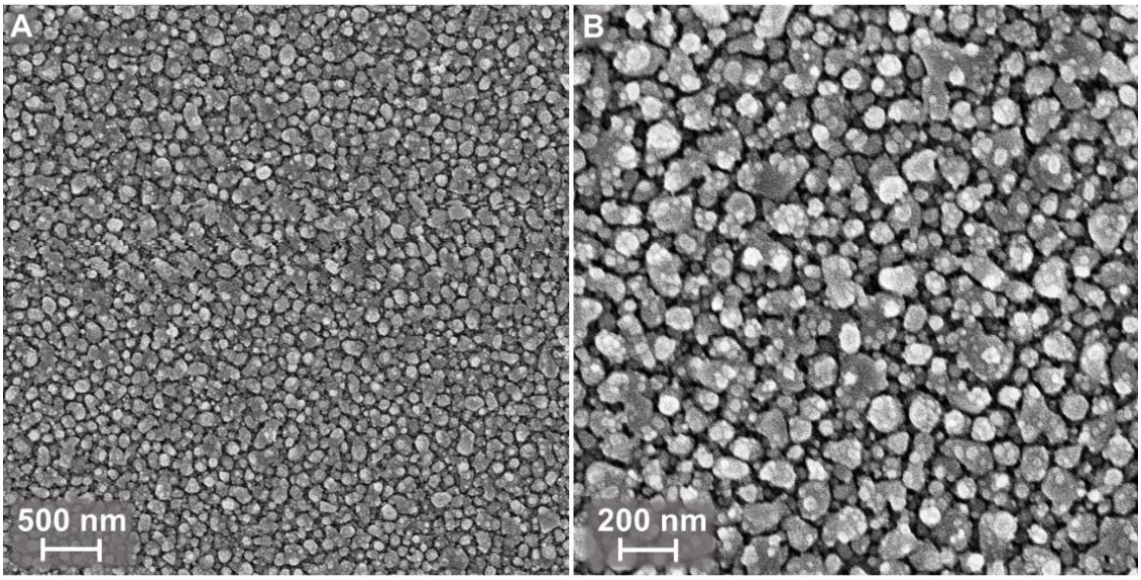

Figure 1. Scanning electron microscopy images of evaporated indium films (250 nm), revealing the surface morphology.

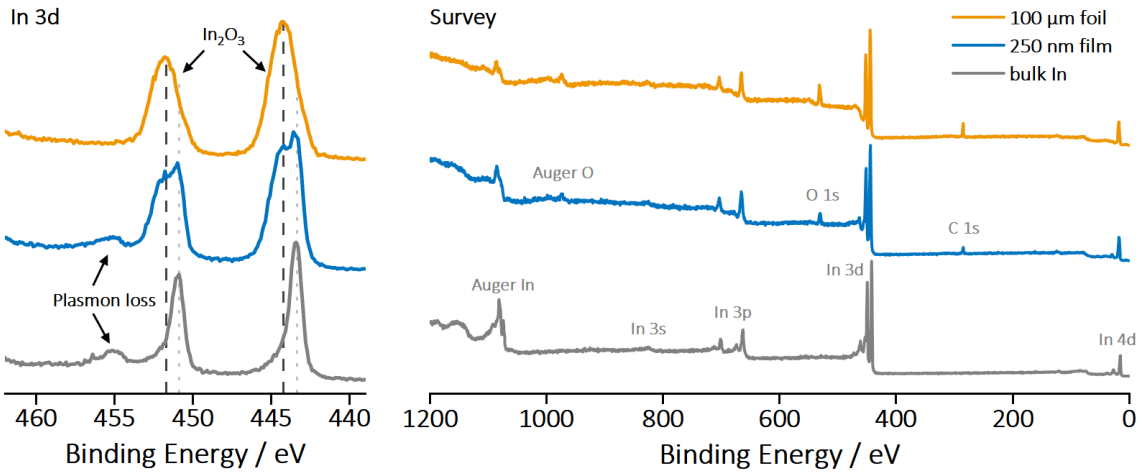

Figure 2. Normalized In 3d (left) and survey (right) spectra of indium thin films (250 nm thick) on stainless-steel discs and 100 µm indium foil used in CTTA experiments (Figure 3). A reference for bulk indium (*i.e.*, a sputter-cleaned indium foil) is shown in gray. Signals were identified according to reference 5. Plasmon loss features indicated the partially passivated surface of indium films.

In the early 2000s, In_2O_3 (and other metal oxides) were extensively studied as a promising negative electrode (*i.e.*, anode) material for lithium-ion batteries due to its high theoretical capacity (965 mAh g^{-1}) and well-established production technologies from other tech sectors.[4,6,7] However, it has received little attention in both the development of solid-state batteries (SSBs) and studies of solid-electrolyte interphase (SEI) formation at In–Li electrodes. As a result, recent studies might have mistakenly attributed In_2O_3 signals to the formation of In_xS_y compounds at the interface between In/$(InLi)_x$ and Li_6PS_5Cl (LPSCl) in *post-mortem* XPS analysis.[8,9] Initial findings from our *operando* XPS study (not included here), however, suggest the formation of Li_2S, consistent with reports by Huang *et al.*[10].

It is commonly assumed that interphase formation is minimized when the electrode potential is close to the electrochemical stability window of the respective solid electrolyte (*e.g.*, LPSCl). Consequently, SEI formation is often not considered when using high-potential electrodes (E_H > 0 V *vs.* Li^+/Li), such as lithium alloys. However, no comprehensive studies have been reported on quantifying and tracking SEI growth for lithium alloys. Therefore, the prepared indium films and reference foils were lithiated in small lithiation steps during CTTA experiments to investigate interphase growth at the In/$(InLi)_x$|LPSCl interface. Furthermore, this study may serve as a representative analysis of lithium alloys in SSBs and RFCs, highlighting substantial solid electrolyte (SE) degradation at elevated potentials and associated challenges in developing practical RFCs.

The results of the CTTA experiments are presented in **Figure 3**, with the stainless-steel reference (*taken from Figure 5 of this doctoral thesis*). The accumulated charge (q_Σ), which represents the consumption of active lithium through side reactions, is plotted against t (Figure 3A) and $t^{0.5}$ (Figure 3B). Following an initial alloying and possibly native oxide reduction phase of In_2O_3 (at potentials below 1 V vs. Li^+/Li)[6] – most evident in the 100 µm indium foil – the lithium consumption exhibited linear trends in Figure 3B for each sample. This indicates a diffusion-controlled degradation process consistent with the Wagner diffusion model. Additionally, the results revealed that the degradation process is suppressed at 0.62 V *vs.* Li^+/Li, as q_Σ for the stainless-steel reference (shown in green) was significantly higher than that of the commercial 100 µm indium foil. However, it was also observed that the charge consumption of the prepared indium thin films, for both thicknesses of 100 and 250 nm, was higher than that of the 100 µm indium foil.

In the following discussion, three key aspects must be considered when analyzing the CTTA results, highlighting open questions that should be applied to other systems and explored in future research. Those aspects are summarized in **Figure 4**.

The suppressed interphase formation (see Figure 4A) can be explained using the Wagner diffusion model. Revisiting eq. 4 (*in Chapter 2.2.ii. of this doctoral thesis*), the degradation reaction is driven by the chemical potential gradient of lithium ($\nabla\mu_{Li}$). However, at higher electrode potentials (*e.g.*, E_H = 0.62 V *vs.* Li^+/Li), this gradient is lower, leading to reduced material consumption and slower interphase growth. By introducing a new parabolic rate constant (k''), the respective electrode potential (E_H) is considered to describe the degradation reaction and interphase growth at alloy electrode interfaces:

$$d = \sqrt{\frac{2}{F^2 \cdot \rho_{int} \cdot x_{Li}} \cdot \frac{M_{int} \cdot \sigma_{el} \cdot \sigma_{ion}}{\sigma_{el} + \sigma_{ion}} \cdot \sqrt{(\Delta\mu_{Li} - F \cdot E_H)} \cdot \sqrt{t}} = k'' \cdot \sqrt{t} \qquad \textbf{(eq. 1)}$$

with F, ρ_{int}, x_{Li}, M_{int}, σ_{ion}, σ_{el}, and t being the Faraday constant, the mean density of the interphase, the stoichiometric factor (moles of the lithium metal required for the stoichiometric decomposition), the mean molar mass of the interphase, the ionic and electronic partial conductivity, and the reaction time, respectively. Here, the reaction driving force (*i.e.*, $\Delta\mu_{Li}$) is reduced by the product of F and E_H, which accounts for the higher electrode potential, as given by $\mu_{Li}(\text{electrode}) = \mu^0_{Li} + F \cdot E_H$. Consequently, $\Delta\mu_{Li} - F \cdot E_H$ equals approximately 100 kJ mol^{-1} for $In/(InLi)_x$ with E_H = 0.62 V (*vs.* Li^+/Li), leading to a reduced parabolic rate constant. In this context, it is assumed that the properties of the product phases remain unchanged compared to those formed with lithium metal electrodes.

However, the lower slope observed in Figure 3B could also be attributed to a lower effective σ_{el} of the interphase, suggesting a shift in composition different from the assumed one for lithiated LPSCl. Consequently, the slope could be analyzed through linear fitting to estimate k'' in eq. 1, *as was done in the first publication of this thesis*. However, these approaches require precise knowledge of the interphase composition to accurately estimate SEI thicknesses from q_Σ – based on the specific degradation reaction and the density of product phases. This challenge motivated the effort to conduct *operando* XPS measurements, as recent reports remained inconclusive regarding SEI composition at the $In/(InLi)_x$|LPSCl interface.

Assuming no involvement of indium as a reactant, the interphase thickness can be estimated using q_Σ in Figure 3B, yielding parabolic rate constants ranging from k'' = 0.25 nm·s$^{-0.5}$ to k = 0.46 nm·s$^{-0.5}$ for the 100 µm indium foil and the stainless-steel reference. If $\sigma_{ion} \gg \sigma_{el}$ of the degradation layer, these values correspond to an effective σ_{el} of 8.4 pS cm^{-1} for the 100 µm indium foil and of 18.2 pS cm^{-1} for the stainless-steel reference, as determined by eq. 1 (*and eq. 12 of this doctoral thesis for stainless-steel*). Since this indicates only a slight variation in σ_{el}, the results are inconclusive regarding potential compositional changes involving indium as a reactant. However, the findings indicate that such reduced k'' or σ_{el} remain too high to mitigate the detrimental consequences of SEI growth at the cell-level, *as outlined in the guidelines established in the first publication of this thesis.*

In the second publication of this thesis, it was demonstrated that the active contact area plays a crucial role in impedance experiments for tracking SEI growth, highlighting potential pitfalls for misinterpretation. While this study focused on EIS data analysis, its key findings can also be applied to tracking charge consumption in CTTA experiments. In addition to possible shifts in composition and properties, an increased contact area (as recently reported by Sivavec *et al.*[11], depicted in Figure 4B) may account for variations in observations. The higher charge consumption of indium thin films can likely be attributed to their rough and porous morphology (see Figure 1). This, in turn, accelerates material consumption in CTTA measurements due to larger contact area.

Lastly, metal oxide surface layers, such as In_2O_3 (an n-type semiconductor with an electronic bandgap energy above 3 eV), must also be considered (see Figure 4C). Aktekin *et al.*[12] unveiled that commercial LPSCl contains a considerable amount of residual oxygen, which

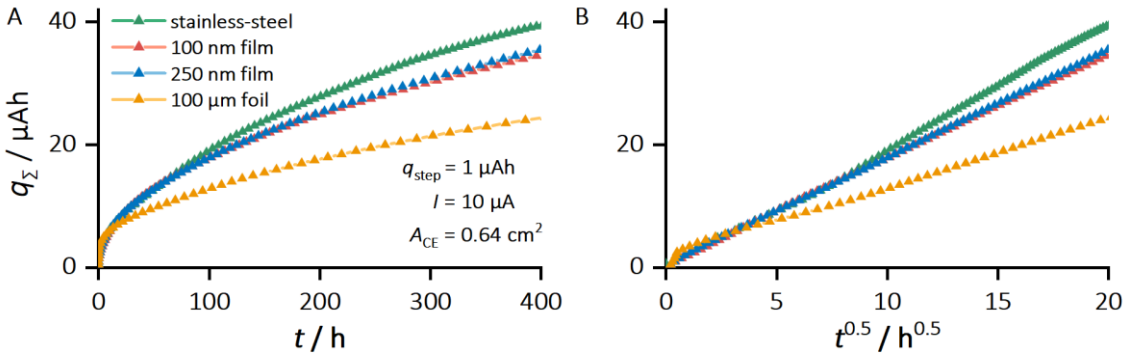

Figure 3. The consumption of active lithium through side reactions (*i.e.*, SEI formation) shown as accumulated charge (q_Σ) in In/(InLi)$_x$|LPSCl|In cells during CTTA experiments, plotted against t (A) and $t^{0.5}$ (B). Titration parameters are detailed in the SI. The data for a stainless-steel disc as working electrode is shown in green as reference for degradation in contact with lithium metal.

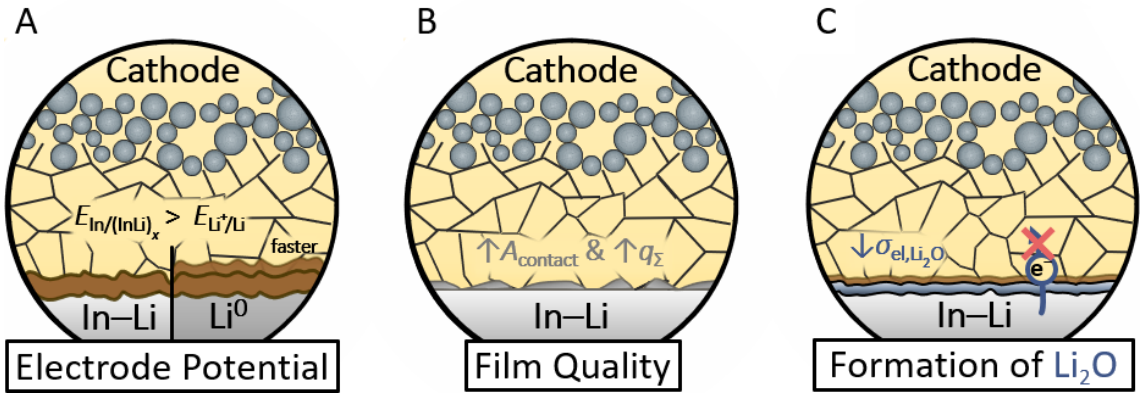

Figure 4. Reduced SEI formation due to the higher potentials of lithium alloy electrodes (A), the increase in charge consumption and SEI growth caused non-uniform indium films and increased active area (B), and the influence of metal oxide layers forming Li_2O (eq. 2) during lithiation (C).

could further oxidize indium surfaces, even when fabricated under an inert atmosphere.

Furthermore, the (ir-)reversible reaction of In_2O_3 to Li_2O during lithiation has been reported (eq. 2).[4,6,13] Similar observations have also been reported for tin and copper oxides.[14–16]

$$In_2O_3 + 6\,Li^+ + 6\,e^- \rightarrow 2\,In + 3\,Li_2O \qquad \textbf{(eq. 2)}$$

On the one hand, electrochemically active metal oxides could contribute to lithium consumption in CTTA experiments. On the other hand, lithium oxide could – at least theoretically – serve a protective role by passivating the interface and reducing the effective σ_{el} at the interface (as approximated from Figure 3B). As a wide bandgap material (approximately 8 eV), Li_2O may passivate the interface, mitigate lithium metal consumption at the SE interface, and therefore decrease the degree of SE degradation. Tests with post-deposition oxidized indium thin films (*i.e.*, exposed to ambient conditions for 8 days to complete In_2O_3 formation and passivation) showed reduced charge consumption in CTTA experiments (see Figure S1 of the Supporting Information – *in Chapter 7.5.ii. of this thesis*), suggesting a possible passivating effect of In_2O_3 and Li_2O. Unfortunately, detecting the conversion of In_2O_3 to Li_2O in (*operando*) XPS studies presents challenges, as the interface is usually buried within the cell and corresponding binding energies in the O 1s and Li 1s spectra overlap with each other or with Li_2S, making clear identification difficult.[13]

Conclusion

Focused on interphase growth at the In/(InLi)$_x$ electrode, this study addresses a key challenge in developing practical RFCs. The findings highlight difficulties in achieving a uniform indium film morphology. Moreover, factors such as the contact conditions and the reduction of metal oxides (*e.g.*, In_2O_3) on metal surfaces were identified to influence CTTA measurements. Nevertheless, the study demonstrated that CTTA measurements can be effectively applied to (thin) alloying materials and quantification of interphase growth. Using a modified Wagner diffusion model confirmed a reduced

degradation of LPSCl in contact with In/$(InLi)_x$ electrodes (compared to lithium metal). However, despite the higher electrode potential being closer to the ESW, interphase formation is still suspected to compromise the long-term viability of such RFCs.

Although CTTA results highlighted that previous studies have often overlooked the impact of metal oxide surface layers (*e.g.*, In_2O_3), these findings offer initial insights into interphase formation at passivated alloying interlayers. Therefore, further investigation is needed to understand such SEI growth, including the underlying chemical reaction mechanisms, the role of metal oxide surface layers, and their potential conversion into low electron-conducting interlayers, such as Li_2O. Therefore, these combined findings provide a comprehensive understanding to inform *operando* XPS experiments focused on interphase composition, and the evolving species at alloying interlayers.

References

1. Bertran, E. *et al.* Indium Thin Films on Metal-Coated Substrates. *Thin Solid Films* **129,** 103–109; 10.1016/0040-6090(85)90099-9 (1985).
2. Lin, Q. *et al.* Scalable Indium Phosphide Thin-Film Nanophotonics Platform for Photovoltaic and Photoelectrochemical Devices. *ACS nano* **11,** 5113; 10.1021/acsnano.7b02124 (2017).
3. Singh, H. P. & Murr, L. E. Nucleation and Growth Characteristics of Palladium and Indium Thin Films. *Metall Trans* **3,** 983–988; 10.1007/BF02647676 (1972).
4. Ho, W.-H. *et al.* Electrochemical Performance of In_2O_3 Thin Film Electrode in Lithium Cell. *Journal of Power Sources* **175,** 897–902; 10.1016/j.jpowsour.2007.10.020 (2008).
5. Chastain, J. (ed.). *Handbook of X-ray Photoelectron Spectroscopy. A reference book of standard spectra for identification and interpretation of XPS data* (Perkin-Elmer, Eden Prairie, Minn., 1995).
6. Zhou, Y. *et al.* The Electrochemistry of Nanostructured In_2O_3 with Lithium. *Journal of Power Sources* **162,** 1373–1378; 10.1016/j.jpowsour.2006.08.031 (2006).
7. Xu, H. *et al.* Ultra-Stable and High-Rate Lithium Ion Batteries based on Metal–organic Framework-derived In_2O_3 Nanocrystals/Hierarchically Porous Nitrogen-doped Carbon Anode. *Energy & Environ Materials* **3,** 177–185; 10.1002/eem2.12065 (2020).
8. Wan, J. *et al.* Micromechanism in All-Solid-State Alloy-Metal Batteries: Regulating Homogeneous Lithium Precipitation and Flexible Solid Electrolyte Interphase Evolution. *Journal of the American Chemical Society* **143,** 839–848; 10.1021/jacs.0c10121 (2021).
9. Luo, S. *et al.* Growth of Lithium-Indium Dendrites in All-Solid-State Lithium-Based Batteries with Sulfide Electrolytes. *Nat Commun* **12,** 6968; 10.1038/s41467-021-27311-7 (2021).
10. Huang, Di, Liu, G. & Tong, W. Stability of the Argyrodite Electrolyte in Li–In Based All-Solid-State Batteries. *ACS Appl. Energy Mater.* **7,** 10376; 10.1021/acsaem.4c01873 (2024).
11. Sivavec, J., Kravchyk, K. V. & Kovalenko, M. V. Impact of Stack Pressure on Coulometric Titration Time Analysis. *Comm chemistry* **8,** 96; 10.1038/s42004-025-01496-0 (2025).
12. Aktekin, B. *et al.* Operando Photoelectron Spectroscopy Analysis of Li_6PS_5Cl Electrochemical Decomposition Reactions in Solid-State Batteries. *ACS Energy Lett.*, 3492–3500; 10.1021/acsenergylett.4c01072 (2024).
13. Liu, W.-P. *et al.* Unravelling the Electrochemical Evolution Mechanism of In_2O_3 Anode in Long-Cycle All-Solid-State Lithium Batteries with Sulfide Electrolytes. *Rare Met.*; 10.1007/s12598-025-03293-z (2025).
14. Courtney, I. A. & Dahn, J. R. Electrochemical and In Situ X-Ray Diffraction Studies of the Reaction of Lithium with Tin Oxide Composites. *J. Electrochem. Soc.* **144,** 2045–2052; 10.1149/1.1837740 (1997).
15. Li, H., Huang, X. & Chen, L. Anodes based on Oxide Materials for Lithium Rechargeable Batteries. *Solid State Ionics* **123,** 189–197; 10.1016/S0167-2738(99)00081-8 (1999).
16. Yoon, J. S. *et al.* Thermodynamics, Adhesion, and Wetting at Li/Cu(-Oxide) Interfaces: Relevance for Anode-Free Lithium-Metal Batteries. *ACS Applied Materials & Interfaces* **16,** 18790–18799; 10.1021/acsami.3c19034 (2024).

4. Conclusions

While substantial progress has been made toward the commercialization of SSBs, critical challenges at electrode|SE interfaces demand focused attention. This doctoral thesis makes a significant contribution to the understanding of intrinsic degradation processes. It provides a fundamental basis for accurate interphase growth predictions and future stabilization strategies aimed at controlling interphase formation and mitigating its impact on SSB performance.

Therefore, this work delivers novel insights into the transport properties and growth kinetics of degradation layers in sulfide SEs, emphasizing their detrimental effects on cell operation. The experimental assessment of interphase growth, combined with a comprehensive investigation of the electronic properties in solid lithium-ion conductors, increases the accuracy of long-term predictions for interphase growth and associated resistance increase. In addition, this work explored the integration of alloy electrodes (specifically, the In–Li alloy system) with a focus on preparation, resulting microstructure, and associated SE degradation.

RFCs require the efficient utilization of active lithium (*i.e.*, Coulomb efficiency near 100%), with the gradual degradation of SEs contributing to capacity fading. To address the limitations of conventional methods, a novel approach was introduced to determine the bulk-material partial conductivities of reduced sulfide SE, establishing a basis for quantifying interphase growth. By applying the Wagner diffusion model, the quantified transport properties enabled the effective modeling of diffusion-controlled interphase kinetics at the Li|LPSCl interface. The findings emphasize the detrimental impact of SE degradation, which increases the cell resistance drastically and compromises the viability of conventional SSBs and RFCs. Thus, while enhancing the modeling of SEI transport properties, design guidelines were established to support the stabilization of interphase growth through precise control of both σ_{ion} and σ_{el}.

Time-resolved experiments (*e.g.*, EIS and CTTA) are frequently combined with the Wagner diffusion model for extracting interphase rate constants in SSBs. Thus, their reliability to solid|solid interfaces has been examined through 3D transport simulations of microscopic diffusion-controlled interphase growth. Factors such as current constriction at the interface, complex contact conditions, or partially passivated interfaces influence the cell's impedance response. Therefore, these aspects must be considered in data interpretation to avoid overestimating reaction kinetics or misattributing deviations from the expected time dependence. In conclusion, a detailed understanding of the electrode|SE interface morphology and contact condition is essential for improving interphase growth predictions in SSBs (*e.g.*, for the Wagner diffusion model combined with time-resolved experiments like CTTA and EIS). This highlights the practical relevance of the bulk-material synthesis developed in the first publication for reliably estimate rate constants and interphase growth with improved accuracy.

Moreover, the electronic properties of individual interphase constituents must be considered, as they influence interphase rate constants via σ_{el} and are essential for improving the predictive accuracy. Thus, a comprehensive study was conducted, incorporating fundamental

derivations and precise testing protocols from a defect-chemical perspective to systematically evaluated σ_{el} of relevant lithium halides (Li*X*, with *X* = Cl, Br, or I) using Hebb-Wagner-type measurements. This approach effectively decoupled electronic charge carrier contributions (*i.e.*, electron and electron hole conduction), demonstrating that σ_{el} varies substantially across the investigated range of lithium activities. By addressing the partial electronic transport properties of lithium halides, their impact on interphase kinetics, formation, and resulting properties is revealed. Furthermore, the critical importance of evaluating the electronic properties of lithium-ion conductors and their impact on SE degradation is emphasized.

The final section of this doctoral thesis is focused on the investigation of alloy electrodes, specifically the In/$(InLi)_x$ eutectic, where reduced SE degradation is anticipated compared to LMEs. However, careful preparation of In/$(InLi)_x$ electrodes is crucial and the gradual degradation of LPSCl at 0.62 V (*vs*. Li^+/Li) for the In/$(InLi)_x$ electrode requires further research.

Through a systematic study of planar and composite electrode structures, the impact of preparation on electrode microstructure and, consequently, on electrode performance is revealed. One key finding is that conscious fabrication protocols are crucial for improving electrode kinetics. Therefore, proper control of the electrode's microstructure is essential to prevent current constriction at the In/$(InLi)_x$|SE interface, ensuring reliable performance at high rates and comparability between research labs. Gained insights advance In–Li electrode processing and the accurate benchmarking of high-capacity solid-state cathodes.

While interphase studies have mostly focused on the Li|SE interface, this doctoral thesis provides fundamental insights into SEI growth for alloy electrodes, gained through electrochemical titration experiments conducted on indium thin films. By tracking the consumption of active redox species, a significant degradation of LPSCl at 0.62 V (*vs*. Li^+/Li) was observed. SEM and XPS analyses revealed key challenges associated with integrating indium thin films into RFCs. These challenges – such as film morphology and the reactivity of surface metal oxides (*e.g.*, In_2O_3) – must be considered during data interpretation. As a result, it was emphasized that alloying interlayers do not completely inhibit, but effectively minimize SE degradation, which remains a major challenge hindering the viability of RFCs. The findings provide a systematic understanding for *operando* XPS investigations focused on the composition of the corresponding interphases at alloy|SE interfaces.

Overall, this doctoral thesis enhances the knowledge and understanding of material compatibility and degradation processes in SSBs. Interphase formation is examined from multiple perspectives toward its growth kinetics. Conventional physicochemical concepts were revisited and combined with novel approaches to determine (electronic) transport properties of lithium-ion conductors, while also addressing potential pitfalls in data interpretation. The scope is extended to lithium alloys, their microstructure, and the corresponding SE degradation at respective electrode potentials. The combined findings improve the accuracy of analytical models for the prediction of performance decay in SSBs due to interphase growth and emphasize the need for thorough assessments of effective stabilization strategies.

5. Outlook

Material incompatibility and SE degradation remain critical barriers to the viability of both conventional SSBs and RFCs. Evolving interphases significantly increase cell resistance, deplete active materials, and impair capacity retention. Despite extensive research, no effective strategy has yet been reported to effectively minimize SEI formation, posing a major challenge to the large-scale implementation of high-capacity electrodes.

This doctoral thesis was focused on improving analytical models to predict interphase growth and performance decay in SSBs. To this end, transferable experimental approaches were developed to complement established concepts and assess transport properties, particularly σ_{el}, in relevant solid ion conductors and interphases. The findings reveal substantial interphase growth kinetics and inform future investigations, deepening the understanding of interphase dynamics in SSBs. Ultimately, the conceptual understanding developed in this thesis provides a strong foundation for addressing the remaining challenges in controlling degradation processes across various battery chemistries, paving the way toward realizing the anticipated benefits of SSBs. Key remaining challenges and gaps in understanding include: (*i*) *Protective Concepts at the metal|SE interface*, (*ii*) *Microstructure and Spatial Distribution of Phases within Interphases*, and (*iii*) *Transfer to Cathode Materials and Other Battery Chemistries*.

i. Protective Concepts at the metal|SE interface

Most practical inorganic SEs are thermodynamically unstable in contact with alkali metals due to their limited ESW. Therefore, protective strategies are necessary to protect susceptible SEs from the low potential of negative electrodes, as demonstrated in the first publication of this doctoral thesis. Two key stabilization concepts have emerged to mitigate SE degradation at the metal|SE interface: (a) artificial interlayers applied between the components and (b) modified SEI compositions. The first approach limits alkali metal deposition at the SE interface by maintaining low σ_{el}, while requiring high σ_{ion} to minimize resistance and preserve cell performance. Here, native oxide layers (*i.e.*, Li_2O, as studied for indium interlayers) represent only an initial step toward utilizing protective interlayers. The second approach involves chemical engineering to control the composition of the forming interphase, ensuring favorable multiphase properties to sustain optimal cell performance. Therefore, guidelines were established in the first publication and theoretical studies and calculations should support these efforts.[168,170] Additionally, recent studies have introduced the concept of fully reduced SEs with sufficient σ_{ion}, presenting another potential route toward stable metal|SE interfaces.[145,146]

As discussed in Chapter 2.3.ii., the σ_{el} of SEs ($< 10^{-8}$ S cm^{-1}) is believed to compromise the electrochemical stability of inorganic SEs, potentially accelerating SE degradation. Therefore, a comprehensive examination of the electronic properties of relevant SEs – as explored in the third publication of this doctoral thesis – could provide insights to effectively control σ_{el}, mitigate degradation processes, and enhance the lifetime of SSBs. LiPON SEs, in particular, are of interest due to their extremely low σ_{el} and slow interphase growth rates, providing valuable insights to target potential stabilization strategies.

ii. Microstructure and Spatial Distribution of Phases within Interphases

The bulk-material synthesis approach from the first publication introduced a transferable method to determine effective transport properties and partial conductivities of interphases, enabling accurate estimation of interphase rate constants. However, to develop effective stabilization strategies, it is also crucial to gain additional knowledge about the microstructural composition and morphology of interphases. Here, especially the chemical environment of phosphorous is of particular interest, initiating the degradation reaction. Sophisticated techniques such as high-resolution transmission electron microscopy, *operando* X-ray computed tomography, and nuclear magnetic resonance could provide further understanding of the microstructure and composition of interphases. Although these approaches are complex and time-intensive, they may also offer new insights into interphase growth mechanisms. Consequently, the results from CTTA measurements in the fifth publication informed *operando* XPS studies, enabling the identification of interphase composition in lithiated LPSCl in contact with In/$(InLi)_x$. Such insights drive advancements in the chemical engineering of stabilization strategies and help to establish selection protocols for artificial interlayers.

Thus, so far, only preliminary observations and suggestions have been made in the literature to mechanistically explain the conduction pathways across multiphase degradation layers in SSBs. As a result, the identification of preferential electronic percolation pathways within the interphase microstructure remains largely speculative, with only initial hypotheses regarding the underlying growth mechanisms. For instance, Burton *et al.*[158] suggested that a lithiation gradient of phosphorus species influences and promotes SEI formation.

iii. Transfer to Cathode Materials and Other Battery Chemistries

The second publication demonstrated that interphase rate constants derived from EIS or CTTA are strongly influenced by complex contact conditions in solid-state systems. In contrast, the introduced bulk-material synthesis offers a broadly applicable alternative to estimate interphase rate constants. Its applicability to other materials in future research was demonstrated by Mandal *et al.*[268], who extended it from sulfide to halide SE. Additionally, while numerous studies focus on alkali metal electrodes (*e.g.*, in symmetrical cells), research on alloy materials remains limited. The presented study on the In–Li alloy system offers a systematic approach using CTTA measurements to investigate interphase formation transferable to various alloy|SE interfaces, including those with silicon alloy electrodes. Degradation on the cathode side also contributes to performance losses in SSBs, which is particularly critical for RFCs and necessitates detailed investigations into degradation processes related to CAMs and triple-phase boundaries. Through the comprehensive application of the Hebb-Wagner method, as analyzed and derived in the third publication, design rules for MIECs as catholytes in solid-state sulfur cathodes could be established.

Finally, gained understanding along with the presented investigations and perspectives should be extended to other solid-state battery systems, such as sodium- or potassium-based chemistries and their alloys, which encounter similar challenges related to material incompatibility.

6. References

1. Summary for Policymakers. In *Climate Change 2022 – Impacts, Adaptation and Vulnerability*, Intergovernmental Panel on Climate Change (IPCC) ; Cambridge University Press, 3–34; 10.1017/9781009325844.001 (2023).
2. Barros, V. R. *et al. Climate Change 2014: Impacts, Adaptation and Vulnerability* (Cambridge University Press, Cambridge, 2014).
3. Field, C. B. *et al. Climate Change 2014 Impacts, Adaptation, and Vulnerability* (Cambridge University Press, Cambridge, 2014).
4. Gielen, D. *et al.* The Role of Renewable Energy in the Global Energy Transformation. *Energy Strategy Reviews* **24,** 38–50; 10.1016/j.esr.2019.01.006 (2019).
5. Dunn, J. B. *et al.* The Significance of Li-Ion Batteries in Electric Vehicle Life-Cycle Energy and Emissions and Recycling's Role in its Reduction. *Energy Environ. Sci.* **8,** 158–168; 10.1039/C4EE03029J (2015).
6. Larcher, D. & Tarascon, J.-M. Towards Greener and More Sustainable Batteries for Electrical Energy Storage. *Nature Chemistry* **7,** 19–29; 10.1038/nchem.2085 (2015).
7. Nitta, N. *et al.* Li-Ion Battery Materials: Present and Future. *Materials Today* **18,** 252–264; 10.1016/j.mattod.2014.10.040 (2015).
8. Armand, M. & Tarascon, J.-M. Building Better Batteries. *Nature* **451,** 652–657; 10.1038/451652a (2008).
9. Winter, M., Barnett, B. & Xu, K. Before Li Ion Batteries. *Chemical Reviews* **118,** 11433–11456; 10.1021/acs.chemrev.8b00422 (2018).
10. Janek, J. & Zeier, W. G. A Solid Future for Battery Development. *Nat Energy* **1,** 16141; 10.1038/nenergy.2016.141 (2016).
11. Albertus, P. *et al.* Challenges for and Pathways toward Li-Metal-Based All-Solid-State Batteries. *ACS Energy Lett.*, 1399–1404; 10.1021/acsenergylett.1c00445 (2021).
12. Weiss, M. *et al.* Fast Charging of Lithium-Ion Batteries: A Review of Materials Aspects. *Adv. Energy Mater.* **11**; 10.1002/aenm.202101126 (2021).
13. Liu, J. *et al.* Pathways for Practical High-Energy Long-Cycling Li-Metal Batteries. *Nat Energy* **4,** 180–186; 10.1038/s41560-019-0338-x (2019).
14. Monroe, C. & Newman, J. The Effect of Interfacial Deformation on Electrodeposition Kinetics. *J. Electrochem. Soc.* **151,** A880; 10.1149/1.1710893 (2004).
15. Monroe, C. & Newman, J. The Impact of Elastic Deformation on Deposition Kinetics at Lithium/Polymer Interfaces. *J. Electrochem. Soc.* **152,** A396; 10.1149/1.1850854 (2005).
16. Bachman, J. C. *et al.* Inorganic Solid-State Electrolytes for Lithium Batteries: Mechanisms and Properties Governing Ion Conduction. *Chem. Rev.* **116,** 140–162; 10.1021/acs.chemrev.5b00563 (2016).
17. Lau, J. *et al.* Sulfide Solid Electrolytes for Lithium Battery Applications. *Adv. Energy Mater.* **8**; 10.1002/aenm.201800933 (2018).
18. Famprikis, T. *et al.* Fundamentals of Inorganic Solid-State Electrolytes for Batteries. *Nat Mater* **18,** 1278–1291; 10.1038/s41563-019-0431-3 (2019).

19. Wang, M. J. *et al.* Transitioning Solid-State Batteries from Lab to Market: Linking Electro-Chemo-Mechanics with Practical Considerations. *Joule* **5,** 1371–1390; 10.1016/j.joule.2021.04.001 (2021).

20. Shen, Y. *et al.* Unlocking the Energy Capabilities of Lithium Metal Electrode with Solid-State Electrolytes. *Joule* **2,** 1674–1689; 10.1016/j.joule.2018.06.021 (2018).

21. Janek, J. & Zeier, W. G. Challenges in Speeding up Solid-State Battery Development. *Nat Energy* **8,** 230–240; 10.1038/s41560-023-01208-9 (2023).

22. Koerver, R. *et al.* Capacity Fade in Solid-State Batteries: Interphase Formation and Chemomechanical Processes in Nickel-Rich Layered Oxide Cathodes and Lithium Thiophosphate Solid Electrolytes. *Chem. Mater.* **29,** 5574–5582; 10.1021/acs.chemmater.7b00931 (2017).

23. Koerver, R. *et al.* Chemo-Mechanical Expansion of Lithium Electrode Materials - On the Route to Mechanically Optimized All-Solid-State Batteries. *Energy Environ. Sci.* **11,** 2142–2158; 10.1039/C8EE00907D (2018).

24. Krauskopf, T. *et al.* Physicochemical Concepts of the Lithium Metal Anode in Solid-State Batteries. *Chem. Rev.* **120,** 7745–7794; 10.1021/acs.chemrev.0c00431 (2020).

25. Kasemchainan, J. *et al.* Critical Stripping Current Leads to Dendrite Formation on Plating in Lithium Anode Solid Electrolyte Cells. *Nature Materials* **18,** 1105–1111; 10.1038/s41563-019-0438-9 (2019).

26. Raj, V. *et al.* Direct Correlation Between Void Formation and Lithium Dendrite Growth in Solid-State electrolytes with Interlayers. *Nature Materials* **21,** 1050–1056; 10.1038/s41563-022-01264-8 (2022).

27. Bates, A. M. *et al.* Are Solid-State Batteries Safer than Lithium-Ion Batteries? *Joule* **6,** 742–755; 10.1016/j.joule.2022.02.007 (2022).

28. Luo, Y. *et al.* Safety Concerns in Solid-State Lithium Batteries: From Materials to Devices. *Energy Environ. Sci.* **17,** 7543–7565; 10.1039/D4EE02358G (2024).

29. Kim, T. *et al.* Thermal Runaway Behavior of Li_6PS_5Cl Solid Electrolytes for $LiNi_{0.8}Co_{0.1}Mn_{0.1}O_2$ and $LiFePO_4$ in All-Solid-State Batteries. *Chem. Mater.* **34,** 9159–9171; 10.1021/acs.chemmater.2c02106 (2022).

30. Otto, S.-K. *et al.* Storage of Lithium Metal: The Role of the Native Passivation Layer for the Anode Interface Resistance in Solid State Batteries. *ACS Appl. Energy Mater.* **4,** 12798–12807; 10.1021/acsaem.1c02481 (2021).

31. Otto, S.-K. *et al.* In-Depth Characterization of Lithium-Metal Surfaces with XPS and ToF-SIMS: Toward Better Understanding of the Passivation Layer. *Chem. Mater.* **33,** 859–867; 10.1021/acs.chemmater.0c03518 (2021).

32. Wang, M. J. *et al.* Enabling "Lithium-Free" Manufacturing of Pure Lithium Metal Solid-State Batteries through in-situ Plating. *Nat Commun* **11,** 5201; 10.1038/s41467-020-19004-4 (2020).

33. Lee, Y.-G. *et al.* High-Energy Long-Cycling All-Solid-State Lithium Metal Batteries Enabled by Silver–Carbon Composite Anodes. *Nat Energy* **5,** 299; 10.1038/s41560-020-0575-z (2020).

34. Heubner, C. *et al.* From Lithium-Metal toward Anode-Free Solid-State Batteries: Current Developments, Issues, and Challenges. *Adv Funct Materials* **31,** 2106608; 10.1002/adfm.202106608 (2021).
35. Walther, F. *et al.* Visualization of the Interfacial Decomposition of Composite Cathodes in Argyrodite-Based All-Solid-State Batteries Using Time-of-Flight Secondary-Ion Mass Spectrometry. *Chem. Mater.* **31,** 3745–3755; 10.1021/acs.chemmater.9b00770 (2019).
36. Hatzell, K. B. *et al.* Challenges in Lithium Metal Anodes for Solid-State Batteries. *ACS Energy Lett.* **5,** 922–934; 10.1021/acsenergylett.9b02668 (2020).
37. Zuo, T.-T. *et al.* Formation of an Artificial Cathode–Electrolyte Interphase to Suppress Interfacial Degradation of Ni-Rich Cathode Active Material with Sulfide Electrolytes for Solid-State Batteries. *ACS Energy Lett.* **8,** 1322; 10.1021/acsenergylett.2c02835 (2023).
38. Peled, E. The Electrochemical Behavior of Alkali and Alkaline Earth Metals in Nonaqueous Battery Systems—The Solid Electrolyte Interphase Model. *J. Electrochem. Soc.* **126,** 2047–2051; 10.1149/1.2128859 (1979).
39. Wenzel, S. *et al.* Direct Observation of the Interfacial Instability of the Fast Ionic Conductor $Li_{10}GeP_2S_{12}$ at the Lithium Metal Anode. *Chem. Mater.* **28,** 2400–2407; 10.1021/acs.chemmater.6b00610 (2016).
40. Otto, S.-K., Riegger, L. M., Fuchs, T., Kayser, S., Schweitzer, P., Burkhardt, S., Henss, A., Janek, J. In Situ Investigation of Lithium Metal–Solid Electrolyte Anode Interfaces with ToF-SIMS. *Adv. Mater. Interfaces* **13**; 10.1002/admi.202102387 (2022).
41. Aktekin, B. *et al.* SEI Growth on Lithium Metal Anodes in Solid-State Batteries Quantified with Coulometric Titration Time Analysis. *Nat Commun* **14,** 6946; 10.1038/s41467-023-42512-y (2023).
42. Dai, W. *et al.* All-Solid-State Thin-Film Batteries Based on Lithium Phosphorus Oxynitrides. *Mater. Futures* **1,** 32101; 10.1088/2752-5724/ac7db2 (2022).
43. Tippens, J. *et al.* Visualizing Chemomechanical Degradation of a Solid-State Battery Electrolyte. *ACS Energy Lett.* **4,** 1475–1483; 10.1021/acsenergylett.9b00816 (2019).
44. Lee, C. *et al.* Stack Pressure Measurements to Probe the Evolution of the Lithium–Solid-State Electrolyte Interface. *ACS Energy Lett.* **6,** 3261; 10.1021/acsenergylett.1c01395 (2021).
45. Zhu, Y., He, X. & Mo, Y. Origin of Outstanding Stability in the Lithium Solid Electrolyte Materials: Insights from Thermodynamic Analyses Based on First-Principles Calculations. *ACS Appl. Mater. Interfaces* **7,** 23685–23693; 10.1021/acsami.5b07517 (2015).
46. Zhu, Y., He, X. & Mo, Y. First Principles Study on Electrochemical and Chemical Stability of Solid Electrolyte–Electrode Interfaces in All-Solid-State Li-Ion Batteries. *J. Mater. Chem. A* **4,** 3253–3266; 10.1039/C5TA08574H (2016).
47. Richards, W. D. *et al.* Interface Stability in Solid-State Batteries. *Chem. Mater.* **28,** 266–273; 10.1021/acs.chemmater.5b04082 (2016).
48. Seymour, I. D. & Aguadero, A. Suppressing Void Formation in All-Solid-State Batteries: The Role of Interfacial Adhesion on Alkali Metal Vacancy Transport. *J. Mater. Chem. A* **9,** 19901–19913; 10.1039/D1TA03254B (2021).
49. Schmalzried, H. & Janek, J. Chemical Kinetics of Phase Boundaries in Solids. *Ber Bunsenges Phys Chem* **102,** 127–143; 10.1002/bbpc.19981020202 (1998).

50. Kroeger, F. A. & Vink, H. J. Relations between the Concentrations of Imperfections in Crystalline Solids. *Solid State Physics* **3,** 307–435; 10.1016/S0081-1947(08)60135-6 (1956).

51. Jow, T. R. & Liang, C. C. Interface between Solid Electrode and Solid Electrolyte—A Study of the Li/LiI(Al_2O_3) Solid-Electrolyte System. *J. Electrochem. Soc.* **130,** 737–740; 10.1149/1.2119795 (1983).

52. Meyer, M., Rickert, H. & Schwaitzer, U. Investigations on the Kinetics of the Anodic Dissolution of Lithium at the Interface Li/Li_3N. *Solid State Ionics* **9-10,** 689–693; 10.1016/0167-2738(83)90315-6 (1983).

53. Krauskopf, T. *et al.* Toward a Fundamental Understanding of the Lithium Metal Anode in Solid-State Batteries—An Electrochemo-Mechanical Study on the Garnet-Type Solid Electrolyte $Li_{6.25}Al_{0.25}La_3Zr_2O_{12}$. *ACS Applied Materials & Interfaces* **11,** 14463–14477; 10.1021/acsami.9b02537 (2019).

54. Wang, M. J., Choudhury, R. & Sakamoto, J. Characterizing the Li-Solid-Electrolyte Interface Dynamics as a Function of Stack Pressure and Current Density. *Joule* **3,** 2165–2178; 10.1016/j.joule.2019.06.017 (2019).

55. Spencer Jolly, D. *et al.* Sodium/Na β″ Alumina Interface: Effect of Pressure on Voids. *ACS Applied Materials & Interfaces* **12,** 678–685; 10.1021/acsami.9b17786 (2020).

56. Spencer Jolly, D. *et al.* Temperature Dependence of Lithium Anode Voiding in Argyrodite Solid-State Batteries. *ACS Applied Materials & Interfaces* **13,** 22708–22716; 10.1021/acsami.1c06706 (2021).

57. Hänsel, C. *et al.* Favorable Interfacial Chemomechanics Enables Stable Cycling of High-Li-Content Li–In/Sn Anodes in Sulfide Electrolyte-Based Solid-State Batteries. *Chem. Mater.* **33,** 6029–6040; 10.1021/acs.chemmater.1c01431 (2021).

58. Krauskopf, T. *et al.* Diffusion Limitation of Lithium Metal and Li–Mg Alloy Anodes on LLZO Type Solid Electrolytes as a Function of Temperature and Pressure. *Adv. Energy Mater.* **9,** 1902568; 10.1002/aenm.201902568 (2019).

59. Alexander, G. V. *et al.* Extreme Lithium-Metal Cycling Enabled by a Mixed Ion- and Electron-Conducting Garnet Three-Dimensional Architecture. *Nature Materials* **22,** 1136–1143; 10.1038/s41563-023-01627-9 (2023).

60. Fuchs, T. *et al.* Increasing the Pressure-Free Stripping Capacity of the Lithium Metal Anode in Solid-State-Batteries by Carbon Nanotubes. *Adv. Energy Mater.* **12**; 10.1002/aenm.202201125 (2022).

61. Aspinall, J., Armstrong, D. E. & Pasta, M. EBSD-Coupled Indentation: Nanoscale Mechanics of Lithium Metal. *Materials Today Energy* **30**; 10.1016/j.mtener.2022.101183 (2022).

62. Fuchs, T. *et al.* Imaging the Microstructure of Lithium and Sodium Metal in Anode-free Solid-State Batteries using Electron Backscatter Diffraction. *Nature Materials* **23,** 1678–1685; 10.1038/s41563-024-02006-8 (2024).

63. Becker, J. *et al.* Microstructure of Lithium Metal Electrodeposited at the Steel|Li_6PS_5Cl Interface in "Anode-Free" Solid-State Batteries. *Adv. Energy Mater.*; 10.1002/aenm.202404975 (2024).

64. Brodusch, N., Zaghib, K. & Gauvin, R. Electron Backscatter Diffraction Applied to Lithium Sheets Prepared by Broad Ion Beam Milling. *Microscopy research and technique* **78,** 30–39; 10.1002/jemt.22441 (2015).

65. Jäckle, M. *et al.* Self-Diffusion Barriers: Possible Descriptors for Dendrite Growth in Batteries? *Energy Environ. Sci.* **11,** 3400–3407; 10.1039/c8ee01448e (2018).

66. Jäckle, M. & Groß, A. Microscopic Properties of Lithium, Sodium, and Magnesium Battery Anode Materials Related to Possible Dendrite Growth. *The Journal of Chemical Physics* **141,** 174710; 10.1063/1.4901055 (2014).

67. Singh, D. K. *et al.* Overcoming Anode Instability in Solid-State Batteries through Control of the Lithium Metal Microstructure. *Adv Funct Materials* **33**; 10.1002/adfm.202211067 (2023).

68. Aota, L. S. *et al.* Grain Boundaries Control Lithiation of Solid Solution Substrates in Lithium Metal Batteries. *Advanced Science,* e2409275; 10.1002/advs.202409275 (2024).

69. Haslam, C. G. *et al.* The Effect of Alloying Interlayers on Lithium Anode Morphology and Microstructure in "Anode-Free" Solid-State Batteries. *ACS Energy Lett.,* 2285–2291; 10.1021/acsenergylett.5c00149 (2025).

70. Zhang, M. *et al.* Grain selection growth of soft metal in electrochemical processes. *Joule* **9,** 101847; 10.1016/j.joule.2025.101847 (2025).

71. Cao, D. *et al.* Lithium Dendrite in All-Solid-State Batteries: Growth Mechanisms, Suppression Strategies, and Characterizations. *Matter* **3,** 57; 10.1016/j.matt.2020.03.015 (2020).

72. Wang, M., Wolfenstine, J. B. & Sakamoto, J. Temperature Dependent Flux Balance of the $Li/Li_7La_3Zr_2O_{12}$ Interface. *Electrochimica Acta* **296,** 842–847; 10.1016/j.electacta.2018.11.034 (2019).

73. Masias, A. *et al.* Elastic, Plastic, and Creep Mechanical Properties of Lithium Metal. *J Mater Sci* **54,** 2585–2600; 10.1007/s10853-018-2971-3 (2019).

74. Liu, H. *et al.* Controlling Dendrite Growth in Solid-State Electrolytes. *ACS Energy Lett.* **5,** 833–843; 10.1021/acsenergylett.9b02660 (2020).

75. Tsai, C.-L. *et al.* $Li_7La_3Zr_2O_{12}$ Interface Modification for Li Dendrite Prevention. *ACS Applied Materials & Interfaces* **8,** 10617–10626; 10.1021/acsami.6b00831 (2016).

76. Flatscher, F. *et al.* The Natural Critical Current Density Limit for $Li_7La_3Zr_2O_{12}$ Garnets. *J. Mater. Chem. A* **8,** 15782–15788; 10.1039/C9TA14177D (2020).

77. Krauskopf, T. *et al.* Lithium-Metal Growth Kinetics on LLZO Garnet-Type Solid Electrolytes. *Joule* **3,** 2030–2049; 10.1016/j.joule.2019.06.013 (2019).

78. Cheng, L. *et al.* Effect of Surface Microstructure on Electrochemical Performance of Garnet Solid Electrolytes. *ACS Applied Materials & Interfaces* **7,** 2073; 10.1021/am508111r (2015).

79. Liang, C. *et al.* Effect of Charging Modes and Parameters on Lithium Dendrite Growth Studied by Phase-Field Modeling. *J. Phys. Chem. C*; 10.1021/acs.jpcc.4c08243 (2025).

80. Kazyak, E. *et al.* Li Penetration in Ceramic Solid Electrolytes: Operando Microscopy Analysis of Morphology, Propagation, and Reversibility. *Matter* **2,** 1025–1048; 10.1016/j.matt.2020.02.008 (2020).

81. Wu, B. *et al.* The Role of the Solid Electrolyte Interphase Layer in Preventing Li Dendrite Growth in SSBs. *Energy Environ. Sci.* **11,** 1803; 10.1039/C8EE00540K (2018).

82. Duan, J. *et al.* Solid Electrolyte Cracking due to Lithium Filament Growth and Concept of Mechanical Reinforcement – An Operando Study. *Materials Today* **70,** 33–43; 10.1016/j.mattod.2023.10.003 (2023).

83. Qiu, H. *et al.* Stable Lithium Metal Anode Enabled by Lithium Metal Partial Alloying. *Nano Energy* **65,** 103989; 10.1016/j.nanoen.2019.103989 (2019).

84. Lewis, J. A. *et al.* The Promise of Alloy Anodes for Solid-State Batteries. *Joule* **6,** 1418–1430; 10.1016/j.joule.2022.05.016 (2022).

85. Zhang, W.-J. A Review of the Electrochemical Performance of Alloy Anodes for Lithium-Ion Batteries. *Journal of Power Sources* **196,** 13–24; 10.1016/j.jpowsour.2010.07.020 (2011).

86. Heligman, B. T. & Manthiram, A. Elemental Foil Anodes for Lithium-Ion Batteries. *ACS Energy Lett.* **6,** 2666–2672; 10.1021/acsenergylett.1c01145 (2021).

87. Han, S. Y. *et al.* Porous Metals from Chemical Dealloying for Solid-State Battery Anodes. *Chem. Mater.* **32,** 2461–2469; 10.1021/acs.chemmater.9b04992 (2020).

88. Jeong, W. J. *et al.* Electrochemical Behavior of Elemental Alloy Anodes in Solid-State Batteries. *ACS Energy Lett.,* 2554–2563; 10.1021/acsenergylett.4c00915 (2024).

89. Gu, X., Dong, J. & Lai, C. Li-Containing Alloys Beneficial for Stabilizing Lithium Anode: A Review. *Engineering Reports* **3**; 10.1002/eng2.12339 (2021).

90. Jing, W. *et al.* Li-Indium Alloy Anode for High-Performance Li-Metal Batteries. *Journal of Alloys and Compounds,* 166517; 10.1016/j.jallcom.2022.166517 (2022).

91. Qu, J. *et al.* High Rate Transfer Mechanism of Lithium Ions in Lithium–Tin and Lithium–Indium Alloys for Lithium Batteries. *J. Phys. Chem. C* **124,** 24644–24652; 10.1021/acs.jpcc.0c07880 (2020).

92. Obrovac, M. N. & Chevrier, V. L. Alloy Negative Electrodes for Li-Ion Batteries. *Chemical Reviews* **114,** 11444–11502; 10.1021/cr500207g (2014).

93. Choi, S. *et al.* Highly Elastic Binders Integrating Polyrotaxanes for Silicon Microparticle Anodes in Lithium Ion Batteries. *Science* **357,** 279–283; 10.1126/science.aal4373. (2017).

94. Nitta, N. & Yushin, G. High-Capacity Anode Materials for Lithium-Ion Batteries: Choice of Elements and Structures for Active Particles. *Part & Part Syst Charact* **31,** 317–336; 10.1002/ppsc.201300231 (2014).

95. Wang, C. *et al.* Common Capacity Fade Mechanisms of Metal Foil Alloy Anodes with Different Compositions for Lithium Batteries. *ACS Energy Lett.* **8,** 2252–2258; 10.1021/acsenergylett.3c00455 (2023).

96. Huo, H. & Janek, J. Silicon as Emerging Anode in Solid-State Batteries. *ACS Energy Lett.* **7,** 4005–4016; 10.1021/acsenergylett.2c01950 (2022).

97. Nelson, D. L. *et al.* Fracture Dynamics in Silicon Anode Solid-State Batteries. *ACS Energy Lett.* **9,** 6085–6095; 10.1021/acsenergylett.4c02800 (2024).

98. Shi, P. *et al.* A Review of Composite Lithium Metal Anode for Practical Applications. *Adv Materials Technologies* **5**; 10.1002/admt.201900806 (2020).

99. Sandoval, S. E. *et al.* Structural and Electrochemical Evolution of Alloy Interfacial Layers in Anode-free Solid-State Batteries. *Joule* **7,** 2054–2073; 10.1016/j.joule.2023.07.022 (2023).

100. Xu, P. *et al.* Anode-Free Alkali Metal Batteries: From Laboratory to Practicability. *Adv Funct Materials* **34**; 10.1002/adfm.202406080 (2024).

101. Jin, S. *et al.* Solid-Solution-Based Metal Alloy Phase for Highly Reversible Lithium Metal Anode. *Journal of the American Chemical Society* **142,** 8818; 10.1021/jacs.0c01811 (2020).

102. Li, J. *et al.* Li Alloys in All Solid-State Lithium Batteries: A Review of Fundamentals and Applications. *Electrochem. Energy Rev.* **7**; 10.1007/s41918-024-00221-0 (2024).

103. Wakasugi, J., Munakata, H. & Kanamura, K. Effect of Gold Layer on Interface Resistance between Lithium Metal Anode and $Li_{6.25}Al_{0.25}La_3Zr_2O_{12}$ Solid Electrolyte. *J. Electrochem. Soc.* **164,** A1022-A1025; 10.1149/2.0471706jes (2017).

104. Haslam, C. & Sakamoto, J. Stable Lithium Plating in "Lithium Metal-Free" Solid-State Batteries Enabled by Seeded Lithium Nucleation. *J. Electrochem. Soc.* **170,** 40524; 10.1149/1945-7111/accab4 (2023).

105. European Commission *et al. Study on the critical raw materials for the EU 2023 – Final report* (Publications Office of the European Union, 2023).

106. Takada, K. *et al.* Solid State Lithium Battery with Oxysulfide Glass. *Solid State Ionics* **86-88,** 877–882; 10.1016/0167-2738(96)00199-3 (1996).

107. Hertle, J. *et al.* Miniaturization of Reference Electrodes for Solid-State Lithium-Ion Batteries. *J. Electrochem. Soc.* **170,** 40519; 10.1149/1945-7111/accb6f (2023).

108. Dugas, R. *et al.* Engineered Three-Electrode Cells for Improving Solid State Batteries. *J. Electrochem. Soc.* **168,** 90508; 10.1149/1945-7111/ac208d (2021).

109. Tatsumisago, M., Mizuno, F. & Hayashi, A. All-Solid-State Lithium Secondary Batteries using Sulfide-Based Glass–Ceramic Electrolytes. *Journal of Power Sources* **159,** 193–199; 10.1016/j.jpowsour.2006.04.037 (2006).

110. Wen, C. & Huggins, R. A. Thermodynamic and Mass Transport Properties of "LiIn". *Materials Research Bulletin* **15,** 1225–1234; 10.1016/0025-5408(80)90024-0 (1980).

111. Ikezawa, A. *et al.* Performance of $Li_4Ti_5O_{12}$-Based Reference Electrode for the Electrochemical Analysis of All-Solid-State Lithium-Ion Batteries. *Electrochemistry Communications* **116,** 106743; 10.1016/j.elecom.2020.106743 (2020).

112. Wang, C. *et al.* The Influence of Pressure on Lithium Dealloying in Solid-State and Liquid Electrolyte Batteries. *Nature Materials*; 10.1038/s41563-025-02198-7 (2025).

113. Santhosha, A. L. *et al.* The Indium−Lithium Electrode in Solid-State Lithium-Ion Batteries: Phase Formation, Redox Potentials, and Interface Stability. *Batteries & Supercaps* **2,** 524–529; 10.1002/batt.201800149 (2019).

114. Thümmel, R. & Klemm, W. Das Verhalten der Alkalimetalle zu den Metallen der Gruppe III B. *Zeitschrift fur anorganische und allgemeine Chemie* **376,** 44–63 (1970).

115. Alexander, W. A. *et al.* The Lithium–Indium System. *Can. J. Chem.* **54,** 1052–1060; 10.1139/v76-150 (1976).

116. Lu, Y. *et al.* The Carrier Transition from Li Atoms to Li Vacancies in Solid-State Lithium Alloy Anodes. *Science Advances* **7,** eabi5520; 10.1126/sciadv.abi5520 (2021).

117. Yanev, S. *et al.* Editors' Choice—Alleviating the Kinetic Limitations of the Li-In Alloy Anode in All-Solid-State Batteries. *J. Electrochem. Soc.*; 10.1149/1945-7111/ad2594 (2024).

118. Wang, Z. *et al.* Tailoring Lithium Concentration in Alloy Anodes for Long Cycling and High Areal Capacity in Sulfide-Based All Solid-State Batteries. *eScience* **3,** 100087; 10.1016/j.esci.2022.100087 (2023).

119. Aspinall, J. *et al.* Effect of Microstructure on the Cycling Behavior of Li–In Alloy Anodes for Solid-State Batteries. *ACS Energy Lett.*, 578–585; 10.1021/acsenergylett.3c02274 (2024).

120. Jin, S. *et al.* Fast-Charge, Long-Duration Storage in Lithium Batteries. *Joule*; 10.1016/j.joule.2023.12.022 (2024).

121. Nam, Y. J. *et al.* Diagnosis of Failure Modes for All-Solid-State Li-Ion Batteries Enabled by Three-Electrode Cells. *J. Mater. Chem. A* **6,** 14867–14875; 10.1039/C8TA03450H (2018).

122. Sedlmeier, C. *et al.* A Micro-Reference Electrode for Electrode-Resolved Impedance and Potential Measurements in All-Solid-State Battery Pouch Cells and its Application to the Study of Indium-Lithium Anodes. *J. Electrochem. Soc.* **170,** 30536; 10.1149/1945-7111/acc699 (2023).

123. Qu, J. *et al.* High Rate Transfer Mechanism of Lithium Ions in Lithium–Tin and Lithium–Indium Alloys for Lithium Batteries. *J. Phys. Chem. C* **124,** 24644–24652; 10.1021/acs.jpcc.0c07880 (2020).

124. Puls, S. *et al.* Benchmarking the Reproducibility of All-Solid-State Battery Cell Performance. *Nat Energy* **9,** 1310–1320; 10.1038/s41560-024-01634-3 (2024).

125. Ong, S. P. *et al.* Phase Stability, Electrochemical Stability and Ionic Conductivity of the $Li_{10\pm1}MP_2X_{12}$ (M = Ge, Si, Sn, Al or P, and X = O, S or Se) Family of Superionic Conductors. *Energy Environ. Sci.* **6,** 148–156; 10.1039/C2EE23355J (2013).

126. Weppner, W. Fundamental Aspects of Electrochemical, Chemical and Electrostatic Potentials in Lithium Batteries. In *Materials for Lithium-Ion Batteries*, C. Julien & Z. Stoynov ; Springer Netherlands, 401–412; 10.1007/978-94-011-4333-2_20 (2000).

127. Weppner, W. Engineering of Solid State Ionic Devices. *Ionics* **9,** 444–464; 10.1007/BF02376599 (2003).

128. Wang, S. *et al.* Lithium Argyrodite as Solid Electrolyte and Cathode Precursor for Solid-State Batteries with Long Cycle Life. *Adv. Energy Mater.* **11**; 10.1002/aenm.202101370 (2021).

129. Tong, Z. *et al.* Interface Between Solid-State Electrolytes and Li-Metal Anodes: Issues, Materials, and Processing Routes. *ACS Applied Materials & Interfaces* **12,** 47181–47196; 10.1021/acsami.0c13591 (2020).

130. Ma, C. *et al.* Interfacial Stability of Li Metal-Solid Electrolyte Elucidated via in-situ Electron Microscopy. *Nano Letters* **16,** 7030–7036; 10.1021/acs.nanolett.6b03223 (2016).

131. Connell, J. G. *et al.* Kinetic versus Thermodynamic Stability of LLZO in Contact with Lithium Metal. *Chem. Mater.* **32,** 10207–10215; 10.1021/acs.chemmater.0c03869 (2020).

132. Hofstetter, K. *et al.* Present Understanding of the Stability of Li-Stuffed Garnets with Moisture, Carbon Dioxide, and Metallic Lithium. *Journal of Power Sources* **390,** 297–312; 10.1016/j.jpowsour.2018.04.016 (2018).

133. Wenzel, S. *et al.* Interphase Formation and Degradation of Charge Transfer Kinetics between a Lithium Metal Anode and Highly Crystalline $Li_7P_3S_{11}$ Solid Electrolyte. *Solid State Ionics* **286,** 24–33; 10.1016/j.ssi.2015.11.034 (2016).

134. Wenzel, S. *et al.* Interfacial Reactivity and Interphase Growth of Argyrodite Solid Electrolytes at Lithium Metal Electrodes. *Solid State Ionics* **318,** 102; 10.1016/j.ssi.2017.07.005 (2018).

135. Wenzel, S. *et al.* Interphase Formation on Lithium Solid Electrolytes—An in-situ Approach to Study Interfacial Reactions by Photoelectron Spectroscopy. *Solid State Ionics* **278,** 98–105; 10.1016/j.ssi.2015.06.001 (2015).

136. Lorger, S., Usiskin, R. E. & Maier, J. Transport and Charge Carrier Chemistry in Lithium Sulfide. *Adv. Funct. Mater.* **29**; 10.1002/adfm.201807688 (2019).

137. Maltsev, A. P. *et al.* Ionic Conductivity of Lithium Phosphides. *Crystals* **13,** 756; 10.3390/cryst13050756 (2023).

138. Sharon, M. & Pradhananga, R. R. Ionic Conductivity of Pure and Ca^{2+}- and Sr^{2+}-Doped Single Crystals of LiCl. *J. of Solid State Chem.* **40,** 20–27; 10.1016/0022-4596(81)90355-8 (1981).

139. Armstrong, R. D. & Landles, K. Lithium Ion Conducting Solids for Ambient Applications. *J. of Appl Electrochem* **12,** 533–535; 10.1007/BF00614979 (1982).

140. Jackson, B. & Young, D. A. Ionic Conduction in Pure and Doped Single-Crystalline Lithium Iodide. *J. Phys. Chem. Solids* **30,** 1973–1976; 10.1016/0022-3697(69)90174-7. (1969).

141. Poulsen, F. W. Ionic Conductivity of Solid Lithium Iodide and its Monohydrate. *Solid State Ionics* **2,** 53–57; 10.1016/0167-2738(81)90020-5. (1981).

142. R. Mercier, M. Tachez, J.P. Malugani, G. Robert. Effect of Homovalent (I^-−Br^-) Ion Substitution on the Ionic Conductivity of LiI_{1-x} Br_x Systems. *Solid State Ionics* **15,** 109–112; 10.1016/0167-2738(85)90088-8 (1985).

143. Nazri, G. Preparation, Structure and Ionic Conductivity of Lithium Phosphide. *Solid State Ionics* **34,** 97–102; 10.1016/0167-2738(89)90438-4. (1989).

144. Li, J. *et al.* Mixed Ion-Electron Conducting Li_3P for Efficient Cathode Prelithiation of All-Solid-State Li-Ion Batteries. *SmartMat* **4,** e1200; 10.1002/smm2.1200 (2023).

145. Landgraf, V. *et al.* Li_5NCl_2: A Fully-Reduced, Highly-Disordered Nitride-Halide Electrolyte for Solid-State Batteries with Lithium-Metal Anodes. *ACS Appl. Energy Mat.* **6,** 1661–1672; 10.1021/acsaem.2c03551 (2023).

146. Landgraf, V. *et al.* Disorder-Mediated Ionic Conductivity in Irreducible Solid Electrolytes. *Journal of the American Chemical Society* **147,** 18840–18852; 10.1021/jacs.5c02784 (2025).

147. Hartmann, P. *et al.* Degradation of NASICON-Type Materials in Contact with Lithium Metal: Formation of Mixed Conducting Interphases (MCI) on Solid Electrolytes. *J. Phys. Chem. C* **117,** 21064–21074; 10.1021/jp4051275 (2013).

148. Riegger, L. M. *et al.* Lithium-Metal Anode Instability of the Superionic Halide Solid Electrolytes and the Implications for Solid-State Batteries. *Angewandte Chemie (International ed. in English)* **60,** 6718–6723; 10.1002/anie.202015238 (2021).

149. Bron, P., Roling, B. & Dehnen, S. Impedance Characterization Reveals Mixed Conducting Interphases between Sulfidic Superionic Conductors and Lithium Metal Electrodes. *Journal of Power Sources* **352,** 127–134; 10.1016/j.jpowsour.2017.03.103 (2017).

150. Alt, C. D. *et al.* Quantifying Multiphase SEI Growth in Sulfide Solid Electrolytes. *Joule* **8,** 2755–2776; 10.1016/j.joule.2024.07.006 (2024).

151. Riegger, L. M. *et al.* Evolution of the Interphase between Argyrodite-Based Solid Electrolytes and the Lithium Metal Anode ─ The Kinetics of Solid Electrolyte Interphase Growth. *Chem. Mater.* **35,** 5091–5099; 10.1021/acs.chemmater.3c00676 (2023).

152. Banerjee, A. *et al.* Interfaces and Interphases in All-Solid-State Batteries with Inorganic Solid Electrolytes. *Chemical Reviews* **120,** 6878–6933; 10.1021/acs.chemrev.0c00101 (2020).

153. Guo, R., Hobold, G. M. & Gallant, B. M. The Ionic Interphases of the Lithium Anode in Solid State Batteries. *Current Opinion in Solid State and Materials Science* **26**; 10.1016/j.cossms.2021.100973 (2022).

154. Gibson, J. S. *et al.* Gently Does It!: In-situ Preparation of Alkali Metal-Solid Electrolyte Interfaces for Photoelectron Spectroscopy. *Faraday Discuss.* **236,** 267–287; 10.1039/d1fd00118c (2022).

155. Aktekin, B. *et al.* Operando Photoelectron Spectroscopy Analysis of Li_6PS_5Cl Electrochemical Decomposition Reactions in Solid-State Batteries. *ACS Energy Lett.,* 3492–3500; 10.1021/acsenergylett.4c01072 (2024).

156. Narayanan, S. *et al.* Effect of Current Density on the Solid Electrolyte Interphase Formation at the Lithium|Li_6PS_5Cl Interface. *Nat Commun* **13,** 7237; 10.1038/s41467-022-34855-9 (2022).

157. Ren, F. *et al.* Visualizing the SEI Formation between Lithium Metal and Solid-State Electrolyte. *Energy Environ. Sci.* **17,** 2743–2752; 10.1039/d3ee03536k (2024).

158. Burton, M. *et al.* The Role of Phosphorus in the Solid Electrolyte Interphase of Argyrodite Solid Electrolytes. *Nature Communications* **16,** 9304; 10.1038/s41467-025-64357-3 (2025).

159. Liang, Y. *et al.* In-situ XPS Investigation of the SEI Formed on LGPS and LAGP with Metallic Lithium. *Chemical communications (Cambridge, England)* **60,** 12597–12600; 10.1039/D4CC04462B (2024).

160. Jagger, B. & Pasta, M. Solid Electrolyte Interphases in Lithium Metal Batteries. *Joule* **7,** 2228–2244; 10.1016/j.joule.2023.08.007 (2023).

161. Turrell, S. J. *et al.* Origin of Stability in the Solid Electrolyte Interphase formed between Lithium and Lithium Phosphorus Oxynitride. *Chem. Mater.*; 10.1021/acs.chemmater.5c00483 (2025).

162. Cheng, D. *et al.* Unveiling the Stable Nature of the Solid Electrolyte Interphase between Lithium Metal and LiPON via Cryogenic Electron Microscopy. *Joule* **4,** 2484–2500; 10.1016/j.joule.2020.08.013 (2020).

163. Hood, Z. D. *et al.* Elucidating Interfacial Stability between Lithium Metal Anode and Li Phosphorus Oxynitride via In Situ Electron Microscopy. *Nano Letters* **21,** 151–157; 10.1021/acs.nanolett.0c03438 (2021).

164. Cheng, T. *et al.* Quantum Mechanics Reactive Dynamics Study of Solid Li-Electrode/Li_6PS_5Cl-Electrolyte Interface. *ACS Energy Lett.* **2,** 1454–1459; 10.1021/acsenergylett.7b00319 (2017).

165. Schwietert, T. K. *et al.* Clarifying the Relationship between Redox Activity and Electrochemical Stability in Solid Electrolytes. *Nature Materials* **19,** 428–435; 10.1038/s41563-019-0576-0 (2020).

166. Chaney, G. *et al.* Two-Step Growth Mechanism of the Solid Electrolyte Interphase in Argyrodyte/Li-Metal Contacts. *ACS Applied Materials & Interfaces* **16,** 24624–24630; 10.1021/acsami.4c02548 (2024).

167. Temprano, I. *et al.* Advanced Methods for Characterizing Battery Interfaces: Towards a Comprehensive Understanding of Interfacial Evolution in Modern Batteries. *Energy Storage Materials* **73,** 103794; 10.1016/j.ensm.2024.103794 (2024).

168. Wang, C. *et al.* Ionic Conduction through Reaction Products at the Electrolyte-Electrode Interface in All-Solid-State Li^+ Batteries. *ACS Applied Materials & Interfaces* **12,** 55510–55519; 10.1021/acsami.0c17285 (2020).

169. Golov, A. & Carrasco, J. Unveiling Solid Electrolyte Interphase Formation at the Molecular Level: Computational Insights into Bare Li-Metal Anode and $Li_6PS_{5-x}Se_xCl$ Argyrodite Solid Electrolyte. *ACS Energy Lett.* **8,** 4129–4135; 10.1021/acsenergylett.3c01363 (2023).

170. Camacho-Forero, L. E. & Balbuena, P. B. Exploring Interfacial Stability of Solid-State Electrolytes at the Lithium-Metal Anode Surface. *Journal of Power Sources* **396,** 782–790; 10.1016/j.jpowsour.2018.06.092 (2018).

171. Golov, A. & Carrasco, J. Molecular-Level Insight into the Interfacial Reactivity and Ionic Conductivity of a Li-Argyrodite Li6PS5Cl Solid Electrolyte at Bare and Coated Li-Metal Anodes. *ACS Applied Materials & Interfaces* **13,** 43734; 10.1021/acsami.1c12753 (2021).

172. Schmalzried, H. *Chemical Kinetics of Solids* (Wiley-VCH, Weinheim, 1995).

173. Tammann, G. Über Anlauffarben von Metallen. *Z. anorg. allg. Chem.* **111,** 78–89; 10.1002/zaac.19201110107 (1920).

174. Wagner, C. Beitrag zur Theorie des Anlaufvorgangs. *Zeitschrift für Physikalische Chemie* **21B,** 25–41; 10.1515/zpch-1933-2105 (1933).

175. Wagner, C. Beitrag zur Theorie des Anlaufvorganges. II. *Zeitschrift für Physikalische Chemie* **32B,** 447–462; 10.1515/zpch-1936-3239 (1936).

176. Wagner, C. & Hammen, H. Bestimmung des Sauerstoff-Überschußgehaltes der Kupferoxydulphase. *Zeitschrift für Physikalische Chemie* **40B,** 197–206; 10.1515/zpch-1938-4013 (1938).

177. Riegger, L. M. *et al.* Evolution of the Interphase between Argyrodite-Based Solid Electrolytes and the Lithium Metal Anode ─ The Kinetics of Solid Electrolyte Interphase Growth. *Chem. Mater.* **35,** 5091–5099; 10.1021/acs.chemmater.3c00676 (2023).

178. Attia, P. M., Chueh, W. C. & Harris, S. J. Revisiting the $t^{0.5}$ Dependence of SEI Growth. *J. Electrochem. Soc.* **167,** 90535; 10.1149/1945-7111/ab8ce4 (2020).

179. Broussely, M. *et al.* Aging Mechanism in Li Ion Cells and Calendar Life Predictions. *Journal of Power Sources* **97-98,** 13–21; 10.1016/S0378-7753(01)00722-4 (2001).

180. Keil, P. *et al.* Calendar Aging of Lithium-Ion Batteries. *J. Electrochem. Soc.* **163,** A1872-A1880; 10.1149/2.0411609jes (2016).

181. Kolzenberg, L. von, Latz, A. & Horstmann, B. Chemo-Mechanical Model of SEI Growth on Silicon Electrode Particles. *Batteries & Supercaps* **5**; 10.1002/batt.202100216 (2022).

182. Liu, Y. *et al.* Alloyable Viscous Fluid for Interface Welding of Garnet Electrolyte to Enable Highly Reversible Fluoride Conversion Solid State Batteries. *Adv Funct Materials* **33**; 10.1002/adfm.202208013 (2023).

183. Ploehn, H. J., Ramadass, P. & White, R. E. Solvent Diffusion Model for Aging of Lithium-Ion Battery Cells. *J. Electrochem. Soc.* **151,** A456; 10.1149/1.1644601 (2004).

184. Xiong, Z. *et al.* 4.2V Polymer All-Solid-State Lithium Batteries Enabled by High-Concentration PEO Solid Electrolytes. *Energy Storage Materials* **57,** 171–179; 10.1016/j.ensm.2023.02.008 (2023).

185. Zuo, T.-T. *et al.* A Mechanistic Investigation of the $Li_{10}GeP_2S_{12}|LiNi_{1-x-y}Co_xMn_yO_2$ Interface Stability in All-Solid-State Lithium Batteries. *Nat Mater* **12,** 6669; 10.1038/s41467-021-26895-4 (2021).

186. Zuo, T.-T. *et al.* Impact of the Chlorination of Lithium Argyrodites on the Electrolyte/Cathode Interface in Solid-State Batteries. *Angewandte Chemie* **135**; 10.1002/ange.202213228 (2023).

187. Schmalzried, H. *Solid State Reactions.* 2nd ed. (Verl. Chemie, Weinheim u.a., 1981).

188. Wenzel, S. Thermodynamic and Kinetic Instability of Inorganic Solid Electrolytes at Lithium and Sodium Metal Electrodes. Universitätsbibliothek Gießen, 2016.

189. Bale, C. W. *et al.* FactSage Thermochemical Software and Databases, 2010–2016. *Calphad* **54,** 35–53; 10.1016/j.calphad.2016.05.002 (2016).

190. Wan, J. *et al.* Micromechanism in All-Solid-State Alloy-Metal Batteries: Regulating Homogeneous Lithium Precipitation and Flexible Solid Electrolyte Interphase Evolution. *Journal of the American Chemical Society* **143,** 839–848; 10.1021/jacs.0c10121 (2021).

191. Luo, S. *et al.* Growth of Lithium-Indium Dendrites in All-Solid-State Lithium-Based Batteries with Sulfide Electrolytes. *Nat Commun* **12,** 6968; 10.1038/s41467-021-27311-7 (2021).

192. Huang, Di, Liu, G. & Tong, W. Stability of the Argyrodite Electrolyte in Li–In Based All-Solid-State Batteries. *ACS Appl. Energy Mater.* **7,** 10376; 10.1021/acsaem.4c01873 (2024).

193. Maier, J. Defektchemie: Zusammensetzung, Transport und Reaktionen im festen Zustand–Teil I: Thermodynamik. *Angewandte Chemie* **105,** 333; 10.1002/ange.19931050304 (1993).

194. Maier, J. Defektchemie: Zusammensetzung, Transport und Reaktionen im festen Zustand-Teil II: Kinetik. *Angewandte Chemie* **105,** 558–571; 10.1002/ange.19931050407 (1993).

195. Funke, K. Solid State Ionics: from Michael Faraday to Green Energy - The European Dimension. *Science and Technology of Advanced Materials* **14,** 43502; 10.1088/1468-6996/14/4/043502 (2013).

196. Owens, B. B. Solid State Electrolytes: Overview of Materials and Applications During the Last Third of the Twentieth Century. *Journal of Power Sources* **90,** 2–8; 10.1016/S0378-7753(00)00436-5 (2000).

197. Schweke, D. *et al.* Defect Chemistry of Oxides for Energy Applications. *Advanced Materials* **30,** e1706300; 10.1002/adma.201706300 (2018).

198. Backhaus-Ricoult, M. SOFC – A Playground for Solid State Chemistry. *Solid State Sciences* **10,** 670–688; 10.1016/j.solidstatesciences.2007.11.021 (2008).

199. Randau, S. *et al.* Benchmarking the Performance of All-Solid-State Lithium Batteries. *Nat Energy* **5,** 259–270; 10.1038/s41560-020-0565-1 (2020).

200. Shao, B., Huang, Y. & Han, F. Electronic Conductivity of Lithium Solid Electrolytes. *Advanced Energy Materials* **13**; 10.1002/aenm.202204098 (2023).

201. Deng, R. *et al.* Understanding Calendar Aging of Thiophosphate-Based Solid-State Batteries. *J. Electrochem. Soc.*; 10.1149/1945-7111/ae0f59 (2025).

202. Culver, S. P. *et al.* Designing Ionic Conductors: The Interplay between Structural Phenomena and Interfaces in Thiophosphate-Based Solid-State Batteries. *Chem. Mater.* **30,** 4179 (2018).

203. Kraft, M. A. *et al.* Influence of Lattice Polarizability on the Ionic Conductivity in the Lithium Superionic Argyrodites Li_6PS_5X (X = Cl, Br, I). *J. Am. Chem. Soc.* **139,** 10909–10918; 10.1021/jacs.7b06327 (2017).

204. Zeier, W. G. Structural Limitations for Optimizing Garnet-Type Solid Electrolytes: A Perspective. *Dalton Transactions* **43,** 16133–16138; 10.1039/C4DT02162B (2014).

205. Botros, M. & Janek, J. Embracing Disorder in Solid-State Batteries. *Science* **378,** 1273–1274; 10.1126/science.adf3383 (2022).

206. Maier, J. *Physical Chemistry of Ionic Materials* (Wiley, 2004).

207. Weppner, W. Interfaces in Ionic Devices. *Ionics* **7,** 404–424; 10.1007/BF02373577 (2001).

208. Lotsch, B. V. & Maier, J. Relevance of Solid Electrolytes for Lithium-Based Batteries: A Realistic View. *J Electroceram* **38,** 128–141; 10.1007/s10832-017-0091-0 (2017).

209. Ahmad, N. *et al.* Role of Electronic Conductivities toward Practical All-Solid-State Lithium-Metal/Sulfur Batteries. *Advanced Sustainable Systems*; 10.1002/adsu.202400729 (2024).

210. Dudney, N. J. Solid-State Thin-Film Rechargeable Batteries. *Materials Science and Engineering: B* **116,** 245–249; 10.1016/j.mseb.2004.05.045 (2005).

211. Li, Y., Canepa, P. & Gorai, P. Role of Electronic Passivation in Stabilizing the Lithium-$Li_xPO_yN_z$ Solid-Electrolyte Interphase. *PRX Energy* **1**; 10.1103/PRXEnergy.1.023004 (2022).

212. Han, F. *et al.* High Electronic Conductivity as the Origin of Lithium Dendrite Formation within Solid Electrolytes. *Nat Energy* **4,** 187–196; 10.1038/s41560-018-0312-z (2019).

213. Liu, X. *et al.* Local Electronic Structure Variation Resulting in Li 'Filament' Formation within Solid Electrolytes. *Nature Materials* **20,** 1485–1490; 10.1038/s41563-021-01019-x (2021).

214. Tian, H.-K. *et al.* Interfacial Electronic Properties Dictate Li Dendrite Growth in Solid Electrolytes. *Chem. Mater.* **31,** 7351–7359; 10.1021/acs.chemmater.9b01967 (2019).

215. Han, S. Y. *et al.* Stress Evolution During Cycling of Alloy-Anode Solid-State Batteries. *Joule* **5,** 2450–2465; 10.1016/j.joule.2021.07.002 (2021).

216. Song, Y. *et al.* Revealing the Short-Circuiting Mechanism of Garnet-Based Solid-State Electrolyte. *Adv. Energy Mater.* **9**; 10.1002/aenm.201900671 (2019).

217. Aguesse, F. *et al.* Investigating the Dendritic Growth during Full Cell Cycling of Garnet Electrolyte in Direct Contact with Li Metal. *ACS Applied Materials & Interfaces* **9,** 3808–3816; 10.1021/acsami.6b13925 (2017).

218. Tian, H.-K., Xu, B. & Qi, Y. Computational Study of Lithium Nucleation Tendency in $Li_7La_3Zr_2O_{12}$ (LLZO) and Rational Design of Interlayer Materials to Prevent Lithium Dendrites. *Journal of Power Sources* **392,** 79–86; 10.1016/j.jpowsour.2018.04.098 (2018).

219. Dong, Y. *et al.* Potential Jumps at Transport Bottlenecks Cause Instability of Nominally Ionic Solid Electrolytes in Electrochemical Cells. *Acta Materialia* **199,** 264–277; 10.1016/j.actamat.2020.08.017 (2020).

220. Counihan, M. J. *et al.* Effect of Propagating Dopant Reactivity on Lattice Oxygen Loss in LLZO Solid Electrolyte Contacted with Lithium Metal. *Adv. Energy Mater.*; 10.1002/aenm.202406020 (2025).

221. Nakamura, T. *et al.* Guidelines for All-Solid-State Battery Design and Electrode Buffer Layers Based on Chemical Potential Profile Calculation. *ACS Applied Materials & Interfaces* **11,** 19968–19976; 10.1021/acsami.9b03053 (2019).

222. Zhou, L. *et al.* High Areal Capacity, Long Cycle Life 4 V Ceramic All-Solid-State Li-Ion Batteries Enabled by Chloride Solid Electrolytes. *Nat Energy* **7,** 83–93; 10.1038/s41560-021-00952-0 (2022).

223. Kochetkov, I. *et al.* Different Interfacial Reactivity of Lithium Metal Chloride Electrolytes with High Voltage Cathodes Determines Solid-State Battery Performance. *Energy Environ. Sci.* **15,** 3933–3944; 10.1039/D2EE00803C (2022).

224. Park, J. & Jung, Y. S. Increasing Capacity with Mixed Conductors. *Nature Materials* **24,** 169–170; 10.1038/s41563-024-02105-6 (2025).

225. Wang, D. *et al.* Overcoming the Conversion Reaction Limitation at Three-Phase Interfaces using Mixed Conductors towards Energy-Dense Solid-State Li-S Batteries. *Nature Materials*; 10.1038/s41563-024-02057-x (2025).

226. Buschmann, H. *et al.* Structure and Dynamics of the Fast Lithium Ion Conductor "$Li_7La_3Zr_2O_{12}$". *Phys. Chem. Chem. Phys.* **13,** 19378–19392; 10.1039/C1CP22108F (2011).

227. Zhu, C. *et al.* Understanding the Evolution of Lithium Dendrites at $Li_{6.25}Al_{0.25}La_3Zr_2O_{12}$ Grain Boundaries via operando Microscopy Techniques. *Nat Commun* **14,** 1300; 10.1038/s41467-023-36792-7 (2023).

228. Philipp, M. *et al.* The Electronic Conductivity of Single Crystalline Ga-Stabilized Cubic $Li_7La_3Zr_2O_{12}$: A Technologically Relevant Parameter for All-Solid-State Batteries. *Adv Materials Inter* **7**; 10.1002/admi.202000450 (2020).

229. Squires, A. G. *et al.* Low Electronic Conductivity of $Li_7La_3Zr_2O_{12}$ Solid Electrolytes from First Principles. *Phys. Rev. Materials* **6**; 10.1103/PhysRevMaterials.6.085401 (2022).

230. Su, Y. *et al.* LiPON Thin Films with High Nitrogen Content for Application in Lithium Batteries and Electrochromic Devices Prepared by RF Magnetron Sputtering. *Solid State Ionics* **282,** 63–69; 10.1016/j.ssi.2015.09.022 (2015).

231. Li, J. *et al.* Artificial Solid Electrolyte Interphase to Address the Electrochemical Degradation of Silicon Electrodes. *ACS Appl. Mater. Interfaces* **6,** 10083; 10.1021/am5009419 (2014).

232. Le Van-Jodin, L. *et al.* Dielectric Properties, Conductivity and Li^+ Ion Motion in LiPON Thin Films. *Solid State Ionics* **253,** 151–156; 10.1016/j.ssi.2013.09.031 (2013).

233. Han, F. *et al.* Electrochemical Stability of $Li_{10}GeP_2S_{12}$ and $Li_7La_3Zr_2O_{12}$ Solid Electrolytes. *Advanced Energy Materials* **6**; 10.1002/aenm.201501590 (2016).

234. Riegger, L. M. *et al.* Instability of the Li_7SiPS_8 Solid Electrolyte at the Lithium Metal Anode and Interphase Formation. *Chem. Mater.* **34,** 3659; 10.1021/acs.chemmater.1c04302 (2022).

235. Huggins, R. A. Simple Method to Determine Electronic and Ionic Components of the Conductivity in Mixed Conductors: A Review. *Ionics* **8,** 300; 10.1007/BF02376083 (2002).

236. Hebb, M. H. Electrical Conductivity of Silver Sulfide. *The Journal of Chemical Physics* **20,** 185–190; 10.1063/1.1700165 (1952).

237. Wagner, C. Galvanische Zellen mit festen Elektrolyten mit gemischter Stromleitung. *Zeitschrift für Elektrochemie, Berichte der Bunsengesellschaft für physikalische Chemie* **60,** 4–7; 10.1002/bbpc.19560600104 (1956).

238. Wagner, C. Galvanic Cells with Solid Electrolytes Involving Ionic and Electronic Conduction. *Proc. C. I. T. C. E., Electrochem. Semicond.* **7,** 361–377 (1955).

239. Wagner, J. B. & Wagner, C. Electrical Conductivity Measurements on Cuprous Halides. *The Journal of Chemical Physics* **26,** 1597–1601; 10.1063/1.1743590 (1957).

240. Shimonosona, T. *et al.* Electronic Conductivity Measurement of Sm- and La-Doped Ceria Ceramics by Hebb-Wagner Method. *Solid State Ionics* **174,** 27; 10.1016/j.ssi.2004.07.025 (2004).

241. Weppner, W. & Liu, J. Polarization Studies of the Electronic Minority Charge Carriers in Ag^+-ß"-Alumina. *Zeitschrift für Naturforschung A* **46,** 409; 10.1515/zna-1991-0506 (1991).

242. Rosenkranz, C. Determination of Local Potentials in Mixed Conductors — Two Examples. *Solid State Ionics* **82,** 95–106; 10.1016/0167-2738(95)00208-N (1995).

243. Guo, X. On the Hebb-Wagner Polarisation of $SrTiO_3$ Doped with Redox-Active Ions. *Solid State Ionics* **130,** 267–280; 10.1016/s0167-2738(00)00615-9 (2000).

244. Valov, I. *et al.* Ionic and Electronic Conductivity of Nitrogen-Doped YSZ Single Crystals. *Solid State Ionics* **180,** 1463–1470; 10.1016/j.ssi.2009.09.003 (2009).

245. Ilschner, B. Determination of the Electronic Conductivity in Silver Halides by Means of Polarization Measurements. *The Journal of Chemical Physics* **28,** 1109–1112; 10.1063/1.1744352 (1958).

246. Mizusaki, J. & Fueki, K. Electrochemical Determinations of the Chemical Diffusion Coefficient and Non-Stoichiometry in AgCl. *Solid State Ionics* **6,** 85–91; 10.1016/0167-2738(82)90099-6 (1982).

247. Raleigh, D. O. High-Temperature Hole Conductivity in Silver Bromide. *Journal of Physics and Chemistry of Solids* **26,** 329–341; 10.1016/0022-3697(65)90162-9 (1965).

248. Takahashi, T. & Yamamoto, O. The $Ag/Ag_3SI/I_2$ Solid-Electrolyte Cell. *Electrochimica Acta* **11,** 779–789; 10.1016/0013-4686(66)87055-X (1966).

249. Montani, R. A. & Bazán, J. C. On the Potential Range of Applicability of Wagner's Polarization Method. *Journal of Physics and Chemistry of Solids* **50,** 1207–1210; 10.1016/0022-3697(89)90391-0 (1989).

250. Ahr, N. & Martin, M. Numerical Simulations of the Hebb-Wagner Polarization Kinetics: (I) Weakly Acceptor-Doped Perovskite Oxides. *Solid State Ionics* **386,** 116057; 10.1016/j.ssi.2022.116057 (2022).

251. Alt, C. D. *et al.* The Partial Electronic Conductivity of Lithium Halides and Their Role in SEI Formation in Solid-State Batteries – Hebb-Wagner-Type Measurements. *Solid State Ionics* **429,** 116991; 10.1016/j.ssi.2025.116991 (2025).

252. Riess, I., Safadi, R. & Tuller, H. L. Problems with Hebb-Wagner Polarization Measurements due to Overpotentials and Decomposition of the Sample. *Solid State Ionics* **72,** 3–6; 10.1016/0167-2738(94)90116-3 (1994).

253. Riess, I. Review of the Limitation of the Hebb-Wagner Polarization Method for Measuring Partial Conductivities in Mixed Ionic Electronic Conductors. *Solid State Ionics* **91,** 221–232; 10.1016/S0167-2738(96)83022-0 (1996).

254. Huggins, R. Use of Defect Equilibrium Diagrams to Understand Minority Species Transport in Solid Electrolytes. *Solid State Ionics* **143,** 3–16; 10.1016/S0167-2738(01)00827-X (2001).

255. Poulsen, F. *et al.* Properties of LiI-Alumina Composite Electrolytes. *Solid State Ionics* **9-10,** 119–122; 10.1016/0167-2738(83)90219-9 (1983).

256. Bertran, E. *et al.* Indium Thin Films on Metal-Coated Substrates. *Thin Solid Films* **129,** 103–109; 10.1016/0040-6090(85)90099-9 (1985).

257. Lin, Q. *et al.* Scalable Indium Phosphide Thin-Film Nanophotonics Platform for Photovoltaic and Photoelectrochemical Devices. *ACS nano* **11,** 5113; 10.1021/acsnano.7b02124 (2017).

258. Singh, H. P. & Murr, L. E. Nucleation and Growth Characteristics of Palladium and Indium Thin Films. *Metall Trans* **3,** 983–988; 10.1007/BF02647676 (1972).

259. Ho, W.-H. *et al.* Electrochemical Performance of In_2O_3 Thin Film Electrode in Lithium Cell. *Journal of Power Sources* **175,** 897–902; 10.1016/j.jpowsour.2007.10.020 (2008).

260. Chastain, J. (ed.). *Handbook of X-ray Photoelectron Spectroscopy. A reference book of standard spectra for identification and interpretation of XPS data* (Perkin-Elmer, Eden Prairie, Minn., 1995).

261. Zhou, Y. *et al.* The Electrochemistry of Nanostructured In_2O_3 with Lithium. *Journal of Power Sources* **162,** 1373–1378; 10.1016/j.jpowsour.2006.08.031 (2006).

262. Xu, H. *et al.* Ultra-Stable and High-Rate Lithium Ion Batteries based on Metal–organic Framework-derived In_2O_3 Nanocrystals/Hierarchically Porous Nitrogen-doped Carbon Anode. *Energy & Environ Materials* **3,** 177–185; 10.1002/eem2.12065 (2020).

263. Sivavec, J., Kravchyk, K. V. & Kovalenko, M. V. Impact of Stack Pressure on Coulometric Titration Time Analysis. *Comm chemistry* **8,** 96; 10.1038/s42004-025-01496-0 (2025).

264. Liu, W.-P. *et al.* Unravelling the Electrochemical Evolution Mechanism of In_2O_3 Anode in Long-Cycle All-Solid-State Lithium Batteries with Sulfide Electrolytes. *Rare Met.*; 10.1007/s12598-025-03293-z (2025).

265. Courtney, I. A. & Dahn, J. R. Electrochemical and In Situ X-Ray Diffraction Studies of the Reaction of Lithium with Tin Oxide Composites. *J. Electrochem. Soc.* **144,** 2045–2052; 10.1149/1.1837740 (1997).

266. Li, H., Huang, X. & Chen, L. Anodes based on Oxide Materials for Lithium Rechargeable Batteries. *Solid State Ionics* **123,** 189–197; 10.1016/S0167-2738(99)00081-8 (1999).

267. Yoon, J. S. *et al.* Thermodynamics, Adhesion, and Wetting at Li/Cu(-Oxide) Interfaces: Relevance for Anode-Free Lithium-Metal Batteries. *ACS Applied Materials & Interfaces* **16,** 18790–18799; 10.1021/acsami.3c19034 (2024).

268. Mandal, L. *et al.* Evolution of Interfacial Electro-Chemo-Mechanics between Lithium Metal and Halide Solid Electrolyte. *Chem. Mater.* **36,** 10336–10350; 10.1021/acs.chemmater.4c02307 (2024).

269. Alt, C. D. *et al.* In–Li Counter Electrodes in Solid-State Batteries – A Comparative Approach on Kinetics, Microstructure, and Chemomechanics. *Adv. Energy Mater.*; 10.1002/aenm.202404055 (2024).

7. Appendix

7.1. Supporting Information – 1st Publication

Joule, Volume *8*

Supplemental information

Quantifying multiphase SEI growth in sulfide solid electrolytes

Christoph D. Alt, Nadia U.C.B. Müller, Luise M. Riegger, Burak Aktekin, Philip Minnmann, Klaus Peppler, and Jürgen Janek

A: Scanning Electron Microscopy Images of Lithium Metal Powder and Particle Size Distribution

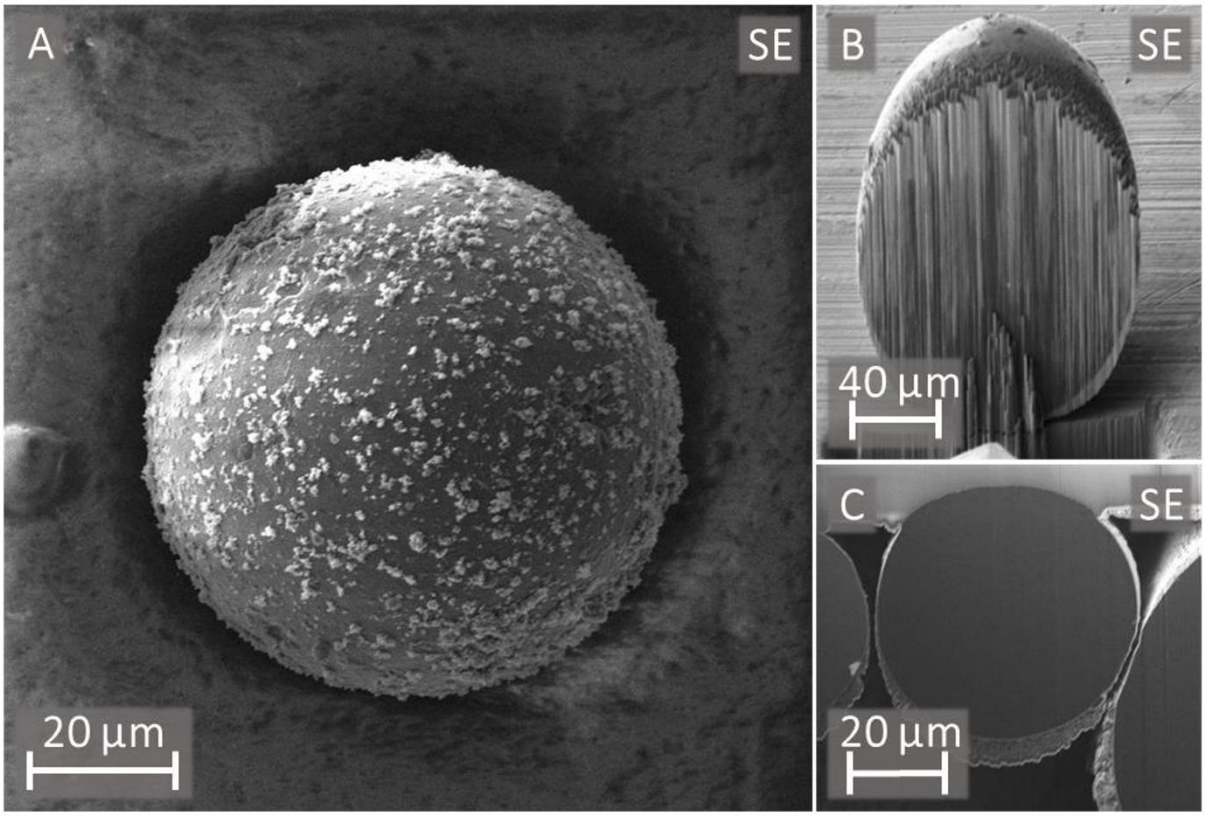

Figure S1: SEM images of single lithium metal powder particles, related to Figure 1. A) After the preparation process, B) and C) after additional Focused Ion Beam (FIB) cutting. The observed lithium metal particles exhibit nearly perfect sperical shapes, while being dense. B) and C) show curtaining effects and redeposition resulting from FIB sputtering, respectively.

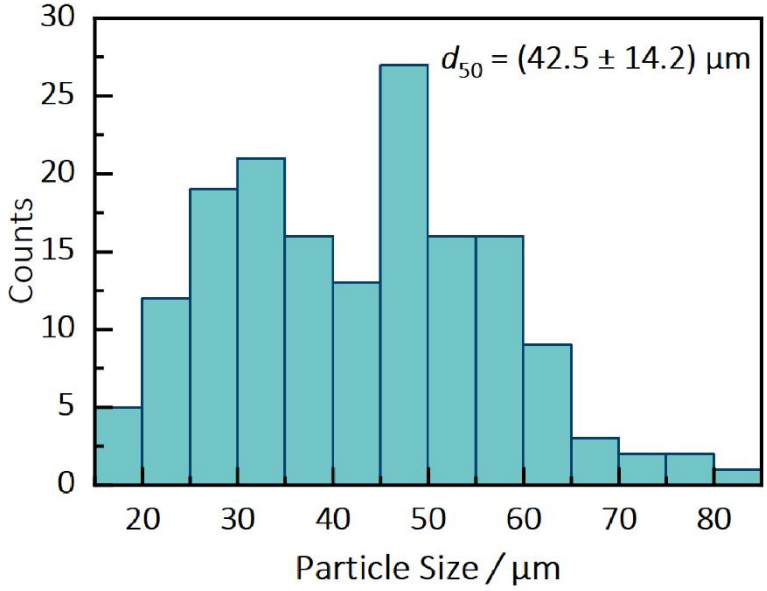

Figure S2.: Particle size distribution of the synthesized lithium metal powder particles, related to Figure 1. The size of individual particles was determined by reviewing the size of 160 particles in SEM images. The mean size (d_{50}) is (42.5 ± 14.2) µm.

B: Additional SEM Images of bulk-SEI Particles for Morphology Analysis

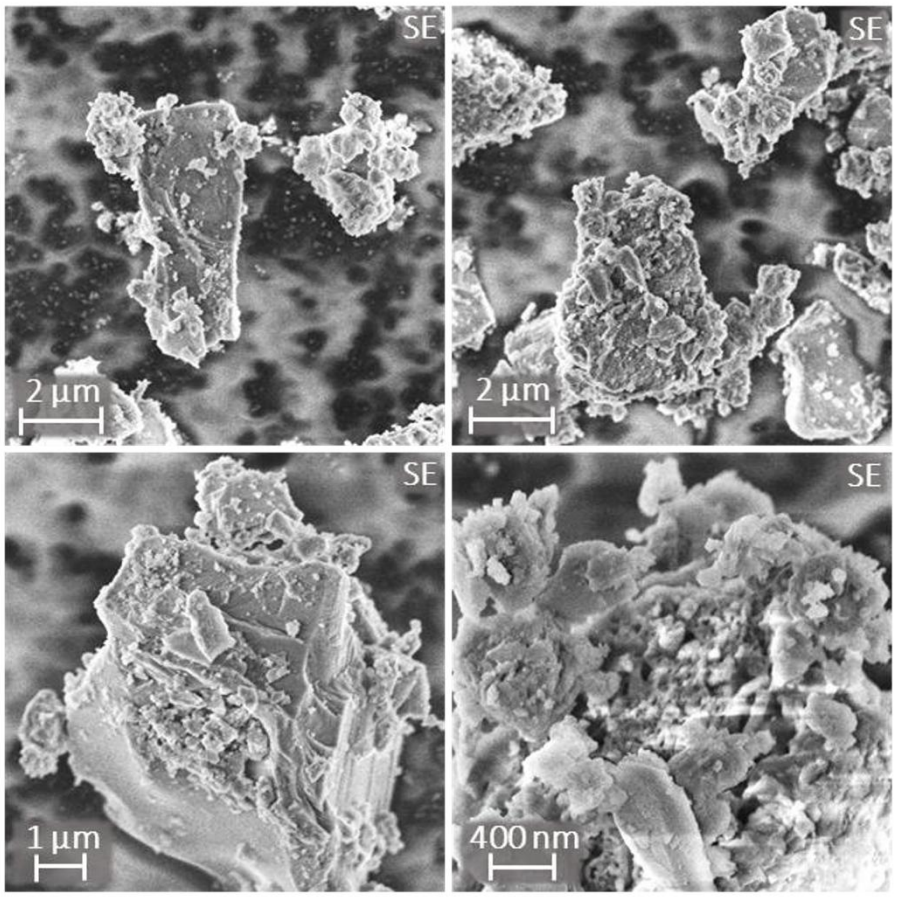

Figure S3: Morphology analysis of bulk-SEI particles, related to Figure 1. SEM images of the synthesized bulk-SEI of different particles at different magnifications.

C: Reference Measurements of Lithium Metal Powder, Li_6PS_5Cl and Their Mixture (Serving as Precursor) for XRD Analysis

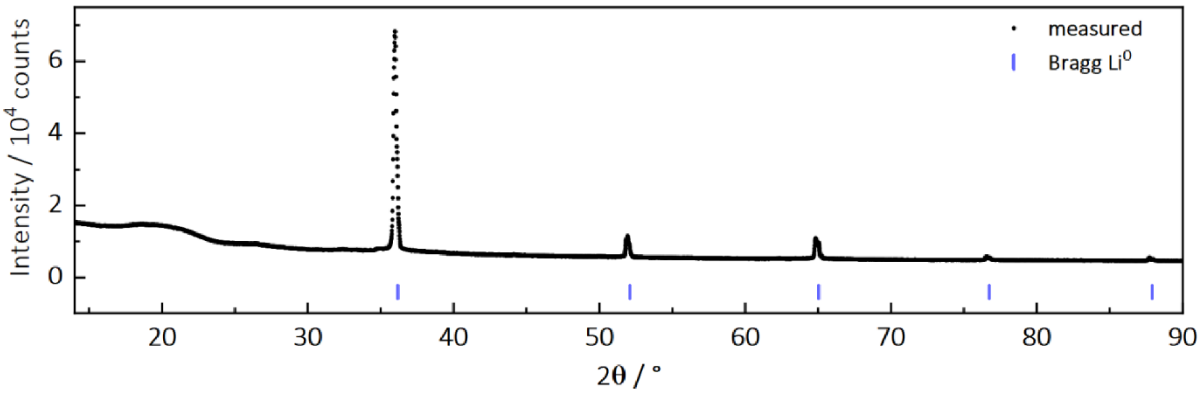

Figure S4: X-ray diffraction pattern of the synthesized lithium metal powder, identified by ICSD: 44367, related to Figure 2. No traces of other chemical substances are detected. However, we suspect passivation of the particle surface. The interfering background in the 2θ range of 17 – 23° is caused by the polyimide cover.

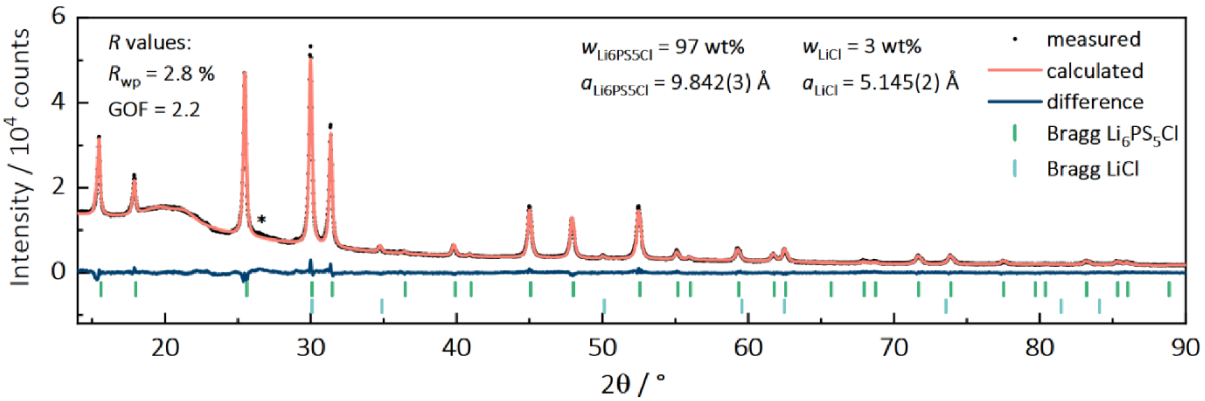

Figure S5: X-ray diffraction pattern of the commercial Li_6PS_5Cl material (ICSD: 259205), and the corresponding Rietveld refinements, related to Figure 2. One minor residual (3 wt%) of LiCl (ICSD: 52235) is identified, and we suspect remains of amorphous Li_2S (*) for the discrepancy at ~ 26.5°. *w*, *a*, R_{wp} and GOF are the mass fraction, lattice constant, weighted profile R-factor and goodness of fit, respectively. The interfering background in the 2θ range of 17 – 23° is caused by the polyimide cover.

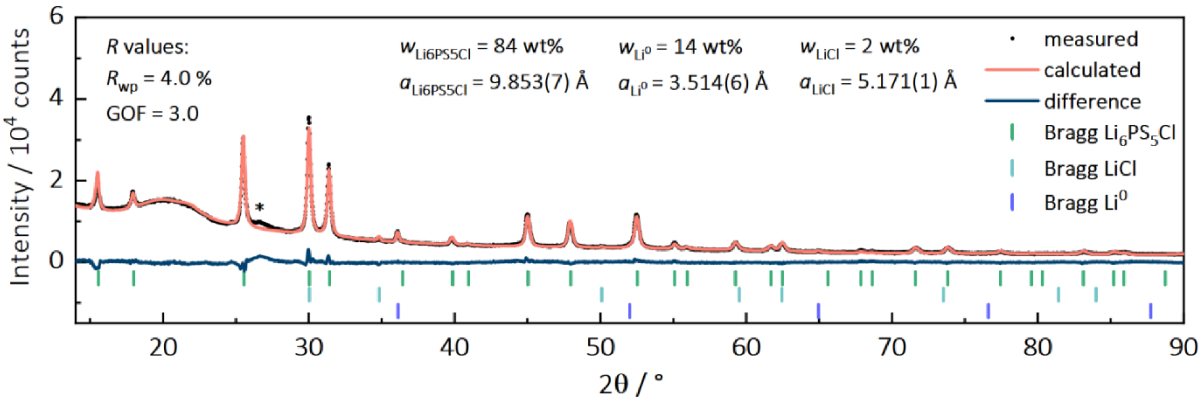

Figure S6: X-ray diffraction pattern of the precursor material for the heat treatment, and the corresponding Rietveld refinements, related to Figure 2. Reflections of LiCl (2 wt%, ICSD: 52235) and probable residuals of amorphous Li_2S (*) can be attributed to the impurities in LPSCl (compare Figure S4). However, this primarily suggests that there are only minor indications of a reaction, as evidenced by clear reflections of the initial constituents Li_6PS_5Cl (ICSD: 259205) and lithium metal (ICSD: 44367). *w*, *a*, R_{wp} and GOF are the mass fraction, lattice constant, weighted profile R-factor and goodness of fit, respectively. The interfering background in the 2θ range of 17 – 23° is caused by the polyimide cover.

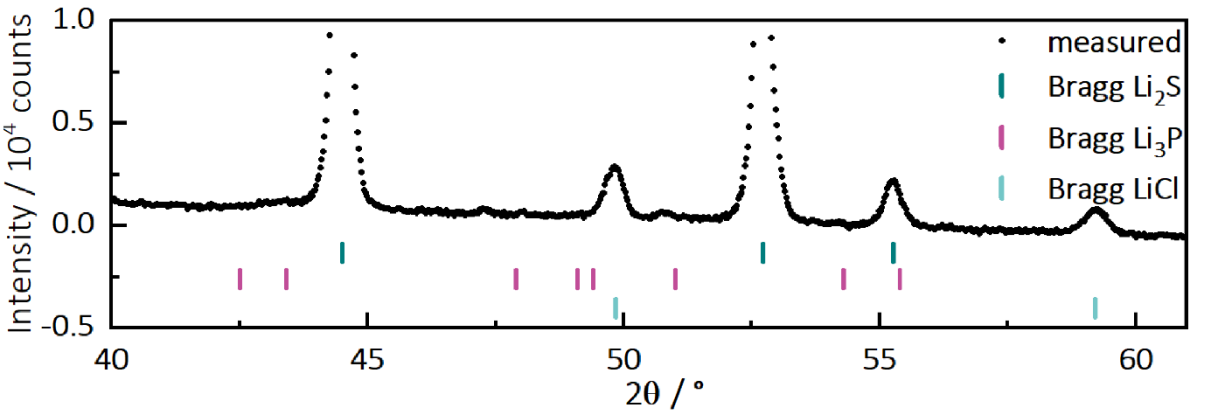

Figure S7: Magnified X-ray diffraction pattern (raw data) of the synthesized bulk-SEI in the range of 40° to 62°, related to Figure 2. Reflection positions of Li_2S (ICSD: 196932), Li_3P (ICSD: 26880), and LiCl (ICSD: 52235) are indicated. Arguably, slight intensity increases can be seen at positions of Li_3P, especially at 43.4°, 47.9°, 51.0°, and 54.3°, and shoulders to reflections of Li_2S and LiCl at 49.4° and 55.4°.

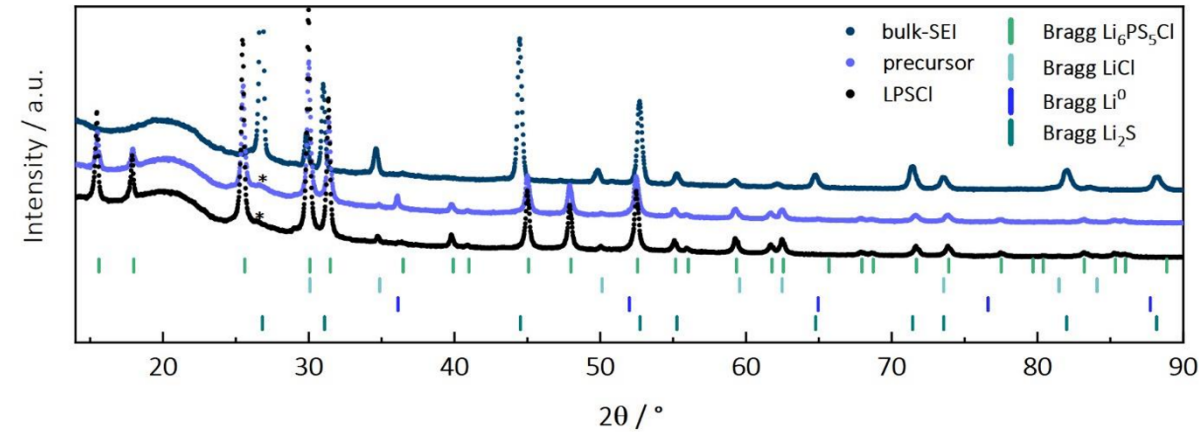

Figure S8: Comparison of X-ray diffraction pattern of Li_6PS_5Cl, precursor mixture, and synthesized bulk-SEI (raw data), related Figure 2. We suspect remains of amorphous Li_2S (*) for the discrepancy at ~ 26.5° for the precursor, which can be attributed to the impurities in LPSCl (compare Figure S4).

D: Depth-Profiling XPS Measurements of Lithium Metal Powder

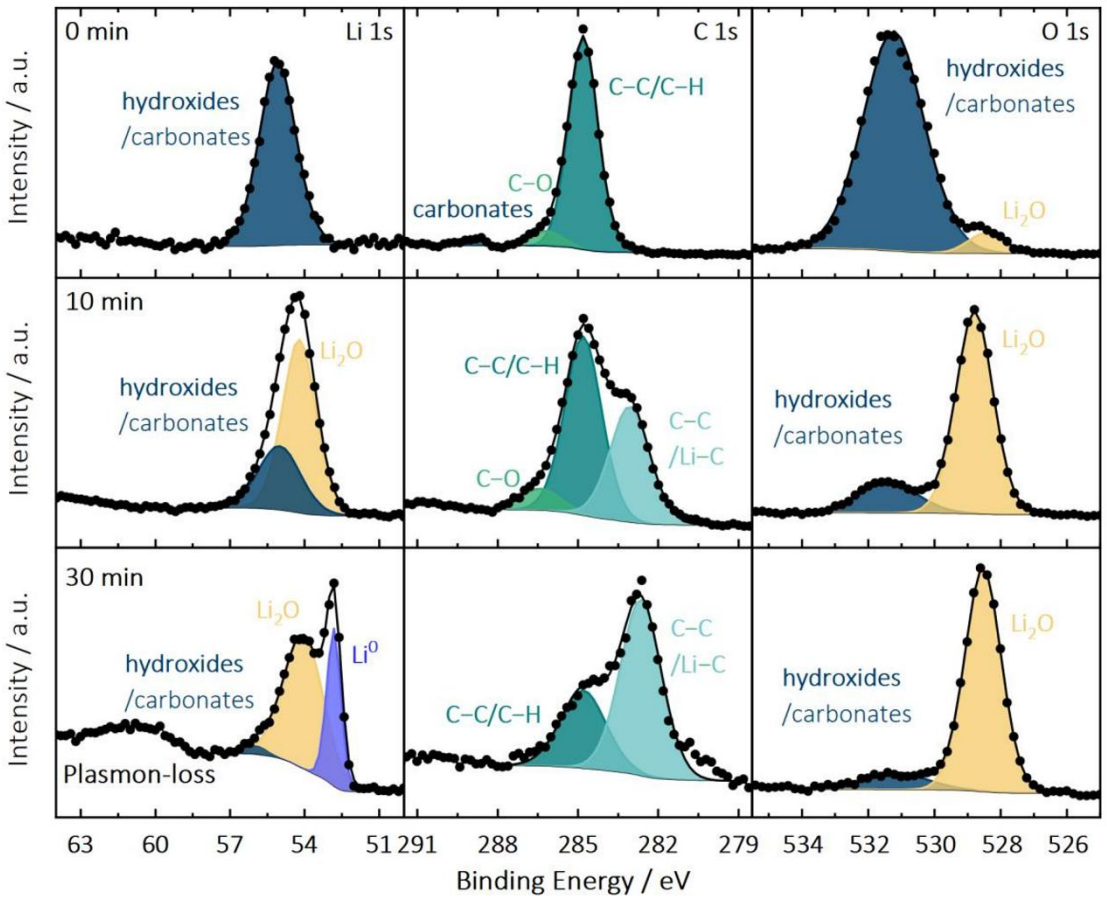

Figure S9: Depth-profile X-ray photoelectron Li 1s, C 1s and O 1s spectra of the synthesized lithium metal powder, serving as synthesis starting material, related to Figure 3. The analysis of these spectra unveiled a progressive reduction in surface passivation species (such as LiOH, Li_2O, lithium carbonate, carbon species) and a simultaneous increase in the signal attributed to lithium metal (*i.e.*, at 52.8 eV and the distinct plasmon-loss features at ~ 60 eV) as the depth-profiling and sputter time increased. This demonstrates the high purity of the lithium metal powder underneath a thin passivation layer. However, the thickness of the passivation layer has not been quantified. It is important to note that species like Li-C and Li_2O may form as a result of sputter damage. Depth-profiling parameters are described in the Supplemental Experimental Procedures section. The initial sputtering sequence, lasting one minute at a reduced sputtering voltage of 0.5 kV, was not considered when labeling the sputtering times.

E: Additional X-ray Photoelectron Spectra of the bulk-SEI and Quantitative Analysis

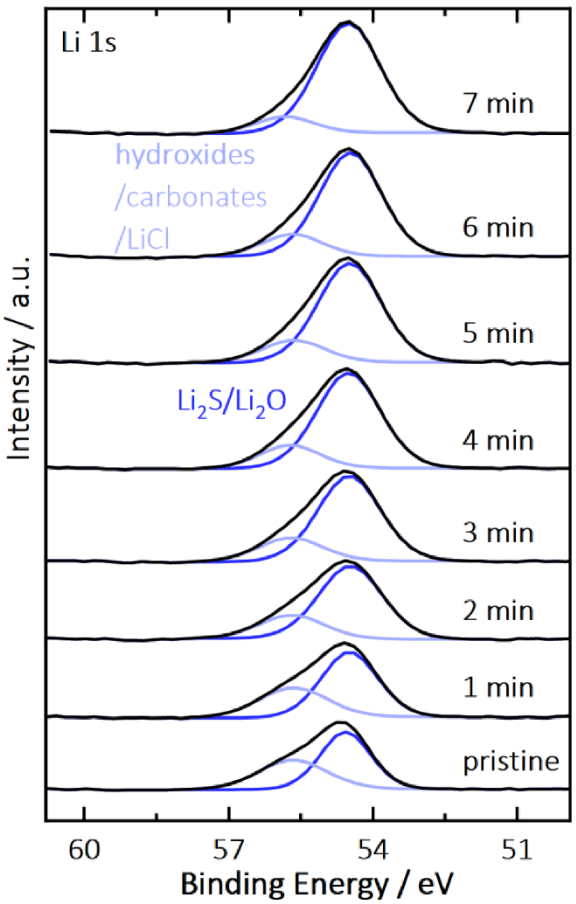

Figure S10: Depth-profile X-ray photoelectron Li 1s spectra of the synthesized bulk-SEI, related to Figure 3. Neither a Li^0 peak (at 52.8 eV) nor plasmon-loss features (at ~ 60 eV) were observed. It's important to note that ratios of both observed peaks may shift as a result of sputter damage. Depth-profiling parameters are described in the Supplemental Experimental Procedures section.

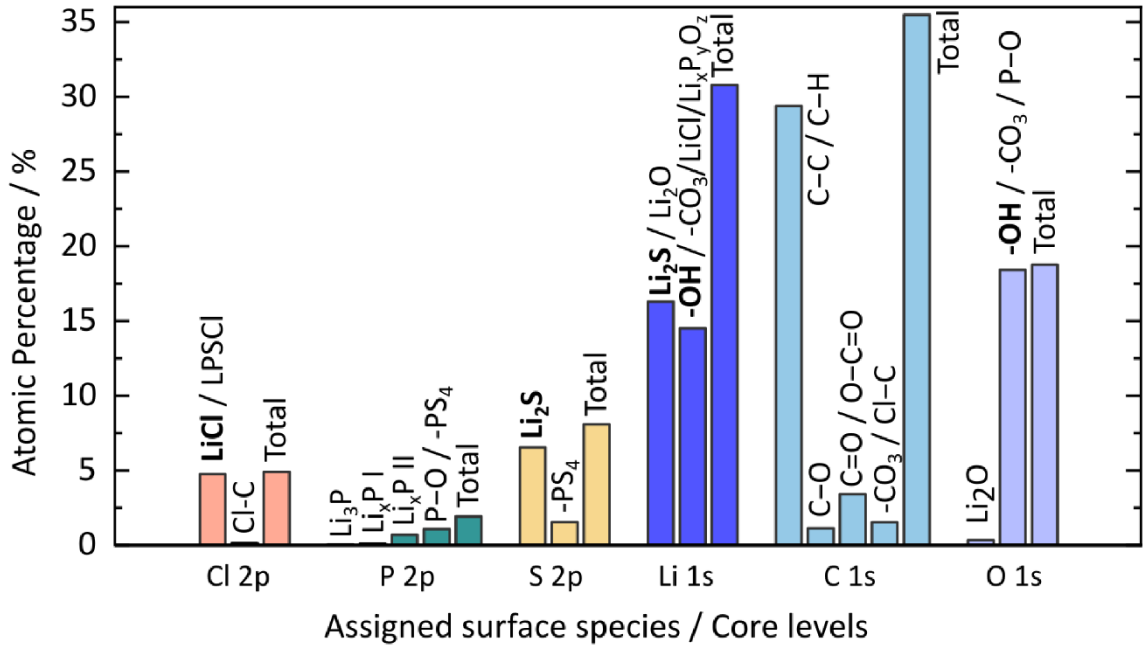

Figure S11: Quantitative analysis of the synthesized bulk-SEI was performed for each spectrum with the assigned surface species, related to Figure 3 and Figure S12. It should be noted that no sputtering step was performed prior to measurements (*i.e.*, for surface cleaning purposes) in order not to induce any sputter damage. Therefore, a considerable contribution (*i.e.*, atomic fraction) arises from surface contaminations (*e.g.*, CC–CH species).

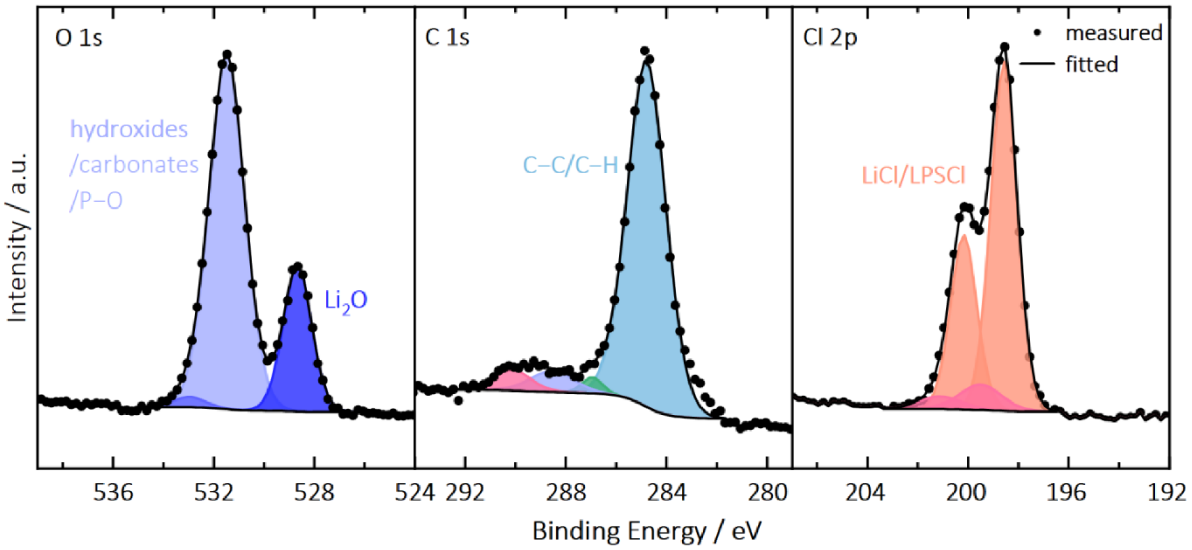

Figure S12: Additional X-ray photoelectron O 1s, C 1s, and Cl 2p spectra of the synthesized bulk-SEI, related to Figure 3.

F: Reference Measurements of Li_3P and Li_6PS_5Cl for XPS Analysis

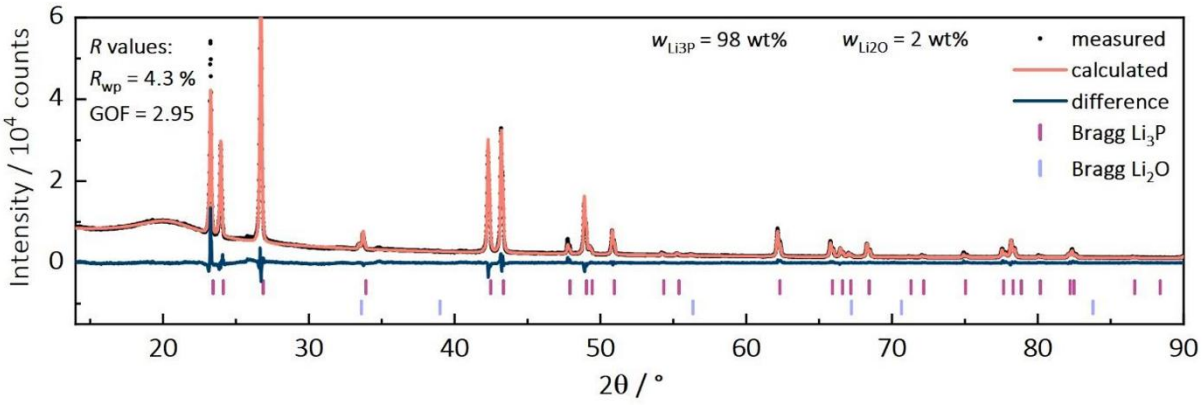

Figure S13: X-ray diffraction pattern of the synthesized Li_3P material (ICSD: 26880), and the corresponding Rietveld refinements, related to Figure S14. Reflections of Li_3P (98 wt%, ICSD: 52235) and Li_2O impurities (2 wt%, ICSD: 60431) are identified. The synthesis of Li_3P is described in the Supplemental Experimental Procedures section.

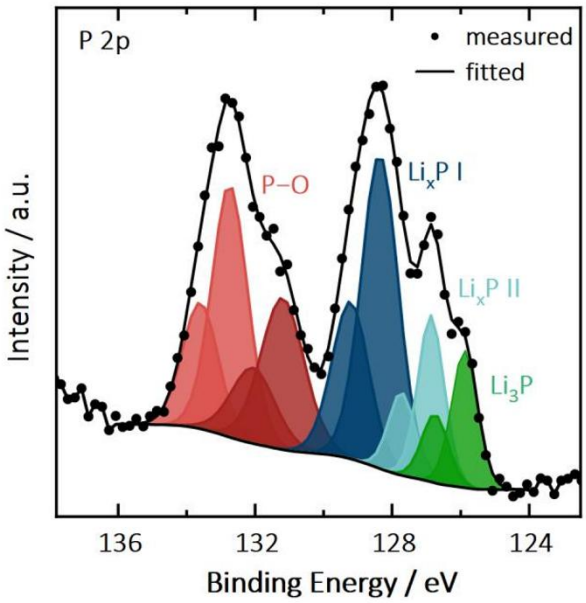

Figure S14: X-ray photoelectron P 2p spectra of the synthesized Li_3P material, related to Figure 3. Li_3P and two reduced phosphorous species (lithium polyphosphides Li_xP) as well as oxygenated phosphorous species (P−O) are identified. Li_xP and P–O may result from reaction with trace amounts of oxygen and moisture during storage, transfer, or measurement, highlighting the high reactivity of Li_3P. The synthesis of Li_3P is described in the Supplemental Experimental Procedures section.

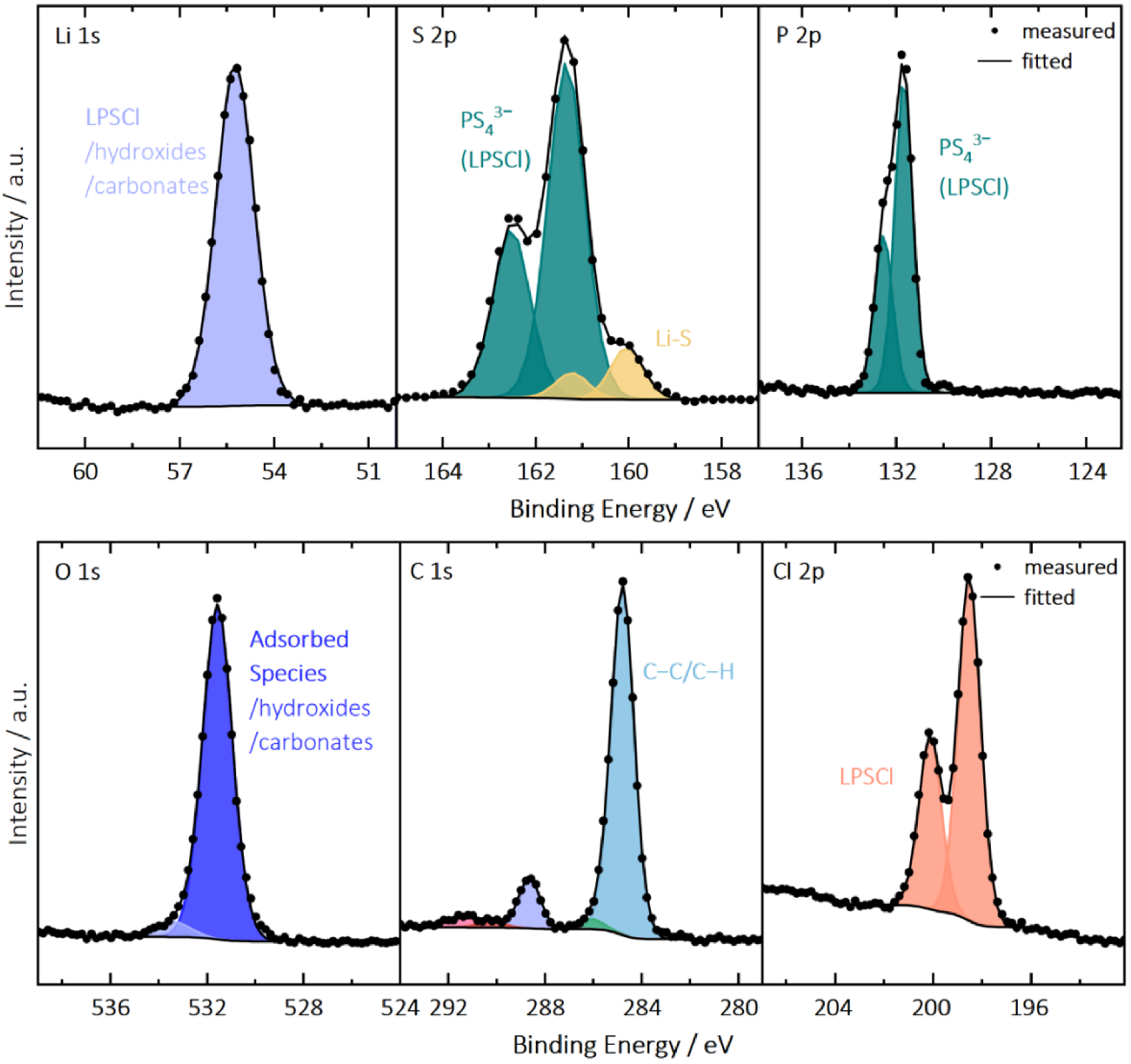

Figure S15: X-ray photoelectron Li 1s, S 2p, P 2p, O 1s, C 1s, and Cl 2p spectra of the commercial Li_6PS_5Cl material, serving as synthesis starting material, related to Figure 3.

G: Additional EDX Mappings of Li_6PS_5Cl and the bulk-SEI

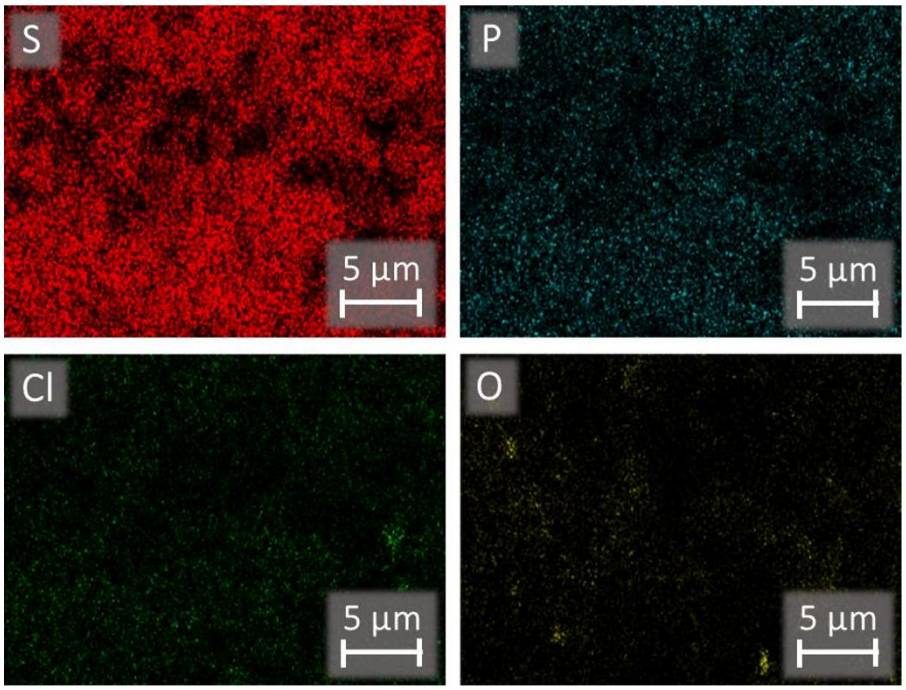

Figure S16: Comparison of EDX element mappings of Li_6PS_5Cl particles, serving as synthesis starting material, related to Figure 4. EDX element mappings were recorded at 8 kV for the elements sulfur, phosphorous, chloride, and oxygen. Areas with elevated concentrations of each element are found, represented by the corresponding $K_{\alpha1}$ lines.

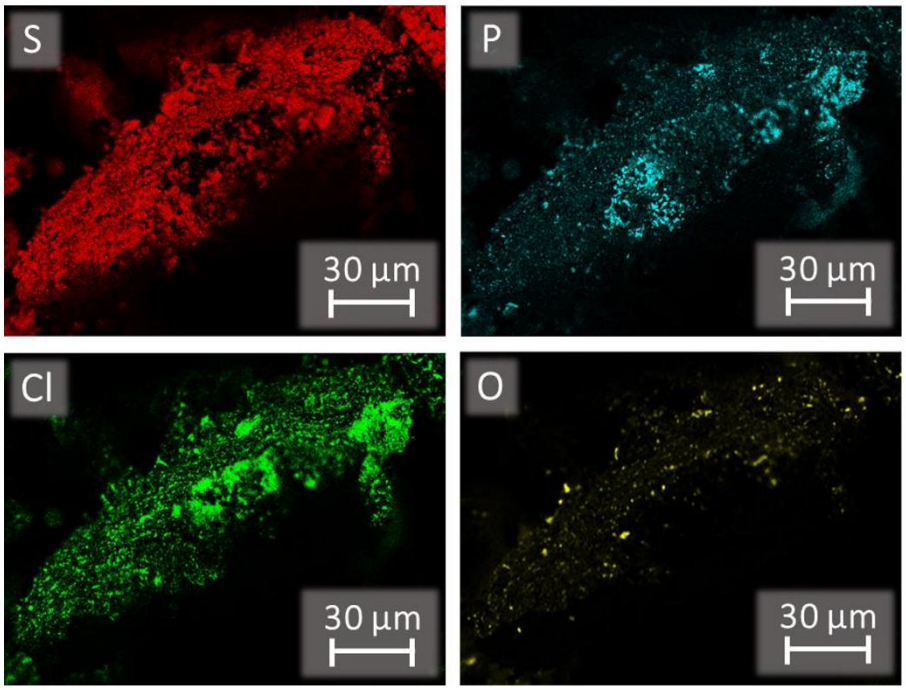

Figure S17: Comparison of EDX element mappings of one synthesized bulk-SEI particle, related to Figure 4. EDX element mappings were recorded at 8 kV for the elements sulfur, phosphorous, chloride, and oxygen. Areas with elevated concentrations of each element are found, represented by the corresponding $K_{\alpha1}$ lines.

H: Temporal Evolution of SEI determined by CTTA and bulk-SEI Conductivity Analysis

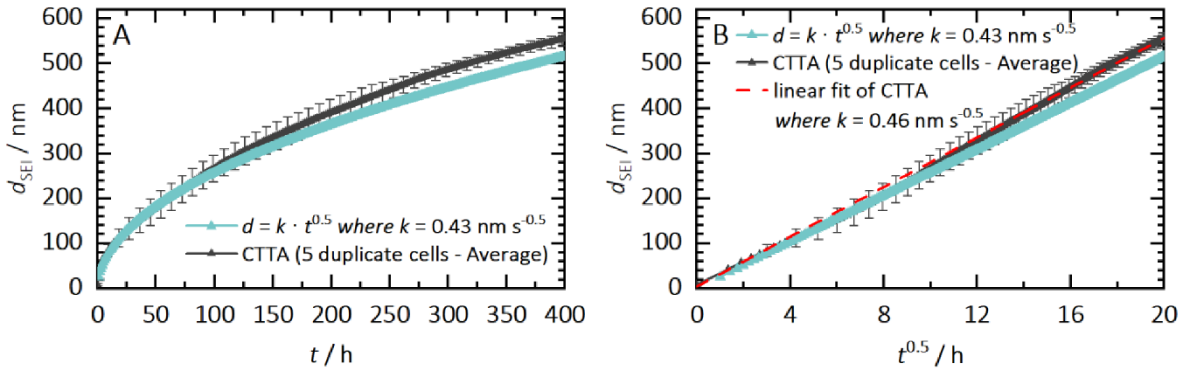

Figure S18: Evolution and Growth of the multiphase SEI of LPSCl – comparing results of CTTA[S1] and bulk-SEI conductivity analysis, related to Figure 7. d_{SEI} values are plotted as a function A) of t and B) of $t^{0.5}$ (right). d_{SEI} determined by Coulometric Titration Time Analysis (CTTA) was calculated based on measurements published by Aktekin *et al.*[S1]. For the CTTA measurement, the value of the parabolic constant k = 0.46 nm $s^{-0.5}$ was calculated from the slope of the linear fit (right). Using k, one can estimate the electronic conductivity σ_{el} (determined by CTTA) using eq. 3, yielding σ_{el} = 0.34 nS cm^{-1}. This value is quite close to experimentally determined σ_{el} of synthesized bulk-SEI in this study (*i.e.*, 0.3 nS cm^{-1}). Determining SEI layer thickness (*i.e.*, its calculation) using CTTA is described in the Supplemental Experimental Procedures section.

Supplemental Experimental Procedures

XPS Depth-Profiling Parameters

XPS depth-profiling was performed by Ar^+ sputtering with a grid size of 2x2 mm^2 with an initial sputtering step of 0.5 kV for one minute. For lithium metal powder (Figure S9, Section D), six sputtering steps were performed at 1 kV for five minutes each. One sputtering step of 1 kV for one minute and five sputtering steps of 2 kV for one minute each were used for the synthesized bulk-SEI (Figure S10, Section E).

Li_3P Synthesis

Synthesis was carried out in an argon-filled glovebox (*LabMasterPRO*, MBraun, Garching, Germany), with $p(O_2)/p$ and $p(H_2O)/p$ < 1 ppm. 200 mg of lithium metal and 300 mg of red phosphorous were placed inside a tantalum crucible. The crucible was closed with a lid and then sealed in a quartz ampoule under vacuum. Brittle samples of Li_3P were obtained by gradually heating the ampoules to 600 °C at a rate of 100 K h^{-1}, with holding steps of 6 h every 200 °C. The ampoule was then cooled down to room temperature at 100 K h^{-1}, yielding 480 mg of product after opening of the ampoule in the glovebox. The obtained material is used for reference measurements in Figure S13 and S14.

SEI Layer Thickness in Anode-free Cells determined from the Accumulated Charge using CTTA

The coulometric titration time analysis (CTTA) method was recently introduced by Aktekin *et al.*[S1] for the characterization of electrolyte side reactions at active metal electrode surfaces. Using this electrochemical method, SEI is formed on a noble current collector (in a so-called anode-free cell configuration) by *in situ* depositing small amount of lithium metal followed by an open-circuit waiting time hold until the deposited lithium is totally consumed by side reactions. These steps are subsequently repeated and the data is later compiled to quantify SEI growth with respect to time and consumed lithium capacity (*i.e.*, accumulated charge).

Cell preparation (Li | LPSCl | stainless steel) followed the method described by Aktekin *et al.*[S1]. Lithium was deposited on the stainless-steel current collector (working electrode – WE) at 15.6 µA cm^{-2}. Each titration charge was 1.56 µAh cm^{-2}. After each titration step, the cell voltage is around 0 V and is continuously monitored. When the voltage increased to a threshold of 0.05 V, the next titration step was applied, indicating that the lithium metal at the WE had been completely consumed by side reactions. This procedure was repeated multiple times (e.g., ~400 h in this study).

By summing the accumulated charge q_Σ (from each titration step) and considering the Faraday constant F, the amount of deposited lithium metal n_{Li} can be calculated using: $n_{Li} = q_\Sigma / F$. Assuming homogeneous lithium metal deposition and a dense SEI layer at the WE, the degradation reaction (1) in the main text, and a WE area A_{WE} of 0.64 cm^{-2}, the SEI layer thickness d_{SEI} can be determined according to:

$$d_{SEI} = \frac{n_{Li}}{8 \cdot A_{WE}} \cdot \left(5 \cdot V_{mol,Li2S} + 1 \cdot V_{mol,Li3P} + 1 \cdot V_{mol,LiCl}\right) \quad (1)$$

where $V_{mol,x}$ is the molar volume of x = Li_2S (27.5 $cm^3\,mol^{-1}$), Li_3P (19.8 $cm^3\,mol^{-1}$), and LiCl (35 $cm^3\,mol^{-1}$), respectively. In our case, a charge of 1.56 µAh cm^{-2} results in n_{Li} = $3.73 \cdot 10^{-8}$ mol cm^{-2} of deposited lithium, and d_{SEI} = 14 nm.

Supplemental References

S1. Aktekin, B., Riegger, L.M., Otto, S.-K., Fuchs, T., Henss, A., and Janek, J. (2023). SEI Growth on Lithium Metal Anodes in Solid-State Batteries Quantified with Coulometric Titration Time Analysis. Nat commun *14,* 6946.

7.2. Supporting Information – 2nd Publication

Supporting Information

Interphase Formation in Solid-State Batteries: Influence of Contact Conditions on Impedance-Derived SEI Growth Kinetics

Sascha Kremer[1,2⊥], Christoph D. Alt[1,2⊥], Luca Schuster[1,2], Jürgen Janek[1,2], and Janis K. Eckhardt[2*]

[1]Institute of Physical Chemistry, Justus-Liebig-University Giessen, Heinrich-Buff-Ring 17, Giessen D-35392, Germany.
[2]Center for Materials Research (ZfM), Justus-Liebig-University Giessen, Heinrich-Buff-Ring 16, D-35392 Giessen, Germany.

⊥ S.K. and C.D.A. contributed equally to this work.

* janis.k.eckhardt@theo.physik.uni-giessen.de

S1: Deriving the Decomposition Reaction at the Li|Li_6PS_5Cl Interface

The chemical potential of lithium $\mu_{Li}(\text{electrode})$ in a lithium metal electrode can be assumed by its standard chemical potential (μ_{Li}^0). Consequently, the lithium chemical potential difference across the interphase ($\Delta\mu_{Li}$), is given by $\Delta\mu_{Li} = \mu_{Li}(\text{reaction front}) - \mu_{Li}^0$.

$$Li_6PS_5Cl + 8\,Li^0 \rightarrow 5\,Li_2S + Li_3P + LiCl \qquad \textbf{(eq. S1)}$$

For the decomposition reaction at the Li|Li_6PS_5Cl interface (see **(eq. S1)**), the stoichiometric factor x_{Li} is 8, and μ_{Li}^0 = 8.35 kJ mol^{-1}.

Thus, for the stoichiometric decomposition of Li_6PS_5Cl, $\Delta\mu_{Li}$ is approximated by the corresponding change of standard free energy $\Delta_r G$ for the decomposition of Li_6PS_5Cl, divided by x_{Li}:

$$\Delta\mu_{Li} = \frac{\Delta_r G}{x_{Li}} \qquad \textbf{(eq. S2)}$$

Based on available thermodynamic data,[1] $\Delta_r G(Li_6PS_5Cl)$ is 1269.75 kJ mol^{-1}. This yields an estimated $\Delta\mu_{Li}$ of approximately 158.7 kJ mol^{-1} for the decomposition reaction at the Li|Li_6PS_5Cl interface.

S2: The Influence of Spatial Contact Distribution

To study the influence of contact distribution on the interpretation of impedance data and derived interphase kinetics (k'_{exp}), we conducted a series of simulations. In this series, A_r was held constant at 10% of $A_{electrode}$, but the size and spatial distribution of the contact spots was varied (see **Figure S1a**). The resulting impedance spectra shown in **Figure S1b** reveal that R_{cstr} decreases with a finer contact distribution,[3–5] while $(R_{tot} - R_{bulk})$ seems to increase with the same rate, independent of the contact geometry.

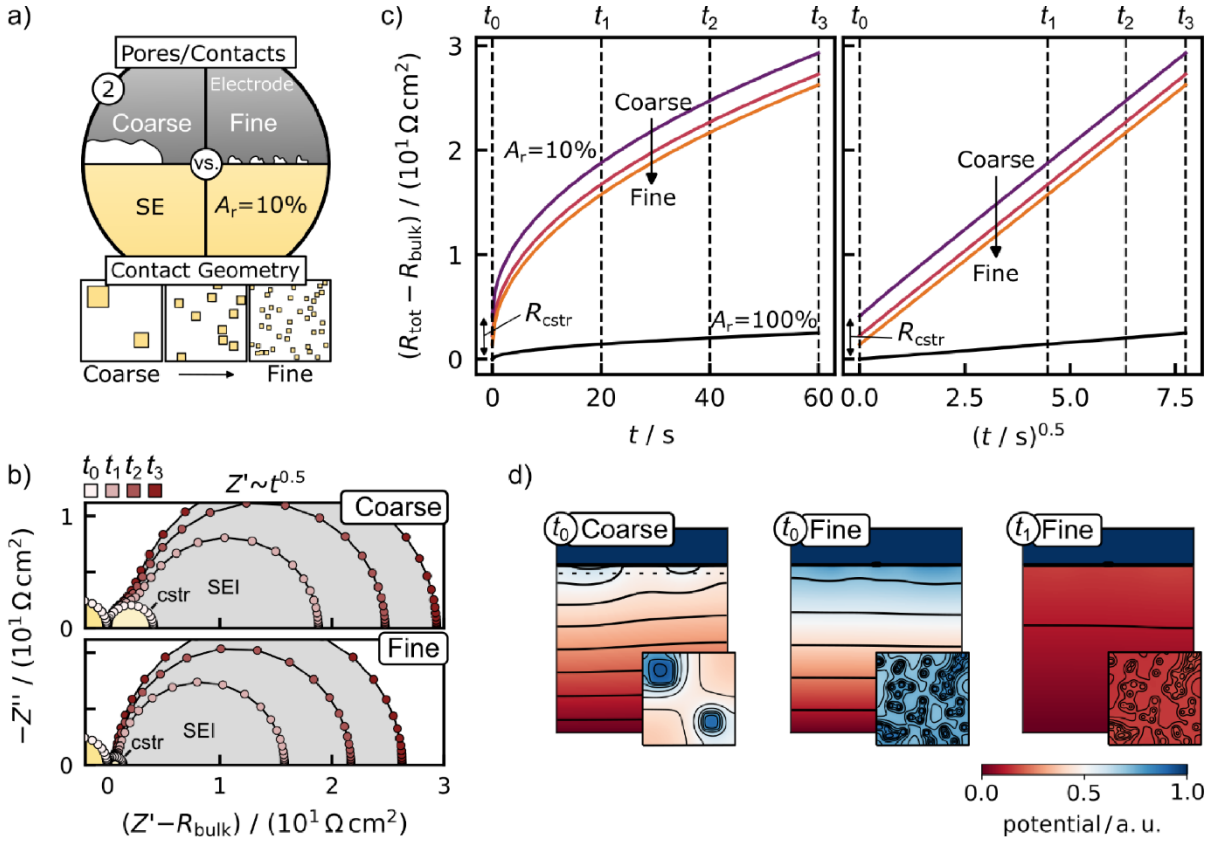

Figure S1. **Effect of Contact Distribution on SEI Growth Analysis**. The microscopic interphase growth rate k' was kept constant in the simulations. (a) Contact spots of different sizes are randomly distributed at the interface with a constant A_r of 10% between a homogeneous electrode and SE. (b) The constriction signal in the impedance spectrum decreases with finer contact distribution, while the SEI signal is unaffected. (c) The macroscopic rate constant k'_{exp}, describing SEI resistance growth over time, is independent of the contact distribution. It solely depends on A_r. The contact distribution affects only the magnitude of the constriction resistance R_{cstr}, resulting in a shift along the y-axis of the resistance curves. (d) The cumulative DC potential distribution shows that the compensation of pore-induced potential gradients is more effective with a finer contact distribution.

This is also reflected in the extracted resistance curves (vs. t and $t^{0.5}$), as shown in **Figure S1c**. They only differ in their offset along the y-axis due to the varying R_{cstr}, while their slope in the linearized plot is equal. The differences in R_{cstr} arise from differences in the DC potential distribution in the SE (**Figure S1d**).

At time t_0, the potential drop close to the interface is more pronounced for coarse contacts than for fine contacts: A finer contact distribution leads to more homogenous potential distribution close to the interface and thus a smaller potential drop and lower R_{cstr}. For a fine and homogenously distributed arrangement of contacts, it is likely that R_{cstr} is negligible compared to R_{tot}, although the actual A_r might be considerably lower than $A_{electrode}$.

S3: The Influence of (Native) Surface Passivation

S3.1. Areal Coverage

To investigate how the areal coverage with passivation layers impacts impedance data and the reliability of extracted rate constants (k'_{exp}), we conducted another series of simulations. Here, R_p was fixed at $4R_{ref}$ (with R_{ref} = 9 Ω·cm^2) and randomly distributed contact spots were introduced at the interface. A_r, defined as the fraction of the interface where SEI formation occurs (*i.e.*, where the passivation layer is penetrated by SE surface asperities), was systematically varied from 1% to 99% of $A_{electrode}$ (see schematic in **Figure S2a**). Thus, the remaining fraction $(1 - A_r)$ was assumed to be covered by an intact passivation layer.

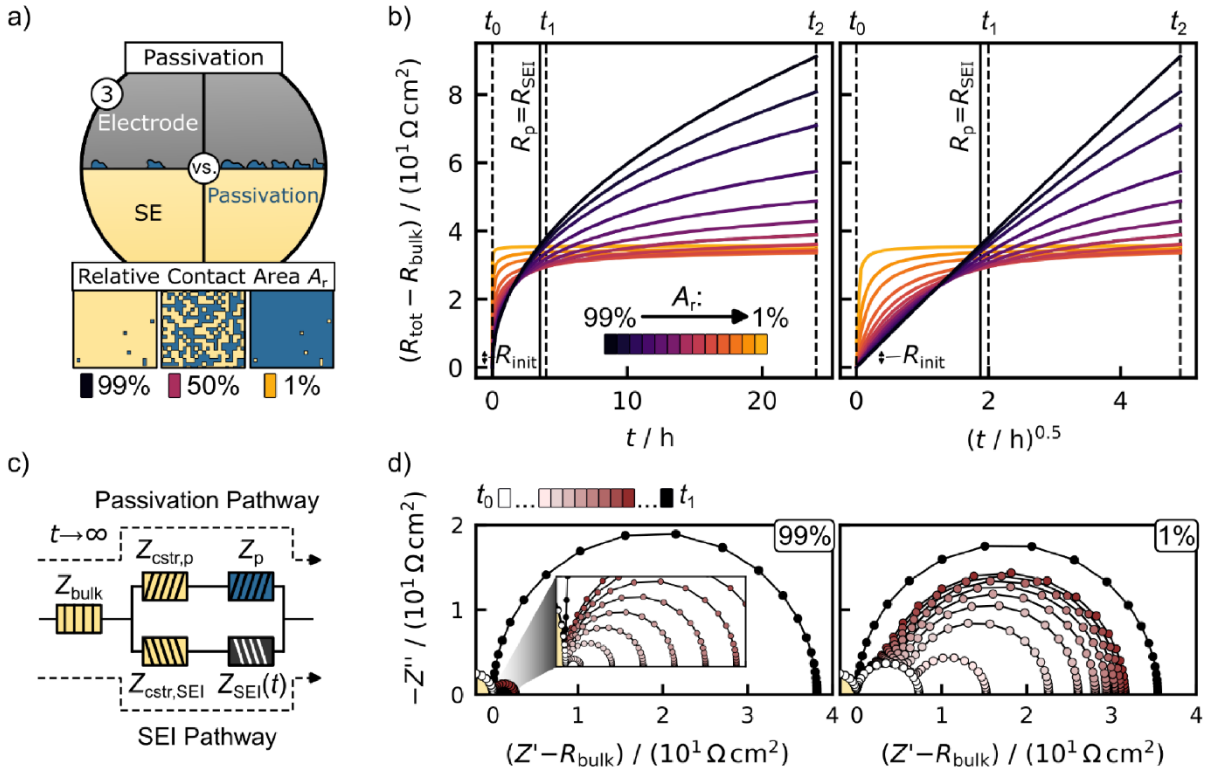

Figure S2. Effect of Contact Distribution on SEI Growth Analysis. The microscopic interphase growth rate k', and the interlayer resistance $R_p = 4R_{ref}$ were kept constant in the simulations. (a) A_r at the interface between a homogeneous electrode and SE is systematically varied between 1% and 99% by randomly flipping individual voxels. (b) As A_r decreases, there is a transition in the resistance evolution curves from a square root time behavior (black) to an almost instantaneous increase (*i.e.*, step function) that reaches a plateau (yellow). Note that each curve reaches a plateau for sufficiently long simulation times. (c) The behavior results from competing transport pathways at the interface, where the size of the initial resistances is determined by A_r. (d) At t_1, the interface impedances are approximately the same for a nearly intimate (99%) or non-ideal (1%) contact, but the time evolution is significantly different.

Figure S2b shows the time evolution of $(R_{tot} - R_{bulk})$. With increasing A_r, the transition from a square-root-of-time dependence to a time-independent $(R_{tot} - R_{bulk})$ takes more time.

For large values of A_r, such as 99%, the transition is not fully captured within the simulation timeframe (up to t_2), resulting in an almost ideal linear time dependence in the plot of $(R_{tot} - R_{bulk})$ vs. $t^{0.5}$. In contrast, at a small A_r (*e.g.*, 1%), the resistance evolution resembles a smoothed step function: The resistance appears to rise rapidly at first, but quickly saturates. The size of the saturated resistance increases with increasing A_r, while the initial resistance offset R_{init} becomes smaller.

The resistance evolution can be well understood considering the simple equivalent circuit model depicted in **Figure S2c**. It consists of a bulk impedance Z_{bulk} that is connected in series to two parallel interfacial pathways characterized by transport through the passivation Z_p or across the growing SEI $Z_{SEI}(t)$. Each interfacial pathway includes an individual constriction impedance (*i.e.*, $Z_{cstr,p}$ and $Z_{cstr,SEI}$) due to current focusing near the interface. This constriction impedance differs for the SEI and interlayer pathway due to differences in coverage and spatial distribution of the respective phases.

Both R_p and $R_{SEI}(t)$ are anti-proportional to the areal coverage of the interface with the respective phases. R_{SEI} becomes smaller when A_r becomes larger. In contrast, R_p becomes larger when A_r becomes smaller. The same trends are observed for the changes in $R_{cstr,p}$ and $R_{cstr,SEI}$. As a result of the decrease of $R_{SEI}(t)$ with increasing A_r, the times till reaching the resistance plateau is increased. These trends are also reflected in the impedance spectra shown in **Figure S2d**. At $A_r = 99\%$ of $A_{electrode}$, the initial impedance is low but increases steadily over time. In contrast, at $A_r = 1\%$ of $A_{electrode}$, the initial impedance is larger, but saturation occurs much earlier in time. At time t_1, the impedance of the system with $A_r = 99\%$ already exceeds that of the system with $A_r = 1\%$.

R_{init} is also evident in the impedance data: At t_0, before any SEI has formed, the impedance of the system with $A_r = 99\%$ of $A_{electrode}$ closely matches the bulk response. At this point, current predominantly flows through the SEI pathway, which spans most of the interface. In contrast, when $A_r = 1\%$ of $A_{electrode}$, the small interface coverage leads to a significant initial constriction impedance, which manifests as an additional contribution clearly visible in the impedance data at t_0. The signal roughly corresponds to the constriction impedance of the SEI pathway, neglecting small fractions of the current that may already flow through the passivation layer at that time.

S3.2. Transition Time Estimation

If the transport properties and thickness of the passivation layer are known, the transition time (t_{trans}), which marks the shift of preferred transport from across the SEI layer to through the passivation layer, can be estimated. The transition occurs when $R_{\mathrm{SEI}}(t)$ and R_{p} become comparable (see **eq. 2**), *i.e.*, when $R_{\mathrm{SEI}} \approx R_{\mathrm{p}}$. Assuming that they are identical, t_{trans} can be calculated via:

$$t_{\mathrm{trans}} = \left(\frac{R_{\mathrm{p}} \cdot A_{\mathrm{p}}}{k' \cdot A}\right)^2 \qquad \textbf{(eq. S3)}$$

Where R_{p} and A_{p} are the ionic resistance and contact area of the passivation layer, respectively, k' is the parabolic rate constant for the ionic resistance of interphases (**eq. 2** of the main text), and A denotes the contact area between the SE and the electrode.

R_{p} can be calculated from the ionic conductivity and layer thickness of the passivation layer. For passivated lithium foils, Otto *et al.*[8,9] reported passivation thicknesses ranging from 5 nm to 65 nm. Based on literature values, the primary components of these native films (*e.g.*, Li_2O, Li_2CO_3, LiOH) exhibit ionic conductivities between 10^{-8} and 10^{-10} S cm^{-1}.[10–15] Assuming a negligible partial electronic conductivity and $A_{\mathrm{p}} = 50\%$ of $A_{\mathrm{electrode}}$, the estimated t_{trans} can vary widely from a few minutes up to several years.

The timeframe in which this transition can be observed is a function of R_{p}. At t_{trans}, the local current density for transport through the passivation layer begins to exceed that of transport through the SEI layer. However, this local shift in preferred current pathways does not immediately manifest in the macroscopic impedance: A measurable change at the cell level becomes apparent when the *total* current through the interlayer becomes significant (*i.e.*, comparable in magnitude to the current through the SEI). This second transition is decisive and depends not only on the interfacial transport properties but also on the relative areal coverage of the interface with SEI and passivation.

S4: Analysis of Experimental Data

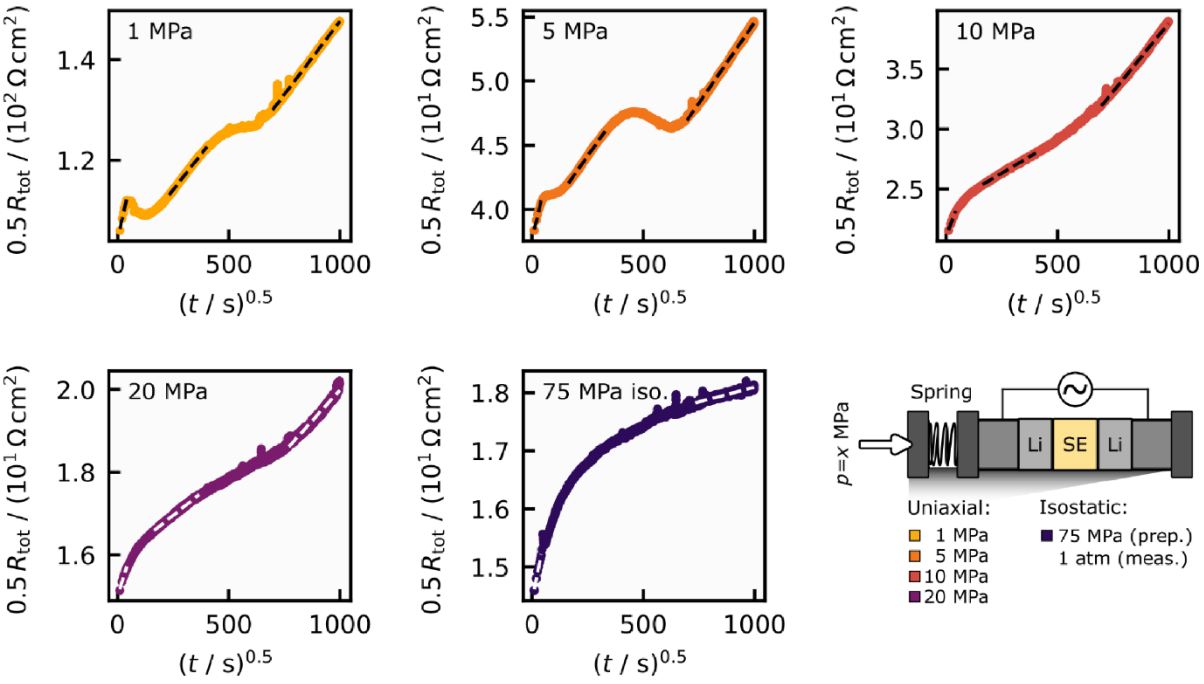

Figure S3. R_{tot} vs. $t^{0.5}$ for different pressure conditions. The evolution of R_{tot} over $t^{0.5}$ exhibits complex curvature. The dashed lines represent linear interpolation curves for distinct regions. It is important to stress that the choice of fitting windows is somehow arbitrary and not grounded on a rigorous mechanistic model. Rather, this approach is used to qualitatively illustrate general trends and to highlight the impact of pressure conditions on the apparent interphase evolution and corresponding rate constants. The extracted slopes, *i.e.*, k', are plotted over pressure in **Figure 5**.

References

1. Bale, C. W. *et al.* FactSage Thermochemical Software and Databases, 2010–2016. *Calphad* **54,** 35–53; 10.1016/j.calphad.2016.05.002 (2016).
2. Holm, R. *Electric Contacts* (Springer Berlin Heidelberg, Berlin, Heidelberg, 1967).
3. Eckhardt, J. K. *et al.* Interplay of Dynamic Constriction and Interface Morphology between Reversible Metal Anode and Solid Electrolyte in Solid State Batteries. *ACS Applied Materials & Interfaces* **14,** 35545–35554; 10.1021/acsami.2c07077 (2022).
4. Fleig, J. & Maier, J. Finite-Element Calculations on the Impedance of Electroceramics with Highly Resistive Grain Boundaries: I, Laterally Inhomogeneous Grain Boundaries. *J Am Ceram Soc.* **82,** 3485–3493; 10.1111/j.1151-2916.1999.tb02270.x (1999).
5. Limon, M. S. R., Duffee, C. & Ahmad, Z. Constriction and Contact Impedance of Ceramic Solid Electrolytes, 2025.
6. Eckhardt, J. K. *et al.* Guidelines for Impedance Analysis of Parent Metal Anodes in Solid-State Batteries and the Role of Current Constriction at Interface Voids, Heterogeneities, and SEI. *Adv Materials Inter* **10**; 10.1002/admi.202202354 (2023).
7. Koerver, R. *et al.* Chemo-Mechanical Expansion of Lithium Electrode Materials - On the Route to Mechanically Optimized All-Solid-State Batteries. *Energy Environ. Sci.* **11,** 2142–2158; 10.1039/C8EE00907D (2018).
8. Otto, S.-K. *et al.* In-Depth Characterization of Lithium-Metal Surfaces with XPS and ToF-SIMS: Toward Better Understanding of the Passivation Layer. *Chem. Mater.* **33,** 859–867; 10.1021/acs.chemmater.0c03518 (2021).
9. Otto, S.-K. *et al.* Storage of Lithium Metal: The Role of the Native Passivation Layer for the Anode Interface Resistance in Solid State Batteries. *ACS Appl. Energy Mater.* **4,** 12798–12807; 10.1021/acsaem.1c02481 (2021).
10. Fujita, Y. *et al.* Amorphous Li_2O–LiI Solid Electrolytes Compatible to Li Metal. *Electrochemistry* **89,** 334–336; 10.5796/electrochemistry.21-00049 (2021).
11. Guo, R. & Gallant, B. M. Li_2O Solid Electrolyte Interphase: Probing Transport Properties at the Chemical Potential of Lithium. *Chem. Mater.* **32,** 5525–5533; 10.1021/acs.chemmater.0c00333 (2020).
12. Lorger, S., Usiskin, R. & Maier, J. Transport and Charge Carrier Chemistry in Lithium Oxide. *J. Electrochem. Soc.* **166,** A2215-A2220; 10.1149/2.1121910jes (2019).
13. Shi, S. *et al.* Defect Thermodynamics and Diffusion Mechanisms in Li_2CO_3 and Implications for the Solid Electrolyte Interphase in Li-Ion Batteries. *J. Phys. Chem. C* **117,** 8579–8593; 10.1021/jp310591u (2013).
14. Deshpande, V., Raghuwanshi, F. & Singh, K. Electrical Conductivity of the Li_2SO_4 · LiOH System. *Solid State Ionics* **18-19,** 378–381; 10.1016/0167-2738(86)90145-1 (1986).
15. Dissanayake, M. Phase Diagram and Electrical Conductivity of the Li_2SO_4-Li_2CO_3 system. *Solid State Ionics* **21,** 279–285; 10.1016/0167-2738(86)90190-6 (1986).

7.3. Supporting Information – 3rd Publication

Supporting Information

The Partial Electronic Conductivity of Lithium Halides and their Role in SEI Formation in Solid-State Batteries – Hebb-Wagner-type Measurements

Christoph D. Alt[a,b], Jill Kessler-Kühn[a,b], Janis K. Eckhardt[b], Markus Stein[b,c], Sangam Chatterjee[b,c], Matthias T. Elm[b,c*], and Jürgen Janek[a,b,*]

[a]Institute of Physical Chemistry, Justus Liebig University, Heinrich Buff Ring 17, 35392 Giessen, Germany

[b]Center for Materials Research, Justus Liebig University, Heinrich Buff Ring 16, 35392 Giessen, Germany

[c]Institute of Experimental Physics I, Justus Liebig University, Heinrich Buff Ring 16, 35392 Giessen, Germany

*corresponding author: matthias.elm@physik.uni-giessen.de; juergen,janek@pc.jlug.de

7. Appendix

A: Derivation of Brouwer Diagram for LiCl with One Oxygen Impurity Level

Li_2O acts as an acceptor-type dopant (*i.e.*, p-type), promoting the formation of chlorine vacancies ($V_{Cl}^{\bullet}$) via the following defect incorporation reaction:

$$Li_2O(LiCl) \leftrightharpoons 2\,Li_{Li}^{X} + O_{Cl}' + V_{Cl}^{\bullet} \qquad \text{(eq. S1)}$$

To preserve overall charge neutrality within the crystal, the substitution of oxygen onto chlorine sites (O_{Cl}') must be accounted for. Consequently, the general charge neutrality condition (modifying eq. 6 from the main text) becomes:

$$[e'] + [V_{Li}'] + [O_{Cl}'] = [V_{Cl}^{\bullet}] + [h^{\bullet}] \qquad \text{(eq. S2)}$$

As in the case of undoped LiCl, the concentrations of ionic point defects are assumed to be largely independent of a_{Li} and significantly exceed those of intrinsic electronic. However, if the impurity concentration exceeds the intrinsic concentration of ionic defects, the oxygen impurities fix the concentration of chlorine vacancies:

$$[O_{Cl}'] \approx [V_{Cl}^{\bullet}] > [V_{Li}'] \gg [h^{\bullet}], [e'] \qquad \text{(eq. S3)}$$

Here, the concentration of V_{Li}' is defined by eq. 2 in the main text. This leads to the same dependence of electronic defect concentrations on lithium activity near the SP for pure LiCl:

$$[h^{\bullet}] = \frac{K_{Li}'}{[V_{Li}']}\frac{1}{a_{Li}} \propto a_{Li}^{-1} \text{ and } [e'] = \frac{[V_{Li}']K_{el}}{K_{Li}'}a_{Li} \propto a_{Li}^{+1} \qquad \text{(eq. S4)}$$

At higher a_{Li} far from the SP, the concentration of e' approaches $[V_{Cl}^{\bullet}]$. Neglecting the minority charge carriers (as done in eq. 9 of the main text), the characteristic dependences of pure LiCl in the extrinsic (non-stoichiometric) region are retained:

$$[e'] = \sqrt{\frac{K_S \cdot K_{el}}{K_{Li}'}a_{Li}} \propto a_{Li}^{+½} \qquad \text{(eq. S5)}$$

However, at lower a_{Li}, the incorporation of Li_2O introduces a distinct doping regime (indicated in gray in Figure 1B). By reducing a_{Li}, the hole concentration increases (eq. S4) and finally gets pinned (*i.e.*, is constant) by the oxygen defect level O_{Cl}':

$$[h^{\bullet}] \approx [O_{Cl}'] \gg [e'], [V_{Li}'], \qquad \text{(eq. S6)}$$

Taking eq. S6 into account, and using eqs. 2, 3, and 5 of the main text, the dependencies of the vacancy concentrations within this doping regime can be expressed as:

$$[V'_{Li}] = \frac{K'_{Li}}{[h^{\bullet}]}\frac{1}{a_{Li}} \propto a_{Li}^{-1} \text{ and } [V^{\bullet}_{Cl}] = \frac{[h^{\bullet}]K_S}{K'_{Li}} a_{Li} \propto a_{Li}^{+1} \qquad \text{(eq. S7)}$$

At the same time, the concentration of e' is defined by eq. 3 in the main text and is constant. Finally, at even lower a_{Li} far from the SP, $[V'_{Li}]$ approaches the concentration of $h^{\bullet}$. The same approximation for minority charge carriers (as done in eq. 9 of the main text) result in the characteristic dependences of electronic defect concentrations in the extrinsic (non-stoichiometric) region:

$$[h^{\bullet}] = \sqrt{\frac{K'_{Li}}{a_{Li}}} \propto a_{Li}^{-½} \qquad \text{(eq. S8)}$$

B: Impedance Spectra of Li|Li*X*|Au with *X* = Cl, Br, or I

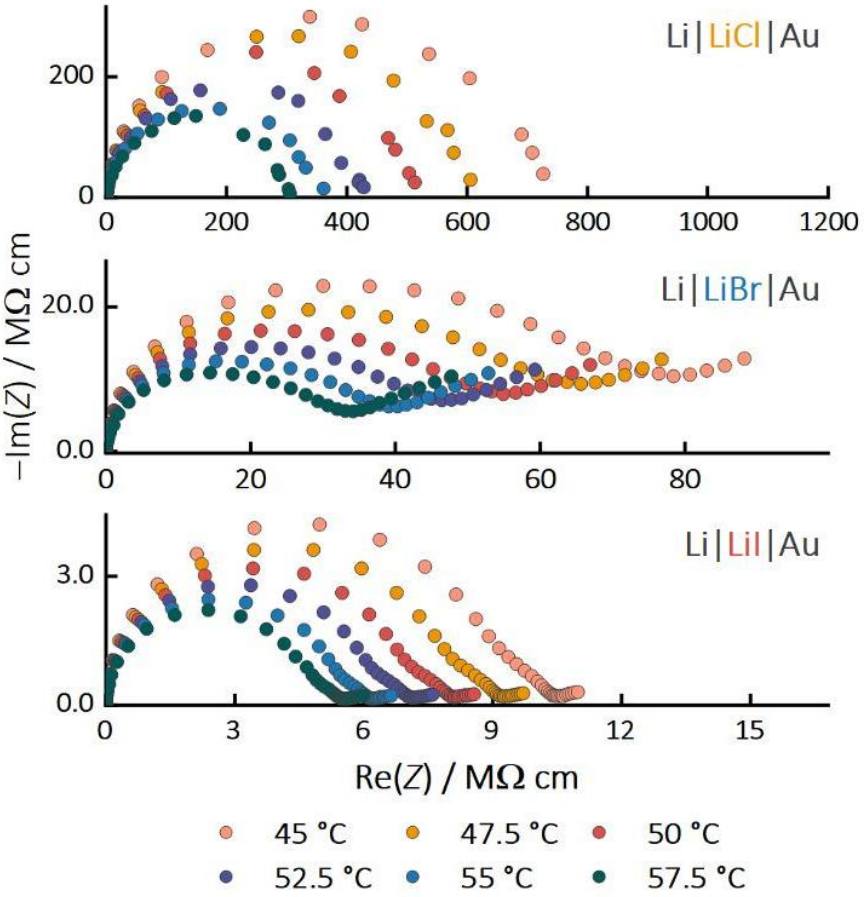

Figure S1: Impedance spectra (normalized to the cell constant) obtained from Hebb-Wagner measurements conducted in an ion-blocking configuration Li|Li*X*|Au, where *X* represents Cl, Br, or I. The dc offset was 0 V relative to the OCV. The temperature *T* was gradually increased from 45 to 57.7 °C.

C: Photoluminescence Measurements of Li*X* with *X* = Cl, Br, or I

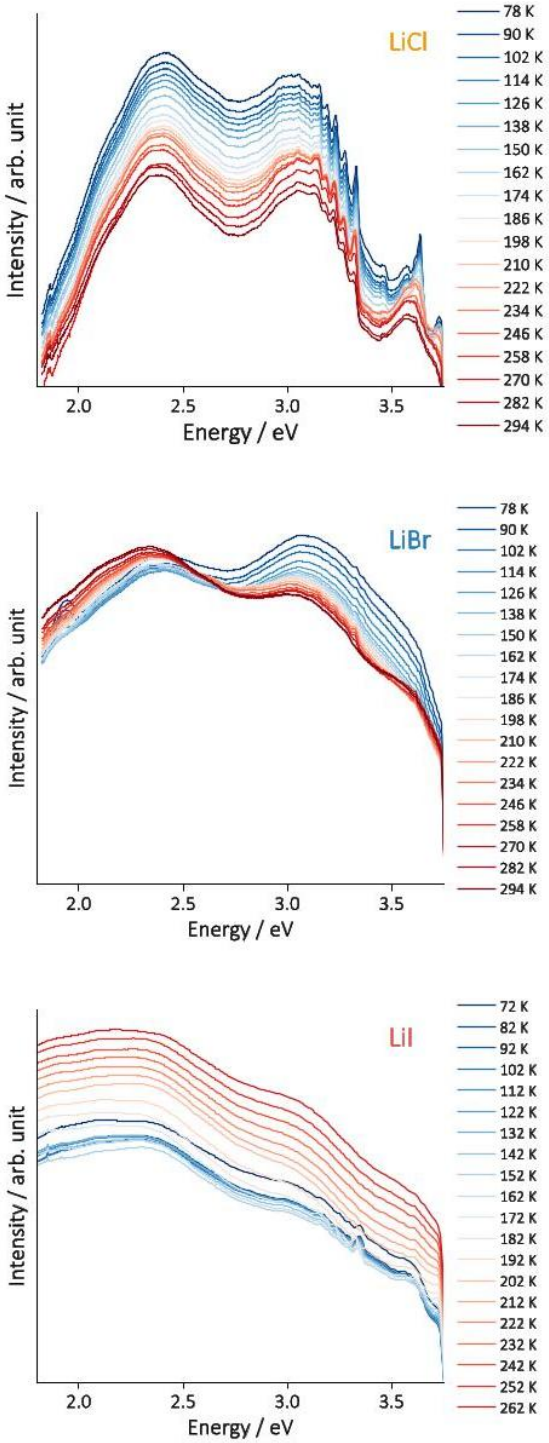

Figure S2: The photoluminescene spectra of Li*X* pellets, where *X* represents Cl, Br, or I. Spectra were acquired under dynamic vacuum, using an Andor Shamrock 500i spectrometer equipped with a grating featuring a groove density of 150 lines mm^{-1} and a 300 nm blaze. A silicon CCD camera was used for detection. As the excitation source, we employed a 325 nm helium-cadmium (He-Cd) laser with an excitation power of 2.5 mW.

D: X-Ray Photoelectron Spectroscopy Measurements of LiCl

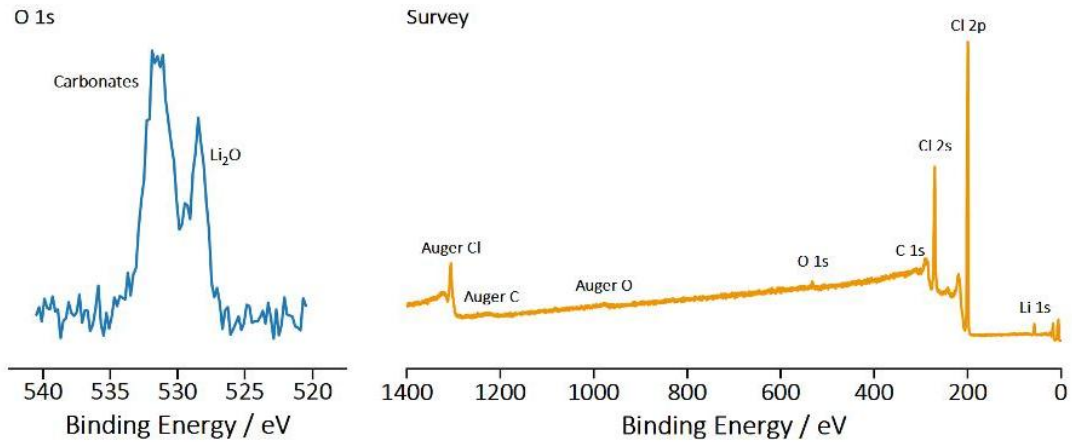

Figure S3: O 1s (left) and survey (right) spectra of LiCl. The pelletized sample was sputter-cleaned using Ar^+ ions to expose the underlying bulk and reveal the presence of Li_2O impurities in the O 1s spectrum. Peak assignments were made based on reference 1.

Experimental

XPS measurements were performed using a VersaProbe 4 system (ULVAC-PHI, USA) equipped with a monochromatic Al K_α X-ray source (beam diameter of 200 µm, X-ray power of 50 W). The chamber pressure during measurements was maintained between 10^{-7} and 10^{-6} Pa. To minimize surface charging effects, charge neutralization was applied throughout the acquisition. Sputter-cleaning was conducted via Ar^+ sputtering over a 2 × 2 mm^2 area, using a 2 kV ion beam for 2 minutes. A vacuum transfer shuttle was used to prevent air exposure and atmospheric contamination during sample handling. Survey as well as detailed spectra were processed and analyzed using the *CasaXPS* software package (Casa Software, UK).

E: Exponential Pre-Factors and Activation Energies

	LiCl	**LiBr**	**LiI**
$\Delta H_{mig} = E_A$ / eV	0.66	0.63	0.50
σ_0 / S K cm^{-1}	$9 \cdot 10^3$	$3 \cdot 10^4$	$8 \cdot 10^3$
u_0 / cm^2 K V^{-1}s^{-1}	$4.2 \cdot 10^2$	$6.9 \cdot 10^2$	$9.3 \cdot 10^2$
n_{ex} / cm^{-3}	$1 \cdot 10^{20}$	$3 \cdot 10^{20}$	$2 \cdot 10^{19}$

Table S1: Summary of the exponential pre-factors and activation energy of LiCl, LiBr, and LiI, derived through linear regression using eqs. 24, 25, and 26. It should be noted that the results of Haven[2] were used to approximate u_0, while E_A (from $\log(\sigma_{ion} \cdot T)$ vs. $1000/T$) was assumed for ΔH_{mig}.

F: Current Response in Hebb-Wagner Measurements of Li|Li*X*|Au with *X* = Cl, Br, or I

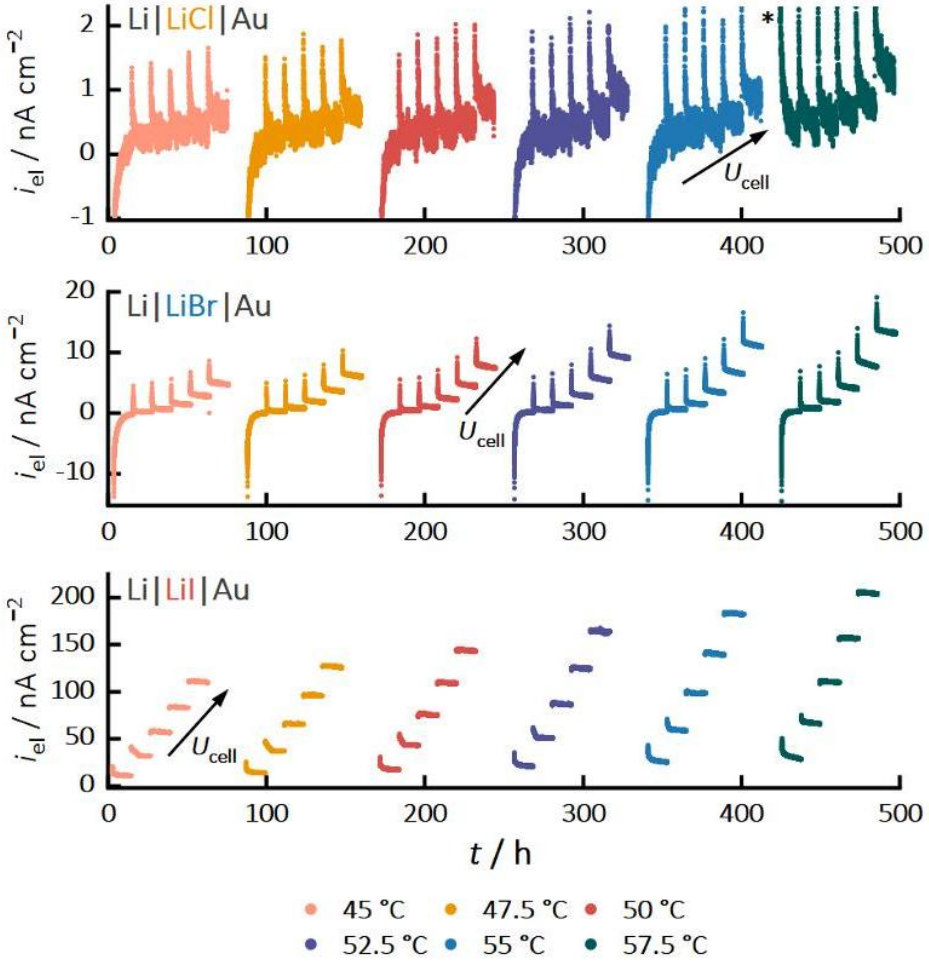

Figure S4: Current density profiles obtained from Hebb-Wagner measurements performed in an ion-blocking configuration Li|Li*X*|Au, where *X* represents Cl, Br, or I. The voltage U_{cell} was gradually increased by U_{source}, as outlined in the experimental description, while the temperature *T* was varied between 45 and 57.5 °C. For LiCl, the measurement experienced a brief interruption due to a device error, with the subsequent restart marked by an asterisk (*).

G: Deriving Current Density Profiles from Brouwer Diagrams

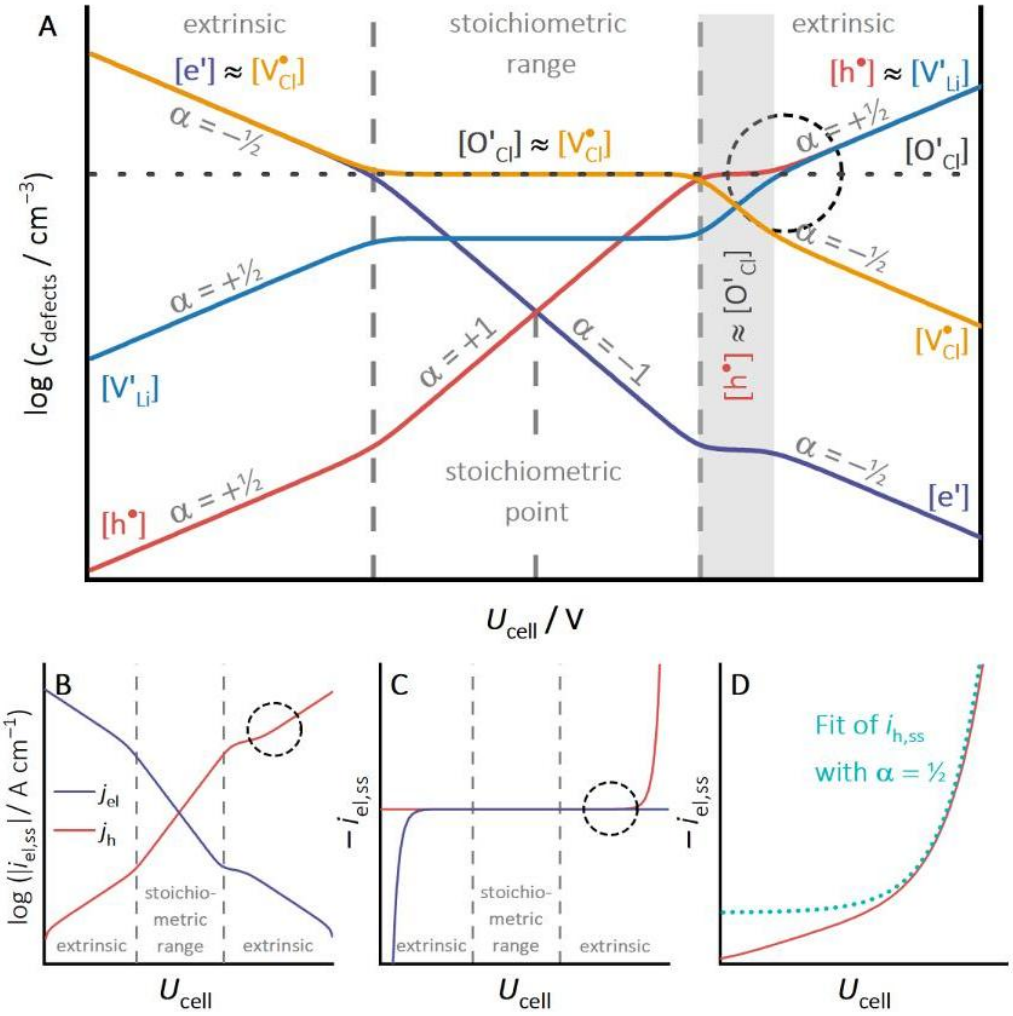

Figure S5: Derivation of current density profiles based on the calculated Brouwer diagram shown in Figure 1B. The *x*-axis of Figure 1B was transformed using the relation $U_{\mathrm{cell}} = -RT/F \cdot \ln(a_{\mathrm{Li}})$ (A). The electronic current density i_{el} was computed from the defect concentrations (c_{defects}) of electrons and electron holes via integration, according to eq. 19 in the main text, assuming constant mobilities of electronic charge carriers. $i_{\mathrm{el,ss}}$ is plotted as a function of U_{cell} (B, C, and D). The dashed circles indicate the magnified region (D), where one exemplary fit using $\alpha = ½$ (applied in Figures 4A and S6) is represented by the dotted blue line. Note that all plots are based on calculated Brouwer diagrams, the *x*-axis remains consistent across panels A, B, and C, and all units are arbitrary.

H: Fits of the Electronic Steady-State Currents in Li|LiCl|Au and Li|LiBr|Au

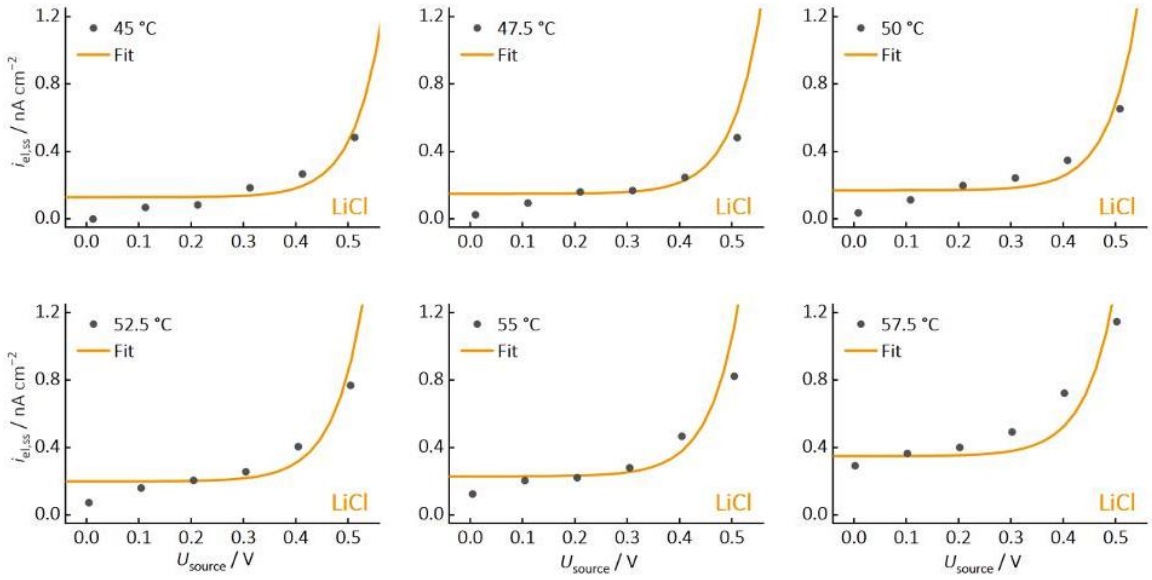

Figure S6: Data for $i_{el,ss}$ as a function of U_{source} and corresponding fits (see Figure 4A and S4) in an ion-blocking configuration Li|LiCl|Au. Fitting was performed as described in the main text, using eq. 27 and α = ½. The voltage U_{source} was gradually increased, as outlined in the experimental description, while the temperature T was varied between 45 and 57.5 °C. Fitting parameters and results are given in Figure 6.

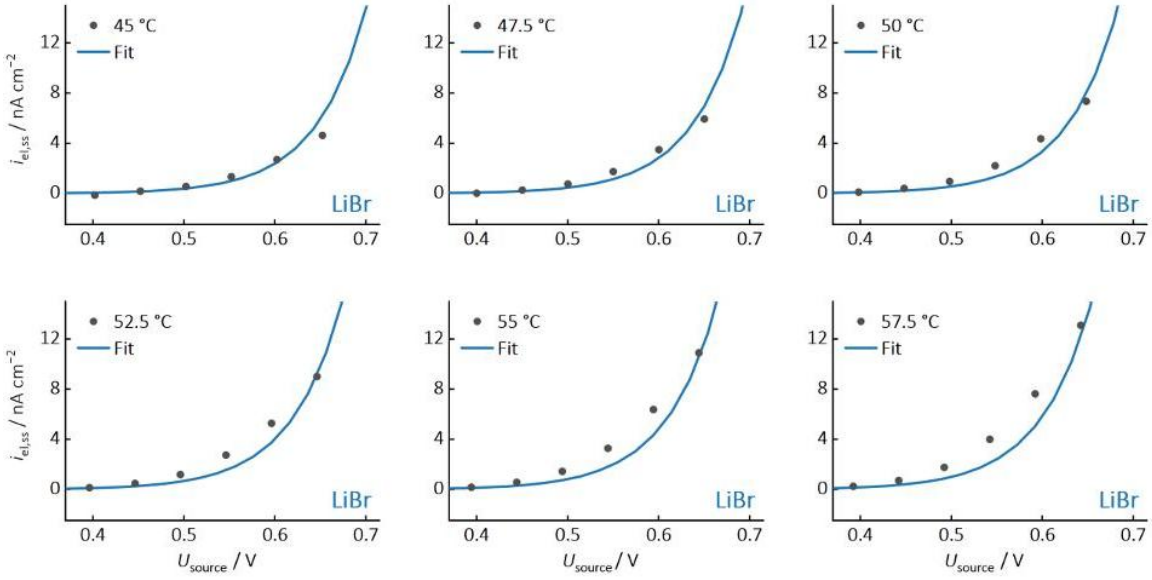

Figure S7: Data for $i_{el,ss}$ as a function of U_{source} and corresponding fits (see Figure 4B and S4) in an ion-blocking configuration Li|LiBr|Au. Fitting was performed as described in the main text, using eq. 27 and α = ½. The voltage U_{source} was gradually increased, as outlined in the experimental description, while the temperature T was varied between 45 and 57.5 °C. Fitting parameters and results are given in Figure 6.

References

1. Chastain, J. (ed.). *Handbook of X-ray Photoelectron Spectroscopy. A reference book of standard spectra for identification and interpretation of XPS data* (Perkin-Elmer, Eden Prairie, Minn., 1995).
2. Haven, Y. The ionic conductivity of Li-halide crystals. *Recl. Trav. Chim. Pays-Bas* **69,** 1471–1489; 10.1002/recl.19500691203 (1950).

7.4. Supporting Information – 4th Publication

ADVANCED ENERGY MATERIALS

Supporting Information

for *Adv. Energy Mater.*, DOI 10.1002/aenm.202404055

In–Li Counter Electrodes in Solid-State Batteries – A Comparative Approach on Kinetics, Microstructure, and Chemomechanics

*Christoph D. Alt, Sören Keuntje, Inga L. Schneider, Johannes Westphal, Philip Minnmann, Janis K. Eckhardt, Klaus Peppler and Jürgen Janek**

WILEY-VCH

Supporting Information

In–Li Counter Electrodes in Solid-State Batteries – A Comparative Approach on Kinetics, Microstructure and Chemomechanics

*Christoph D. Alt, Sören Keuntje, Inga L. Schneider, Johannes Westphal, Philip Minnmann, Janis K. Eckhardt, Klaus Peppler, and Jürgen Janek**

Christoph D. Alt, Sören Keuntje, Inga L. Schneider, Johannes Westphal, Philip Minnmann, Janis K. Eckhardt, Klaus Peppler, and Jürgen Janek*
Institute of Physical Chemistry, Justus Liebig University, Heinrich-Buff Ring 17, 35392 Giessen, Germany
E-mail: juergen.janek@phys.chemie.uni-giessen.de

Christoph D. Alt, Sören Keuntje, Inga L. Schneider, Johannes Westphal, Philip Minnmann, Janis K. Eckhardt, Klaus Peppler, and Jürgen Janek
Center for Materials Research, Justus Liebig University, Heinrich-Buff Ring 16, 35392 Giessen, Germany

Janis K. Eckhardt
Institute for Theoretical Physics, Justus Liebig University, Heinrich-Buff-Ring 16, 35392 Giessen, Germany

A: Reference Measurements with Indium Metal Anodes

Cells were prepared with pure indium foil as electrode (9 mm diameter, 100 µm thickness). A NCM cathode composite (12 mg) and an In–Li anode ($In/Li_{stacked}$) were used as CE for full and symmetric cell configuration, respectively. Preparation, assembly, and testing are performed as described in detail in the experimental section.

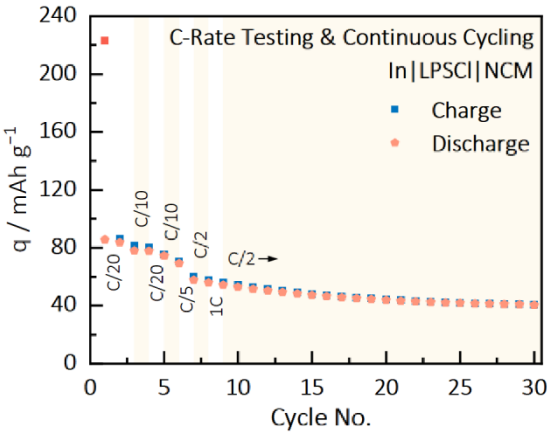

Figure S1: Results of C-rate capability tests, followed by continuous cycling for indium foil (9 mm diameter, 100 µm thickness), utilized as CE in full cell configuration (In | LPSCl | NCM). Cycled capacities for various C-rates, as well as the cycled capacities throughout continuous cycling are presented (measured at 25°C and 75 MPa). The first charging process, marked by substantial capacity losses, is depicted in red.

In full cell configuration (In | LPSCl | NCM), the decreased reversibility (*i.e.*, severe lithium inventory losses) after the first charge process (depicted in red) and consecutive cycles is associated with the formation of the $In/(InLi)_x$ alloy causing unstable CE conditions. The inconsistency of the CE potential (as a result of the alloying reaction) further impacts the cycling stability and efficiency, as it serves as the reference potential in our cell configuration.

In the cell configuration (WE | LPSCl | $In/Li_{stacked}$), the inferior performance and lower capacity of the pure indium anode (violet) are associated with the enhanced lithium diffusion properties within In–Li anodes. Consequently, pre-lithiation of indium is advantageous for enhancing both anode kinetics and performance. Furthermore, pre-lithiation ensures stable potentials within a specific range (depending on its Li:In ratio), which is beneficial for its utilization as a CE. The OCV of the pure indium anode was initially 1.4 V before decreasing to approximately 0 V with the initiation of the lithiation process and creating a symmetric cell.

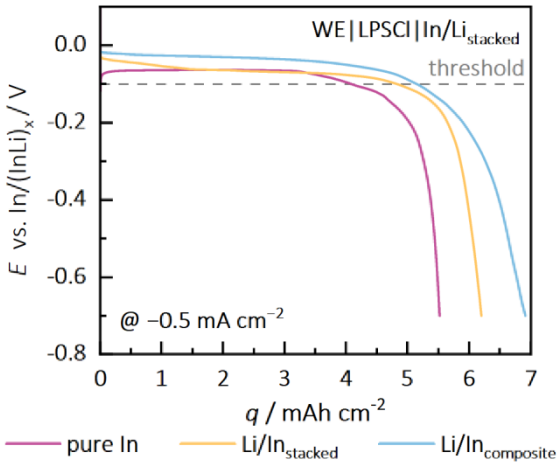

Figure S2: Results of current-dependent lithiation experiments of pure indium foil (violet) in comparison to $In/Li_{stacked}$ (yellow) and $In/Li_{composite}$ (light blue) in symmetric cell configuration (WE | LPSCl | $In/Li_{stacked}$). Potential profiles (vs. $In/(InLi)_x$) at −0.5 mA cm^{-2}, 25 °C and 30 MPa are recorded until the cut-off potential of −0.7 V is reached. The threshold of −100 mV is indicated in gray. The enhanced lithium diffusion within In–Li anodes is clearly evidenced by their improved performance when compared to pure indium foil. In particular, when considering the theoretical lithiation capacities of 7 and 15.3 mAh cm^{-2} for the In–Li anodes and pure indium, respectively.

B: Comparison of the Accessible Capacities in Delithiation Experiments at 0.5 mA cm^{-2}

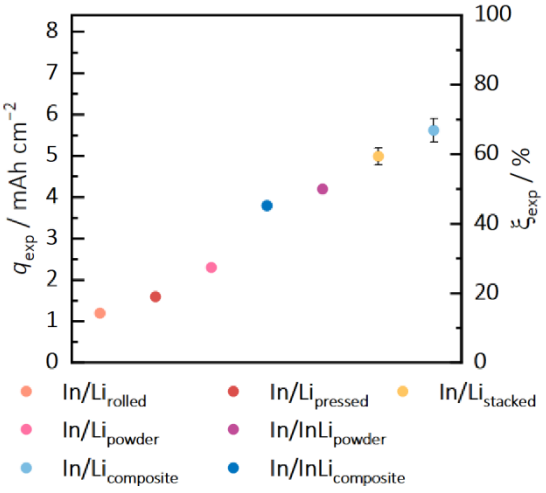

Figure S3: Comparison of the accessible capacities (q_{exp}) and lithium accessibility (ξ_{exp}), including averages and standard deviations for $In/Li_{stacked}$ and $In/Li_{composite}$ based on three cells each. The statistical analysis yields q_{exp} values of (5.00 ± 0.21) and 5.62 ± 0.29) mAh cm^{-2}, respectively. This underscores the satisfactory reproducibility of these two promising electrodes. Please note that only a single cell was tested for the other, less promising electrodes.

C: Rate Testing of In/Li$_{stacked}$ and In/Li$_{composite}$ in Delithiation Experiments

As before, we identify reliable capacities for both electrode types based on the point where significant polarization (> 100 mV) initiates, and refer to it as q_{exp}. Notably, extracted capacities of up to q_{exp} = 6 mAh cm^{-2} ($\xi_{exp} \approx 70$ %) were achieved. Higher onset potentials and early polarization are observed with increasing current density, especially for In/Li$_{stacked}$. This shift in onset potential above 100 mV suggests that insufficient kinetics will limit the accessible capacity for rates between 1.5 and 5 mA cm^{-2}. The early onset of polarization is attributed to inadequate transport kinetics and, at least temporarily, reduced or hampered lithium replenishment for both electrode types, especially at 5 mAh cm^{-2}.

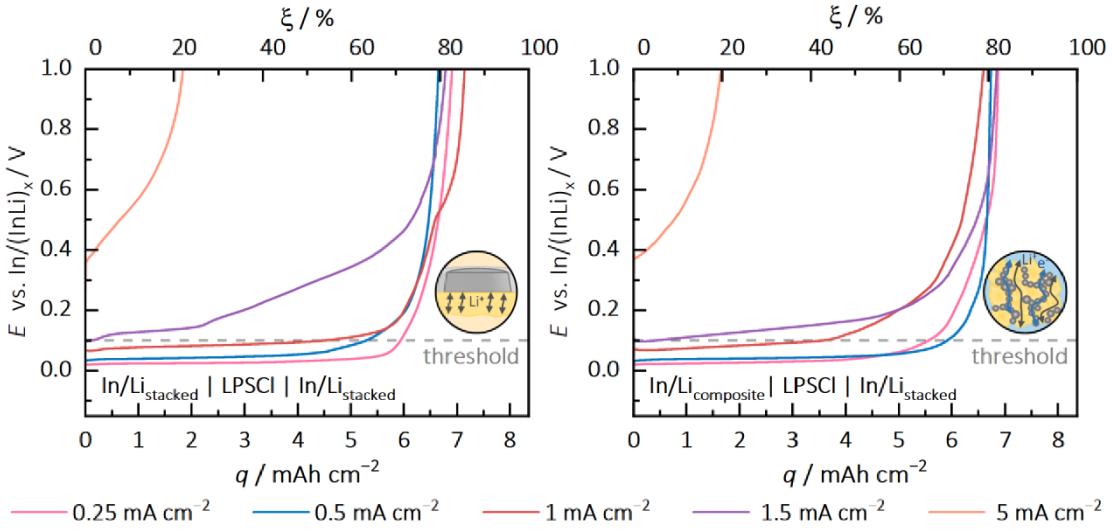

Figure S4: Results of current-dependent delithiation experiments of In/Li$_{stacked}$ (left) and In/Li$_{composite}$ (right) (WE | LPSCl | In/Li$_{stacked}$). Potential profiles (vs. In/(InLi)$_x$) for different stripping currents at 25 °C and 30 MPa are recorded until the cut-off potential of 1 V is reached. The threshold of 100 mV is indicated in gray.

D: Plating Performance of In/Li$_{composite}$ in Unidirectional Experiments

Here, In/Li$_{stacked}$ (CE) is delithiated and serves as lithium source in this experiment, while In/Li$_{composite}$ is now lithiated and used as WE. Hereby, the theoretical lithiation capacity of 7 mAh cm^{-2} is almost reached. Nevertheless, independent of the current density (between 0.5 and 5 mAh cm^{-2}), the formation of dendrites could not be observed (*i.e.*, the potential would drop back to ~0 V) until the cut-off potential of −0.7 V was reached.

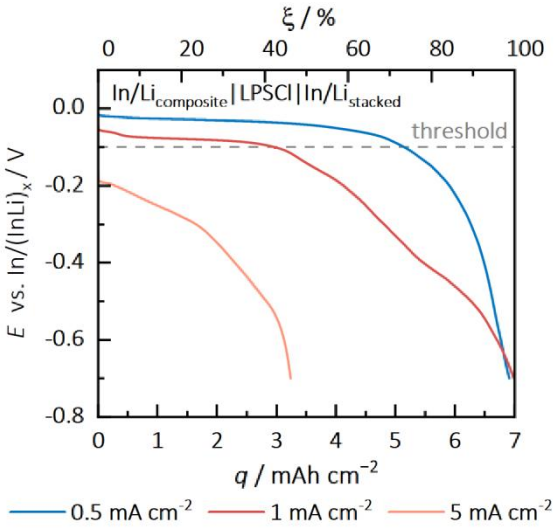

Figure S5: Results of current-dependent lithiation experiments of In/Li$_{composite}$ in symmetric cell configuration (In/Li$_{composite}$ | LPSCl | In/Li$_{stacked}$). Potential profiles (vs. In/(InLi)$_x$) for different plating currents at 25 °C and 30 MPa are recorded until the cut-off potential of −0.7 V is reached. The theoretical lithiation capacity is 7 mAh cm^{-2}.

E: Variations of Lithium Metal Thickness for In/Li$_{stacked}$

Symmetric cells (Li$_d$/In$_{100\ \mu m}$ | LPSCl | Li$_{100\ \mu m}$/In$_{100\ \mu m}$) were prepared with indium foil (9 mm diameter, 100 µm thickness), while the thickness (d) and diameter of the lithium metal foil was varied between 52 and 244 µm (corresponding to 9 and 4 mm in diameter). We maintained the composition (*i.e.*, volume, mass, and capacity) constant.

The homogeneous distribution of lithium atoms and their replenishment (during ongoing stripping) are measured by the available lithium at the interface to the SE. Consequently, these capacities indicate the significant impact on electrode performance of different lithium metal foil thicknesses and diameters. We identified an optimum (light yellow) for the lithium metal foil thickness of 100 µm (and 6 mm diameter) combined with 100 µm indium foil.

Assuming the same area for both metal foils, an 82 µm thick lithium film reacts with 100 µm of indium to fully form the intermetallic InLi phase. However, the loss of lithium due to passivation reactions must be compensated for. The thickness of the lithium foil should be chosen to match the dimension of the indium foil. We suggest a thickness ratio of d_{Li}/d_{In} between 0.9 and 1 to ensure a complete alloying reaction up to the interface with the SE. However, this results in the lithium foil having a smaller area than the indium foil.

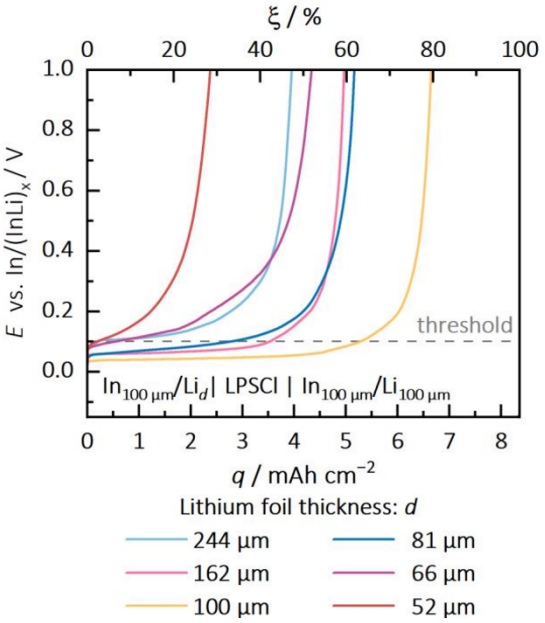

Figure S6: Results of delithiation experiments for variations of In/Li$_{stacked}$ geometrics in symmetric cell configuration (Li$_d$/In$_{100\ \mu m}$ | LPSCl | Li$_{100\ \mu m}$/In$_{100\ \mu m}$). Potential profiles (vs. In/(InLi)$_x$) for unidirectional galvanostatic stripping at 0.4 mA, 25 °C, and 30 MPa are recorded until the cut-off potential of 1 V is reached. The thickness of the lithium metal foil is varied between 52 and 244 µm. The threshold of 100 mV is indicated in gray. The theoretical delithiation capacity is 8.4 mAh cm^{-2}.

F: Electrode Relaxation Analysis after Delithiation Experiments

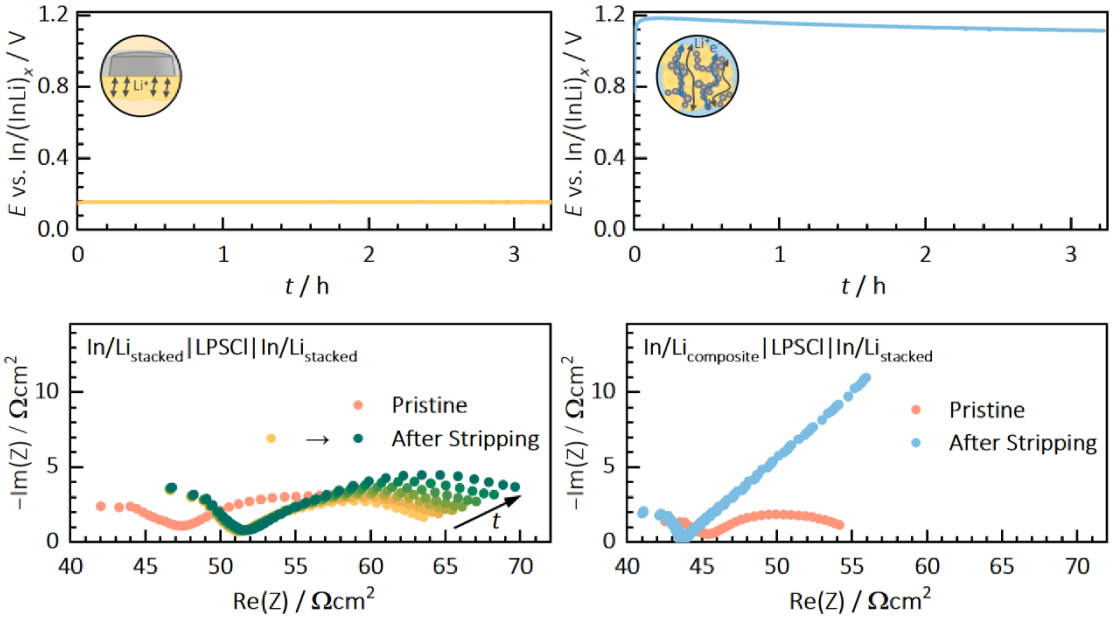

Figure S7: Results of relaxation measurements of In/$Li_{stacked}$ (left) and In/$Li_{composite}$ (right) (WE | LPSCl | In/$Li_{stacked}$) after unidirectional galvanostatic stripping at 0.5 mA cm^{-2}, 25 °C, and 30 MPa with a cut-off potential of 1 V. The results shown correspond to the single cells tested in Figure 3. While the OCV (top) is continuously monitored for 3.25 h, impedance spectra (bottom) are recorded. The spectra taken before stripping (pristine, light red) and at 30-minute time intervals after stripping (light green to dark green or light blue, respectively) are presented. We believe that the increase in low-frequency impedance of the In/$Li_{stacked}$ cell (left) can be attributed to SEI formation (*i.e.*, most likely at the highly-lithiated CE), while the low-frequency impedance of the In/$Li_{composite}$ cell should be dominated by the blocking behavior of the stripped electrode due to significant deterioration of the composite structure.

G: Reference Measurement of Pristine Indium Foil for EBSD Analysis

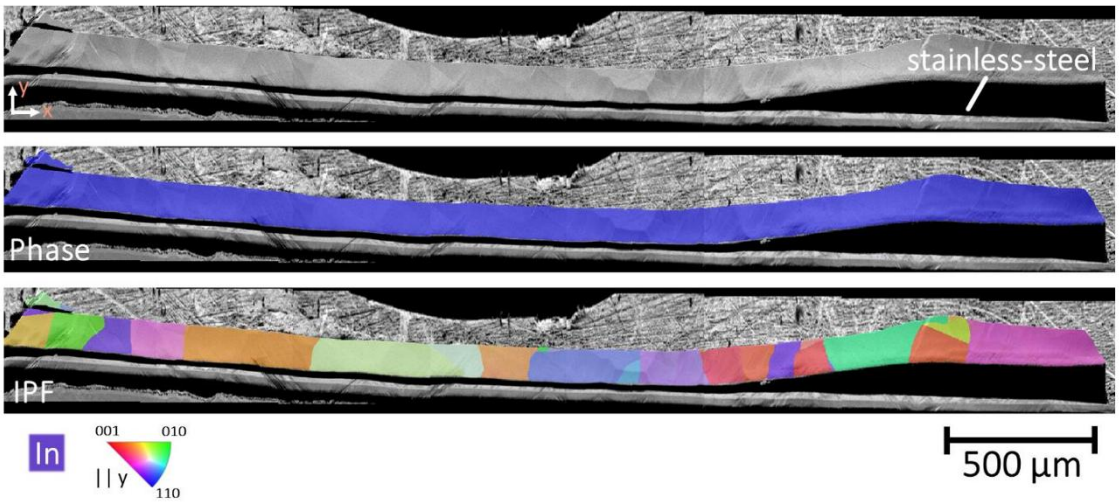

Figure S8: Polished cross-sections of pristine indium metal foil, which served as base material for the preparation of In/$Li_{stacked}$ electrodes. SEM images are complemented by phase and IPF maps (given parallel to the *y*-direction) for indium to reveal its columnar microstructure using EBSD.

H: Magnification of the Pristine In/$Li_{stacked}$ Electrode for EBSD Analysis

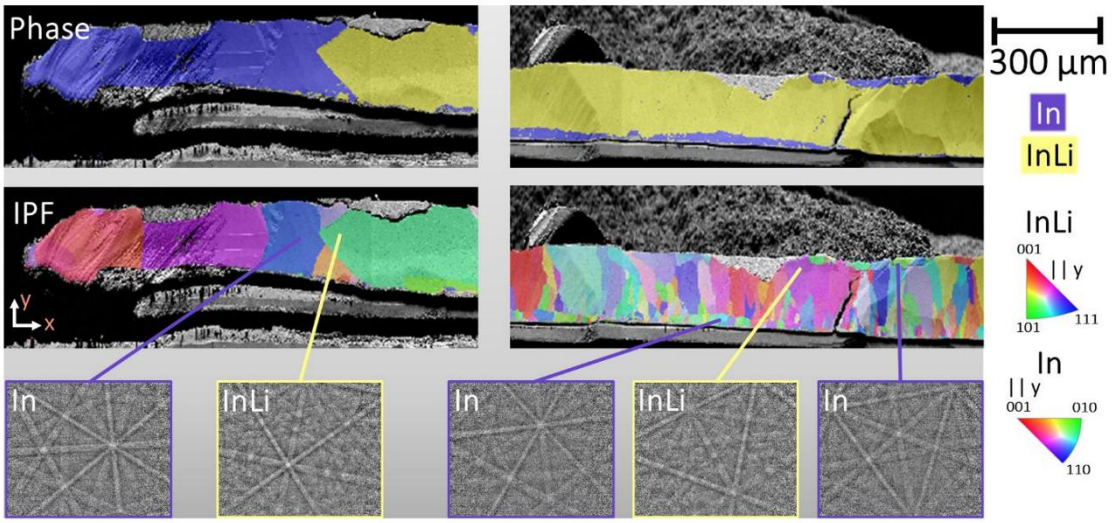

Figure S9: Magnified phase (top) and IPF maps in *y*-direction (middle) of different areas of the pristine In/$Li_{stacked}$ electrode (shown in Figure 6). Selected electron backscattering patterns are depicted (bottom), confirming the presence of small residuals of indium metal at various locations.

I: Galvanostatic Cycling at C/2 in Full Cell Configuration

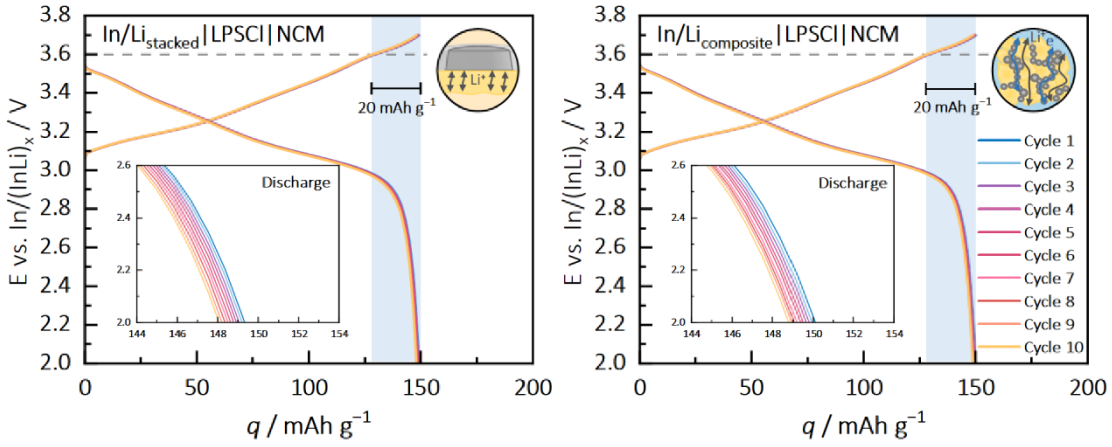

Figure S10: Results of galvanostatic cycling at C/2 for In/Li$_{stacked}$ (left) and In/Li$_{composite}$ (right), utilized as CE in full cell configuration (CE | LPSCl | NCM). The dashed line indicates a reduced cut-off potential (by 100 mV), while the blue background highlights the capacity loss caused by early termination due to an overpotential of 100 mV.

J: Potential Profiles of the NCM Cathode Composite (WE) during C-rate Testing

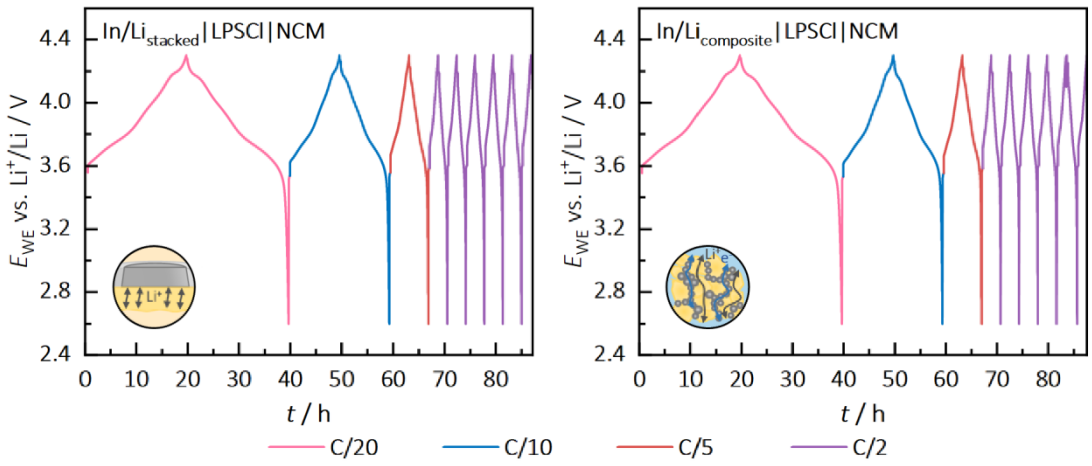

Figure S11: Results of cathode kinetic measurements during C-rate capability tests for In/Li$_{stacked}$ (left) and In/Li$_{composite}$ (right), utilized as CE in 3E configuration (CE | LPSCl | NCM with lithiated Au-RE). The potential profiles of the WE (vs. In/(InLi)$_x$) are presented for both electrodes (measured at 25°C and 75 MPa).

K: Chemomechanical Measurements in Full Cell Configuration during Cycling at C/2

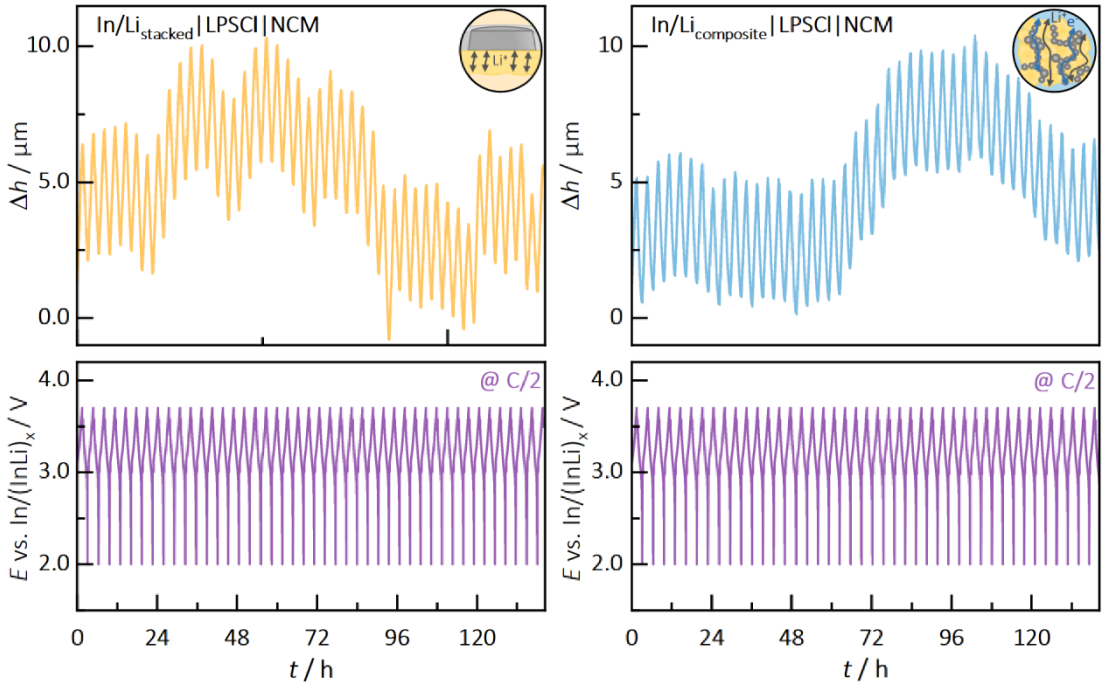

Figure S12: Results of the chemomechanic investigations for continuous cycling at C/2 for In/Li$_{stacked}$ (left) and the In/Li$_{composite}$ (right), utilized as CEs in full cell configuration (CE | LPSCl | NCM). The high chemomechanical reversibility is demonstrated as the height changes Δ*h* (top) agree well with the charge-discharge curves (bottom). The full cell experiences volume expansion during charging and compression during discharge (measured at 25°C and 75 MPa). However, accurate measurements are hindered by the background alterations.

7.5. Supporting Information – 5th Manuscript

i. Experimental

Deposition and cell assembly were carried out in an argon-filled glovebox (*LabMasterPRO*, MBraun, Germany), with $p(O2)/p$ and $p(H2O)/p < 1$ ppm.

Materials and Electrolyte. The stainless-steel discs (9.6 mm in diameter) were punched from 20 µm thick foils (*AISI 304*, Goodfellow, UK). The discs were then ultrasonically cleaned for 3 min each in acetone and isopropanol, followed by vacuum drying for at least 10 h at 60 °C. Thin indium electrodes (100 and 250 nm) were deposited onto the stainless-steel discs under dynamic vacuum using a custom thermal evaporation system connected to a glovebox. The deposition rate was set between 0.1 and 0.2 nm s^{-1}, monitored by an oscillating quartz sensor. LPSCl (POSCO JK Solid Solution Co., South Korea), with σ_{ion} = 1.1 mS cm^{-1} at 25 °C, was investigated as the separator material. For reference, (passivated) indium foil (100 µm, 9 mm diameter, 99.999%, ChemPUR, Germany) was used. Passivated indium films (100 and 250 nm) were prepared by exposing them to ambient atmosphere for 8 days at room temperature.

Cell Assembly. Each CTTA cell was prepared by pelletizing LPSCl (80 mg, ~600 µm thick) within a polyether-ether-ketone casing (10 mm diameter) between stainless-steel rods as contacts. Densification was performed at 380 MPa of uniaxial pressure for 3 min at room temperature. Indium-coated discs and the In–Li counter electrode (CE), which serves as a lithium reservoir, were then placed on either side of the separator. The CE was constructed by positioning indium foil (100 µm, 9 mm diameter) between the SE and lithium foil (100 µm, 6 mm diameter, 99.9%, China Energy Lithium, China). Lithium diffuses into the indium metal, forming an $In/(InLi)_x$ eutectic with a stable potential of 0.62 V *vs*. Li^+/Li.[1]

CTTA Analysis. CTTA measurements were performed as described by Aktekin *et al*.[2]. Cells were tested using a *Maccor* battery cycler at 25 °C under an applied stack pressure of approximately 15 MPa. The initial open-circuit voltage of such cell was typically around 1.6 V vs. $In/(InLi)_x$. During each titration step (i = 10 µA), a small amount of lithium metal (corresponding to a charge of 0.5 µAh) was deposited, causing lithiation of the indium layer. After each titration step, the cell voltage dropped to around 0 V and was continuously monitored. When the voltage increased to a threshold of 0.1 V, the next titration step was applied, indicating that the lithium metal at the working electrode had been completely consumed by side reactions. This procedure was repeated multiple times over approximately 400 h in this study.

XPS Measurements. XPS measurements on indium films and the corresponding reference foil were performed using a *Versaprobe 4* spectrometer (ULVAC-PHI, Inc., USA), equipped with a monochromatized Al K_α X-ray source (beam diameter of 200 µm, X-ray power of 50 W). The chamber pressure ranged from 10^{-7} to 10^{-6} Pa during measurements, while the sample surface was charge-neutralized using slow electrons and Ar^+. A pass energy of 55 eV with 0.1 eV steps was used for the detail spectra. All data were calibrated in relation to the signal of adventitious carbon at 284.8 eV. XPS depth profiling was performed by Ar^+

sputtering with a grid size of 2×2 mm^2 and an acceleration voltage of 1 kV, first for 2 min, followed by 4 min. Cross contamination with atmosphere were avoided using a transfer shuttle. Data analysis was carried out with *CasaXPS* (Version 2.3.25, Casa Software, UK).

ii. Additional CTTA Experiments on the Effect of In_2O_3

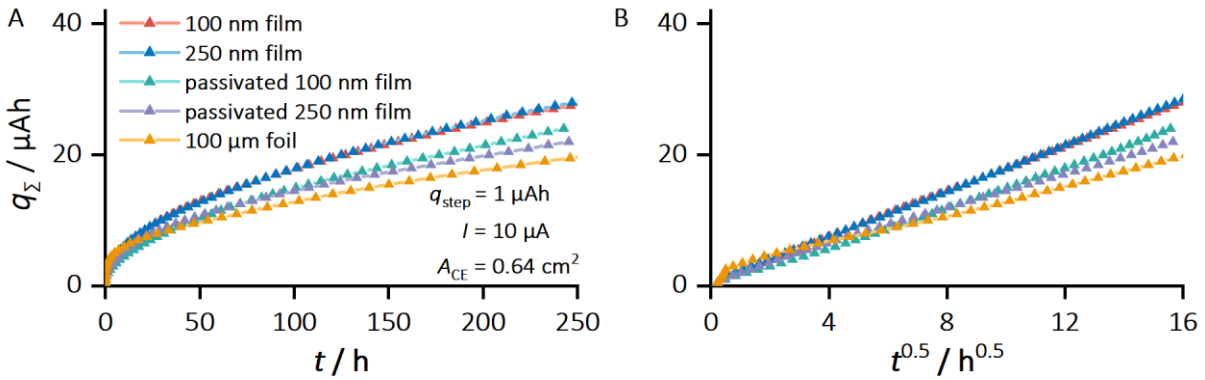

Figure S1: Comparison of as-deposited and post-deposition oxidized indium thin films, the latter labeled as "passivated". Here, the consumption of active lithium through side reactions (*i.e.*, SEI formation) is compared based on the accumulated charge (q_Σ) consumed in In|LPSCl|In/(InLi)$_x$ cells during CTTA experiments, plotted against t (A) and $t^{0.5}$ (B). Experiments were conducted at 25 °C and approximately 13 MPa. As-deposited films were exposed to ambient conditions for 8 days to facilitate In_2O_3 formation and passivation. The post-deposition passivation was confirmed through XPS analysis.

References

1. Alt, C. D. *et al.* In–Li Counter Electrodes in Solid-State Batteries – A Comparative Approach on Kinetics, Microstructure, and Chemomechanics. *Adv. Energy Mater.*; 10.1002/aenm.202404055 (2024).
2. Aktekin, B. *et al.* SEI Growth on Lithium Metal Anodes in Solid-State Batteries Quantified with Coulometric Titration Time Analysis. *Nat Commun* **14,** 6946; 10.1038/s41467-023-42512-y (2023).

8. List of Abbreviations

AAM	Alloy anode material
BE	Blocking electrode
CAM	Cathode active material
CC	Current Collector
CE	Counter electrode
CEI	Cathode electrolyte interphase
CTTA	Coulometric titration time analysis
dc	Direct current
e	Electron
EBSD	Electron backscatter diffraction
EDX	Energy dispersive X-ray spectroscopy
EIS	Electrochemical impedance spectroscopy
el	Electronic
ESW	Electrochemical stability window
h	Electron hole
ion	Ionic
LE	Liquid electrolyte
LIB	Lithium-ion batteries
LiPON	Lithium phosphorus oxynitride
LLZO	$Li_7La_3Zr_2O_{12}$
LME	Lithium metal electrode
LPS	β-Li_3PS_4
LPSCl	Li_6PS_5Cl
LPSX	Li_6PS_5X with X = Cl, Br, or I
MCI	Mixed conducting interphase
MIEC	Mixed ionic-electronic conductor
n	n-type referring to electrons
OCV	Open-circuit voltage

p	p-type referring to electron holes
RE	Reversible electrode
RFC	Reservoir-free cell
SE	Solid electrolyte
SEI	Solid-electrolyte interphase
SEM	Scanning electron microscopy
SHE	Standard hydrogen electrode
SOFC	Solid oxide fuel cell
ss	Steady state
SSB	Solid-state battery
V	Vacancy
XPS	X-ray photoelectron spectroscopy
XRD	X-ray diffraction

9. List of Symbols

a	Activity
A	Area
α	Characteristic exponent
c	Concentration
D	Diffusion coefficient
e	Elementary charge
E_{H}	Standard redox potential
F	Faraday constant
ΔG^0	Change of standard Gibbs free energy for a reaction
i	Current density
j	Flux (of species)
k	Parabolic rate constant
K	Equilibrium constant
l	Sample thickness
L	Phenomenological transport coefficient
M	Mean molar mass
μ	Chemical potential
μ^0	Standard chemical potential
$\tilde{\mu}$	Electrochemical potential
n	Charge carrier concentration
φ	Electric potential
q_Σ	Accumulated charge
R	Ideal gas constant
R_{int}	Interphase resistance
ρ	Mass density
σ	Partial conductivity
t	Reaction time
T	Temperature

u	Mobility
U_{cell}	Cell voltage
U_{decomp}	Decomposition voltage
x_{Li}	Stoichiometric factor of lithium
ξ	Interphase thickness
z	Charge number

10. Acknowledgements

I would like to express my heartfelt gratitude to everyone who has supported and accompanied me throughout my studies.

First and foremost, my sincerest thanks go to Prof. Jürgen Janek for giving me the opportunity to work, explore science, and grow within his research group. His constant support, curiosity – no matter the topic – and his patient, calm attitude provided a warm environment for professional and personal development under his supervision.

I am also sincerely grateful to Prof. Matthias Elm for his supervision and for serving as the second reviewer of my doctoral thesis. I greatly appreciated our discussions – chaotic as they sometimes were – and his patience in explaining solid-state physics. My gratitude also extends to Prof. Anja Henß for being part of my doctoral examination committee.

A special thanks goes to Prof. Matthew McDowell, who made my research stay at the Georgia Institute of Technology possible, supervised my work in his group, and kindly serves as a member of my examination committee. My time in Atlanta was truly memorable, and I am thankful to my friends and colleagues there: Dr. Stephanie Sandoval, John Harris, Lars Nelson, Udo Eze, Sonakshi Saini, and Matthew Yen – you made my stay a rewarding experience.

I am also very grateful to Dr. Janis K. Eckhardt, Dr. Till Fuchs, Dr. Burak Aktekin, and Dr. Sebastian Benz for their invaluable support and countless insightful discussions throughout my research. My highest appreciation goes to Dr. Philip Minnmann, who has guided and inspired me in every possible way – from answering my many early-stage questions to offering continuous advice throughout my journey. Thank you for "luring" me into joining RG Janek.

To my colleagues and friends in the RG Janek, thank you for the fun times, both at work and beyond, which made for a friendly and enjoyable atmosphere. Sometimes, it's not just about the destination, but the friends made along the way. In particular, I am grateful to Dr. Laura Goodwin, Dr. Jonas Hertle, David Schäfer, Thomas Schall, Simon Kunz, Dr. Luise Riegger, and Max Wacha for all the memorable moments and countless activities outside the lab. I refuse to call it *Zentrale*, but those who do know that I am grateful for their friendship. I also appreciate the hard work and dedication of my students, Nadia Müller, Sören Keuntje, Inga Lene Schneider, and Johannes Westphal, whose support and (wo-)manpower in the lab were invaluable. A big thank you to Dr. Klaus Peppler and Dr. Bjoern Luerssen for always having an open ear for my questions – and, of course, for always approving my vacation requests!

Beyond academia, I want to thank my friends for their encouragement and support – despite not always fully understanding what I was working on – and for providing much-needed distractions on weekends.

Finally, my deepest gratitude goes to my family for believing in me, standing by my side through challenges, and paving the way for my professional journey. And to my girlfriend Lisa, who had to endure my workload far too often during my doctoral studies, but on whom I could always rely – with you, life feels a little easier!